

NON-INVASIVE ACOUSTIC DETECTION OF VASCULAR DISEASES
FROM SKIN SURFACE USING COMPUTATIONAL TECHNIQUES WITH
FLUID-STRUCTURE INTERACTION

A THESIS SUBMITTED TO
THE GRADUATE SCHOOL OF NATURAL AND APPLIED SCIENCES
OF
MIDDLE EAST TECHNICAL UNIVERSITY

BY

HÜSEYİN ENES SALMAN

IN PARTIAL FULFILLMENT OF THE REQUIREMENTS
FOR
THE DEGREE OF DOCTOR OF PHILOSOPHY
IN
MECHANICAL ENGINEERING

SEPTEMBER 2018

Approval of the thesis:

**NON-INVASIVE ACOUSTIC DETECTION OF VASCULAR DISEASES
FROM SKIN SURFACE USING COMPUTATIONAL TECHNIQUES
WITH FLUID-STRUCTURE INTERACTION**

submitted by **HÜSEYİN ENES SALMAN** in partial fulfillment of the requirements for the degree of **Doctor of Philosophy in Mechanical Engineering, Middle East Technical University** by,

Prof. Dr. Halil Kalıpçılar
Dean, Graduate School of **Natural and Applied Sciences** _____

Prof. Dr. Mehmet Ali Sahir Arıkan
Head of Department, **Mechanical Engineering** _____

Assoc. Prof. Dr. Yiğit Yazıcıoğlu
Supervisor, **Mechanical Engineering Dept., METU** _____

Examining Committee Members:

Assoc. Prof. Dr. Mehmet Metin Yavuz
Mechanical Engineering Dept., METU _____

Assoc. Prof. Dr. Yiğit Yazıcıoğlu
Mechanical Engineering Dept., METU _____

Assoc. Prof. Dr. Oğuz Uzol
Aerospace Engineering Dept., METU _____

Prof. Dr. Selin Aradağ Çelebioğlu
Mechanical Engineering Dept.,
TOBB University of Economics and Technology _____

Assoc. Prof. Dr. Tuncay Karaçay
Mechanical Engineering Dept., Gazi University _____

Date: _____ **04.09.2018** _____

I hereby declare that all information in this document has been obtained and presented in accordance with academic rules and ethical conduct. I also declare that, as required by these rules and conduct, I have fully cited and referenced all material and results that are not original to this work.

Name, Last name: HÜSEYİN ENES SALMAN

Signature:

ABSTRACT

NON-INVASIVE ACOUSTIC DETECTION OF VASCULAR DISEASES FROM SKIN SURFACE USING COMPUTATIONAL TECHNIQUES WITH FLUID-STRUCTURE INTERACTION

Salman, Hüseyin Enes

Ph.D., Department of Mechanical Engineering

Supervisor: Assoc. Prof. Dr. Yiğit Yazıcıoğlu

September 2018, 223 pages

Atherosclerosis is a cardiovascular disease in which arterial occlusion adversely affects blood circulation. Because of the narrowing of the artery, the blood flow is disturbed and a recirculating flow occurs at the downstream of the stenosis exit. The dynamic pressure fluctuations on the inner arterial wall cause the blood vessel wall to vibrate and the resulting acoustic energy propagates through the surrounding soft tissue and reaches the skin surface. To understand the problem in more detail, computational analyses and experimental studies have been carried out. Vein, blood, muscle, fat and bones are modeled by means of computational analysis. The turbulence-induced dynamic pressure fluctuations are applied to the inner wall of the artery and the radial displacement, velocity and acceleration responses on the skin surface are investigated considering various flow rates, stenosis severities and structural material properties. The computational results show good agreement with the experimental findings. Vibration of the phantom tissue used in the experimental studies is determined using a contact microphone, an electronic stethoscope and a laser Doppler vibrometer. 70% stenosis is an important threshold value, because severities higher than 70% lead to significant

increase in vibration amplitudes. If the severity of stenosis is increased from 70% to 90%, the arterial vibration amplitudes increase by more than ten times. Arterial vibration is approximately proportional to the third power of the Reynolds number. When thickness of the tissue surrounding the artery is increased from 6.5 to 16.5 mm, the amplitudes are reduced by about 35%. The highest excitation is obtained about 20 mm downstream of the stenosis exit for a tissue thickness of 16.5 mm. The first two highly excited frequencies are determined as 30 and 60 Hz for the thigh, 100 and 200 Hz for the upper arm, 120 and 190 Hz for the neck. The optimum range for stenosis detection is between 200 and 500 Hz.

Keywords: Stenosis detection, Cardiovascular biomechanics, Turbulence-induced sound and vibration, Modal analysis

ÖZ

DAMAR HASTALIKLARINA GİRİŞİMSEL OLMAYAN AKUSTİK METOTLARLA TANI KOYMANIN KATI-SIVI ETKİLEŞİMLİ SAYISAL TEKNİKLER KULLANILARAK İNCELENMESİ

Salman, Hüseyin Enes

Doktora, Makina Mühendisliği Bölümü

Tez Yöneticisi: Doç. Dr. Yiğit Yazıcıoğlu

Eylül 2018, 223 sayfa

Ateroskleroz, arter içinde oluşan tıkanıklığın kan dolaşımını olumsuz etkilediği kardiyovasküler bir hastalıktır. Arterin daralması nedeniyle kan akışı bozulur ve tıkanıklık çıkışında bir devridaim akış bölgesi oluşur. İç arter duvarındaki dinamik basınç dalgalanmaları damarın titreşmesine neden olur ve ortaya çıkan akustik enerji damarı çevreleyen doku boyunca yayılarak cilt yüzeyine ulaşır. Problemi daha iyi anlamak için hesaplamalı analizler ve deneysel çalışmalar gerçekleştirilmiştir. Damar, kan, kas, yağ ve kemikler hesaplamalı çalışmalarda modellenmiştir. Türbülanslı akış nedeni ile oluşan dinamik basınç dalgalanmaları arterin iç duvarına uygulanmış ve çeşitli akış hızları, darlık şiddetleri ve malzeme özellikleri dikkate alınarak cilt yüzeyinde elde edilen radyal deplasman, hız ve ivmeler incelenmiştir. Sayısal modelleme ile elde edilen sonuçların deneysel bulgularla iyi bir şekilde uyduğu görülmüştür. Deneysel çalışmalarda kullanılan fantom dokusu üzerindeki titreşim, yüzey mikrofonu, elektronik stetoskop ve lazer Doppler titreşim ölçer kullanılarak belirlenmiştir. %70 tıkanıklık seviyesi önemli bir eşik değeridir, çünkü %70'in üzerindeki seviyelerde titreşim genliklerinde belirgin bir artış görülmüştür. Eğer tıkanıklık seviyesi %70'den %90'a çıkarsa,

damarın dış yüzeyindeki titreşim genlikleri on kattan daha fazla artmaktadır. Damar titreşimi yaklaşık olarak Reynolds sayısının üçüncü kuvveti ile orantılıdır. Damarı çevreleyen doku kalınlığı 6.5 mm'den 16.5 mm'ye çıkarıldığında, titreşim genlikleri yaklaşık olarak %35 oranında azalmıştır. 16.5 mm'lik bir doku kalınlığı için, doku yüzeyindeki en yüksek genlikler yaklaşık olarak tıkanıklık çıkışının 20 mm uzağında görülmüştür. Yüksek titreşim genliğine sahip ilk iki frekans, üst bacak için 30 Hz ve 60 Hz değerlerinde, üst kol için 100 Hz ve 200 Hz değerlerinde, boyun için 120 Hz ve 190 Hz değerlerinde gözlenmiştir. Damar tıkanıklığını tespit etmek için en uygun frekans aralığı 200 Hz ile 500 Hz arasındadır.

Anahtar Kelimeler: Damar tıkanıklığı teşhisi, Kardiyovasküler biyomekanik, Türbülans kaynaklı ses ve titreşim, Modal analiz

To the Ones who Care About Others

ACKNOWLEDGEMENTS

First of all, I would like to express my deepest gratitude to my supervisor Assoc. Prof. Dr. Yiğit Yazıcıoğlu for his guidance, criticism, encouragements, advice and insight throughout my research. I would like to thank Assoc. Prof. Dr. M. Metin Yavuz, Assoc. Prof. Dr. Oğuz Uzol and Assoc. Prof. Dr. Cüneyt Sert for their guidance, advice and inspiration throughout the research. I also would like to thank my colleague and roommate Kamil Özden for his moral support and encouragement.

Special thanks go to the Center of Wind Energy (METUWIND) for the use of scanning Laser Doppler vibrometer (PSV-400-B, Polytech, Auburn, MA) and the facilities.

I would like to thank BTech Innovation (Ankara, Turkey) for providing technical support for the reconstruction of three-dimensional models. I also would like to thank Servet Şehirli for the technical support during the tension and compression tests for the mechanical characterization of tissue phantom models.

I gratefully acknowledge the financial support from the Scientific and Technological Research Council of Turkey (TUBITAK) within the scope of BİDEB 2211/C scholarship programme during the research.

Finally, I am deeply grateful to my family for their faith in me. Especially I would like to thank my father Assoc. Prof. Dr. Rasim Ergun Salman who is an experienced cardiovascular surgeon, for sharing his experiences and valuable comments with me and encouraged me to study on this research.

TABLE OF CONTENTS

ABSTRACT	v
ÖZ.....	vii
ACKNOWLEDGEMENTS	x
TABLE OF CONTENTS	xi
LIST OF TABLES	xv
LIST OF FIGURES.....	xvi
CHAPTERS	
1 INTRODUCTION	1
1.1 Statement of the problem	1
1.2 Related studies in the literature	4
1.2.1 Generation of murmurs.....	4
1.2.2 Analytical studies	6
1.2.3 Experimental studies.....	7
1.2.4 Numerical studies	8
1.2.5 Spectral methods.....	10
1.2.6 Acoustic localization and beamforming	12
1.2.7 Noninvasive diagnostic methods	13
1.3 Aim of the study and contribution to the literature	14
1.4 Thesis outline	15
2 THEORY AND BACKGROUND	17
2.1 Formulation of the problem.....	17

2.2 Fluid excitation	21
2.3 Modelling the turbulence-induced acoustic pressure field	22
3 METHODS FOR MODELLING FLOW INDUCED ACOUSTIC FIELD...	33
3.1 Constitutive elements of the problem	34
3.2 Comparison of ANSYS and ADINA	36
3.3 Methods for applying the harmonic acoustic pressure field	38
4 IDEALIZED COMPUTATIONAL MODELS	47
4.1 The problem geometry for the idealized models	47
4.2 Material properties for the idealized models	48
4.3 Bare artery models	49
4.3.1 Mesh independence study for the bare artery analysis.....	50
4.3.2 Responses on the bare artery models	51
4.3.3 Average responses for the bare artery analysis	59
4.4 Soft tissue surrounded models	68
4.4.1 Responses for the soft tissue surrounded models.....	68
4.4.2 Average responses for the soft tissue surrounded models.....	78
5 REALISTIC COMPUTATIONAL MODELS	85
5.1 Mechanical properties of human body tissues	85
5.1.1 Hyperelasticity	88
5.1.2 Viscoelasticity	90
5.1.3 Realistic material properties of soft tissues	93
5.2 Realistic geometries based on the human anatomy	97
5.3 Physiological conditions in the peripheral arteries	101
5.4 Acoustic pressure field in the peripheral arteries.....	101

5.5	Simplistic thigh models	105
5.5.1	Pressure response on the simplistic thigh model	108
5.5.2	Radial velocity response on the simplistic thigh model	110
5.6	Simplistic upper arm models	114
5.6.1	Radial velocity response on the simplistic upper arm model	116
5.6.2	Pressure response on the simplistic upper arm model	123
5.7	Simplistic neck models	126
5.7.1	Radial velocity response on the simplistic neck model	128
5.7.2	Pressure response on the simplistic neck model	133
5.8	CT based models	135
5.9	Effect of modal damping coefficient	146
5.10	Partial derivative analysis for radial velocity responses	152
6	EXPERIMENTAL STUDIES	157
6.1	Experimental set-up	157
6.2	Mechanical characterization of the tissue phantom	161
6.3	Single-point LDV analysis	163
6.3.1	Bare tube analysis	163
6.3.2	Tissue surrounded models	166
6.4	Scanning LDV analysis	177
6.5	Measurements using contact microphone and electronic stethoscope ...	180
7	CONCLUSIONS AND FUTURE WORK	189
7.1	Idealized computational models	189
7.2	Realistic computational models	190
7.3	Experimental findings	192

7.4 State of art sensor technologies for non-invasive diagnosis	193
7.5 Future improvements	194
REFERENCES	195
CURRICULUM VITAE.....	221

LIST OF TABLES

TABLES

Table 2.1 The data used to approximate $F_{n1} \left[\frac{x}{D} \right]$ based on Figure 2.5.....	32
Table 4.1 Details of the meshes for the bare artery models	50
Table 4.2 Details of the meshes for soft tissue thickness of 6.5 mm.....	69
Table 4.3 Details of the meshes for soft tissue thickness of 16.5 mm.....	69
Table 4.4 Details of the meshes for soft tissue thickness of 36.5 mm.....	70
Table 5.1 Viscoelastic material properties	93
Table 5.2 Material parameters employed in the realistic computational analysis.....	96
Table 5.3 Mesh details for simplistic thigh model	107
Table 5.4 Mesh details for simplistic upper arm model	114
Table 5.5 Mesh details for simplistic neck model	126
Table 5.6 Mesh details for CT based thigh model.....	136
Table 5.7 Mesh details for CT based upper arm model.....	137
Table 5.8 Mesh details for CT based neck model	137
Table 6.1 Height difference between the upper and lower reservoirs for all experimental cases.....	159
Table 6.2 Frequency-varying modal damping coefficients employed in the computational models	167

LIST OF FIGURES

FIGURES

Figure 1.1 Obstructed coronary artery diagnosed using arteriography [8].	3
Figure 1.2 The concept of phonoangiography [13].	4
Figure 1.3 Comparison of in vivo experimental results with the turbulence spectrum of flow in a rigid pipe [13].	5
Figure 1.4 Average power spectra of the cardiac sounds from a selected portion of diastole. (a) Normal subject. (b) Patient with 70% stenosis in left coronary artery (adopted from [32]).	11
Figure 1.5 Experimental image of the acoustic shear wave energy field at 300 Hz, with the vessel and occlusion shown schematically (adopted from [34]).	13
Figure 2.1 Five characteristic zones in a stenosed pipe flow (adopted from [19]).	22
Figure 2.2 Effect of Reynolds number on the wall pressure spectra at 2D distance downstream of the constriction exit in case of 90% flow area reduction (adopted from [23]).	23
Figure 2.3 Effect of the distance to the constriction exit on the wall pressure spectra for 90% flow area reduction (adopted from [23]).	24
Figure 2.4 RMS pressure spectra for different stenosis levels and Reynolds numbers (adopted from [23]).	25
Figure 2.5 RMS wall pressure variation with x/D , normalized data – assorted Reynolds numbers and levels of stenosis (adopted from [23]).	26
Figure 2.6 Non-dimensional power spectral density $F_{n2} \left[\frac{fD}{u_j} \right]$ (adopted from [23]).	28
Figure 3.1 The models used for the sample cantilever beam problem. (a) ADINA. (b) ANSYS Workbench.	36
Figure 3.2 Two different harmonic loading cases for the cantilever beam. (a) Harmonic pressure of 1 Pa on the bottom line. (b) Harmonic pressures of 1 Pa and 2 Pa with a phase difference of 90° .	37
Figure 3.3 Comparison of acceleration responses for the top node at the free end of the cantilever beam considering 1 Pa of harmonic pressure load.	38

Figure 3.4 Comparison of acceleration responses for the top node at the free end of the cantilever beam considering 1 Pa and 2 Pa of harmonic pressure loads with a phase difference of 90°	38
Figure 3.5 Acoustic pressure amplitudes (dB ref: 1 Pa) as function of axial position and frequency for $Re = 2000$ with 87% stenosis. The color scale is used for dB.	39
Figure 3.6 Spatial and spectral functions used to generate the acoustic pressure field represented in Figure 3.5.....	40
Figure 3.7 Acoustic pressure amplitudes (dB ref: 1 Pa) and percent errors as function of axial position and frequency. For acoustic pressure contours, the color scale is used for dB. For percent error contours, the color scale is used for the magnitude of the percent error. (a) $Re = 1000$, 90% stenosis. (b) Percent error for (a). (c) $Re = 1000$, 70% stenosis. (d) Percent error for (c). (e) $Re = 2000$, 90% stenosis. (f) Percent error for (e). (g) $Re = 2000$, 70% stenosis. (h) Percent error for (g).....	41
Figure 3.8 Spectral functions at the point of highest sound generation for various Reynolds numbers and stenosis levels.	42
Figure 3.9 Spatial functions at 5 Hz for various Reynolds numbers and stenosis levels.....	42
Figure 3.10 (a) Phase contour plot (10 x 10 resolution) for $Re = 2000$ and 90% stenosis. Color scale is used for degree angle. (b) Acoustic pressure contour (dB re: 1 Pa) on the arterial wall (10 x 10 resolution) for $Re = 2000$ and 90% stenosis. Color scale is used for dB.	43
Figure 3.11 Phase maps for $Re = 2000$ and 87% stenosis considering a lumen diameter of 6.4 mm. The color scale is used for degree angle. (a) 10 x 10 resolution. (b) 20 x 20 resolution.	44
Figure 3.12 Acoustic pressure amplitudes (dB ref: 1 Pa) for a lumen diameter of 6.4 mm as function of axial position and frequency. The color scale is used for dB. (a) $Re = 2000$, 50% stenosis. (b) $Re = 1000$, 50% stenosis. (c) $Re = 2000$, 70% stenosis. (d) $Re = 1000$, 70% stenosis. (e) $Re = 2000$, 90% stenosis. (f) $Re = 1000$, 90% stenosis.....	45
Figure 3.13 Phase maps with resolution of 20 x 20 for a lumen diameter of 6.4 mm. The color scale is used for degree angle. (a) $Re = 2000$, 50% stenosis. (b) $Re = 1000$, 50% stenosis. (c) $Re = 2000$, 70% stenosis. (d) $Re = 1000$, 70% stenosis. (e) $Re = 2000$, 90% stenosis. (f) $Re = 1000$, 90% stenosis.	46
Figure 4.1 Sectional view of the axisymmetric idealized model. Flow is from left to right. Blood, artery and surrounding soft tissue are displayed by blue, green and yellow colors, respectively. Axial and radial coordinates are shown by x and r, respectively.....	48

Figure 4.2 Radial velocity response (dB ref: 1 mm/s) on outer surface of the artery for Re = 2000 with 90% stenosis. (a) Mesh 1. (b) Mesh 2. (c) Mesh 3. The color scale is used for dB. 51

Figure 4.3 Responses on the outer surface of the artery with 90% stenosis considering no phase map. (a) Radial displacement (dB ref: 1 mm) for Re = 1000. (b) Radial displacement (dB ref: 1 mm) for Re = 2000. (c) Radial velocity (dB ref: 1 mm/s) for Re = 1000. (d) Radial velocity (dB ref: 1 mm/s) for Re = 2000. (e) Radial acceleration (dB ref: 1 mm/s²) for Re = 1000. (f) Radial acceleration (dB ref: 1 mm/s²) for Re = 2000. 52

Figure 4.4 Radial velocity response (dB ref: 1 mm/s) on the outer surface of the artery considering no phase map. (a) Re = 1000, 50% Stenosis. (b) Re = 1000, 70% Stenosis. (c) Re = 1000, 90% Stenosis. (d) Re = 1000, 95% Stenosis. (e) Re = 2000, 50% Stenosis. (f) Re = 2000, 70% Stenosis. (g) Re = 2000, 90% Stenosis. (h) Re = 2000, 95% Stenosis. 54

Figure 4.5 (a) Maximum radial velocity response (within 0-600 Hz, 0-100 mm) for Re = 1000 and Re = 2000 as function of stenosis level. (b) Average radial velocity response (within 0-600 Hz, 0-100 mm) for Re = 1000 and Re = 2000 as function of stenosis level. 55

Figure 4.6 Radial velocity response (dB ref: 1 mm/s) on the outer surface of the artery considering 10 x 10 phase map. (a) Re = 1000, 50% Stenosis. (b) Re = 1000, 70% Stenosis. (c) Re = 1000, 90% Stenosis. (d) Re = 2000, 50% Stenosis. (e) Re = 2000, 70% Stenosis. (f) Re = 2000, 90% Stenosis..... 56

Figure 4.7 Radial velocity response (dB ref: 1 mm/s) on the outer surface of the artery considering 20 x 20 phase map. (a) Re = 1000, 50% Stenosis. (b) Re = 1000, 70% Stenosis. (c) Re = 1000, 90% Stenosis. (d) Re = 2000, 50% Stenosis. (e) Re = 2000, 70% Stenosis. (f) Re = 2000, 90% Stenosis..... 57

Figure 4.8 Radial velocity response (dB ref: 1 mm/s) on the outer surface of the artery for Re = 2000 with 87% stenosis. (a) No phase map, 2% modal damping. (b) 10 x 10 phase map, 2% modal damping. (c) 20 x 20 phase map, 2% modal damping. (d) No phase map, 5% modal damping. (e) No phase map, 10% modal damping. (f) No phase map, 20% modal damping. (g) Theory in air [22]. (h) Experiment in air [22]...... 58

Figure 4.9 Average radial velocity response (within 0-100 mm) on the outer surface of the artery as function of frequency considering no phase map. (a) Re = 1000. (b) Re = 2000. 60

Figure 4.10 Average radial velocity response (within 0-100 mm) on the outer surface of the artery as function of frequency considering 10 x 10 phase map. (a) Re = 1000. (b) Re = 2000..... 61

Figure 4.11 Average radial velocity response (within 0-100 mm) on the outer surface of the artery as function of frequency considering 20 x 20 phase map. (a) Re = 1000. (b) Re = 2000. 62

Figure 4.12 Comparison of the radial velocity response (within 0-100 mm) on the outer surface of the artery as function of frequency considering 90% stenosis. (a) Re = 1000. (b) Re = 2000. 63

Figure 4.13 Average radial velocity response (within 0-600 Hz) on the outer surface of the artery as function of axial distance downstream of the constriction exit considering no phase map. (a) Re = 1000. (b) Re = 2000. 64

Figure 4.14 Average radial velocity response (within 0-600 Hz) on the outer surface of the artery as function of axial distance downstream of the constriction exit considering 10 x 10 phase map. (a) Re = 1000. (b) Re = 2000. 65

Figure 4.15 Average radial velocity response (within 0-600 Hz) on the outer surface of the artery as function of axial distance downstream of the constriction exit considering 20 x 20 phase map. (a) Re = 1000. (b) Re = 2000. 66

Figure 4.16 Comparison of average radial velocity responses on the outer surface of the artery (within 0-600 Hz) as function of axial distance downstream of the constriction exit considering 90% stenosis for Re = 1000 and Re = 2000. 67

Figure 4.17 Radial velocity response (dB ref: 1 mm/s) on the outer surface of the surrounding soft tissue (0.1 MPa) for Re = 2000 with 90% stenosis considering no phase map. (a) 6.5 mm thickness, Mesh 1. (b) 6.5 mm thickness, Mesh 2. (c) 6.5 mm thickness, Mesh 3. (d) 16.5 mm thickness, Mesh 1. (e) 16.5 mm thickness, Mesh 2. (f) 16.5 mm thickness, Mesh 3. (g) 36.5 mm thickness, Mesh 1. (h) 36.5 mm thickness, Mesh 2. (i) 36.5 mm thickness, Mesh 3. 71

Figure 4.18 Responses on the outer surface of the surrounding soft tissue (0.1 MPa, 36.5 mm thickness) for Re = 2000 with 90% stenosis considering no phase map. (a) Radial displacement response (mm). (b) Radial velocity response (mm/s). (c) Radial acceleration response (mm/s²). 72

Figure 4.19 Radial velocity response (dB ref: 1 mm/s) on the outer surface of the surrounding soft tissue (0.1 MPa) with 36.5 mm thickness considering no phase map. (a) Re = 1000, 50% Stenosis. (b) Re = 2000, 50% Stenosis. (c) Re = 1000, 70% Stenosis. (d) Re = 2000, 70% Stenosis. (e) Re = 1000, 90% Stenosis. (f) Re = 2000, 90% Stenosis. 73

Figure 4.20 Radial velocity response (dB ref: 1 mm/s) on the outer surface of the surrounding soft tissue (0.1 MPa) with 36.5 mm thickness considering 10 x 10 phase map. (a) Re = 1000, 50% Stenosis. (b) Re = 2000, 50% Stenosis. (c) Re = 1000, 70% Stenosis. (d) Re = 2000, 70% Stenosis. (e) Re = 1000, 90% Stenosis. (f) Re = 2000, 90% Stenosis. 74

Figure 4.21 Responses on the outer surface of the surrounding soft tissue (0.1 MPa) for $Re = 2000$ with 90% stenosis considering no phase map. (a) Radial displacement (dB ref: 1 mm), 6.5 mm thickness. (b) Radial displacement (dB ref: 1 mm), 16.5 mm thickness. (c) Radial displacement (dB ref: 1 mm), 36.5 mm thickness. (d) Radial acceleration (dB ref: 1 mm/s²), 6.5 mm thickness. (e) Radial acceleration (dB ref: 1 mm/s²), 16.5 mm thickness. (f) Radial acceleration (dB ref: 1 mm/s²), 36.5 mm thickness. 75

Figure 4.22 Radial velocity response (dB ref: 1 mm/s) on the outer surface of the surrounding tissue for $Re = 2000$ with 90% stenosis considering no phase map. (a) 6.5 mm thickness, 0.1 MPa. (b) 6.5 mm thickness, 1 MPa. (c) 6.5 mm thickness, 10 MPa. (d) 16.5 mm thickness, 0.1 MPa. (e) 16.5 mm thickness, 1 MPa. (f) 16.5 mm thickness, 10 MPa. (g) 36.5 mm thickness, 0.1 MPa. (h) 36.5 mm thickness, 1 MPa. (i) 36.5 mm thickness, 10 MPa. 76

Figure 4.23 Radial velocity response (dB ref: 1 mm/s) on the outer surface of the surrounding tissue for $Re = 2000$ with 90% stenosis considering 10 x 10 phase map. (a) 6.5 mm thickness, 0.1 MPa. (b) 6.5 mm thickness, 1 MPa. (c) 6.5 mm thickness, 10 MPa. (d) 16.5 mm thickness, 0.1 MPa. (e) 16.5 mm thickness, 1 MPa. (f) 16.5 mm thickness, 10 MPa. (g) 36.5 mm thickness, 0.1 MPa. (h) 36.5 mm thickness, 1 MPa. (i) 36.5 mm thickness, 10 MPa. 77

Figure 4.24 Average radial velocity response (within 0-600 Hz) on the outer surface of the surrounding soft tissue (0.1 MPa, 36.5 mm thickness) as a function of axial distance downstream of the constriction exit considering no phase map. (a) $Re = 1000$. (b) $Re = 2000$ 79

Figure 4.25 Average responses (within 0-600 Hz) on the outer surface of the surrounding soft tissue (0.1 MPa) for $Re = 2000$ with 90% stenosis as function of axial distance downstream of the constriction exit considering no phase map. (a) Average radial displacement response. (b) Average radial acceleration response. 80

Figure 4.26 Comparison of average radial velocity responses (within 0-600 Hz) on the outer surface of the surrounding soft tissue (36.5 mm thickness) for $Re = 2000$ with 90% stenosis. 81

Figure 4.27 Comparison of average radial velocity response (within 0-100 mm) on the outer surface of the surrounding soft tissue (0.1 MPa, 36.5 mm thickness) as function of frequency. (a) $Re = 1000$. (b) $Re = 2000$ 82

Figure 4.28 Average responses (within 0-100 mm) on the outer surface of the surrounding soft tissue (0.1 MPa) as function of frequency for $Re = 2000$ with 90% stenosis considering no phase map. (a) Average radial displacement response. (b) Average radial acceleration response. 83

Figure 4.29 Comparison of average radial velocity responses (within 0-100 mm) on the outer surface of the surrounding soft tissue (36.5 mm thickness, no phase

map) as function of frequency for $Re = 2000$ with 90% stenosis considering various elastic modulus values.....	84
Figure 5.1 Stress-strain response of a typical soft tissue and corresponding collagen fiber alignment (adopted from [66]).....	87
Figure 5.2 Typical response of a viscoelastic solid (adopted from [93]).....	91
Figure 5.3 (a) Generalized Maxwell model. (b) Normalized dissipation W_D versus frequency according to material parameters for artery. Solid line denotes the dissipation of whole model. Each dotted line corresponds to a specific Maxwell element (adopted from [94]).	92
Figure 5.4 Stress-strain response of passive muscle tissue (adopted from [128]).....	94
Figure 5.5 (a) Real cross-sectional view of thigh [145]. (b) Simplistic 3D model of thigh. (c) CT-based 3D model of thigh.	98
Figure 5.6 (a) Real cross-sectional view of the upper arm [147]. (b) Simplistic 3D model of the upper arm. (c) CT-based 3D model of the upper arm.....	99
Figure 5.7 (a) Simplistic 3D model of the neck. (b) Real cross-sectional view of the neck [149]. (c) CT-based 3D model of the neck.	100
Figure 5.8 (a) Average velocity (V_{avg}) for fully developed pipe flow. (b) Sample blood velocity waveform for a peripheral artery (adopted from [151]).....	101
Figure 5.9 Femoral artery in the thigh. (a) Acoustic pressure (dB ref: 1 Pa) for 90% stenosis. (b) Acoustic pressure (dB ref: 1 Pa) for 70% stenosis. (c) Phase map for 90% stenosis. (d) Phase map for 70% stenosis.	103
Figure 5.10 Brachial artery in the upper arm. (a) Acoustic pressure (dB ref: 1 Pa) for 90% stenosis. (b) Acoustic pressure (dB ref: 1 Pa) for 70% stenosis. (c) Phase map for 90% stenosis. (d) Phase map for 70% stenosis.....	104
Figure 5.11 Common carotid artery in the neck. (a) Acoustic pressure (dB ref: 1 Pa) for 90% stenosis. (b) Acoustic pressure (dB ref: 1 Pa) for 70% stenosis. (c) Phase map for 90% stenosis. (d) Phase map for 70% stenosis.	105
Figure 5.12 Radial velocity response (dB ref: 1 mm/s) as function of axial distance and frequency for simplistic thigh model with 90% stenosis. Stenosis exit is placed at 0 mm. (a) Mesh 1. (b) Mesh 2. (c) Mesh 3. (d) Average of radial velocity responses for simplistic thigh model. Amplitudes within 0-250 mm are averaged at each frequency.....	106
Figure 5.13 (a) Simplistic thigh model – (Top line depicts the nodes on the skin which are closest to the femoral artery in radial direction). (b) Fixed regions used to measure the pressure on the skin.....	107

Figure 5.14 Fixed elements to determine the pressure on skin (Black region depicts the center of the fixed region containing four elements used to determine the pressure response). 108

Figure 5.15 Pressure response (dB ref: 1 Pa) on the skin of simplistic thigh model (x, y and z regions are represented in Figure 5.13). (a) Stenosis at 0 mm. (b) Stenosis at 125 mm. (c) Stenosis at 220 mm..... 109

Figure 5.16 (a) Average pressure response (dB ref: 1 Pa) on the skin of simplistic thigh model considering different stenosis levels. (b) Average pressure response of simplistic thigh model for phased and no phased analysis. 110

Figure 5.17 Radial velocity response (dB ref: 1 mm/s) as function of axial distance and frequency for simplistic thigh model with 90% stenosis. Stenosis exit is placed at 0 mm. (a) 10 x 10 phase map. (b) No phase map. (c) Average of radial velocity responses considering 10 x 10 phase map and no phase map..... 111

Figure 5.18 Radial velocity response (dB ref: 1 mm/s) as function of axial distance and frequency for simplistic thigh model considering no phase map. Stenosis exit is placed at 0 mm. (a) 70% stenosis. (b) 90% stenosis. (c) 95% stenosis. (d) Average of radial velocity responses considering various stenosis levels. 112

Figure 5.19 Radial velocity response (dB ref: 1 mm/s) as function of axial distance and frequency for simplistic thigh model with 90% stenosis considering different constriction locations. Sample anti-resonance curves are represented on the response contours. (a) Stenosis exit at 0 mm. (b) Stenosis exit at 50 mm. (c) Stenosis exit at 125 mm. (d) Stenosis exit at 150 mm. (e) Stenosis exit at 200 mm. 113

Figure 5.20 Radial velocity response (dB ref: 1 mm/s) as function of axial distance and frequency for simplistic upper arm model with 90% stenosis. Stenosis exit is placed at 0 mm. (a) Mesh 1. (b) Mesh 2. (c) Mesh 3. (d) Average of radial velocity responses for simplistic upper arm model. Response amplitudes within 0-140 mm are averaged at each frequency. 115

Figure 5.21 (a) Simplistic upper arm model – (Red lines depict the nodes on top and lateral side of the model). (b) Fixed x, y, z-regions used to measure the pressure on skin of the simplistic upper arm model..... 116

Figure 5.22 Radial velocity response (dB ref: 1 mm/s) as function of axial distance and frequency. Stenosis exit is placed at 0 mm. (a) 50% stenosis. (b) 70% stenosis. (c) 90% stenosis. (d) 95% stenosis. (e) Average of radial velocity responses for simplistic upper arm model. Response amplitudes within 0-140 mm are averaged at each frequency. 117

Figure 5.23 Radial velocity response (dB ref: 1 mm/s) as function of axial distance and frequency for simplistic upper arm model with 90% stenosis. Stenosis exit is placed at 0 mm. (a) Bottom line. (b) Lateral line. (c) Top line. (d) Average of radial velocity responses for simplistic upper arm model..... 118

Figure 5.24 Radial velocity response (dB ref: 1 mm/s) as function of axial distance and frequency for simplistic upper arm model with 90% stenosis. Stenosis exit is placed at 0 mm. (a) No phase map. (b) 10 x 10 phase map. (c) Average of radial velocity responses for simplistic upper arm model. 119

Figure 5.25 Radial velocity response (dB ref: 1 mm/s) as function of axial distance and frequency for simplistic upper arm model with 90% stenosis. (a) Without modelling bone. (b) With modelling bone. (c) Average of radial velocity responses for simplistic upper arm model. 120

Figure 5.26 Radial velocity response (dB ref: 1 mm/s) as function of axial distance and frequency for simplistic upper arm model with 90% stenosis. Stenosis exit is placed at 0 mm. (a) Linear fat model (25 kPa). (b) Linear fat (25 kPa) and skin (1 MPa) model. (c) Nonlinear model. (d) Average of radial velocity responses for simplistic upper arm model. 121

Figure 5.27 Radial velocity response (dB ref: 1 mm/s) as function of axial distance and frequency for simplistic upper arm model with 90% stenosis considering different constriction locations. (a) Stenosis exit at 0 mm. (b) Stenosis exit at 40 mm. (c) Stenosis exit at 80 mm. (d) Stenosis exit at 120 mm. 122

Figure 5.28 Pressure response (dB ref: 1 Pa) on the skin surface of simplistic upper arm model (x, y and z regions are represented in Figure 5.21). (a) Stenosis at 0 mm. (b) Stenosis at 40 mm. (c) Stenosis at 80 mm. (d) Stenosis at 120 mm. 124

Figure 5.29 (a) Average pressure response (dB ref: 1 Pa) of simplistic upper arm model considering different stenosis levels. (b) Average pressure response of simplistic upper arm model on top, side and bottom lines. The top line is the radially closest line to the brachial artery. 125

Figure 5.30 Radial velocity response (dB ref: 1 mm/s) as function of axial distance and frequency for simplistic neck model with 90% stenosis. Stenosis exit is placed at 0 mm. (a) Mesh 1. (b) Mesh 2. (c) Mesh 3. (d) Average of radial velocity responses for simplistic neck model. Response amplitudes within 0-70 mm are averaged at each frequency. 127

Figure 5.31 (a) Simplistic neck model – (Red lines depict the nodes on the front of trachea and the closest line to the artery in radial direction). (b) Fixed regions used to measure the pressure on skin of the simplistic neck model. 128

Figure 5.32 Radial velocity response (dB ref: 1 mm/s) as function of axial distance and frequency for simplistic neck model considering 90% stenosis with no phase map. (a) Stenosis at 0 mm. (b) Stenosis at 30 mm. (c) Stenosis at 55 mm. 128

Figure 5.33 Radial velocity response (dB ref: 1 mm/s) as function of axial distance and frequency for simplistic neck model. Stenosis exit is placed at 0 mm. (a) 50% stenosis. (b) 70% stenosis. (c) 90% stenosis. (d) 95% stenosis. (e) Average of radial velocity responses for simplistic neck model. Response amplitudes within 0-70 mm are averaged at each frequency. 129

Figure 5.34 Radial velocity response (dB ref: 1 mm/s) as function of axial distance and frequency for simplistic neck model. Stenosis exit is placed at 0 mm. (a) 10 x 10 phase map. (b) No phase map. (c) Average of radial velocity responses for simplistic neck model. Response amplitudes within 0-70 mm are averaged at each frequency..... 130

Figure 5.35 Radial velocity response (dB ref: 1 mm/s) as function of axial distance and frequency for simplistic neck model. Stenosis exit is placed at 0 mm. (a) Without modelling the vein. (b) With modelling the vein. (c) Average of radial velocity responses for simplistic neck model. Response amplitudes within 0-70 mm are averaged at each frequency. 131

Figure 5.36 Radial velocity response (dB ref: 1 mm/s) as function of axial distance and frequency for simplistic neck model. Stenosis exit is placed at 0 mm. (a) Front line on the neck. (b) Back line on the neck. (c) Closest line to the artery in radial direction. (d) Average of radial velocity responses for simplistic neck model. Response amplitudes within 0-70 mm are averaged at each frequency. 132

Figure 5.37 Pressure response (dB ref: 1 Pa) on the skin of simplistic neck model (x and y regions are represented in Figure 5.31). (a) Stenosis at 0 mm. (b) Stenosis at 30 mm. (c) Stenosis at 55 mm..... 134

Figure 5.38 (a) Average pressure response (dB ref: 1 Pa) of simplistic neck model considering different stenosis levels. (b) Average pressure responses of simplistic neck model on the front of the neck, the back of the neck and the closest line to the artery in the radial direction. 135

Figure 5.39 Radial velocity response (dB ref: 1 mm/s) as function of axial distance and frequency for CT based models with 90% stenosis considering 2% modal damping. Stenosis exit is placed at 0 mm. (a) Thigh, Mesh 1. (b) Thigh, Mesh 2. (c) Thigh, Mesh 3. (d) Upper arm, Mesh 1. (e) Upper arm, Mesh 2. (f) Upper arm, Mesh 3. (g) Neck, Mesh 1. (h) Neck, Mesh 2. (i) Neck, Mesh 3..... 138

Figure 5.40 Radial velocity response (dB ref: 1 mm/s) as function of axial distance and frequency for CT based models considering 10% modal damping. Stenosis exit is placed at 0 mm. (a) Thigh, 70% stenosis. (b) Thigh, 80% stenosis. (c) Thigh, 90% stenosis. (d) Upper arm, 70% stenosis. (e) Upper arm, 80% stenosis. (f) Upper arm, 90% stenosis. (g) Neck, 70% stenosis. (h) Neck, 80% stenosis. (i) Neck, 90% stenosis..... 140

Figure 5.41 Sum of response amplitudes for upper arm models considering 90% stenosis and 10% modal damping. The highest summation amplitudes are shown in circles which are indicating the stenosis location. (a) Simplistic, 0 mm. (b) CT based, 0 mm. (c) Simplistic, 40 mm. (d) CT based, 47 mm. (e) Simplistic, 80 mm. (f) CT based, 93 mm. (g) Simplistic, 120 mm. (h) CT based, 117 mm. 141

Figure 5.42 Radial velocity response (dB ref: 1 mm/s) as function of axial distance and frequency for CT based thigh model considering 90% stenosis and 2% modal

damping. (a) Stenosis at 0 mm. (b) Stenosis at 50 mm. (c) Stenosis at 100 mm. (d) Stenosis at 150 mm. (e) Stenosis at 200 mm..... 142

Figure 5.43 Radial velocity response (dB ref: 1 mm/s) as function of axial distance and frequency for CT based upper arm model considering 90% stenosis and 2% modal damping. (a) Stenosis at 0 mm. (b) Stenosis at 47 mm. (c) Stenosis at 93 mm. (d) Stenosis at 117 mm..... 143

Figure 5.44 Radial velocity response (dB ref: 1 mm/s) as function of axial distance and frequency for CT based neck model considering 90% stenosis and 2% modal damping. (a) Stenosis at 0 mm. (b) Stenosis at 24 mm. (c) Stenosis at 48 mm.. 144

Figure 5.45 Average pressure response (dB ref: 1 Pa) comparison for simplistic and CT based models considering 2% modal damping. Stenosis exit is placed at 0 mm. (a) Thigh model. (b) Upper arm model. (c) Neck model..... 145

Figure 5.46 Radial velocity response (dB ref: 1 mm/s) as function of axial distance and frequency for simplistic thigh model with 90% stenosis severity, considering different constriction locations and modal damping coefficients. (a) 0 mm, 2%. (b) 0 mm, 10%. (c) 0 mm, 20%. (d) 50 mm, 2%. (e) 50 mm, 10%. (f) 50 mm, 20%. (g) 125 mm, 2%. (h) 125 mm, 10%. (i) 125 mm, 20%. (j) 150 mm, 2%. (k) 150 mm, 10%. (l) 150 mm, 20%. (m) 200 mm, 2%. (n) 200 mm, 10%. (o) 200 mm, 20%..... 147

Figure 5.47 Radial velocity response (dB ref: 1 mm/s) as function of axial distance and frequency for simplistic upper arm model with 90% stenosis severity, considering different constriction locations and modal damping coefficients. (a) 0 mm, 2%. (b) 0 mm, 10%. (c) 0 mm, 20%. (d) 40 mm, 2%. (e) 40 mm, 10%. (f) 40 mm, 20%. (g) 80 mm, 2%. (h) 80 mm, 10%. (i) 80 mm, 20%. (j) 120 mm, 2%. (k) 120 mm, 10%. (l) 120 mm, 20%. 148

Figure 5.48 Radial velocity response (dB ref: 1 mm/s) as function of axial distance and frequency for CT based thigh model with 90% stenosis severity, considering different constriction locations and modal damping coefficients. (a) 0 mm, 2%. (b) 0 mm, 10%. (c) 0 mm, 20%. (d) 50 mm, 2%. (e) 50 mm, 10%. (f) 50 mm, 20%. (g) 100 mm, 2%. (h) 100 mm, 10%. (i) 100 mm, 20%. (j) 150 mm, 2%. (k) 150 mm, 10%. (l) 150 mm, 20%. (m) 200 mm, 2%. (n) 200 mm, 10%. (o) 200 mm, 20%..... 149

Figure 5.49 Radial velocity response (dB ref: 1 mm/s) as function of axial distance and frequency for CT based upper arm model with 90% stenosis severity, considering different constriction locations and modal damping coefficients. (a) 0 mm, 2%. (b) 0 mm, 10%. (c) 0 mm, 20%. (d) 47 mm, 2%. (e) 47 mm, 10%. (f) 47 mm, 20%. (g) 93 mm, 2%. (h) 93 mm, 10%. (i) 93 mm, 20%. (j) 117 mm, 2%. (k) 117 mm, 10%. (l) 117 mm, 20%. 150

Figure 5.50 Radial velocity response (dB ref: 1 mm/s) as function of axial distance and frequency for CT based neck model with 90% stenosis severity, considering different constriction locations and modal damping coefficients. (a) 0 mm, 2%. (b)

0 mm, 10%. (c) 0 mm, 20%. (d) 24 mm, 2%. (e) 24 mm, 10%. (f) 24 mm, 20%. (g) 48 mm, 2%. (h) 48 mm, 10%. (i) 48 mm, 20%. 151

Figure 5.51 Partial derivative analysis for CT based thigh model considering 90% stenosis and 2% damping. Stenosis exit is located at 0 mm. (a) Radial velocity response. (b) First derivative with respect to distance $\left(\frac{\partial}{\partial x}\right)$. (c) First derivative with respect to frequency $\left(\frac{\partial}{\partial f}\right)$. (d) Derivative with respect to distance and frequency $\left(\frac{\partial^2}{\partial x \partial f}\right)$. (e) Second derivative with respect to frequency $\left(\frac{\partial^2}{\partial f \partial f}\right)$. (f) Second derivative with respect to distance $\left(\frac{\partial^2}{\partial x \partial x}\right)$. (g) Sum of amplitudes in (a). (h) Sum of amplitudes in (b). (i) Sum of amplitudes in (c). (j) Sum of amplitudes in (d). (k) Sum of amplitudes in (e). (l) Sum of amplitudes in (f)..... 153

Figure 5.52 Partial derivative analysis for CT based upper arm model considering 90% stenosis and 2% damping. Stenosis exit is located at 0 mm. (a) Radial velocity response. (b) First derivative with respect to distance $\left(\frac{\partial}{\partial x}\right)$. (c) First derivative with respect to frequency $\left(\frac{\partial}{\partial f}\right)$. (d) Derivative with respect to distance and frequency $\left(\frac{\partial^2}{\partial x \partial f}\right)$. (e) Second derivative with respect to frequency $\left(\frac{\partial^2}{\partial f \partial f}\right)$. (f) Second derivative with respect to distance $\left(\frac{\partial^2}{\partial x \partial x}\right)$. (g) Sum of amplitudes in (a). (h) Sum of amplitudes in (b). (i) Sum of amplitudes in (c). (j) Sum of amplitudes in (d). (k) Sum of amplitudes in (e). (l) Sum of amplitudes in (f)..... 154

Figure 5.53 Partial derivative analysis for CT based neck model considering 90% stenosis and 2% damping. Stenosis exit is located at 0 mm. (a) Radial velocity response. (b) First derivative with respect to distance $\left(\frac{\partial}{\partial x}\right)$. (c) First derivative with respect to frequency $\left(\frac{\partial}{\partial f}\right)$. (d) Derivative with respect to distance and frequency $\left(\frac{\partial^2}{\partial x \partial f}\right)$. (e) Second derivative with respect to frequency $\left(\frac{\partial^2}{\partial f \partial f}\right)$. (f) Second derivative with respect to distance $\left(\frac{\partial^2}{\partial x \partial x}\right)$. (g) Sum of amplitudes in (a). (h) Sum of amplitudes in (b). (i) Sum of amplitudes in (c). (j) Sum of amplitudes in (d). (k) Sum of amplitudes in (e). (l) Sum of amplitudes in (f)..... 155

Figure 6.1 (a) Parts of the cylindrical mold. (b) Liquid-mixture poured in the hollow-cylindrical mold. (c) Stenosis elements (Left to right, 95, 90, 80 and 70% stenosis)..... 158

Figure 6.2 Schematic representation of experimental setup. 160

Figure 6.3 (a) Tissue phantom with thickness of 16.5 mm. (b) Retroreflective painted surface to improve LDV signal quality. (c) Experimental setup placed on the optical table to measure radial velocity responses on the phantom surface.. 160

Figure 6.4 (a) Stress-strain data for tissue phantom. (b) Relaxation behavior of tissue phantom. Force relaxation is observed within the range of 180 and 280 s. Relaxation function given in (6.1) is obtained by means of Prony series expansion using the data within 180 and 280 s to determine the viscoelastic material parameters. (c) Test setup for tension tests. (d) Test setup for compression tests..... 162

Figure 6.5 Radial velocity response (dB ref: 1 mm/s) on the outer surface of fluid-filled bare latex tube considering 87% stenosis. Stenosis exit is located at 0 mm. (a) $Re = 1000$, ~45 mmHg gauge pressure. (b) $Re = 1000$, ~15 mmHg gauge pressure. (c) $Re = 2000$, ~15 mmHg gauge pressure. (d) Adopted from Ref. [22]. $Re = 1000$, ~45 mmHg gauge pressure. (e) Adopted from Ref. [22]. $Re = 1000$, ~15 mmHg gauge pressure. (f) Adopted from Ref. [22]. $Re = 2000$, ~15 mmHg gauge pressure. 164

Figure 6.6 Radial velocity response (dB ref: 1 mm/s) on the outer surface of fluid-filled bare latex tube considering 90% stenosis. Mean pressure is adjusted to ~35 mmHg gauge. Stenosis exit is located at 0 mm. (a) $Re = 1750$, 0% tube extension. (b) $Re = 1750$, 15% tube extension. (c) $Re = 1000$, 15% tube extension..... 166

Figure 6.7 Radial velocity response (dB ref: 1 mm/s) on the outer surface of 16.5 mm thickness tissue phantom considering 90% stenosis with $Re = 1750$. Stenosis exit is located at 0 mm. Mean pressure is adjusted to ~35 mmHg gauge. (a) Experimental result. (b) Computational result using frequency-varying modal damping coefficients given in Table 6.2. (c) Computational result using 1% modal damping. (d) Computational result using 10% modal damping. Black dash line indicates border line. (e) Computational result using 15% modal damping. Orange dash line indicates border line. (f) Computational result using 20% modal damping. Red dash line indicates border line. 168

Figure 6.8 Radial velocity response (dB ref: 1 mm/s) on the outer surface of 16.5 mm thickness tissue phantom with $Re = 1750$. Stenosis exit is located at 0 mm. Mean pressure is adjusted to ~35 mmHg gauge with 0% tube extension. (a) Experiment, 90% stenosis. (b) Computational result, 90% stenosis. (c) Experiment, 80% stenosis. (d) Computational result, 80% stenosis. (e) Experiment, 70% stenosis. (f) Computational result, 70% stenosis. (g) Experiment, 55% stenosis. (h) Computational result, 55% stenosis. (i) Experiment, 0% stenosis..... 170

Figure 6.9 Average of the experimental radial velocity responses given in Figure 6.8(a), (c), (e) and (g). 171

Figure 6.10 Experimental radial velocity response (dB ref: 1 mm/s) on the outer surface of 16.5 mm thickness tissue phantom considering 90% stenosis with $Re = 1750$. Mean pressure is adjusted to ~35 mmHg gauge with 0% tube extension. (a) Stenosis exit located at 0 mm. (b) Stenosis exit located at 25 mm. (c) Stenosis exit located at 50 mm. (d) Average responses within 0 and 600 Hz for experimental

results presented in (a), (b), and (c). Peak activity points are indicated by arrows..... 172

Figure 6.11 Radial velocity response (dB ref: 1 mm/s) on the outer surface of tissue phantom considering 90% stenosis with $Re = 1750$. Mean pressure is adjusted to ~35 mm Hg gauge with 0% tube extension. Stenosis exit is located at 0 mm. (a) Experiment, 6.5 mm phantom thickness. (b) Experiment, 16.5 mm phantom thickness. (c) Experiment, 36.5 mm phantom thickness. (d) Computational result, 6.5 mm phantom thickness. (e) Computational result, 16.5 mm phantom thickness. (f) Computational result, 36.5 mm phantom thickness. (g) Average responses within 0 and 600 Hz for experimental results presented in (a), (b) and (c). Peak activity points are indicated by arrows. 174

Figure 6.12 Experimental radial velocity response (dB ref: 1 mm/s) on the outer surface of 16.5 mm thickness tissue phantom considering 90% stenosis with $Re = 1000$ and 0% tube extension. (a) Mean pressure of 27 mmHg gauge. (b) Mean pressure of 35 mmHg gauge. (c) Mean pressure of 48 mmHg gauge. 175

Figure 6.13 Radial velocity response (dB ref: 1 mm/s) on the outer surface of 16.5 mm thickness tissue phantom considering 90% stenosis. Mean pressure is adjusted to ~35 mmHg gauge with 0% tube extension. Stenosis exit is located at 0 mm. (a) Experiment, $Re = 1750$. (b) Experiment, $Re = 1000$. (c) Computational result, $Re = 1750$. (d) Computational result, $Re = 1000$. (e) Average responses within 0 and 600 Hz for experimental results presented in (a) and (b)..... 176

Figure 6.14 Rectangular prismatic tissue phantom model. The length, width and height of the rectangular prism are 95, 40 and 60 mm, respectively. 299 points on the lateral surface (23 x 13 grid) are used for scanning LDV measurements. Latex rubber drainage tube is placed at a height of 40 mm from the ground. 177

Figure 6.15 Average velocity amplitudes within 0 and 600 Hz (dB ref: 1 mm/s) on the scanned lateral surface of the rectangular prismatic tissue phantom considering 90% stenosis with $Re = 1000$. Mean pressure is adjusted to ~20 mmHg gauge with 0% tube extension. Flow is from right to left. Stenosis exit is placed at a height of 40 mm and located at a distance of 55 mm from the right side. 178

Figure 6.16 Velocity amplitudes at various frequencies (dB ref: 1 mm/s) on the scanned lateral surface of the rectangular prismatic tissue phantom considering 90% stenosis with $Re = 1000$. Flow is from right to left. Mean pressure is adjusted to ~20 mmHg gauge with 0% tube extension. Relatively increased amplitudes due to the stenosis are shown in black circled regions. Reflected signal quality is not adequate in blue circled regions..... 179

Figure 6.17 Responses at A, B, and C measured by contact microphone for Reynolds number 1750, 16.5 mm phantom material thickness, 35 mmHg gauge pressure and 90% stenosis. 180

Figure 6.18 Responses at A, B, and C measured by electronic stethoscope for Reynolds number 1750, 16.5 mm phantom material thickness, 35 mmHg gauge pressure and 90% stenosis. Stenosis exit is placed at 0 mm. 181

Figure 6.19 Responses at A, B, and C measured by electronic stethoscope for Reynolds number 1750, 16.5 mm phantom material thickness, 35 mmHg gauge pressure and 90% stenosis. Stenosis exit is placed at 25 mm. 182

Figure 6.20 Responses at A, B, and C measured by electronic stethoscope for Reynolds number 1750, 16.5 mm phantom material thickness, 35 mmHg gauge pressure and 90% stenosis. Stenosis exit is placed at 50 mm. 183

Figure 6.21 Comparison of responses for stenosis severities of 70, 80 and 90%. Reynolds number, phantom thickness and gauge pressure are 1750, 16.5 mm and 35 mmHg, respectively (Stet: Electronic stethoscope, Mic: Contact microphone). 184

Figure 6.22 Comparison of responses for 6.5, 16.5 and 36.5 mm (20, 40 and 80 mm outer diameters) thicknesses, respectively. Reynolds number, stenosis severity and gauge pressure are 1750, 90% and 35 mmHg, respectively (Ste: Electronic stethoscope, mic: Contact microphone). 185

Figure 6.23 Comparison of responses for Reynolds numbers 1000 and 1750. Tissue phantom thickness, stenosis severity and gauge pressure are 16.5 mm, 90% and 35 mmHg, respectively (Ste: Electronic stethoscope, Mic: Contact microphone). . 186

Figure 6.24 Comparison of responses using single-point LDV, contact microphone and electronic stethoscope for Reynolds number 1750, 16.5 mm tissue phantom thickness, 90% stenosis and 35 mmHg gauge pressure (STET: Electronic stethoscope, MIC: Contact microphone, LDV: Single point LDV). The peaks in the responses are shown inside the dashed circles. 187

CHAPTER 1

INTRODUCTION

1.1 Statement of the problem

Atherosclerosis is a cardiovascular disease that causes thickening of the arterial wall due to accumulation of fatty substances such as cholesterol [1]. Atherosclerotic lesions chronically expand asymptotically and a soft plaque may rupture forming a thrombus. The intraluminal thrombi can clog small veins in the circulatory system and cause sudden thromboembolism. In addition to embolism, atherosclerotic lesions may enlarge until the blood flow is severely reduced or until the lumen is completely closed (ischemic insufficiency). In the case of an infarct which may be caused by one of the above-mentioned mechanisms, the tissue fed by the artery will die within a few minutes. Atherosclerosis may occur in any part of the circulatory system especially in the arteries feeding the brain, heart, kidneys, arms and legs.

Atherosclerosis is usually found in the major arteries and usually begins in early adolescence. For the vast majority of the population, it is not recognized by most of the diagnostic methods in the first years of the disease progression. Depending on the location of the atherosclerotic lesions, Coronary Artery Disease (CAD), Stroke or Peripheral Arterial Occlusive Disease (PAOD) may develop. CAD is the result of plaque accumulation on the inner walls of coronary arteries that feed myocardium (heart muscle). Symptoms of this disease usually appear at an advanced stage, but most of CAD individuals show no symptoms for years. After years of silent progression, plaque rupture may occur and restrict blood flow to the heart muscle. CAD is not only the leading cause of death in the world, it is also the

most common cause of sudden death, and at the same time is the most common cause of mortality in men and women over 20 years of age [2].

Stroke or Cerebrovascular Accident (CVA) is the rapid loss of brain functions due to decrease in the blood supply to the brain due to ischemia caused by a blockage or a hemorrhage. Affected area of the brain will be unable to function, resulting in impaired motor, sensory, communication and cognitive abilities. A stroke can cause permanent disabilities and even sudden death. It is the leading cause of adult disability in the United States and Europe and the second leading cause of death worldwide [3].

PAOD is the artery occlusion except the heart and brain related ones. It usually refers to the lack of blood supply to the legs, arms and other vital organs. PAOD patients carry a higher risk for other potentially more serious cardiovascular events such as CAD and stroke. For PAOD patients, the risk of CAD in 10 years is more than 20% [4].

Cardiovascular diseases are usually diagnosed by cardiac stress testing and/or angiography. Interestingly, the cardiac stress test can detect only 75% or greater lumen obstruction severities. Angioplasty treatment methods can be applied at later stages of disease, but due to invasive nature of this procedure, it is preferred when there is a doubt about serious arterial occlusion. Therefore, these methods can only be applied in cases where severe stenosis is present, but most of blood flow disruption occurs after 50% lumen narrowing. [5, 6]. It should also be noted that there may be arterial sites with severe plaque formation that do not lead to lumen narrowing. In this case, the plaque may still break and cause a sudden blockage of the lumen.

Atherosclerosis treatments are divided into two main categories. One is the major invasive bypass surgery. The other is relatively less invasive angioplasty procedures. These treatments are usually performed in later stages of the disease due to the limited abilities of existing diagnostic methods. It is of utmost

importance to take protective actions by making life style changes before the disease is detected with a significant vascular damage. Considering the aforementioned facts, it is critical to diagnose the stenotic narrowing at an early stage.

A widely used diagnostic method is arteriography [7]. The basis of the arteriography is the injection of X-ray contrast agent into the body and the acquisition of the X-ray image near the stenosis site. The diseased artery image detected by arteriography is shown in Figure 1.1.

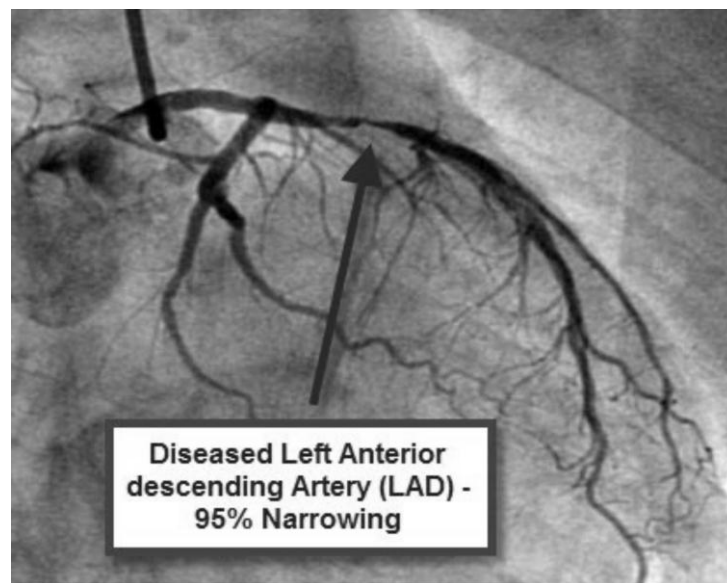


Figure 1.1 Obstructed coronary artery diagnosed using arteriography [8].

Although arteriography is the most common method for diagnosing a stenosis, this method has some disadvantages. Above all, arteriography is an invasive procedure that requires placement of a catheter near the suspected area, causing bleeding or infection after catheter surgery. Arteriography is also performed when the disease shows clinical symptoms [7, 9]. This method is not preferred before the clinical symptoms; this means that it is not a preventive method and is used for the understanding of the disease level. In addition, X-ray angiography is prone to error

if the blood vessel geometry is not sufficiently circular, since the method employs a projected view of the arterial geometry [10, 11].

1.2 Related studies in the literature

1.2.1 Generation of murmurs

The reasons for the generation of vascular sounds (murmurs) are discussed in the literature. Bruns [12] investigated the cause of vascular sounds and concluded that the source of the murmurs was almost periodic fluctuation after the stenotic area. An alternative noninvasive diagnostic method called "phonoangiography" has been proposed by Lees and Dewey [13]. The method of phonoangiography uses acoustic radiation due to abnormal flow conditions in the blood flow. Phonoangiography is a noninvasive diagnostic technique that examines vascular sound generation and its effects on the skin surface. In Figure 1.2, the concept of phonoangiography is represented.

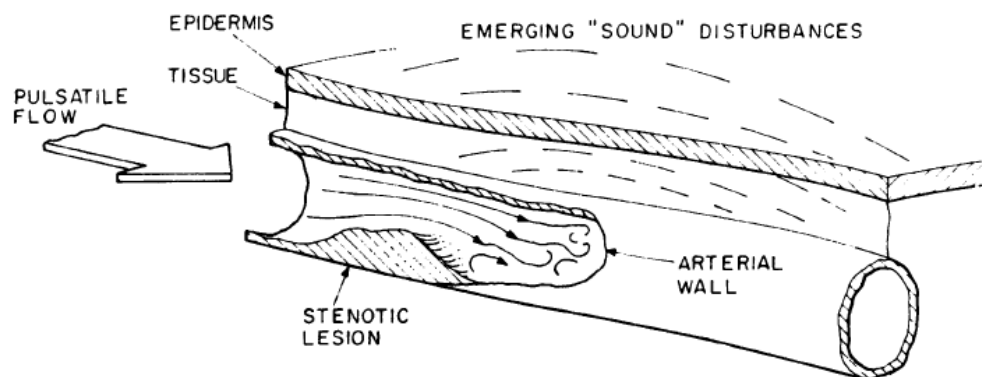


Figure 1.2 The concept of phonoangiography [13].

The vascular sound is generated due to the narrowing in the blood vessel. After passing through the stenotic occlusion, the blood flow turns into turbulent nature, which causes pressure fluctuations in the arterial wall. Sound generated in the artery

wall propagates through the surrounding soft tissues and reaches the skin surface. The basic idea of phonoangiography is to utilize the sound disturbances detected on the skin surface.

Significant results have been obtained in the study of Lees and Dewey [13]. It has been found that the sound spectra obtained for in vivo experiments are almost identical to the wall pressure spectrum for fully developed turbulent pipe flow. In Figure 1.3, Lees and Dewey compared in vivo experimental results with the findings of Bakewell et al. [14] considering fluid flow in a rigid pipe.

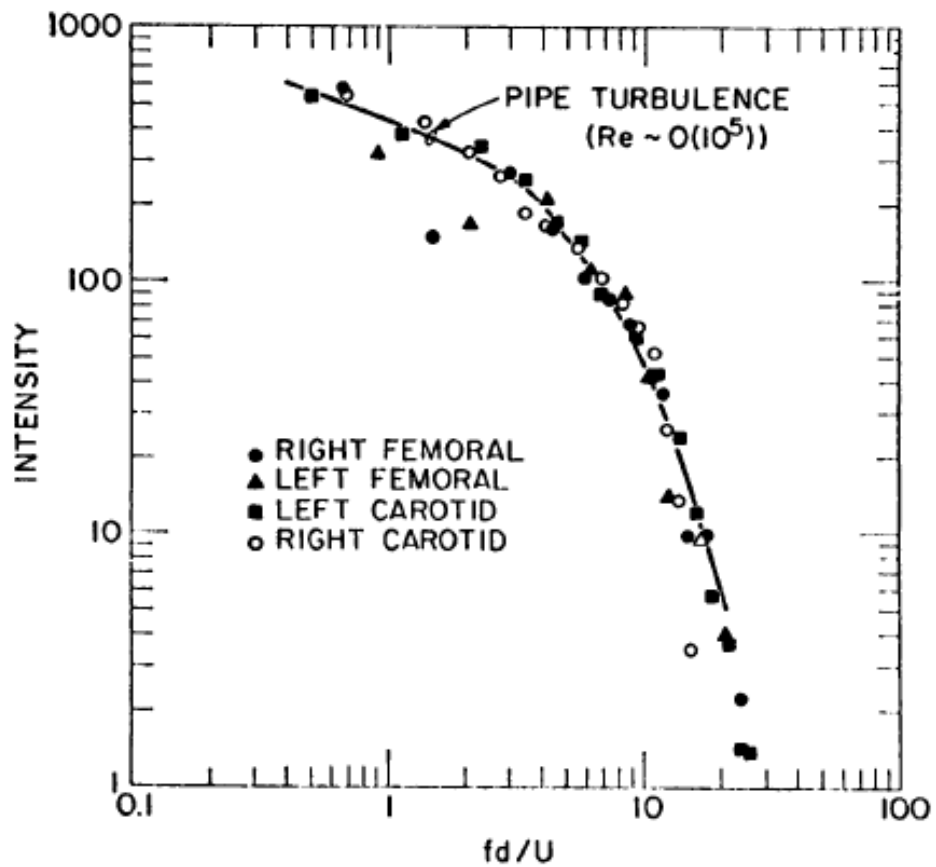


Figure 1.3 Comparison of in vivo experimental results with the turbulence spectrum of flow in a rigid pipe [13].

In Figure 1.3, f , d and U denote the frequency, effective diameter at the stenosis and the mean velocity proximal to the stenosis, respectively. The rigid line is obtained by Bakewell et al. [14] which is found in laboratory conditions using the flow inside a rigid tube. In vivo experimental results of Lees and Dewey [13] were performed for the right femoral, left femoral, left carotid and right carotid arteries, and the results were in good agreement with Bakewell's study [14].

It is stated that even for low Reynolds numbers, an unstable free jet is observed for the flow through an orifice, which causes some of the kinetic energy to turn into turbulent fluctuations [13]. Most researchers have reported that distorted flow due to narrowing and associated turbulence-induced pressure fluctuations are the main sources of murmurs [9, 15-19].

1.2.2 Analytical studies

In analytical studies, a closed form solution may be obtained, but simplifying assumptions have to be made for the complicated turbulent flow. The problem domain also has to be selected as a simple geometry which does not exactly represent the reality.

Borisyuk developed an acoustic model for the human chest, taking into account the stenotic occlusion and elastic properties of the blood vessel [18]. Acoustic generation and transmission of arterial sound from the source to the receiver is modelled assuming simple stenotic constriction. For the developed analytical model, the flow separation in the post-stenotic region is neglected. Borisyuk obtained [18] the acoustic power spectrum for normal and occluded vascular models and indicated the characteristic signs of vascular constriction. Mild thickening of the artery wall leads to a noticeable increase in the sound level and a shift of the peaks at resonance frequencies in the acoustic spectrum. It was stated that a 30% reduction in the arterial diameter, resulted a 10-fold increase in the radiated acoustic power.

Wang et al. [20] studied on a model of sound generation in stenotic coronary arteries. It has been found that the resonance frequencies for the occluded coronary arteries are different from the normal arteries, in which additional high frequency components are observed for the stenosed ones. They also recorded sounds from the chest wall of the patients and the theoretical findings are supported and confirmed by the experimental results.

1.2.3 Experimental studies

Experimental studies in the literature are mostly related to the flow downstream of the stenosis. After passing through the clogged region, it is observed that there are recirculation zones and high level of turbulent flow [21].

Yazicioglu et al. studied flow-induced vibration of thin-walled viscoelastic tube theoretically and experimentally [22]. The vibration is due to a constriction that causes turbulent flow inside the tube. The vibration of the tube is investigated with coupling to internal flow and external tissue-like viscoelastic material. In the experimental studies [22], the intended flow rate is adjusted by changing the height difference between the two reservoirs. Mean flow pressure and vibration on the tube are measured using a catheter type pressure transducer and Laser Doppler Vibrometry (LDV), respectively. The experimental data are processed, and the wall pressure and the frequency spectra of the tube vibration are obtained.

Borisyuk performed in vitro experiments to investigate the properties of the acoustical field in the human chest [19]. Hollow axisymmetric rigid plugs with various internal diameters and lengths are used as stenosis elements. It has been found that there is a general increase in the noise level and production of new frequency components in the power spectrum with increasing stenosis severity. This condition is a characteristic sign for the presence of a blockage in the blood vessel. The acoustic power produced by the stenosis is found to be approximately

proportional to the fourth power of the stenosis severity and the fourth power of the Reynolds number of flow.

Tobin and Chang obtained wall pressure spectra at various locations downstream of the axisymmetric stenosis element [23]. The focus of their investigation was developing a noninvasive clinical diagnostic technique that can determine the degree of the stenosis using the murmurs. They placed an obstruction inside a latex rubber tube which contains a steady water flow. Various stenosis severities and Reynolds numbers are considered for the analysis. Important universal correlations were found between the spectrum frequency and the pressure amplitude. At the peak activity location, a universal power spectral density function is determined using new set of non-dimensional variables.

1.2.4 Numerical studies

Salman et al. [24] modelled the occluded intravenous flow. Geometric parameters are selected as the same with the parameters used in the experimental study of Yazicioglu et al. [22] to verify the results. Since the fluid flow is modeled using Detached Eddy Simulation (DES), the dynamic pressure fluctuations on the inner wall of the blood vessel are obtained computationally. It has been observed that the spectral distribution of the fluctuating wall pressure shows a significant increase at the downstream of the arterial stenosis. As the flow rate increases, the amplitudes also increase over a wide frequency range. The numerical results showed good agreement with the experimental findings in terms of general spectral trend indicating the relative increase in the pressure fluctuations depending on the stenosis severity. The turbulent pressure fluctuations predominantly stimulate the first few natural frequencies of the artery [22].

Seo and Mittal [25] investigated the sound produced by the blood flow in the obstructed veins. They used a hybrid approach in which the flow is solved using an immersed boundary approach employing an incompressible flow solver, and the

wave propagation through the tissue is modeled using a simplified linear structural wave equation.

Lee et al. [26] investigated the blood flow dynamics of a carotid bifurcation performing a numerical simulation by employing spectral element method. Pulsatile blood velocity inlet conditions based on in-vivo color Doppler ultrasound measurements are applied as the boundary conditions. They examined [26] turbulence levels, complex flow field and the biomechanical stresses on the stenosed carotid artery wall. It is stated that areas under severe constriction can have distinct biomechanical environment compared to the healthy blood vessels. The velocity fluctuations were in the audible range within 100 and 300 Hz.

Khanafer and Berguer [27] computationally studied turbulent pulsatile flow and the wall mechanics using an axisymmetric three-layered wall model of the descending aorta. A fully coupled Fluid-Structure Interaction (FSI) analysis is performed using ADINA (Watertown, MA) commercial finite element analysis software. The researchers obtained von Mises wall stresses, streamlines and fluid pressure contours. According to the results, the peak wall stress and maximum shear stress are observed in the media part (i.e., the layer at the middle of the arterial wall).

Tang et al. [28] investigated a three dimensional thick-wall model with FSI using ADINA (Watertown, MA). Wall stress-strain distributions and flow parameters in the carotid arteries with symmetrical and asymmetrical stenosis were obtained performing numerical simulations. According to the results, the stenosis caused considerable compressive stresses that may be associated with the plaque cap rupture in the arterial wall.

Valencia and Villanueva [29] investigated blood flow in symmetrical and asymmetrical occlusions. In their work, the unsteady non-Newtonian blood flow is the main interest. It is reported that FSI has significant effect on the hemodynamics of the stenotic artery models. The stenosis severity and geometry change the length of the recirculating flow zone.

Tang et al. [30] performed numerical simulations in order to quantify the compressive conditions in the constricted arteries. If a severe stenosis is present, the occluded arteries may be compressed under the physiological conditions due to significant drop in the mean pressure. An axisymmetric model is presented to simulate the flow in a compliant tube. ADINA (Watertown, MA) is used to solve the coupled FSI model. The results indicate that severe stenosis leads to critical flow conditions such as pressure drop, artery compression, plaque cap rupture and thrombus formation. A complex pressure field is observed around the stenosis site which can not be resolved in one-dimensional models.

Shurtz [31] performed Large Eddy Simulation (LES) coupled with a finite element structural model. The flow-induced pipe vibration is analyzed and it is found that pipe wall acceleration is inversely proportional to the pipe wall thickness. The structural bending modes are especially effective on long pipes.

1.2.5 Spectral methods

Semmlow et al. [32] analyzed thoracic sounds to detect coronary artery disease. They applied time windowing, frequency windowing and averaging of the thoracic sounds for diseased and normal conditions. A full cardiac cycle is recorded for the patients and only the diastolic part is taken into account for the diagnosis of CAD. Since the highest turbulent fluctuations occurred during the diastolic phase in the coronary arteries, only the diastolic period of the recorded data is used. Due to the lack of use of the systolic period, very loud sounds due to the valve closure have been eliminated. Several diastolic periods are averaged to improve the signal-to-noise ratio. Figure 1.4 shows the average power spectra of the cardiac sounds for normal and diseased coronary arteries.

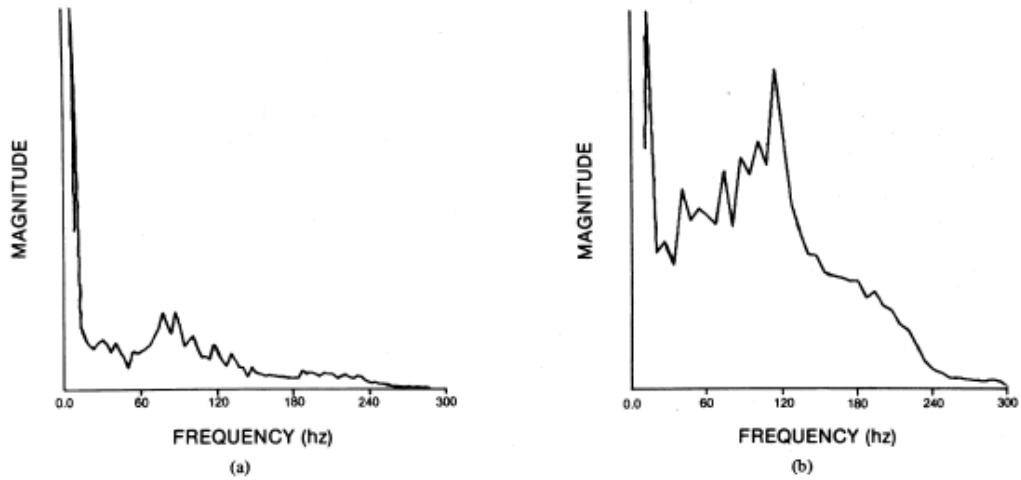


Figure 1.4 Average power spectra of the cardiac sounds from a selected portion of diastole. (a) Normal subject. (b) Patient with 70% stenosis in left coronary artery (adopted from [32]).

The spectrum is obtained by performing Fourier transformation [32]. The most obvious difference between these spectra is the high frequency components in the occluded artery. As a result, high frequency (within 120-200 Hz) energy is associated with the coronary artery narrowing [32]. Only a single feature is used to classify the diseased and normal cases. The feature is selected as the ratio of energy above and below 90 Hz. A sensitivity of 83% is achieved in 24 patients using this classifier.

In another spectral study, the Autoregressive (AR) approach is utilized instead of Fourier transform [33] to detect coronary artery disease. Diastolic isolated segments are recorded and averaged. Using the AR spectra obtained from these segments, it is concluded that a high percentage of the spectral energy is present in the high frequency range (300 Hz) for the diseased coronary arteries.

1.2.6 Acoustic localization and beamforming

Owsley and Hull [34] investigated acoustic localization of a stenosis by applying nearfield beamforming using multiple sensor arrays. For the conventional auscultation method, a single vibroacoustic sensor (stethoscope) is placed on the area close to a specific heart zone. Multiple Auscultation Point (MAP) space-time phonoangiography allows to simultaneously receive data from an array of sensors. It is stated that [34], MAP implementation provides a better Signal-to-Noise Ratio (SNR) estimation and makes it possible to spectrally and spatially resolve the image of the vibratory energy source. The method proposed to localize the arterial stenosis depends on the phased array sensor technology to monitor the shear wave energy field under the sensor array [35].

The vibroacoustic effect, which is caused by turbulence, propagates in the form of wave energy to the body surface as a vibration field. The space-time field is used to track the energy field in a viscoelastic medium enclosing the stenosed vessel [34]. It is proposed that detection and source localization can be performed by filtering and combining the outputs of the vibroacoustic sensor array. A number of noninvasive vibroacoustic sensors are placed on the model of a human body. The spatial identification features of the sensor array are used as a focusing antenna to perform spatial localization. It is stated that [34] turbulence-induced murmur can be distinguished acoustically in temporal, spectral and spatial domains by masking the background sound.

Owsley and Hull [34] performed experiments considering the steady-state flow, because a related study [36] showed that turbulent wall force levels are nearly identical in pulsatile and steady-state conditions. Experiments are conducted in the electromagnetically shielded anechoic chamber to reduce the effect of ambient noise. In Figure 1.5, the occluded region is monitored using the nearfield beamforming method.

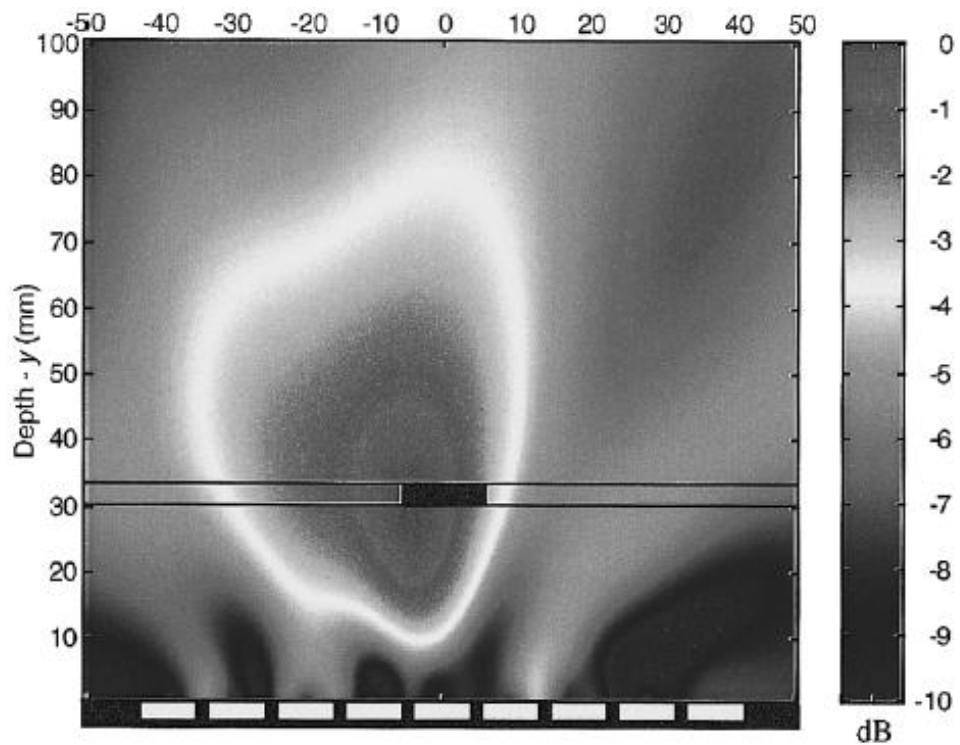


Figure 1.5 Experimental image of the acoustic shear wave energy field at 300 Hz, with the vessel and occlusion shown schematically (adopted from [34]).

1.2.7 Noninvasive diagnostic methods

Various investigations aimed to develop and evaluate noninvasive diagnostic methods. Banks et al. [37] suggested an approach for noninvasive detection of arterial stenosis using shear waves in an experimental chest cavity model. Azimpour et al. [38] evaluated the performance of acoustic signals measured with an electronic stethoscope to investigate the coronary murmurs. Acoustic signals from patients undergoing angiography were analyzed to estimate the diseased cases. Stenosis threshold level for the optimum detection was reported as 50%. At 95% of stenosis severity, the flow is attenuated and the acoustic signals are reduced considerably. With increased stenosis severity, high frequency spectral energy is

significantly increased. Semmlow and Rahalkar [39] summarized signal processing algorithms for the acoustic perception of the vascular sounds.

Tomczak and Kaszynski [40] carried out a nonlinear vibration analysis to investigate the resonance of an aneurysm. Lowe et al. [41] noninvasively estimated aortic blood pressure using suprasystolic brachial pressure waveforms. Campo et al. [42] investigated the diagnosis of arteriosclerosis using Pulse Wave Velocity (PWV) in carotid and femoral arteries. The stiffness of an artery can have significant role in the development of a cardiovascular disease. The pulse wave velocity is an important measure to determine the arterial stiffness in a noninvasive way. In the study of Campo and Dirckx [43], the stiffness of the large arteries was determined using PWV data obtained by laser Doppler vibrometry.

1.3 Aim of the study and contribution to the literature

Much of the work in the literature is concerned with the hemodynamics of the blood flow and effective stress on the arterial wall. The investigation of flow-induced skin surface vibration is very limited. In this study, the main contribution to the literature is a feasibility study that clarifies the diagnostic aspects of vibroacoustic effects on the skin surface due to turbulent flow in the stenotic arteries.

Arterial structure and surrounding soft body tissues are computationally modelled and investigated by performing vibration analysis involving the effect of acoustic pressures caused by the turbulence in the stenotic arteries. ADINA (Watertown, Ma.) commercial finite element analysis software is used for modelling, solving and post-processing. The computationally modelled phenomena is also verified experimentally performing laser Doppler vibrometry. The computational and experimental results agree well and provide a deeper insight on the feasibility of noninvasive detection of vascular stenosis.

It is aimed to emphasize the importance of the vibroacoustic data available on the skin surface and to show that they can be used for diagnosis of stenosis without

using other complex and expensive means. Using the latest technological measurement capabilities, today's measurement technology is evaluated for diagnostic purposes.

1.4 Thesis outline

This study consists of seven chapters. In the first chapter, the problem is stated and related studies in the literature are summarized. In the second chapter, the theory and the background information is provided. Computational modelling studies are described in the third chapter. In the fourth and fifth chapters, the results of idealized and realistic computational models are presented, respectively. Experimental studies and findings are provided in the sixth chapter. Finally, the conclusions and future improvements are outlined in the seventh chapter by summarizing the study and suggesting guidelines for the future work.

CHAPTER 2

THEORY AND BACKGROUND

2.1 Formulation of the problem

In the literature, vascular sound generation and transmission have been investigated using a variety of methods, either by coupling the pipe wall vibration equation with a two-dimensional wave equation of sound radiation [18], or by performing FSI analysis combining a Computational Fluid Dynamics (CFD) analysis with a structural model [24].

In this study, the steady-state structural responses to the applied harmonic loads are determined by performing harmonic vibration analysis using the theory of vibration of discrete systems. Structural responses are obtained by superposing the modal responses. Natural frequencies and corresponding mode shapes are obtained within the interested frequency range by employing the Lanczos method available in ADINA (Watertown, MA), which is suggested for models with acoustic fluid elements [44, 45].

A structural system discretized by finite elements can be expressed as the following [46, 47]:

$$\mathbf{M}\ddot{\mathbf{u}} + \mathbf{C}\dot{\mathbf{u}} + \mathbf{K}\mathbf{u} = \mathbf{F} = \sum_{k=1}^N \mathbf{F}_k \quad (2.1)$$

where, \mathbf{M} is the structural mass matrix, \mathbf{F} is the load matrix, \mathbf{u} is the structural displacement vector, \mathbf{C} is the structural damping matrix, \mathbf{K} is the structural stiffness matrix, N is the total number of load cases, and \mathbf{F}_k is the vector expressing the forces applied for the load case k . If a modal superposition analysis is performed, (2.1) can be decomposed as the following [46, 47]:

$$\ddot{x}_i + 2\xi_i\omega_i\dot{x}_i + \omega_i^2x_i = \sum_{k=1}^N \Gamma_i^k b_k \quad (2.2)$$

where ξ_i is the modal damping ratio for mode i , Γ_i^k is the modal participation factor for mode i and load case k , x_i is the generalized coordinate for mode i , b_k is a dimensionless multiplier for load case k , and ω_i is the angular frequency for mode i . For a harmonic loading, b_k is written in the form:

$$b_k = b_{k0}\sin(\omega_k t - \alpha_k) \quad (2.3)$$

where, b_{k0} is a function of the angular forcing frequency (ω_k), and α_k is the term specifying the phase of the applied harmonic load.

The structural mass matrix (\mathbf{M}) and the structural stiffness matrix (\mathbf{K}) are constructed using the mass densities and material properties of the structural elements, respectively. The structural damping matrix (\mathbf{C}) is defined by determining a modal damping coefficient for the interested frequency range. The system load matrix (\mathbf{F}) is defined by the use of empirical turbulence-induced acoustic pressures. After defining all these parameters, the displacement variable (\mathbf{u}) can be determined by solving the series of equations.

Linear potential based fluid elements which are inviscid, irrotational with no heat transfer and almost incompressible are employed for the frequency domain analysis. These acoustic fluid elements are only used to model the mass properties

of the fluid as well as the wave propagation in the fluid medium [48], which means that the flow cannot be solved using them. The basic equations of continuity and energy are written in the form of fluid velocity potential (ϕ) as follows:

$$\dot{\rho} + \nabla \cdot (\rho \nabla \phi) = 0 \quad (2.4)$$

$$h = \int \frac{dp}{\rho} = \Omega - \dot{\phi} - \frac{1}{2} \nabla \phi \cdot \nabla \phi \quad (2.5)$$

where, ρ is the fluid mass density, h is the specific enthalpy, p is the pressure and Ω is the body forces. In the analysis, the body forces are neglected (i.e., $\Omega = \mathbf{0}$) due to the insignificant effect. The bulk modulus (B) can be expressed in the following form:

$$B = \rho \frac{\dot{p}}{\dot{\rho}} \quad (2.6)$$

For the frequency domain analysis, an infinitesimal velocity formulation is used for linear potential based fluid elements, where the density changes and velocities are assumed to be infinitesimal. By using this assumption and combining (2.4) and (2.6), the following expression is obtained.

$$\dot{\rho} + \nabla \cdot (\rho \nabla \phi) \approx \dot{\rho} + \rho \nabla^2 \phi \approx \frac{\rho \dot{p}}{B} + \rho \nabla^2 \phi = 0 \quad (2.7)$$

With the assumption of infinitesimal density changes and velocities, (2.5) can be simplified as follows:

$$h \approx \frac{p}{\rho} \approx -\dot{\phi} \quad (2.8)$$

Using (2.8), the pressure (p) can be expressed in the following form:

$$p \approx \rho(-\dot{\phi}) \quad (2.9)$$

If (2.9) is substituted in (2.7), the following wave equation is obtained.

$$-\rho\ddot{\phi} + B\nabla^2\phi = 0 \quad (2.10)$$

(2.10) is a special form of the wave equation and it is linear with respect to the variable ϕ [49].

The acoustic fluid medium is directly coupled to the surrounding arterial structure by assigning the same displacements in the fluid-structure interaction boundary S_1 [49, 50]. (2.10) can be expressed in the variational form as the following:

$$-\int_V \rho\ddot{\phi} \delta\phi dV - \int_V B\nabla\phi \cdot \delta\nabla\phi dV - \int_{S_1} B \dot{\mathbf{u}} \cdot \mathbf{n} \delta\phi dS_1 = 0 \quad (2.11)$$

where $\delta\phi$ is the variation in the fluid velocity potential, and \mathbf{n} is the normal vector of surface S_1 . For the fluid domain, the system matrices can be expressed in the following form [49]:

$$\begin{bmatrix} \mathbf{0} & \mathbf{0} \\ \mathbf{0} & \mathbf{M}_{FF} \end{bmatrix} \begin{bmatrix} \ddot{\mathbf{u}} \\ \ddot{\phi} \end{bmatrix} + \begin{bmatrix} \mathbf{0} & \mathbf{C}_{FU}^T \\ -\mathbf{C}_{FU} & \mathbf{0} \end{bmatrix} \begin{bmatrix} \dot{\mathbf{u}} \\ \dot{\phi} \end{bmatrix} + \begin{bmatrix} \mathbf{0} & \mathbf{0} \\ \mathbf{0} & \mathbf{K}_{FF} \end{bmatrix} \begin{bmatrix} \mathbf{u} \\ \phi \end{bmatrix} = \mathbf{0} \quad (2.12)$$

where \mathbf{M}_{FF} is the matrix from $\ddot{\phi}\delta\phi$ term in (2.11), \mathbf{K}_{FF} is the matrix from $\nabla\phi \cdot \delta\nabla\phi$ term in (2.11), \mathbf{C}_{FU} is the matrix from $\dot{\mathbf{u}} \cdot \mathbf{n}\delta\phi$ term in (2.11), \mathbf{u} is the unknown structural displacement vector, and ϕ is the fluid potential vector. Finally, the system matrices of fluid (2.12) and the arterial structure (2.1) are combined in the following form:

$$\begin{bmatrix} \mathbf{M} & \mathbf{0} \\ \mathbf{0} & \mathbf{M}_{FF} \end{bmatrix} \begin{bmatrix} \ddot{\mathbf{u}} \\ \ddot{\phi} \end{bmatrix} + \begin{bmatrix} \mathbf{C} & \mathbf{C}_{FU}^T \\ -\mathbf{C}_{FU} & \mathbf{0} \end{bmatrix} \begin{bmatrix} \dot{\mathbf{u}} \\ \dot{\phi} \end{bmatrix} + \begin{bmatrix} \mathbf{K} & \mathbf{0} \\ \mathbf{0} & \mathbf{K}_{FF} \end{bmatrix} \begin{bmatrix} \mathbf{u} \\ \phi \end{bmatrix} = \begin{bmatrix} \mathbf{F} \\ \mathbf{0} \end{bmatrix} \quad (2.13)$$

By solving the set of equations in the matrices given by (2.13), the structural displacement response \mathbf{u} can be determined. Since the responses are assumed to be harmonic (i.e., $\mathbf{u} = \mathbf{U}e^{i\omega t}$ where \mathbf{U} is the amplitude), the velocity response $\dot{\mathbf{u}}$ can be determined as the following:

$$\dot{\mathbf{u}} = i\omega\mathbf{u} \quad (2.14)$$

where $i = \sqrt{-1}$ and ω is the angular frequency.

2.2 Fluid excitation

In this section, a brief information is provided about the flow in a stenotic pipe. As shown in Figure 2.1, the stenosed flow can be examined in five zones.

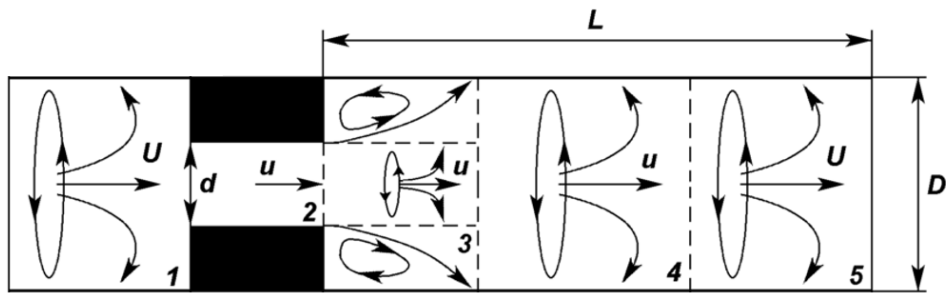


Figure 2.1 Five characteristic zones in a stenosed pipe flow (adopted from [19]).

The first zone is the upstream of the stenosis and laminar flow with an axial flow velocity U is observed if the critical Reynolds number is not exceeded [7, 19, 51, 52]. In the second zone, the lumen diameter is sharply reduced to d , which significantly increases the axial flow velocity. After passing through the stenotic obstruction, the lumen diameter again expands to D with a central jet velocity u in the third zone. This third zone has an extreme turbulent nature, in which the flow separation and recirculation occur. The flow reattachment is observed in the fourth zone [7, 19, 51, 52], and if the pipe is long enough, the flow stabilization and redevelopment is observed in the fifth zone where the flow characteristics are very similar to the first zone.

Arterial sounds are mainly produced at the downstream of the stenosis and the peak generation is observed in the third zone. Therefore, only downstream of the stenosis exit is considered in the computational analysis.

2.3 Modelling the turbulence-induced acoustic pressure field

Tobin and Chang [23] obtained universal correlations using experimental results to find the fluctuating pressures on the inner wall of the blood vessel. Experiments were conducted using a latex rubber tube. Axisymmetric stenotic occlusion was

placed in a latex rubber tube and a steady flow was considered. The wall pressure spectrum was obtained at different locations downstream of the constriction exit.

In the experimental set-up, two reservoirs were used with a certain height difference. A cotton batting with a thickness of 3-4 inches is used to avoid ground disturbances. The Root Mean Square (RMS) wall pressure spectrum is obtained for different Reynolds numbers and stenosis levels. The effect of Reynolds number on the wall pressure spectrum measured at $2D$ (where D is unstricted diameter) distance to the constriction exit is represented in Figure 2.2 considering 90% stenosis.

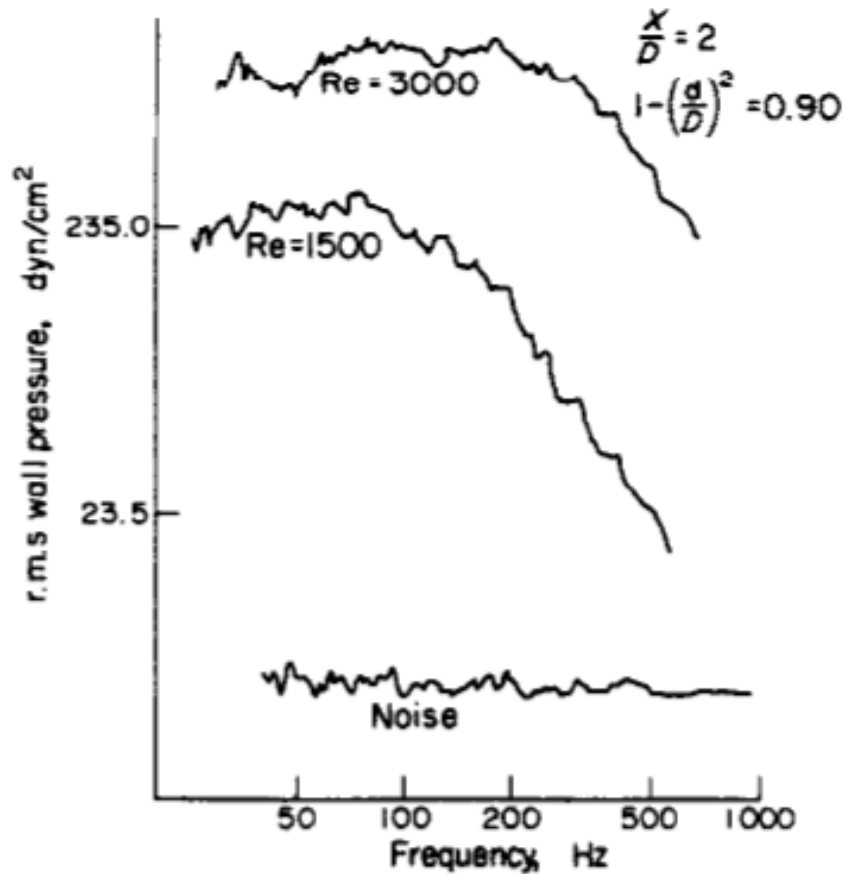


Figure 2.2 Effect of Reynolds number on the wall pressure spectra at $2D$ distance downstream of the constriction exit in case of 90% flow area reduction (adopted from [23]).

A jet is visible at the stenosis exit and there is a recirculation region in which the flow separation is observed. The length of the recirculation region is about three unstricted diameters. As the Reynolds number increases, the RMS wall pressure amplitudes tend to increase in Figure 2.2. Two different Reynolds numbers of 1500 and 3000 show a similar trend in terms of amplitude reduction with the increasing frequency, but higher Reynolds numbers have peak RMS wall pressure at relatively higher frequencies. For locations close to the recirculation zone, there is highly excited pressure response. As the axial position moves away from the constriction exit, the wall pressure amplitudes decrease. The effect of the distance to the constriction exit is represented in Figure 2.3.

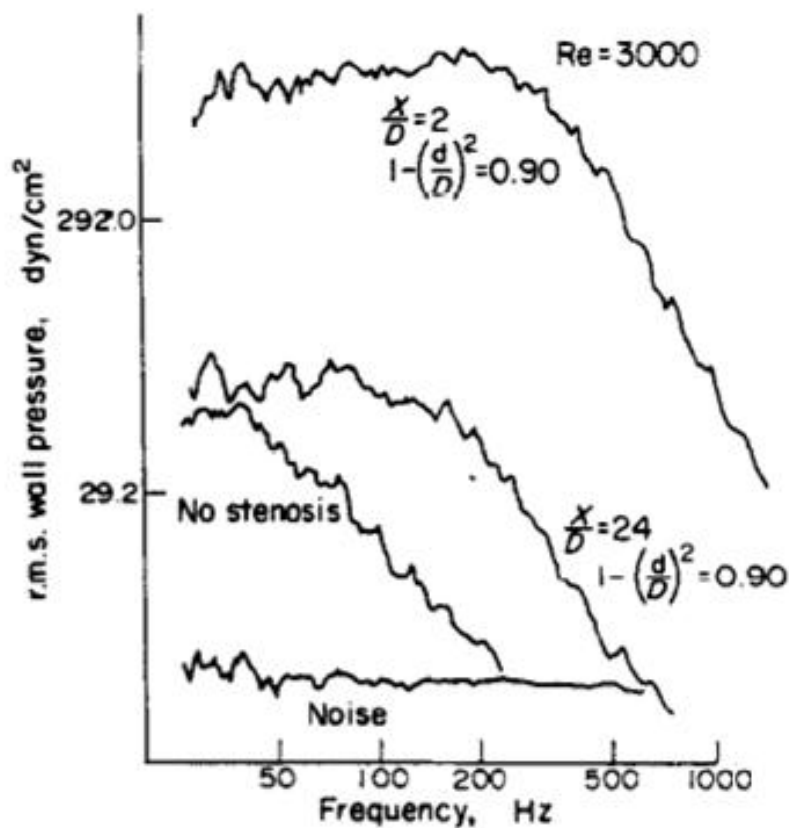


Figure 2.3 Effect of the distance to the constriction exit on the wall pressure spectra for 90% flow area reduction (adopted from [23]).

In Figure 2.3, RMS wall pressures are given at a distance of 2D and 24D to the constriction exit. For 90% stenosis and Reynolds number of 3000, a significant decrease in RMS wall pressure is observed at 24D. At distances of 2D and 24D, the reduction tendency is similar, but a higher peak frequency is observed for 2D distance to the occlusion.

Tobin and Chang [23] considered various Reynolds numbers and stenosis levels in their experimental studies. RMS wall pressure spectra for different Reynolds numbers and stenosis levels are given in Figure 2.4.

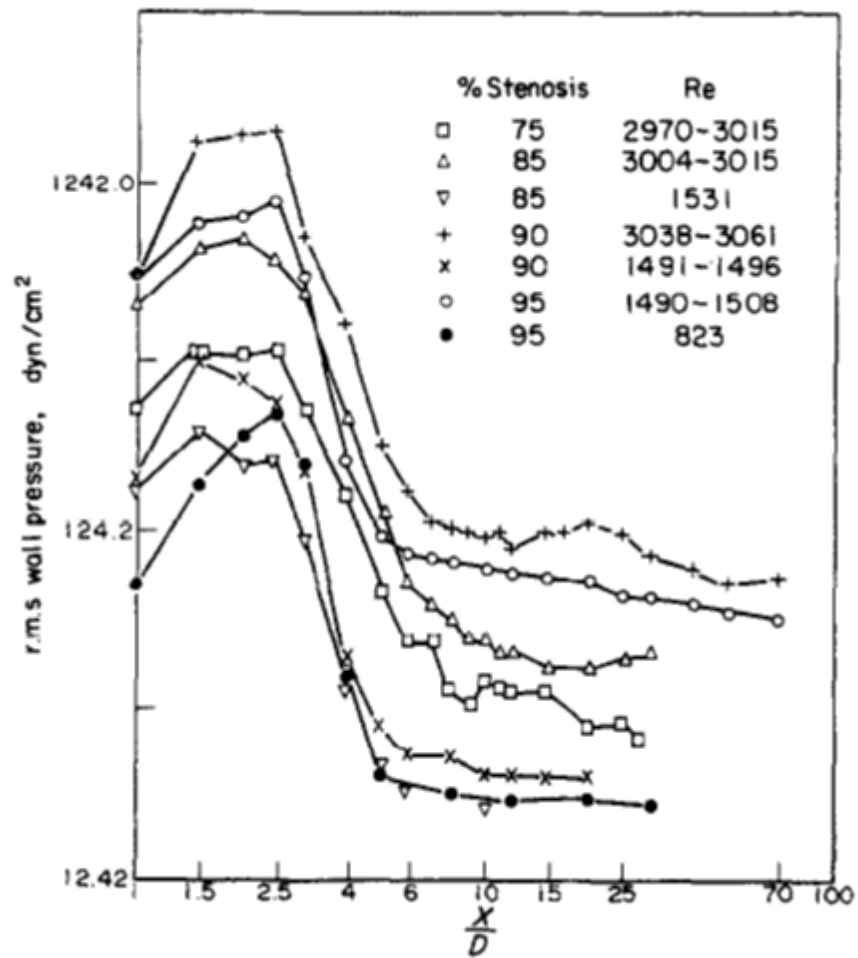


Figure 2.4 RMS pressure spectra for different stenosis levels and Reynolds numbers (adopted from [23]).

As shown in Figure 2.4, the RMS pressure spectrum varies significantly depending on the Reynolds number and the stenosis level. Tobin and Chang [23] developed a common set of parameters to define a universal non-dimensional function for RMS wall pressure spectra. This nonlinear relationship is called $F_{n1} \left[\frac{x}{D} \right]$ and expressed as the following:

$$F_{n1} \left[\frac{x}{D} \right] = \frac{p_{rms} D}{\rho u_j^2 d} \quad (2.15)$$

In the above parameter set, p_{rms} is the RMS pressure, ρ is the fluid mass density, u_j is the axial flow velocity at the constriction exit, d is the constricted diameter and D is the unstricted diameter. Using the non-dimensional function described in (2.15), the pressure spectrum was normalized for various Reynolds numbers and stenosis levels as shown in Figure 2.5.

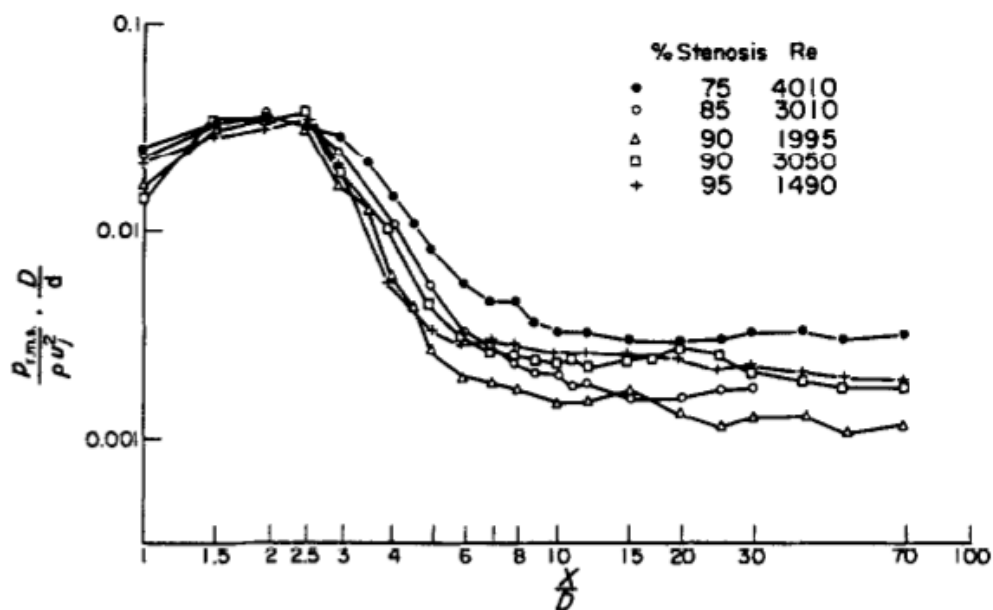


Figure 2.5 RMS wall pressure variation with x/D , normalized data – assorted Reynolds numbers and levels of stenosis (adopted from [23]).

Figure 2.5 shows that, the new non-dimensional function gives very similar results for different Reynolds numbers and stenosis levels, especially around the location where the maximum pressure is observed. This nonlinear relationship is used to define the empirical pressure equation for the stenosis levels ranging from 75% to 95% and the Reynolds numbers within 500 to 4000. The following relationship is found between the dynamic RMS wall pressure (p_{rms}) and the axial distance (x) downstream of the constriction exit:

$$p_{rms} = \rho u_j^2 \frac{d}{D} F_{n1}[x/D] \quad (2.16)$$

where $F_{n1} \left[\frac{x}{D} \right]$ is the non-dimensional function obtained from Figure 2.5.

Tobin and Chang [23] also found another nonlinear relationship between the power spectral density ($E(f)$) and the frequency (f). The power spectral density is defined as the following:

$$E(f) \equiv \frac{p(f)^2}{\Delta f} = \rho^2 D u_j^3 \left(\frac{d}{D} \right)^2 F_{n2}[fD/u_j] \quad (2.17)$$

$$F_{n2} \left[\frac{fD}{u_j} \right] = \frac{p(f)^2}{\Delta f} \frac{1}{\rho^2 D u_j^3} \left(\frac{D}{d} \right)^2 \quad (2.18)$$

where $F_{n2}[fD/u_j]$ is the non-dimensional power spectral density and the expression of $\frac{p(f)^2}{\Delta f}$ is the power spectral density of the wall pressure variation as function of frequency. As the frequency increases, the value of the dimensionless power spectral density $F_{n2} \left[\frac{fD}{u_j} \right]$ approaches a negative slope of 5.3 for completely different conditions, as shown in Figure 2.6.

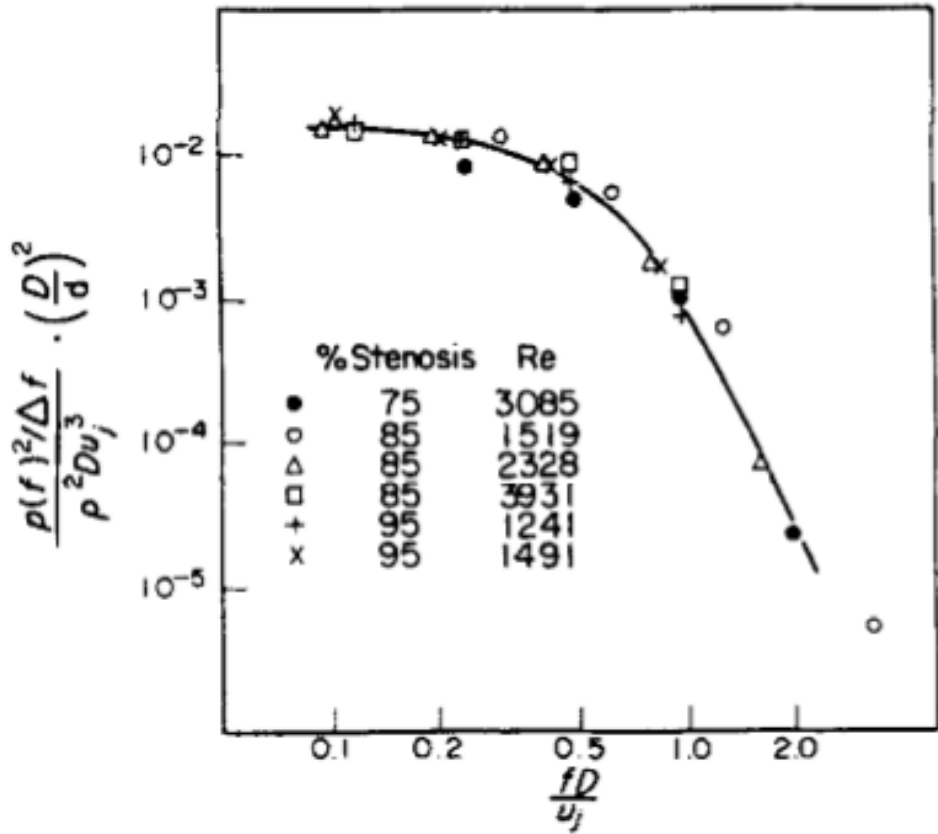


Figure 2.6 Non-dimensional power spectral density $F_{n2} \left[\frac{fD}{u_j} \right]$ (adopted from [23]).

In Figure 2.5, for all conditions examined by Tobin and Chang [23], the maximum RMS pressure was obtained at the same x/D position with $F_{n1} \left[\frac{x}{D} \right]$ value of 0.0355 as described in the following expression.

$$\frac{p_{rms,max} D}{\rho u_j^2 d} = 0.0355 \quad (2.19)$$

Yazicioglu et al. [22] used the empirical relations obtained by Tobin and Chang [23] to perform theoretical analysis of fluid-filled elastic tube vibration. The pressure distribution on the inner wall of the tube is assumed to be axisymmetric.

For this reason, the dynamic (acoustic) pressure p depends on time t , and only one spatial variable x , which is the axial distance downstream of the constriction exit. Yazicioglu et al. [22] developed an expression for $p(x, f)$ and obtained the curve fitting function for $F_{n2} \left[\frac{fD}{u_j} \right]$ using the data represented in Figure 2.6 as the following:

$$F_{n2} \left[\frac{fD}{u_j} \right] = \frac{0.00208}{1 + 20(fD/u_j)^{5.3}} \quad (2.20)$$

The equation used to describe the RMS value is given [22] in (2.21):

$$p_{rms}^2 = \langle p(t)^2 \rangle = \left(\frac{1}{T} \int_0^T p(t)^2 dt \right) = \int_0^\infty E(f) df \quad (2.21)$$

where T is an appropriate averaging time in which the value asymptotically converged. The empirical equation used to find the RMS pressure [22] in the frequency domain is given in (2.22).

$$p_{rms}(f) \approx \rho D^{1/2} u_j^{3/2} \left(\frac{d}{D} \right) F_{n2} [fD/u_j]^{1/2} \quad (2.22)$$

The fluid jet velocity at the stenosis exit can be defined using the flow rate at the unconstricted region as the following:

$$u_j = \frac{D^2}{d^2} U \quad (2.23)$$

(2.23) is substituted in (2.22) and the pressure spectrum is expressed in the following form [22]:

$$p(e^{j2\pi ft}, \vartheta_f) = \sqrt{2}\rho U^{3/2} \frac{D^{5/2}}{d^2} (F_{n2}[fd^2/UD])^{1/2} e^{j(2\pi ft + \vartheta_f)} \quad (2.24)$$

where ϑ_f denotes the phase angle.

When (2.21) and (2.24) are combined, the following expression is obtained to define the RMS pressure:

$$p_{rms} \approx \left(\sum_{f=1}^{\infty} (p[e^{j2\pi ft}, \vartheta_f])^2 \right)^{\frac{1}{2}} \quad (2.25)$$

(2.23) is substituted in (2.16) and the following empirical equation is obtained:

$$p_{rms} \approx \rho U^2 \frac{D^3}{d^3} F_{n1} \left[\frac{x}{D} \right] \quad (2.26)$$

In Figure 2.5, the point of peak activity is observed at $2D$ distance from the constriction exit. As previously defined in (2.19), $F_{n1} \left[\frac{x}{D} \right]$ has a value of 0.0355 at the point of peak activity. By using this information and combining (2.19) and (2.26), the following expression is determined [22].

$$p_{rms} \approx \rho U^2 \frac{D^3}{d^3} F_{n1} \left[\frac{x_{max}}{D} \right] \approx \rho U^2 \frac{D^3}{d^3} (0.0355) \quad (2.27)$$

(2.27) is the equation used to determine the wall pressure spectrum at the peak activity point. According to the study of Tobin and Chang [23], the spectral tendency of the wall pressure variation at different axial locations is almost the same as the spectral tendency of the peak activity point. Therefore, Yazicioglu et

al. [22] assumed that the spectral behavior observed at the peak activity point is valid at all spatial locations.

The phase angle (ϑ_f) is investigated by Keith and Abraham [53] for turbulent flow over a wall. According to their hypothesis, the turbulent wall pressure convection is associated with the flow velocity.

In the study of Owsley and Hull [34], it is assumed that the turbulent wall pressure convection velocity moves axially depending on the jet velocity (u_j) observed at the constriction exit.

Yazicioglu et al. [22] stated that the flow velocity in the regions close to the wall is lower when compared to the central flow rate. Larger and coherent structures with lower frequencies are seen in the central location. The smaller structures located near the wall are dissipated faster as they move away from the stenosis exit [22]. It is stated that the effect of larger structures may be more pronounced in the further downstream region and the velocity of the turbulent wall pressure convection may depend on the frequency. Yazicioglu et al. [22] followed the assumptions of Owsley and Hull [34] and formulated the pressure field considering the phase angle as the following:

$$p[e^{j2\pi ft}, x, \vartheta_f] = P_0 e^{j(2\pi f - \vartheta_f)} \quad (2.28)$$

where,

$$P_0 = 1.8F_{n1}[x/D]\rho U^{3/2} \cdot \frac{D^{5/2}}{d^2} \left(\frac{1}{1 + 20(fd^2/UD)^{5.3}} \right)^{1/2} \quad (2.29)$$

and,

$$\vartheta_f[f, x] = \frac{2\pi f x d^2}{UD^2} \quad (2.30)$$

The amplitude of the acoustic pressure (P_0) depends on several parameters including $F_{n1} \left[\frac{x}{D} \right]$. Using the values given in Figure 2.5, curve fitting is performed to represent $F_{n1} \left[\frac{x}{D} \right]$ as a function. The data points used for the fitting function are given in Table 2.1.

Table 2.1 The data used to approximate $F_{n1} \left[\frac{x}{D} \right]$ based on Figure 2.5

$\frac{x}{D}$	0	1	1.5	2	3	4	6	8	10	15	70
$F_{n1} \left[\frac{x}{D} \right]$	0	0.02	0.03	0.0355	0.025	0.01	0.004	0.003	0.0025	0.002	0.002

Using the values given in Table 2.1, the fitting function is obtained in the following form considering an unstricted diameter of 6.4 mm:

$$F_{n1}[x] = \frac{0.07057x + 0.3849}{x^2 - 23.22x + 167.9} \quad (2.31)$$

(2.31) is substituted in (2.29) and the final form of the acoustic pressure amplitude is defined as:

$$P_0 = 1.8 \frac{0.0705x + 0.385}{x^2 - 23.2x + 168} \rho U^{3/2} \frac{D^{5/2}}{d^2} \left(\frac{1}{1 + 20(fd^2/UD)^{5.3}} \right)^{1/2} \quad (2.32)$$

In the computational studies, the phase data and turbulence-induced acoustic pressure field are determined using (2.30) and (2.32). In Chapter 3, the method used to apply the empirical pressure field to the arterial model is explained in detail.

CHAPTER 3

METHODS FOR MODELLING FLOW-INDUCED ACOUSTIC FIELD

In this study, the main focus is the arterial sound and vibration emitted from the peripheral organs such as arm, leg and neck. Large artery diameters in peripheral organs result in high vascular sound generation when compared to the coronary arteries. The vascular sound generated in coronary arteries is mostly suppressed by the natural sounds of heart valve closure and breathing. These natural sounds make the diagnosis challenging and advanced signal analysis techniques are needed to be applied in order to filter the sounds emitted from the coronary arteries [54]. In this study, the pure effect of flow-induced vascular sound is analyzed by concentrating on the peripheral arteries.

The geometric and anatomical features of the peripheral organs are important reasons to focus on the peripheral arteries. The anatomy of peripheral organs is much simple, regular and similar to an axisymmetric form when compared to the complicated anatomies of abdomen and chest.

In the literature, Peripheral Arterial Occlusive Disease (PAOD) is reported as a critical indication of possible serious cardiovascular diseases such as CAD and stroke. PAOD patients have a higher risk of CAD within 10 years [4]. This fact is supported by a clinical investigation. It is reported that PAOD patients over 50 years of age have 68% and 42% incidence of coexistent CAD and CVA, respectively [55].

The abovementioned facts clearly indicate that early detection of PAOD has great importance to take preventive actions before encountering CVA or CAD, and to

motivate the patient for a healthier life style before facing with serious arterial damage. Considering the stated reasons, analyzing the large arteries in peripheral organs is more feasible for noninvasive diagnosis of arterial occlusion.

3.1 Constitutive elements of the problem

Artery, blood, bones and surrounding soft tissues are the constitutive elements in the problem domain. The large arteries in the peripheral organs are considered as linearly elastic finite pipe with uniform thickness and diameter. In the literature, arterial lumen diameter is reported between 1 to 20 mm [9, 19, 56-59] for the large arteries. The ratio between the lumen diameter and arterial thickness is an important value and it should be in the range of 0.04 to 0.13 for the peripheral arteries. In the computational studies, the lumen diameter and the arterial thickness are considered as 6.4 and 0.3 mm, respectively, to approximate the anatomical relevance and to follow the studies of Yazicioglu et al. [22], Tobin and Chang [23], and Salman et al. [24]. The considered diameter and thickness correspond to a thickness to diameter ratio of 0.047 which is in the stated range for large arteries. The arterial lumen diameters are 4, 6.4 and 10 mm for the brachial, common carotid and femoral arteries, respectively [60, 61]. Therefore, the selected lumen diameter of 6.4 mm is a suitable approximation for the peripheral arteries.

In several studies, the arterial structure is modelled with material properties within 0.129 to 1 MPa of elastic modulus, 0.23 to 0.57 of Poisson's ratio, and 690 to 1350 kg/m³ of mass density [7, 19, 58]. Latex rubber is an appropriate alternative to model the artery where it has elastic modulus of 0.8 MPa, Poisson's ratio of 0.42, and mass density of 1086 kg/m³, which are suitable for the arterial structures [22-24]. The main objective is to investigate the arterial vibration and to see the effects of the most influencing factors such as arterial lumen diameter, blood pressure, blood flow rate and the severity of the occlusion. Prestress, curved artery geometry, structural layers in the arterial wall, density change in the arterial structure have indiscernible effects and they are neglected within the scope of the investigation.

The stenosis inside the artery is modelled with a blunt constriction profile following the studies of Yazicioglu et al. [22], and Tobin & Chang [23]. The calcified material deposited in the stenosis site has much higher stiffness when compared to the arterial structure and can be considered as rigid.

The flow-induced acoustic pressures on the arterial wall are the main cause of vibration. In several studies, these fluctuating acoustic pressures are obtained performing CFD analysis which are time consuming and require high computational power. By considering an alternative approach, the acoustic pressures are determined in a more effective and accurate way using the experiment-based empirical equations defined in the literature as previously explained in Chapter 2. Acoustic fluid elements are employed in the computational studies to model the wave propagation in the fluid medium and the mass properties of the blood. The flow is not solved and only structural modal analysis is performed to obtain the solution. By using this approach, the computational demand is significantly lowered.

Blood is modelled using the material properties of water at room temperature. It is stated that if the shear rate exceeds 50 s^{-1} , the blood can be considered as a homogenous incompressible Newtonian fluid [9, 51, 52], and this condition is satisfied for the large peripheral arteries. The mass density and bulk modulus of the blood are used as 1000 kg/m^3 and 2.2 GPa , respectively.

The blood flow rate is dependent on time due to the pulsatile nature of the cardiovascular system. The highest vascular sound is generated at the instant of peak flow rate. Therefore, the peak flow velocity at the systolic phase is the main focus for the investigation. In the analysis, the interested frequency range of vibration is up to 1000 Hz but the pulsation due to cardiac cycle is around 1 Hz [19]. It means that the change in flow rate is much slower when compared to the interested fluctuations. For this reason, the quasi-steady solution at the peak instantaneous flow rate is utilized in the computational analysis.

3.2 Comparison of ANSYS and ADINA

A sample problem is modelled and solved using ANSYS Workbench (Canonsburg, PA) and ADINA (Watertown, MA) to compare the effectiveness of the softwares. A cantilever beam is considered which is fixed at one end with no displacement. Linearly elastic latex rubber material properties are used for the beam material. The cantilever beam has a square cross-section of 10 mm, with a total length of 100 mm. The same mesh is generated for both ANSYS Workbench (Canonsburg, PA) and ADINA (Watertown, MA) using 10000 hexahedral structural elements. The models created for ANSYS Workbench (Canonsburg, PA) and ADINA (Watertown, MA) are represented in Figure 3.1.

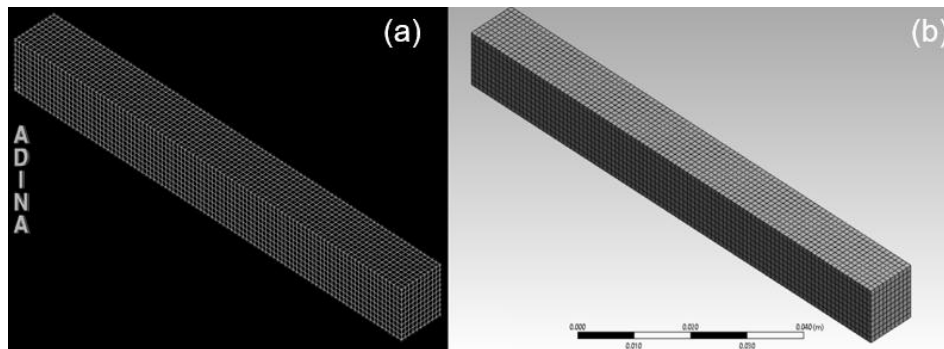


Figure 3.1 The models used for the sample cantilever beam problem. (a) ADINA. (b) ANSYS Workbench.

Thirty natural frequencies and corresponding mode shapes of the cantilever beam are determined within the interested frequency range of 0 to 500 Hz. The total time elapsed for the modal analysis in ANSYS Workbench (Canonsburg, PA) is 145 seconds. This duration is reduced to 46 seconds using ADINA (Watertown, MA), which is three times faster when compared to ANSYS Workbench (Canonsburg, PA).

Two different harmonic loading cases are considered for the cantilever beam. The modal damping coefficient is set to 0.02 (2%) for all interested frequencies and mode shapes assuming light damping conditions in the models. In the first loading case, a harmonic pressure of 1 Pa is applied at the bottom line of the cantilever beam as a distributed force. For the second loading case, a harmonic pressure of 1 Pa is applied on the bottom line and another harmonic pressure of 2 Pa is applied on the top line with a phase angle difference of 90° as shown in Figure 3.2.

The harmonic acceleration response in the loading direction is obtained for the top node at the free end of the cantilever beam. The results of ADINA (Watertown, MA) and ANSYS Workbench (Canonsburg, PA) are given in Figure 3.3 and Figure 3.4 for the first and second harmonic loading cases, respectively. As seen in Figure 3.3 and Figure 3.4, the results of harmonic analysis with phase difference are nearly same for ADINA (Watertown, MA) and ANSYS Workbench (Canonsburg, PA).

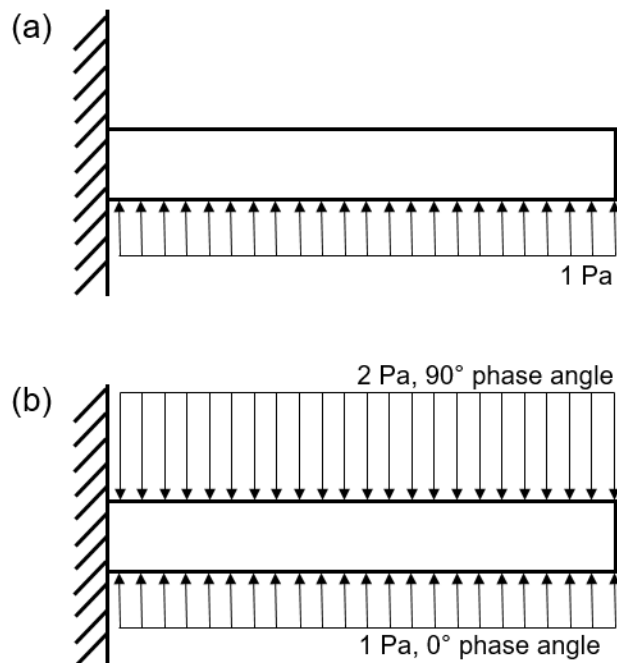


Figure 3.2 Two different harmonic loading cases for the cantilever beam. (a) Harmonic pressure of 1 Pa on the bottom line. (b) Harmonic pressures of 1 Pa and 2 Pa with a phase difference of 90° .

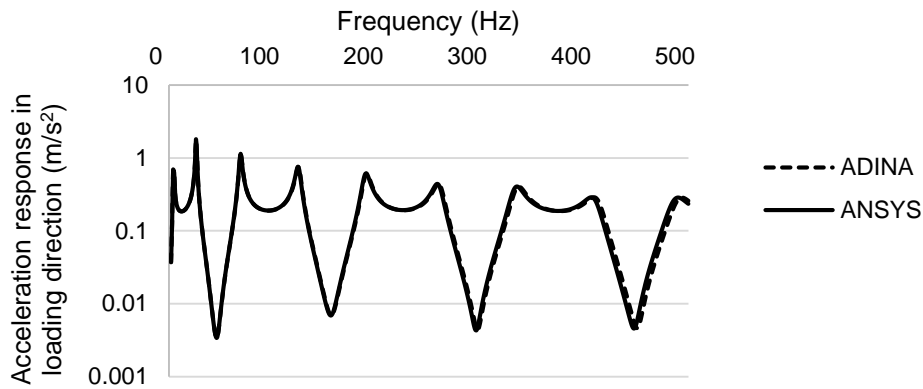


Figure 3.3 Comparison of acceleration responses for the top node at the free end of the cantilever beam considering 1 Pa of harmonic pressure load.

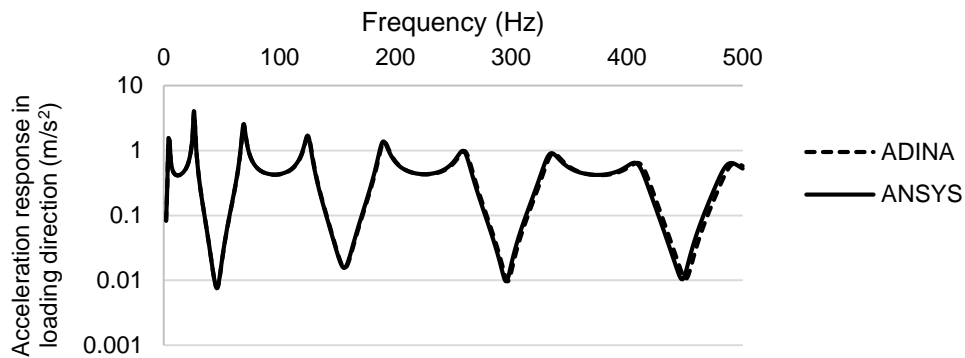


Figure 3.4 Comparison of acceleration responses for the top node at the free end of the cantilever beam considering 1 Pa and 2 Pa of harmonic pressure loads with a phase difference of 90° .

3.3 Methods for applying the harmonic acoustic pressure field

Acoustic pressure fluctuations on the inner arterial wall are assumed as a harmonic load. These pressure fields are determined using the empirical equations [22] presented in Chapter 2 as a function of frequency and axial distance downstream

of the constriction exit. In Figure 3.5, a sample case is considered for an artery with a lumen diameter of 6.4 mm and 87% stenosis. The acoustic pressure field is determined for $Re = 2000$ (Reynolds number of 2000) using the empirical equation (2.32).

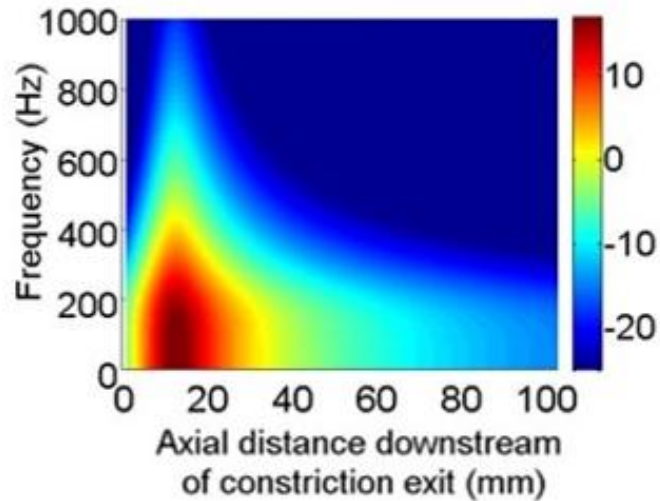


Figure 3.5 Acoustic pressure amplitudes (dB ref: 1 Pa) as function of axial position and frequency for $Re = 2000$ with 87% stenosis. The color scale is used for dB.

The highest sound generation is observed about 15 mm downstream of the constriction exit for a lumen diameter of 6.4 mm. The spectral behavior at this peak activity point is determined by Tobin and Chang [23] and compared to the other points. They stated that for all points nearly the same spectral trend is observed. The spectral behavior can be represented as a function which defines the change in the pressure amplitudes depending on the frequency. In the same manner, the spatial behavior can also be defined as an independent function which represents the variation in the pressure amplitudes depending on the axial distance downstream of the constriction exit. By combining these spectral and spatial functions, the amplitudes in the acoustic pressure field can be obtained in an accurate way as presented in Figure 3.6.

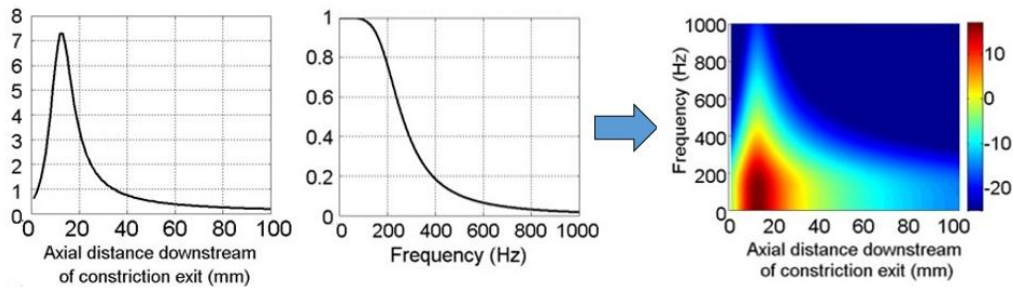


Figure 3.6 Spatial and spectral functions used to generate the acoustic pressure field represented in Figure 3.5.

In Figure 3.6, the same acoustic pressure field presented in Figure 3.5 is obtained accurately using only spatial and spectral functions. The spectral function defines the variation in pressure amplitudes depending on the frequency, at the location of highest sound generation. For the sample case presented in Figure 3.5 and Figure 3.6, the highest sound is generated at 13 mm downstream of the constriction exit. The spatial function is showing the variation in the pressure amplitudes at 5 Hz depending on the axial distance to the constriction exit. By trial and error, it is seen that the spatial function at low frequencies reduces the error while generating the pressure field. Therefore, 5 Hz is chosen to obtain the spatial function correctly. For example, if the spatial function at 100 Hz is used to generate the pressure field, the percent error in the pressure amplitudes increases. As presented in Figure 3.7, the percent errors for the acoustic pressure amplitudes are lower than 0.1% using the spatial function at 5 Hz for various Reynolds numbers (Re) and stenosis severities.

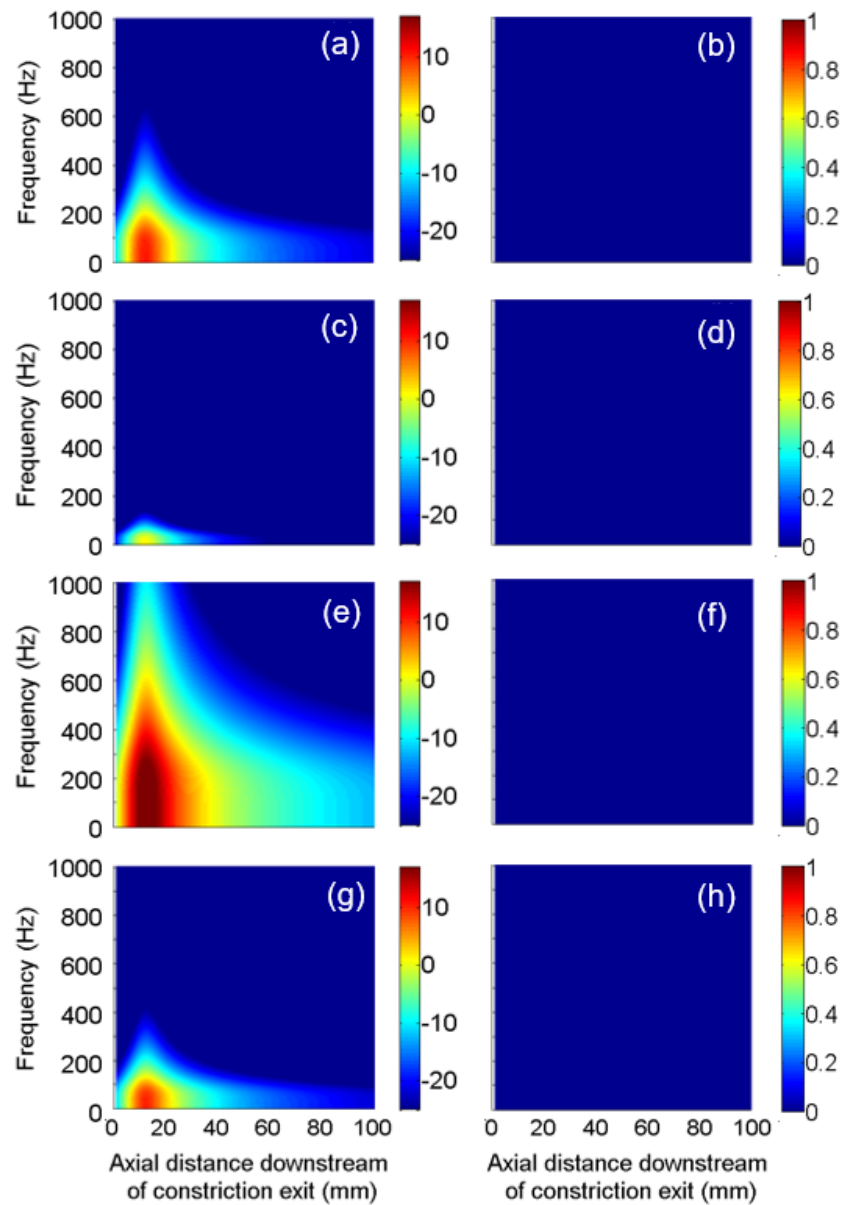


Figure 3.7 Acoustic pressure amplitudes (dB ref: 1 Pa) and percent errors as function of axial position and frequency. For acoustic pressure contours, the color scale is used for dB. For percent error contours, the color scale is used for the magnitude of the percent error. (a) $Re = 1000$, 90% stenosis. (b) Percent error for (a). (c) $Re = 1000$, 70% stenosis. (d) Percent error for (c). (e) $Re = 2000$, 90% stenosis. (f) Percent error for (e). (g) $Re = 2000$, 70% stenosis. (h) Percent error for (g).

The spectral and spatial functions are presented in Figure 3.8 and Figure 3.9, respectively, considering various Reynolds numbers and stenosis levels.

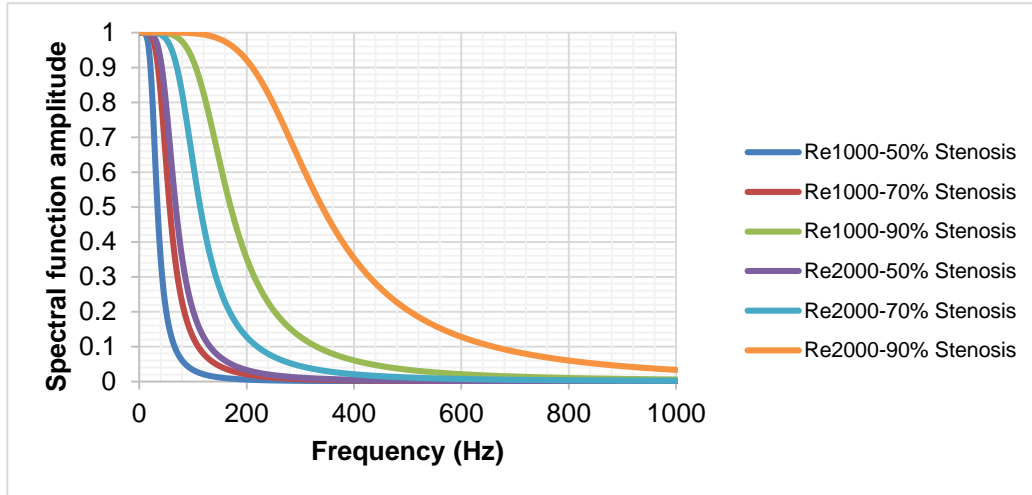


Figure 3.8 Spectral functions at the point of highest sound generation for various Reynolds numbers and stenosis levels.

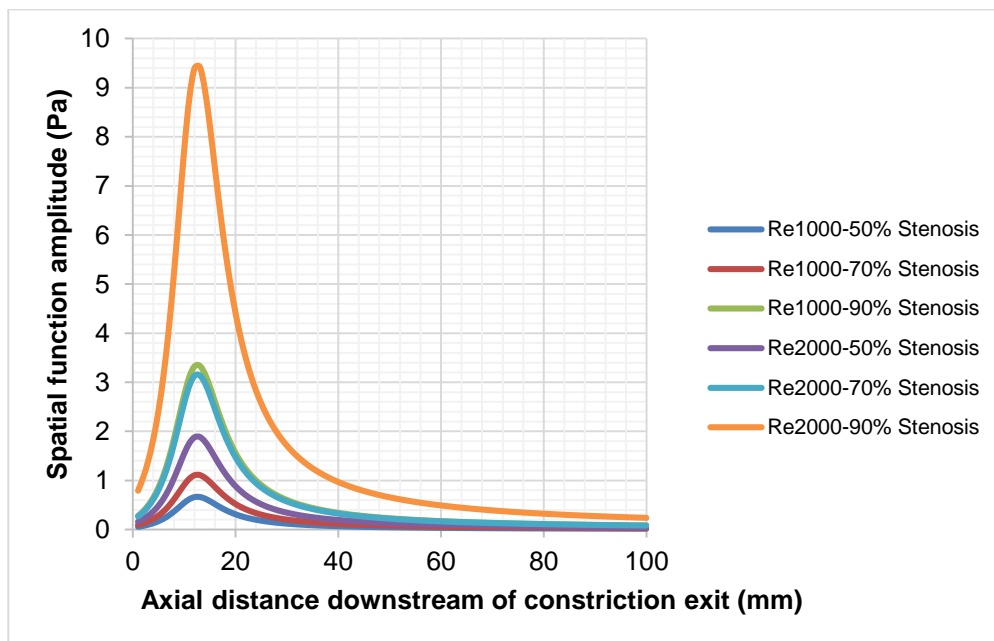


Figure 3.9 Spatial functions at 5 Hz for various Reynolds numbers and stenosis levels.

the pressure load is assumed to be constant for each discretized region and applied to the corresponding discretized region in the amplitude map as shown in Figure 3.10. The phase map can be improved to a resolution of 20 x 20 as represented in Figure 3.11. Using 20 x 20 phase map resolution, the frequency range within 0 to 600 is divided into 20 independent regions with intervals of 30 Hz. Similarly, the total distance of 100 mm is divided into 20 regions with 5 mm intervals.

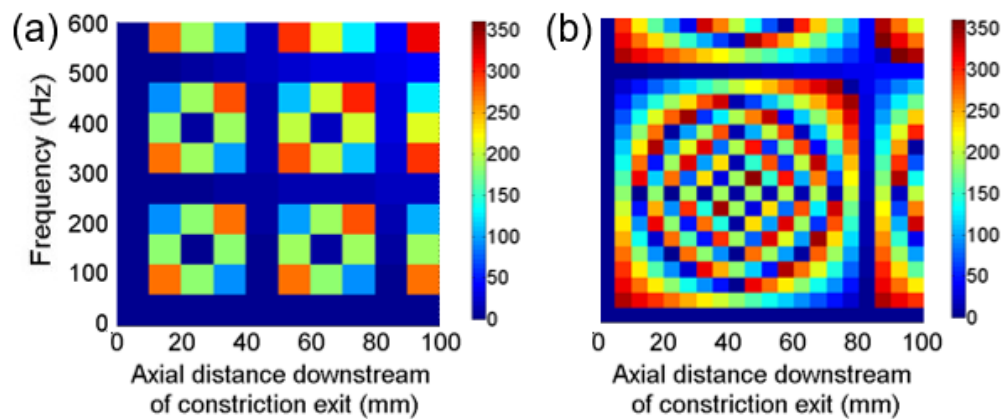


Figure 3.11 Phase maps for $Re = 2000$ and 87% stenosis considering a lumen diameter of 6.4 mm. The color scale is used for degree angle. (a) 10 x 10 resolution. (b) 20 x 20 resolution.

Due to the computational limitations, the phase map is used considering the resolutions of 10 x 10 and 20 x 20. Higher resolutions than 20 x 20 dramatically increased the post-processing time for the harmonic analysis. As will be represented and discussed in the following chapters, 10 x 10 and 20 x 20 phase maps lead to satisfactorily accurate results. The acoustic pressure amplitudes and the corresponding phase maps are given in Figure 3.12 and Figure 3.13, respectively, considering various Reynolds numbers and stenosis severities.

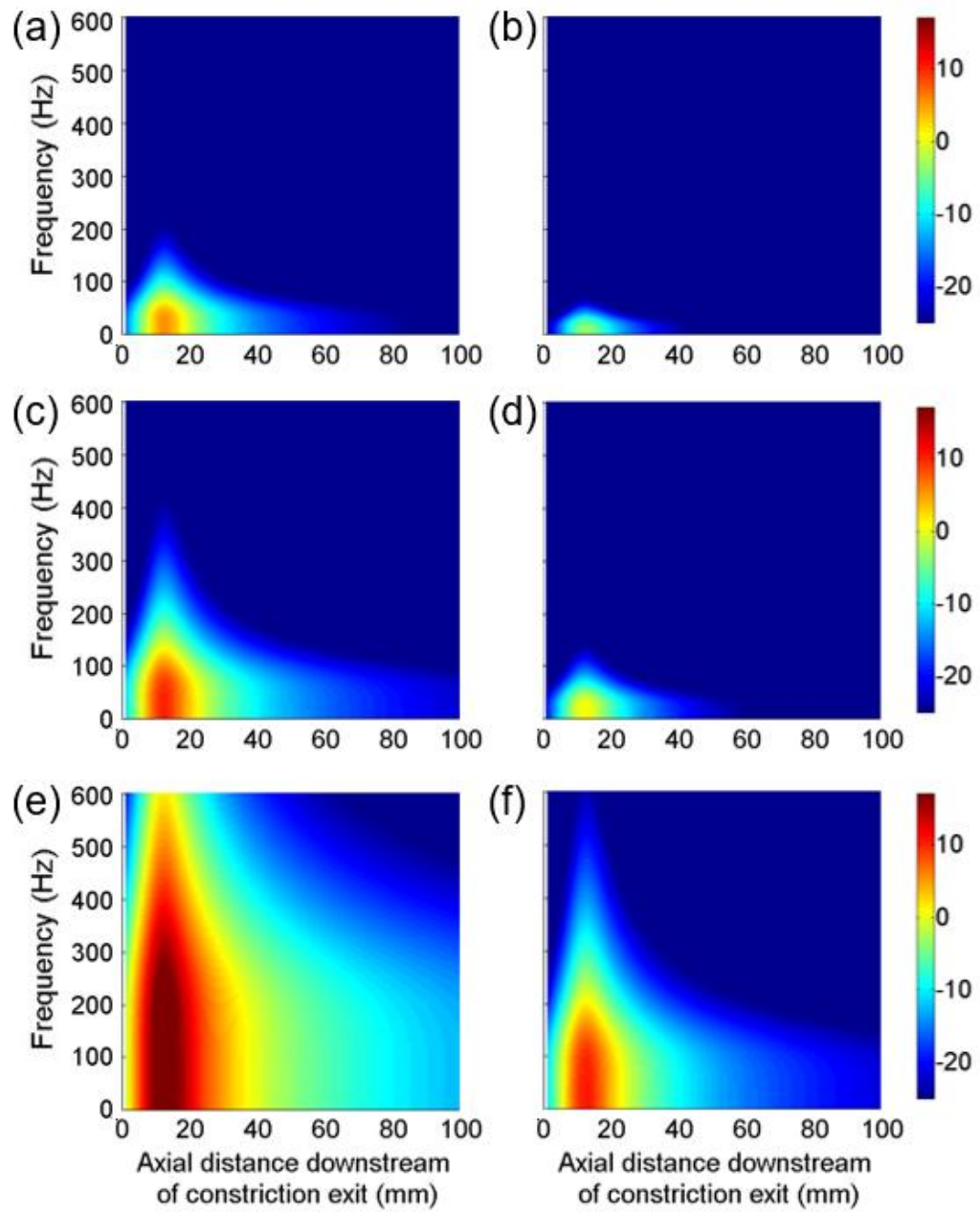


Figure 3.12 Acoustic pressure amplitudes (dB ref: 1 Pa) for a lumen diameter of 6.4 mm as function of axial position and frequency. The color scale is used for dB. (a) $Re = 2000$, 50% stenosis. (b) $Re = 1000$, 50% stenosis. (c) $Re = 2000$, 70% stenosis. (d) $Re = 1000$, 70% stenosis. (e) $Re = 2000$, 90% stenosis. (f) $Re = 1000$, 90% stenosis.

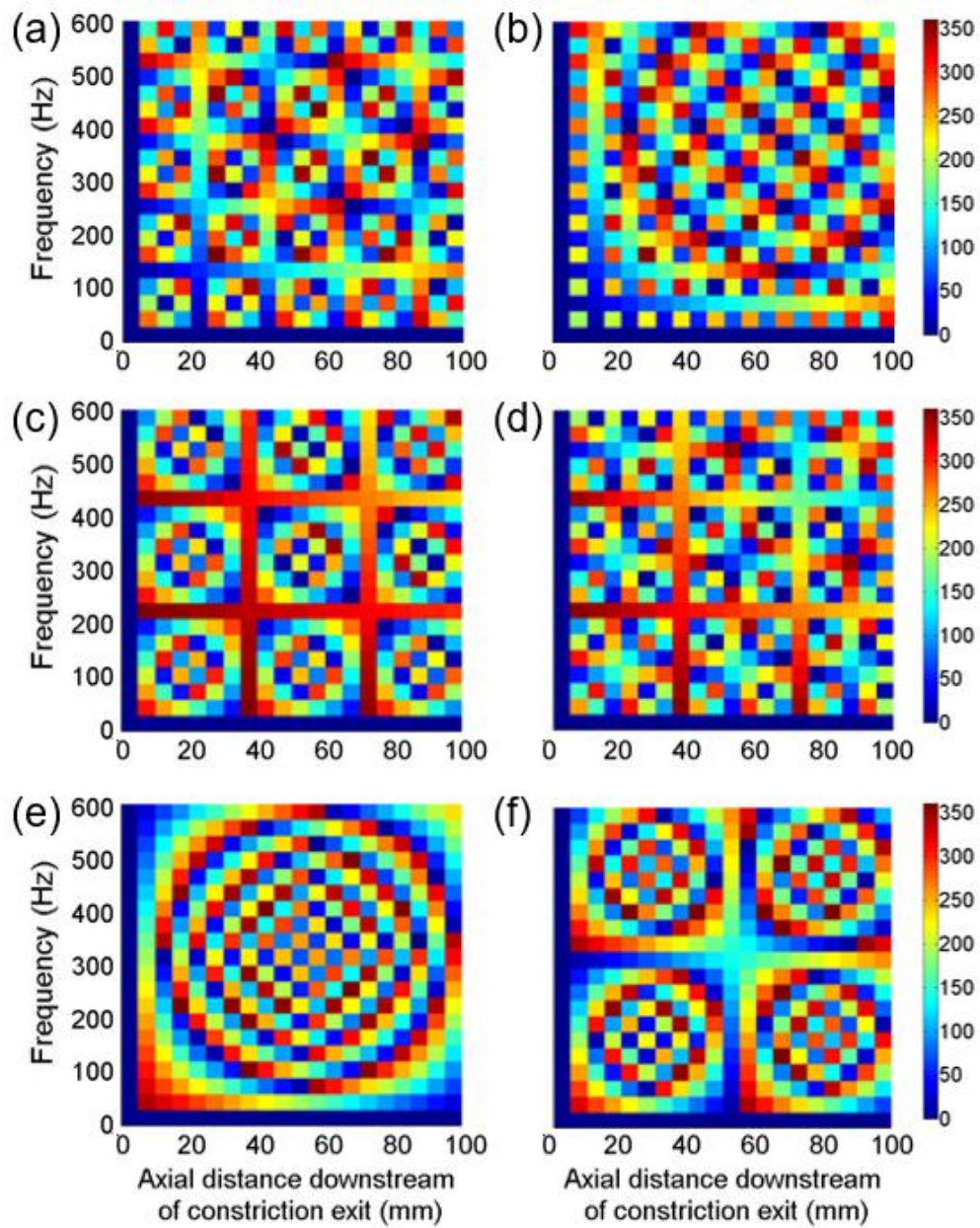


Figure 3.13 Phase maps with resolution of 20×20 for a lumen diameter of 6.4 mm. The color scale is used for degree angle. (a) $Re = 2000$, 50% stenosis. (b) $Re = 1000$, 50% stenosis. (c) $Re = 2000$, 70% stenosis. (d) $Re = 1000$, 70% stenosis. (e) $Re = 2000$, 90% stenosis. (f) $Re = 1000$, 90% stenosis.

CHAPTER 4

IDEALIZED COMPUTATIONAL MODELS

Computational studies are performed in two parts using idealized and realistic models. For the idealized models, some simplifications are considered for the problem geometry and the material properties. For the realistic models which are presented in Chapter 5, material properties and the anatomical geometry of the problem domain are modelled more realistically considering the biological relevance. In this chapter, the idealized models are investigated using the simplified material properties and geometry.

4.1 The problem geometry for the idealized models

Artery, blood and surrounding soft tissue are modelled in the idealized models. The problem geometry is assumed to be in an axisymmetrical form. The lumen diameter of the artery is denoted by D and the arterial thickness is denoted by t_a . Arterial lumen diameter and the arterial thickness are selected as 6.4 and 0.3 mm, respectively, to follow the numerical and experimental studies in the literature [22-24, 62]. The artery is occluded at a particular location and the constricted diameter is denoted by d . The stenosis severity (S) is expressed as the percent flow area reduction in the lumen using the following equation.

$$S = 100 \frac{(D^2 - d^2)}{D^2} \quad (4.1)$$

The artery is surrounded by a hollow cylindrical soft tissue with a thickness of H . Since the highest vibroacoustic excitation is observed at the downstream of the constriction exit, only the downstream region is modelled in the computational studies. The total length of the artery and the surrounding soft tissue are denoted by L . Axial flow velocity at the inlet of the artery is denoted by U . The geometrical parameters of the idealized model are represented in Figure 4.1.

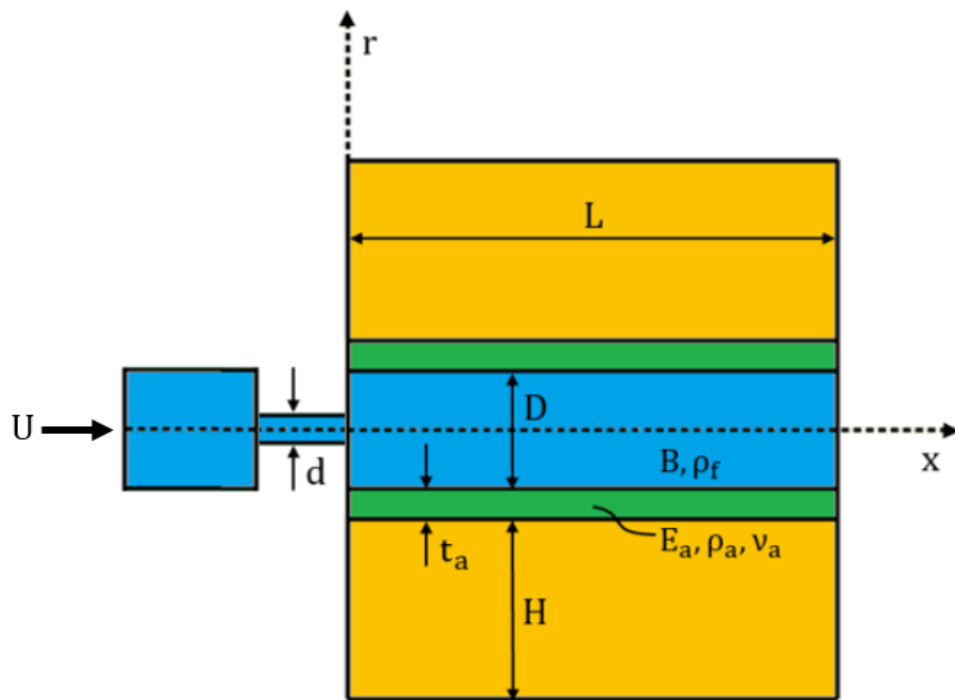


Figure 4.1 Sectional view of the axisymmetric idealized model. Flow is from left to right. Blood, artery and surrounding soft tissue are displayed by blue, green and yellow colors, respectively. Axial and radial coordinates are shown by x and r , respectively.

4.2 Material properties for the idealized models

The artery is modelled as a tubular structure with acoustic fluid elements inside. These acoustic fluid elements are used to model the wave propagation inside the

blood. Structural properties of the artery are modelled using the latex rubber material properties [22]. Linearly elastic material model is used for the arterial structure [22-24] with elastic modulus (E_a) of 800 kPa, Poisson's ratio (ν_a) of 0.42 and mass density (ρ_a) of 1086 kg/m³. Material properties of water are used for modeling the blood with mass density (ρ_f) of 1000 kg/m³ and bulk modulus (B) of 2.2 GPa [7, 19, 22-24]. Since the geometry of the idealized model is axisymmetric, only the radial component of the variables is investigated. Radial displacement, radial velocity and radial acceleration responses are obtained at the outer surface of the models. In the analysis, the radial velocity responses are considered primarily to compare with the radial velocity responses presented in the literature [22]. The two ends of the artery and the surrounding soft tissue are fixed by setting zero displacement (i.e., $u = 0$ at $x = 0$ and $x = L$). The reason for limiting the two ends to zero displacement is to assume that these two sides are joints. Due to high stiffness in the joints, the two sides of the model are considered to be motionless. The flow-induced harmonic pressure load is applied radially on the inner arterial wall. Three different phase maps are applied for the harmonic pressure load as no phase map, 10 x 10 phase map and 20 x 20 phase map. For the no phase map, all points have the same phase and this value does not change with varying frequencies and distances. 10 x 10 phase map and 20 x 20 phase map are previously explained in Figure 3.11. For all mode shapes, 2% of modal damping is employed for the idealized computational models considering the light damping conditions.

4.3 Bare artery models

For idealized models, two different cases are mainly investigated. First, the bare artery models are analyzed without considering the surrounding soft tissue (i.e., $H = 0$). After completing the bare artery analysis, the soft tissue surrounding the artery is taken into account. By this way, the effects on the outer surface of the artery and the surrounding soft tissue are compared. The problem has an

axisymmetric geometry, therefore only the radial variables are recorded for the nodes at the top of the model.

4.3.1 Mesh independence study for the bare artery analysis

Three different mesh densities are used for the idealized bare artery models. In Table 4.1, the details of the meshes are provided.

Table 4.1 Details of the meshes for the bare artery models

Mesh Density	Medium	Number of nodes in axial direction	Number of nodes in radial direction	Number of nodes in circumferential direction	Total number of nodes	Total number of elements
Mesh 1	Artery	41	2	20	3321	3200
	Blood	41	4	20		
Mesh 2	Artery	81	3	30	17091	16800
	Blood	81	6	30		
Mesh 3	Artery	81	4	40	48521	48000
	Blood	81	8	40		

The radial velocity responses on the top line of the bare artery are obtained for a sample case using three mesh densities as shown in Figure 4.2. Average response amplitude (within 0-100 mm, 0-600 Hz) has a difference of 1.86% between Mesh 1 and Mesh 2. This difference is obtained as 0.8% between Mesh 2 and Mesh 3. Results are accepted as mesh-independent if the difference in amplitudes is less than 3%. Therefore, results of Mesh 1 are satisfactorily accurate in terms of spectral content and response amplitudes. For a frequency domain based structural modal analysis, the mesh independent results can be achieved with low density meshes when compared to the time domain based transient structural analysis. The results of Mesh 1 are presented for all remaining bare artery analyses.

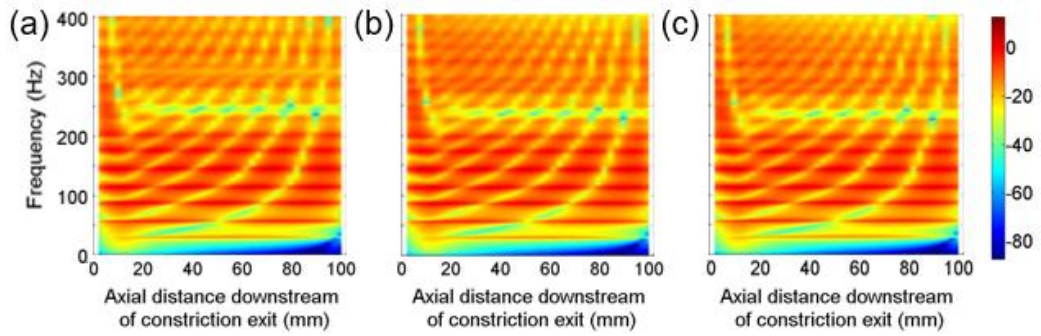


Figure 4.2 Radial velocity response (dB ref: 1 mm/s) on outer surface of the artery for $Re = 2000$ with 90% stenosis. (a) Mesh 1. (b) Mesh 2. (c) Mesh 3. The color scale is used for dB.

4.3.2 Responses on the bare artery models

Radial displacement, velocity and acceleration responses on outer surface of artery are presented in Figure 4.3 for $Re = 2000$ with 90% stenosis considering no phase map. General spectral behaviors of the displacement, velocity and acceleration responses are similar, and bending modes of fluid-filled artery are clearly visible. In all response plots, the first highly excited frequency range is within 25 to 225 Hz. The second excited region is observed within 250 to 400 Hz. The increase in Reynolds number increases the amplitudes due to turbulent pressure fluctuations on arterial wall. The amplitudes in Figure 4.3 indicate that displacements are in the range of -100 dB to -50 dB for a reference displacement of 1 mm which are too low to measure. Radial velocities have higher amplitudes (within 1 to 300 $\mu\text{m/s}$) that can be measured using the state of the art sensor technologies. Laser Doppler Vibrometers (LDV) are capable of measuring velocities higher than 0.02 $\mu\text{m/s}$ (IVS-300, Polytech, Auburn, MA). The highest amplitudes are found for the accelerations, but highest experimental noise is seen for acceleration data which makes the measurement challenging due to low signal to noise ratio. For this reason, the radial velocity is the most suitable parameter for the investigations.

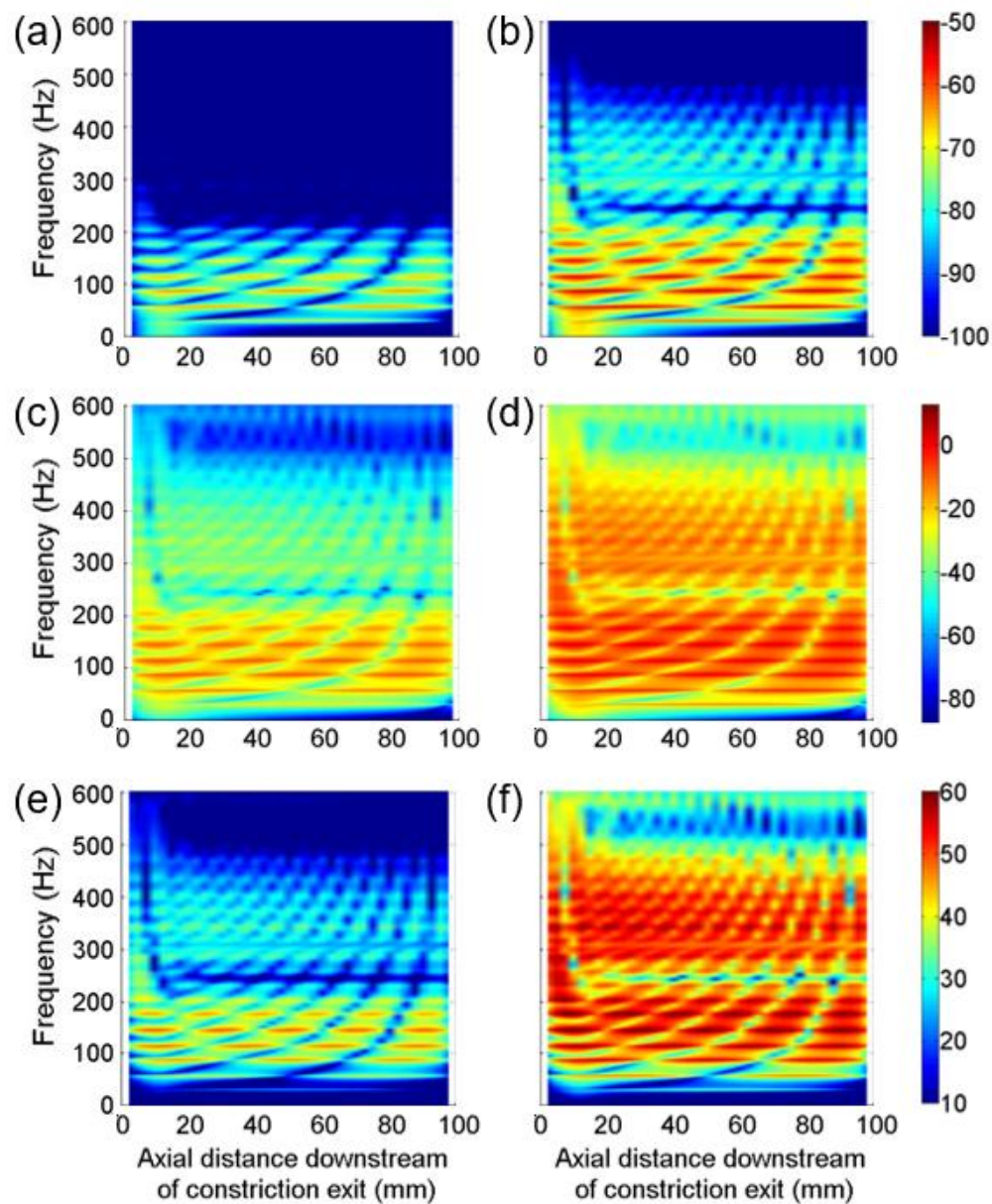


Figure 4.3 Responses on the outer surface of the artery with 90% stenosis considering no phase map. (a) Radial displacement (dB ref: 1 mm) for $Re = 1000$. (b) Radial displacement (dB ref: 1 mm) for $Re = 2000$. (c) Radial velocity (dB ref: 1 mm/s) for $Re = 1000$. (d) Radial velocity (dB ref: 1 mm/s) for $Re = 2000$. (e) Radial acceleration (dB ref: 1 mm/s²) for $Re = 1000$. (f) Radial acceleration (dB ref: 1 mm/s²) for $Re = 2000$.

The same mode shapes and the corresponding natural frequencies are observed for $Re = 1000$ and $Re = 2000$. Increase in the radial velocity amplitudes becomes much more prominent as the flow rate increases. The effect of stenosis severity is investigated in Figure 4.4 considering stenosis levels from 50% to 95%. It is seen that the response amplitudes tend to increase with the increasing stenosis level.

The maximum and average values of the radial velocity responses presented in Figure 4.4 are given in Figure 4.5. It is seen that the response amplitudes increase nonlinearly due to the increase in the stenosis level. As the stenosis level reaches 95%, a dramatic increase is observed for the response amplitudes. The radial velocity amplitudes do not change seriously up to 70% stenosis for both $Re = 1000$ and $Re = 2000$. However, as the stenosis level exceeds 70%, the relative increase in the response amplitudes is observed much more clearly. This important increase in the response amplitudes is a characteristic sign for the presence of a stenosis and 70% stenosis is an important threshold severity to detect an occlusion.

In Figure 4.4 and Figure 4.5, the radial velocity responses are determined considering no phase map in which the phase of the applied pressure load does not vary depending on the axial distance to the stenosis exit and the frequency. In Figure 4.6 and Figure 4.7, the effect of stenosis severity is investigated considering 10 x 10 phase map and 20 x 20 phase map, respectively.

In this chapter, the arterial lumen diameter is used as 6.4 mm. For the selected arterial diameter, the mass flow rate (\dot{m}) is 0.005 kg/s for $Re = 1000$ and 0.010 kg/s for $Re = 2000$.

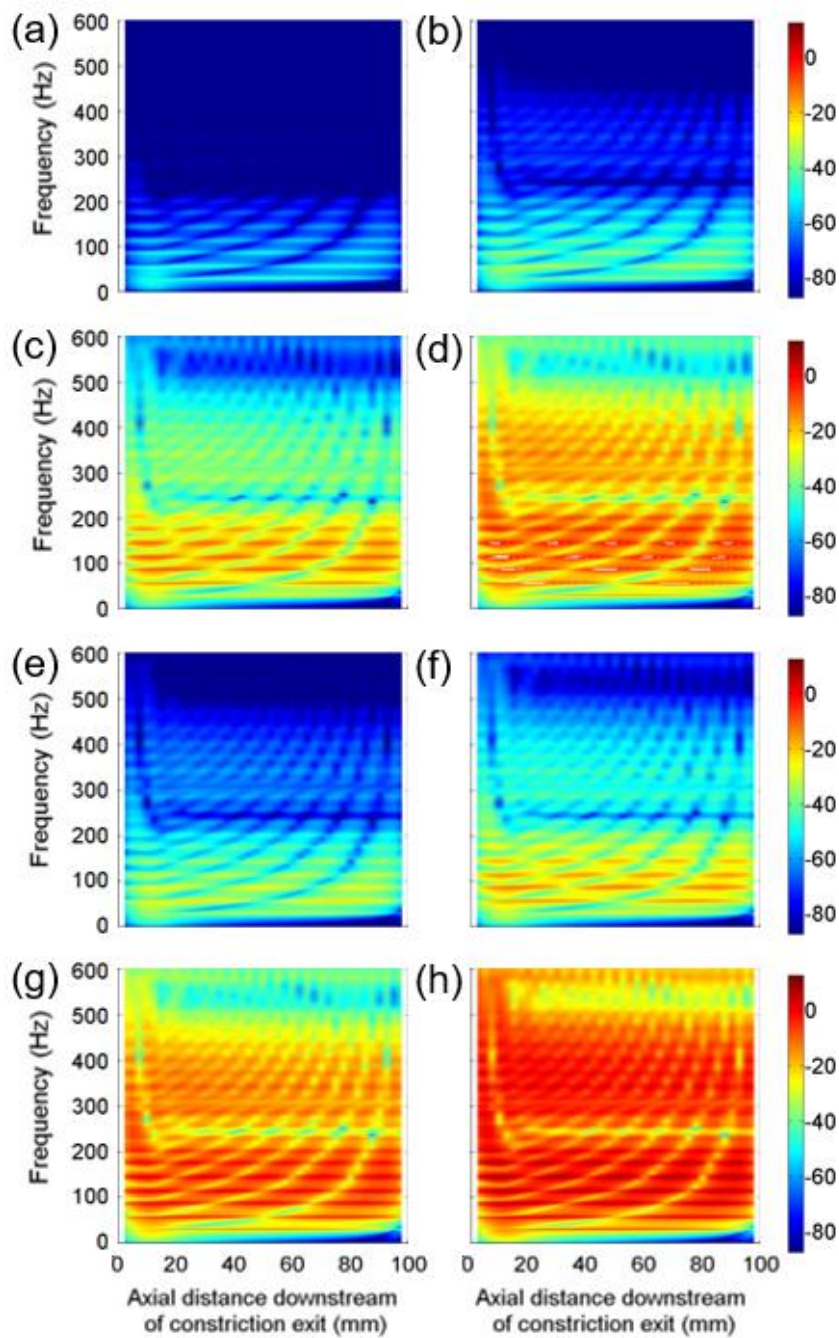


Figure 4.4 Radial velocity response (dB ref: 1 mm/s) on the outer surface of the artery considering no phase map. (a) $Re = 1000$, 50% Stenosis. (b) $Re = 1000$, 70% Stenosis. (c) $Re = 1000$, 90% Stenosis. (d) $Re = 1000$, 95% Stenosis. (e) $Re = 2000$, 50% Stenosis. (f) $Re = 2000$, 70% Stenosis. (g) $Re = 2000$, 90% Stenosis. (h) $Re = 2000$, 95% Stenosis.

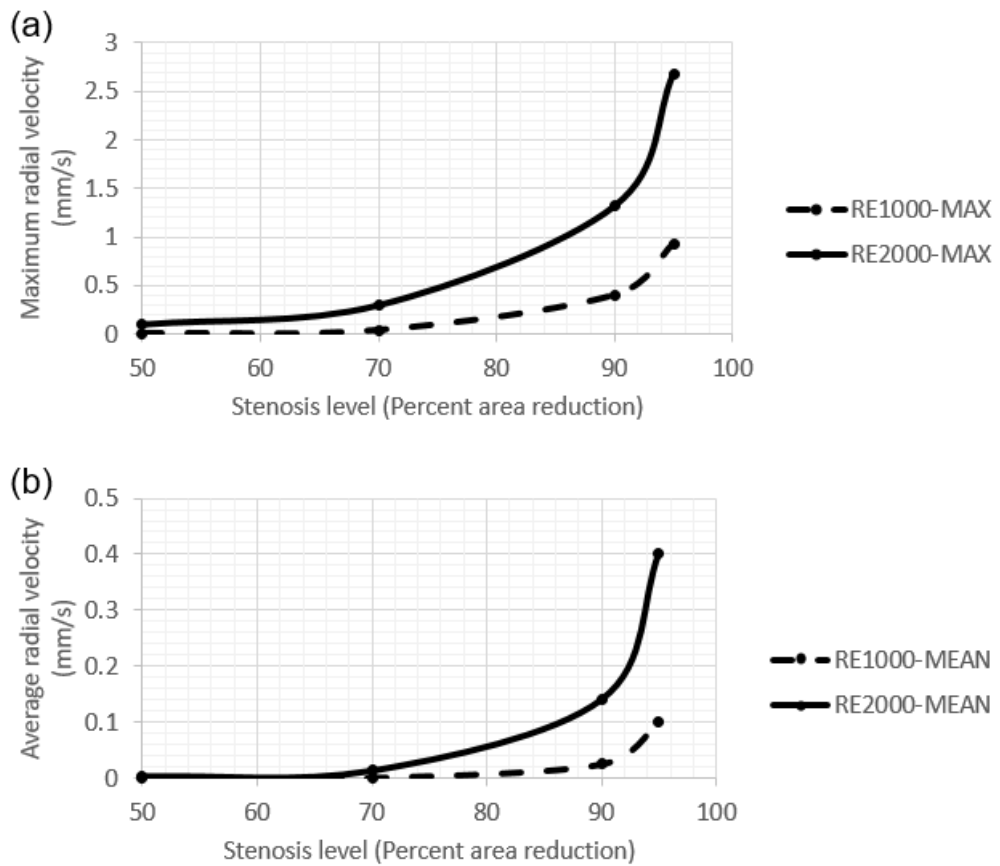


Figure 4.5 (a) Maximum radial velocity response (within 0-600 Hz, 0-100 mm) for $Re = 1000$ and $Re = 2000$ as function of stenosis level. (b) Average radial velocity response (within 0-600 Hz, 0-100 mm) for $Re = 1000$ and $Re = 2000$ as function of stenosis level.

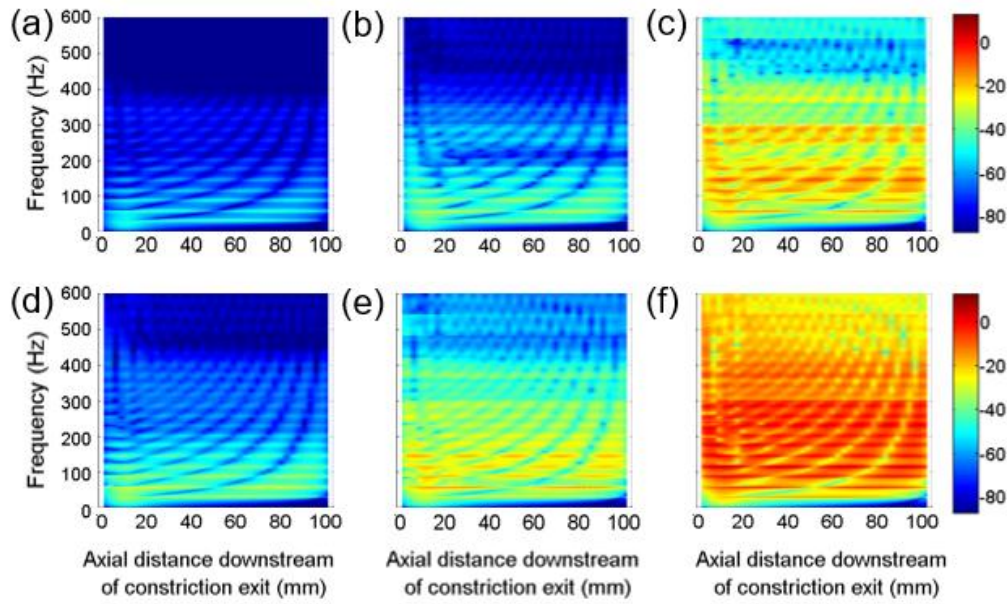


Figure 4.6 Radial velocity response (dB ref: 1 mm/s) on the outer surface of the artery considering 10 x 10 phase map. (a) $Re = 1000$, 50% Stenosis. (b) $Re = 1000$, 70% Stenosis. (c) $Re = 1000$, 90% Stenosis. (d) $Re = 2000$, 50% Stenosis. (e) $Re = 2000$, 70% Stenosis. (f) $Re = 2000$, 90% Stenosis.

The same natural frequencies are observed for the no phase map, 10 x 10 phase map and 20 x 20 phase map. However, the spectral content slightly changed depending on the applied phase map. The response plots presented in Figure 4.4 demonstrate smooth and regular characteristics. On the other hand, a more complicated and piecewise continuous trend is obtained for the radial velocity responses given in Figure 4.6 and Figure 4.7 considering 10 x 10 and 20 x 20 phase maps, respectively.

In Figure 4.8, the radial velocity responses are obtained for $Re = 2000$ with 87% stenosis considering different phase maps, and the computational results are compared to the experimental findings in the literature [22]. The amplitudes of the computational results are in good agreement with the theoretical and experimental findings in the literature.

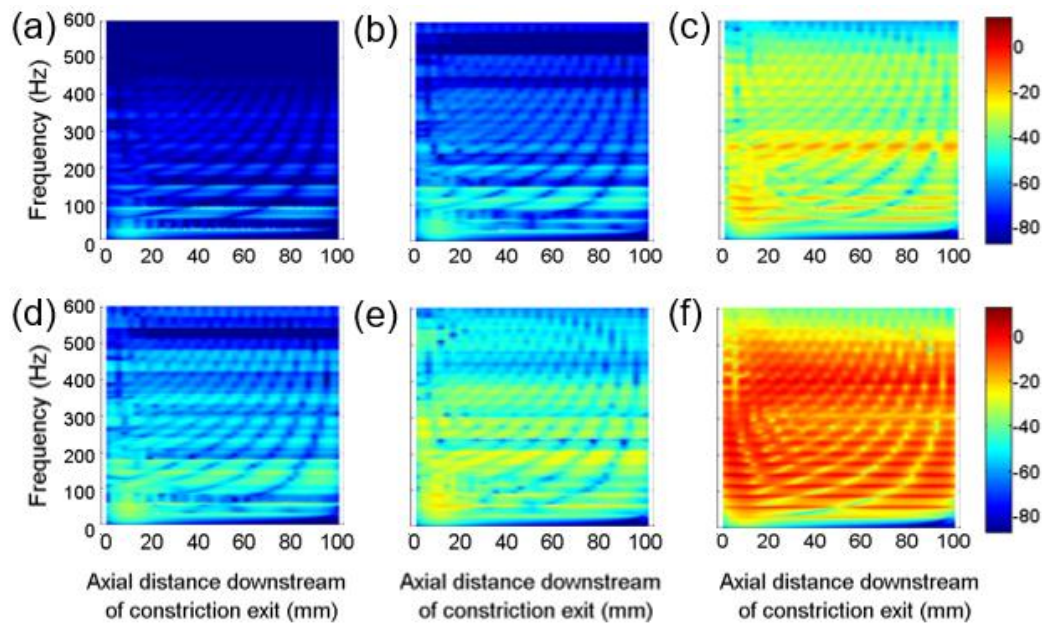


Figure 4.7 Radial velocity response (dB ref: 1 mm/s) on the outer surface of the artery considering 20 x 20 phase map. (a) $Re = 1000$, 50% Stenosis. (b) $Re = 1000$, 70% Stenosis. (c) $Re = 1000$, 90% Stenosis. (d) $Re = 2000$, 50% Stenosis. (e) $Re = 2000$, 70% Stenosis. (f) $Re = 2000$, 90% Stenosis.

The first three mode shapes of the bare artery model are obtained at 30, 60 and 90 Hz by using sharp peaks in Figure 4.8(f). The determined natural frequencies agree well with the theoretical results in Figure 4.8(g). However, the same mode shapes appear at slightly lower frequencies in the experimental results given in Figure 4.8(h). Internal mean dynamic pressure may be the reason for this frequency shift. In the experimental studies, the mean pressure results increased circumferential prestress on the arterial wall. This condition leads to an increase in radial dimensions and consequently an increase in arterial blood volume. The additional fluid mass shifts the natural frequencies slightly downward.

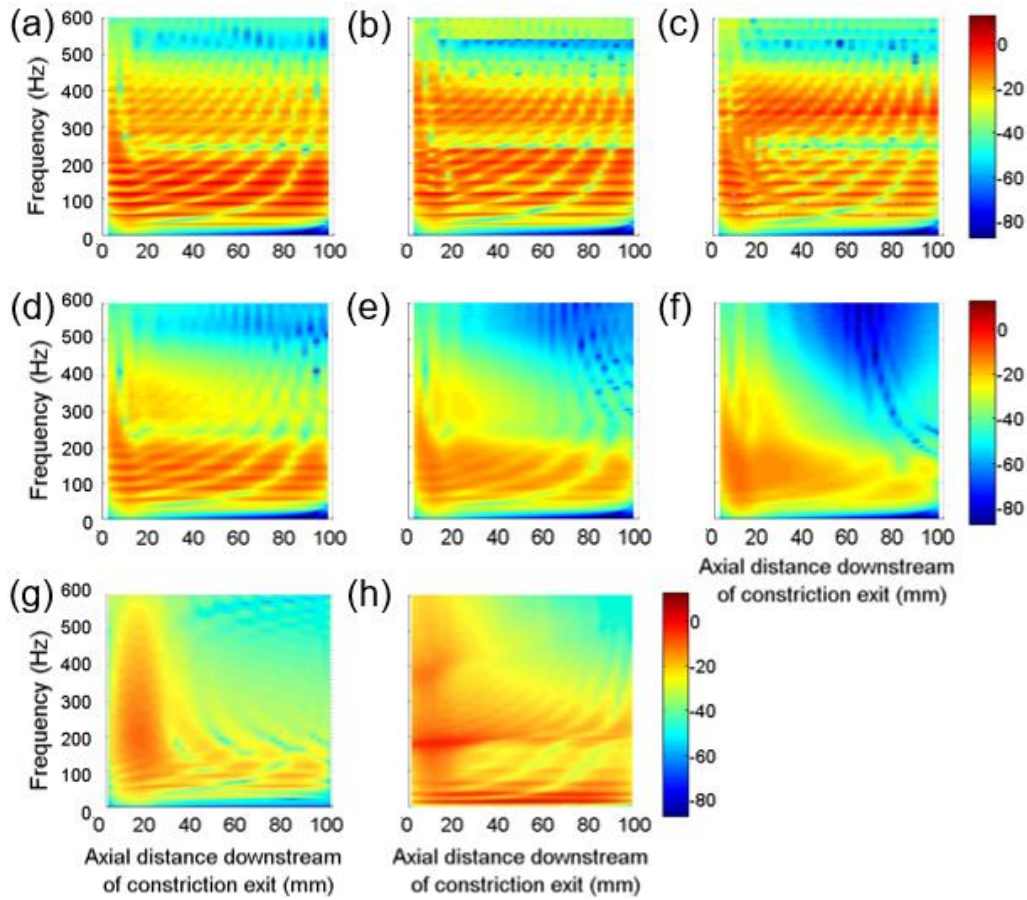


Figure 4.8 Radial velocity response (dB ref: 1 mm/s) on the outer surface of the artery for $Re = 2000$ with 87% stenosis. (a) No phase map, 2% modal damping. (b) 10 x 10 phase map, 2% modal damping. (c) 20 x 20 phase map, 2% modal damping. (d) No phase map, 5% modal damping. (e) No phase map, 10% modal damping. (f) No phase map, 20% modal damping. (g) Theory in air [22]. (h) Experiment in air [22].

In the experimental results shown in Figure 4.8(h), high activity is mainly observed at three regions, within 0-100 Hz, around 200 Hz, and around 400 Hz. Similarly, three highly excited regions are observed in the computational analyses shown in Figure 4.8(a), (b) and (c), within 0-220 Hz, within 300-400 Hz, and around 575 Hz. These three regions can be considered as the same excited regions with a slight

frequency shift when compared to the experimental results, as a consequence of the additional fluid mass loading due to prestress.

In the theoretical and experimental results given in Figure 4.8(g) and (h), the response amplitudes are relatively higher within 0-25 mm. After passing the distance of 25 mm, the amplitudes tend to decrease gradually. The first 25 mm is the recirculating flow region at which the highest sound generation is recorded, so the radial velocity amplitudes at this region are relatively high. However, the relatively high excitation is not clearly seen in the computational results given in Figure 4.8(a), (b) and (c) within 0-25 mm. Modal damping of 2% is employed for all modes of the model, since a light damping condition is considered for the bare artery analysis. If the damping is increased in the arterial model, the directional dependence of the response amplitudes becomes more apparent as seen in Figure 4.8(d), (e) and (f). When the modal damping is increased to 20%, the radial velocity amplitudes sharply decrease with increasing axial distance, and the amplitudes within 0-25 mm appear to be more dominant. However, the amplitude scale of the response plot shifts to lower values as the modal damping increases.

4.3.3 Average responses for the bare artery analysis

In this section, the averages of the previously presented response plots are examined in detail. For the bare artery analysis, 41 nodes are placed at a total distance of 100 mm. The radial velocity responses are averaged considering all 41 nodes on the top line of the artery and the average responses are obtained as function of frequency. In Figure 4.9, the average responses are investigated to see the effect of stenosis severity. The highest average response amplitude in Figure 4.9(a) is lower than 1 mm/s for $Re = 1000$. When the flow rate increases to $Re = 2000$, the highest amplitude becomes 2 mm/s in Figure 4.9(b). The increase depending on the stenosis severity is more obvious for the high frequency range, within 250-600 Hz. For $Re = 2000$ with 95% stenosis, the average radial velocity

amplitude at 600 Hz is determined as 0.1 mm/s. This value decreased to 0.01 mm/s for 90% stenosis. The 5% difference in the stenosis level caused a 10-fold reduction in the average amplitudes at 600 Hz. The amplitude difference at high frequencies may indicate severe stenosis in the artery.

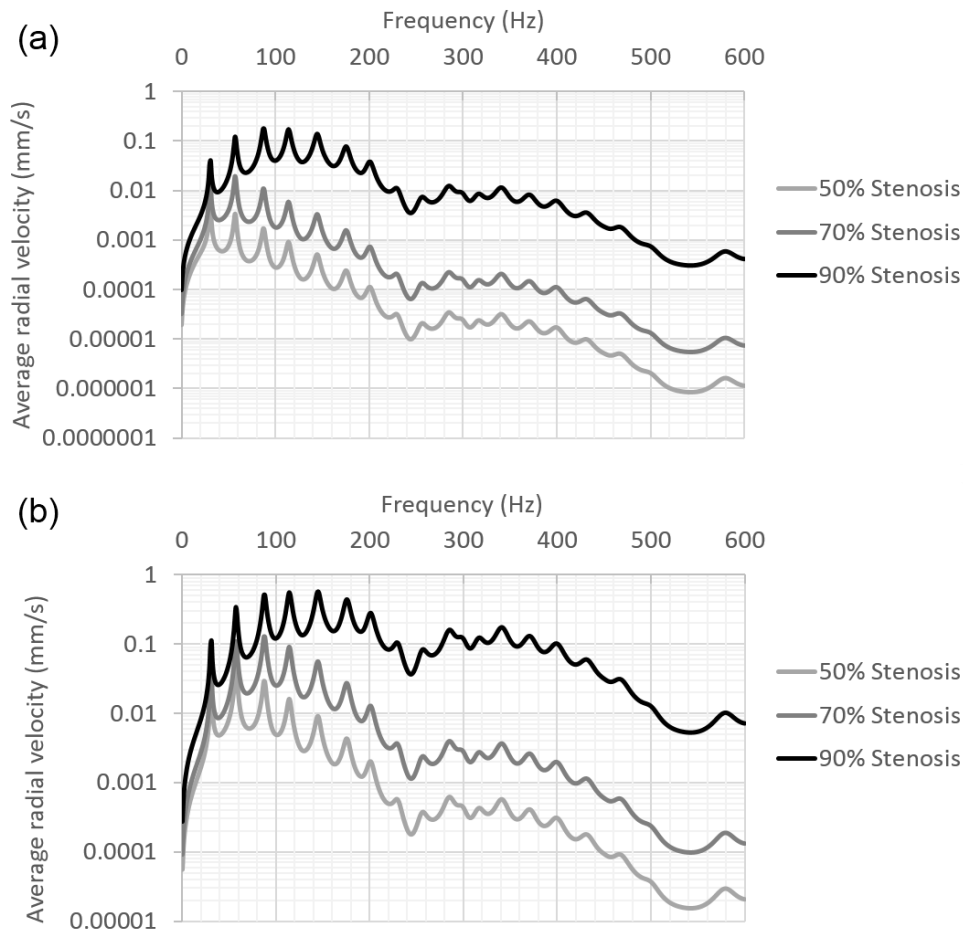


Figure 4.9 Average radial velocity response (within 0-100 mm) on the outer surface of the artery as function of frequency considering no phase map. (a) $Re = 1000$. (b) $Re = 2000$.

The effect of the applied phase map is shown in Figure 4.10 and Figure 4.11 considering 10 x 10 and 20 x 20 phase maps, respectively.

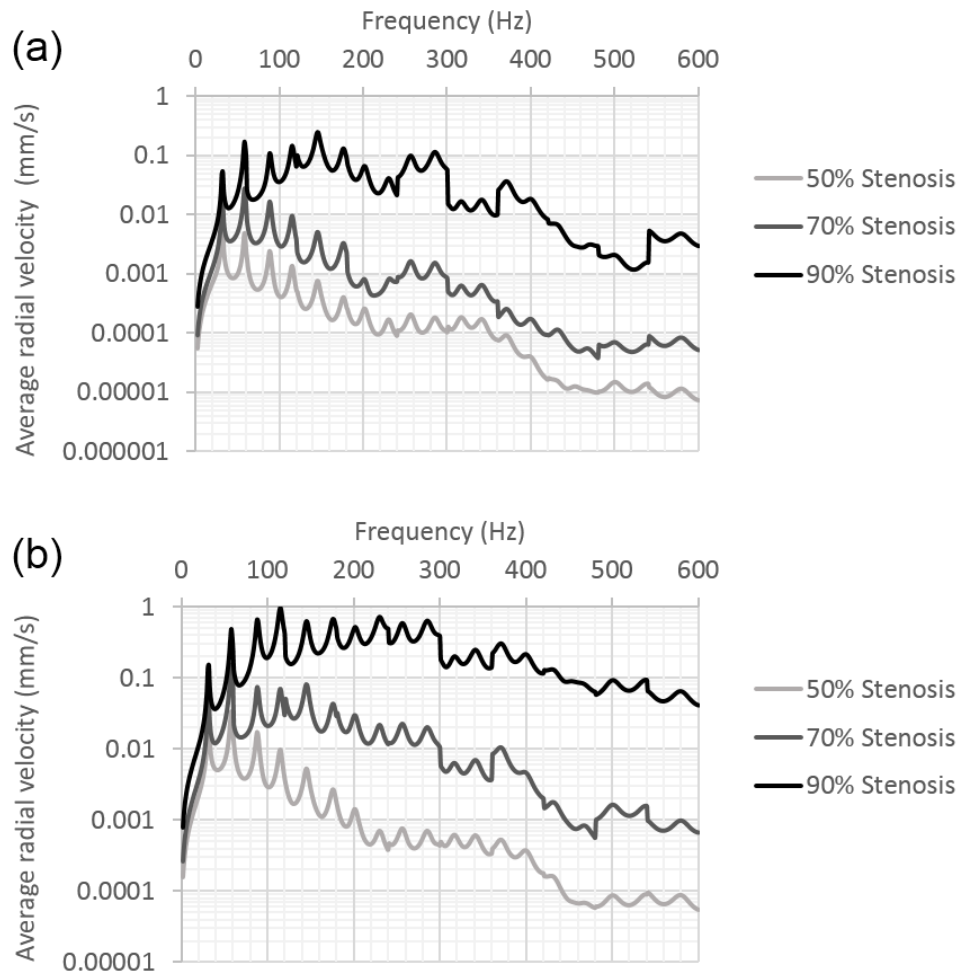


Figure 4.10 Average radial velocity response (within 0-100 mm) on the outer surface of the artery as function of frequency considering 10 x 10 phase map. (a) $Re = 1000$. (b) $Re = 2000$.

The smooth and regular trend is not observed for the results of the 10 x 10 and 20 x 20 phase maps, and a segmented average response is obtained in Figure 4.10 and Figure 4.11.

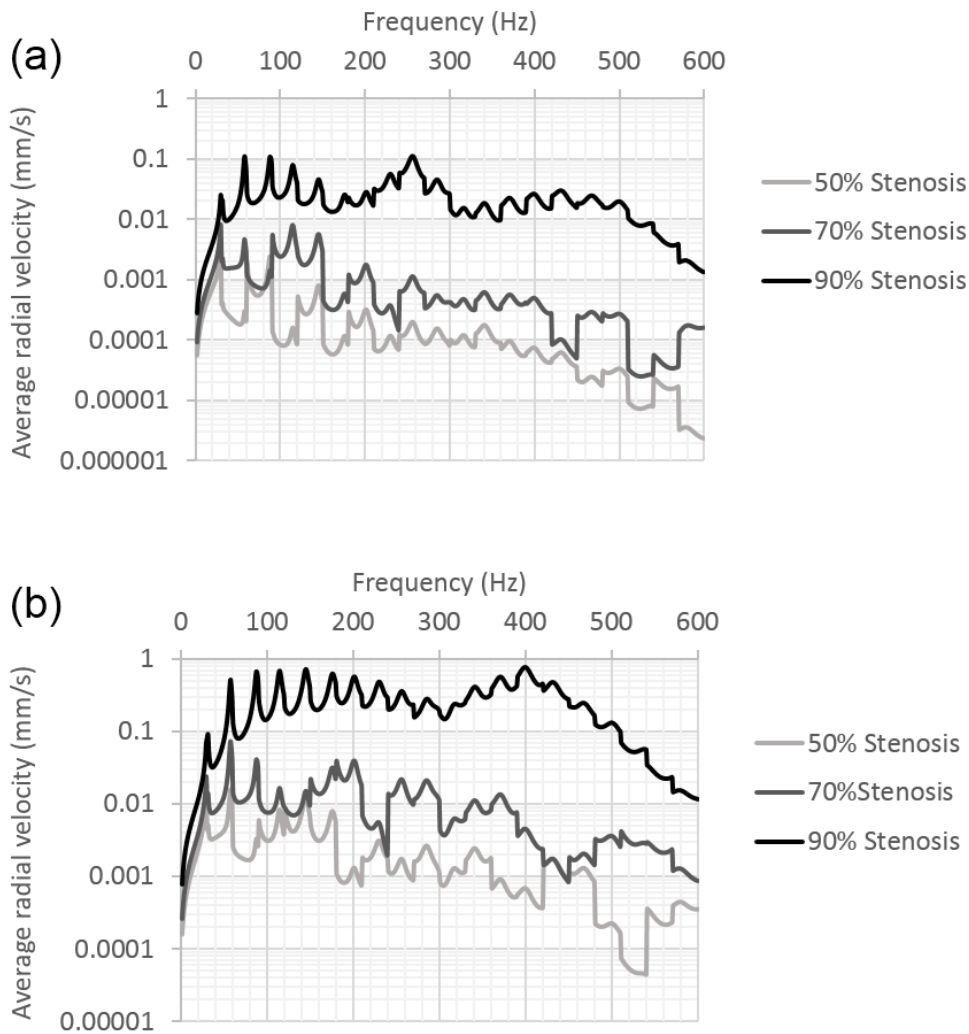


Figure 4.11 Average radial velocity response (within 0-100 mm) on the outer surface of the artery as function of frequency considering 20 x 20 phase map. (a) $Re = 1000$. (b) $Re = 2000$.

The change of the radial velocity responses depending on the phase map is clearly visible in the average results presented in Figure 4.12. The average responses have similar spectral content within 0-200 Hz. However, a certain difference is observed in the amplitudes as the frequency increases. The highest response amplitude is observed around 400 Hz for 20 x 20 phase map considering $Re = 2000$ with 90%

stenosis. For the no phase map and 10 x 10 phase map, the highest amplitude is observed around 100 Hz considering the same case. This fact shows that the applied phase map may affect the response for the bare artery analysis, especially at frequencies higher than 200 Hz.

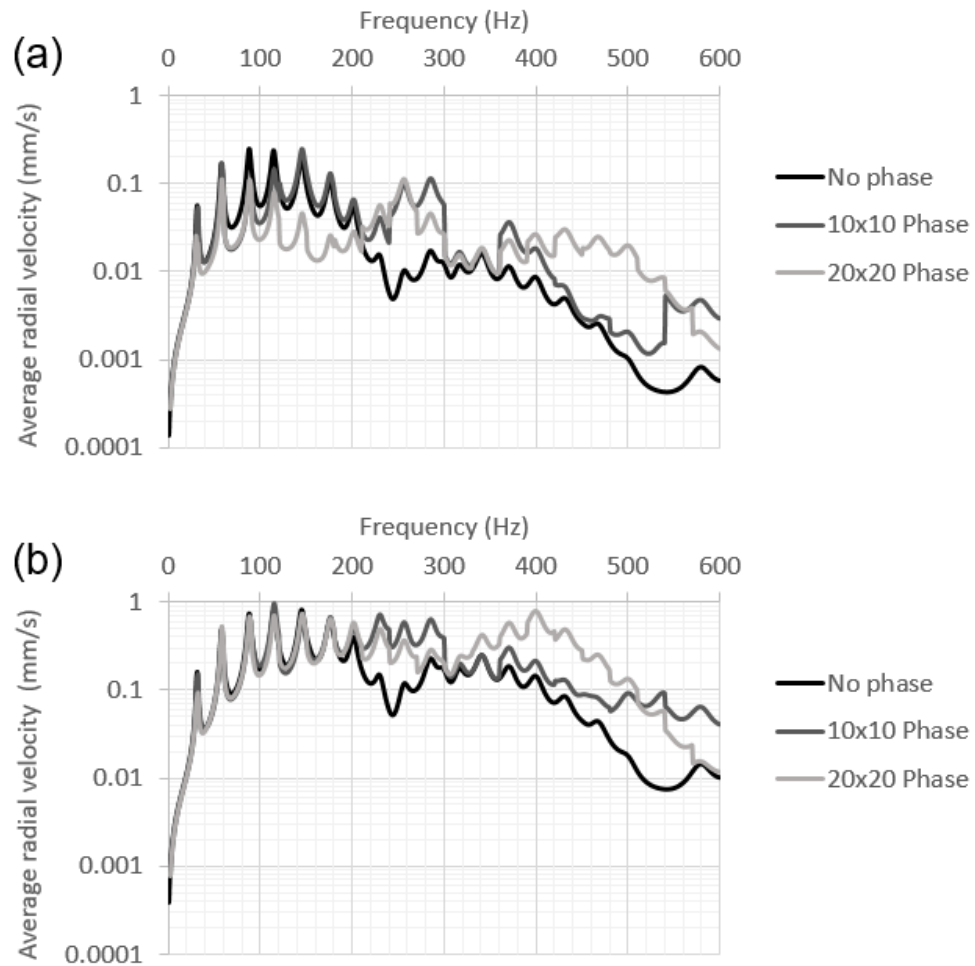


Figure 4.12 Comparison of the radial velocity response (within 0-100 mm) on the outer surface of the artery as function of frequency considering 90% stenosis. (a) $Re = 1000$. (b) $Re = 2000$.

In addition, the average responses are determined as function of axial distance downstream of the constriction exit to see the directional dependence of the average

amplitudes. This time, average responses are obtained using the results between 0 to 600 Hz. In Figure 4.13, Figure 4.14, and Figure 4.15, the average responses are shown as function of the axial distance to the stenosis exit considering no phase map, 10 x 10 phase map, and 20 x 20 phase map, respectively. Two sides of the model are considered as joint ends and fixed with zero displacement. For this reason, responses at 0 and 100 mm tend to approach zero.

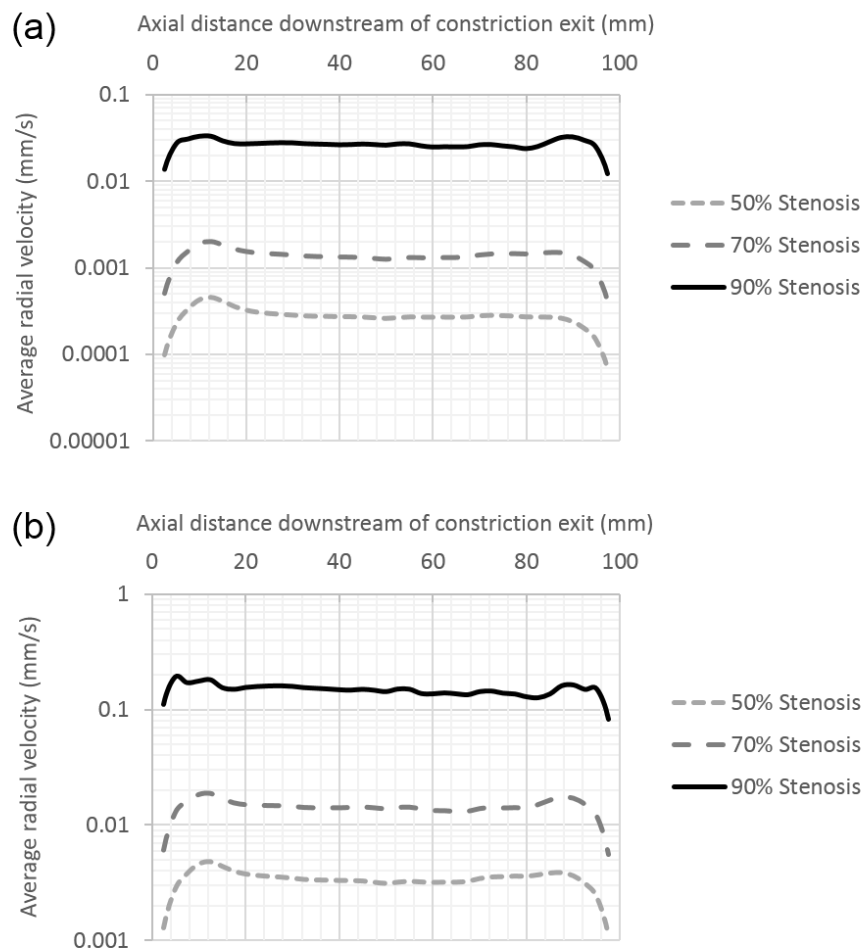


Figure 4.13 Average radial velocity response (within 0-600 Hz) on the outer surface of the artery as function of axial distance downstream of the constriction exit considering no phase map. (a) $Re = 1000$. (b) $Re = 2000$.

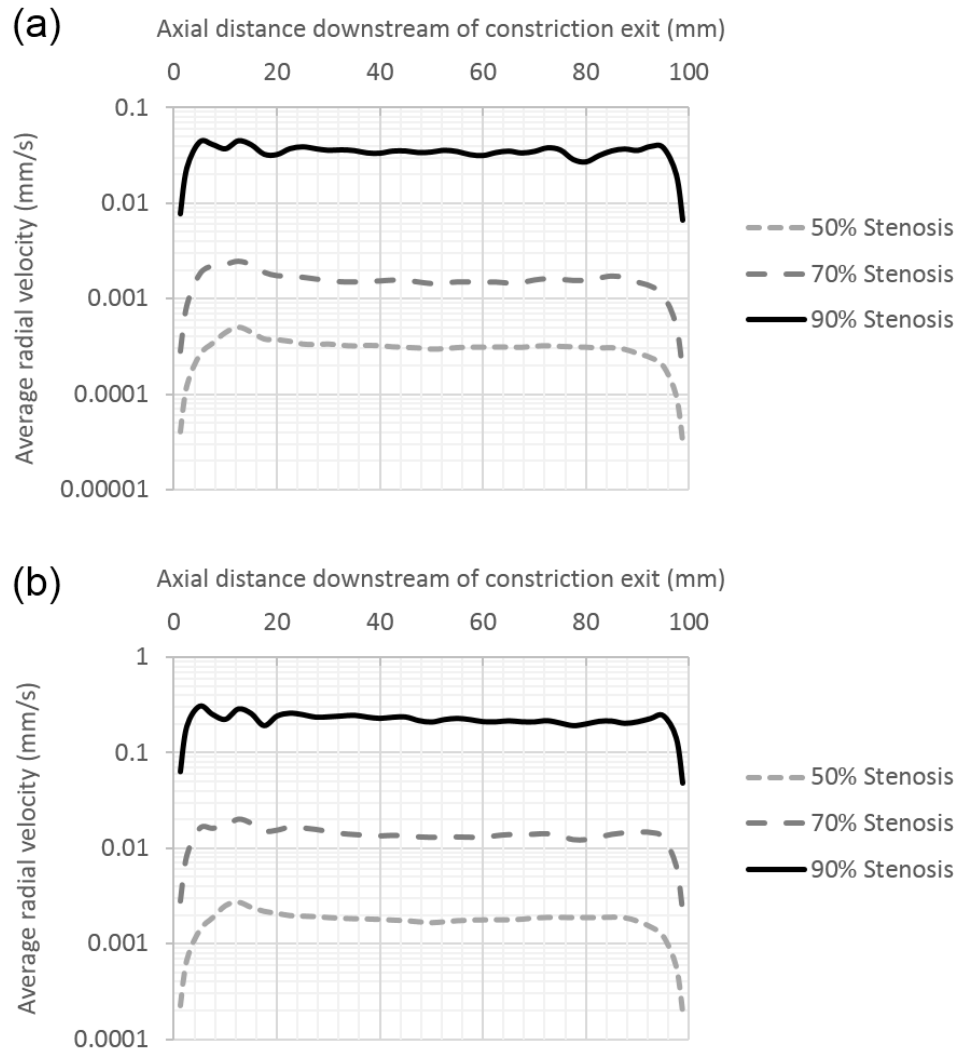


Figure 4.14 Average radial velocity response (within 0-600 Hz) on the outer surface of the artery as function of axial distance downstream of the constriction exit considering 10 x 10 phase map. (a) $Re = 1000$. (b) $Re = 2000$.

Relatively higher amplitudes are observed within the distance of 0-20 mm, since the stenosis exit is placed at 0 mm. The response amplitudes gradually decrease with the increasing downstream distance from the stenosis exit.

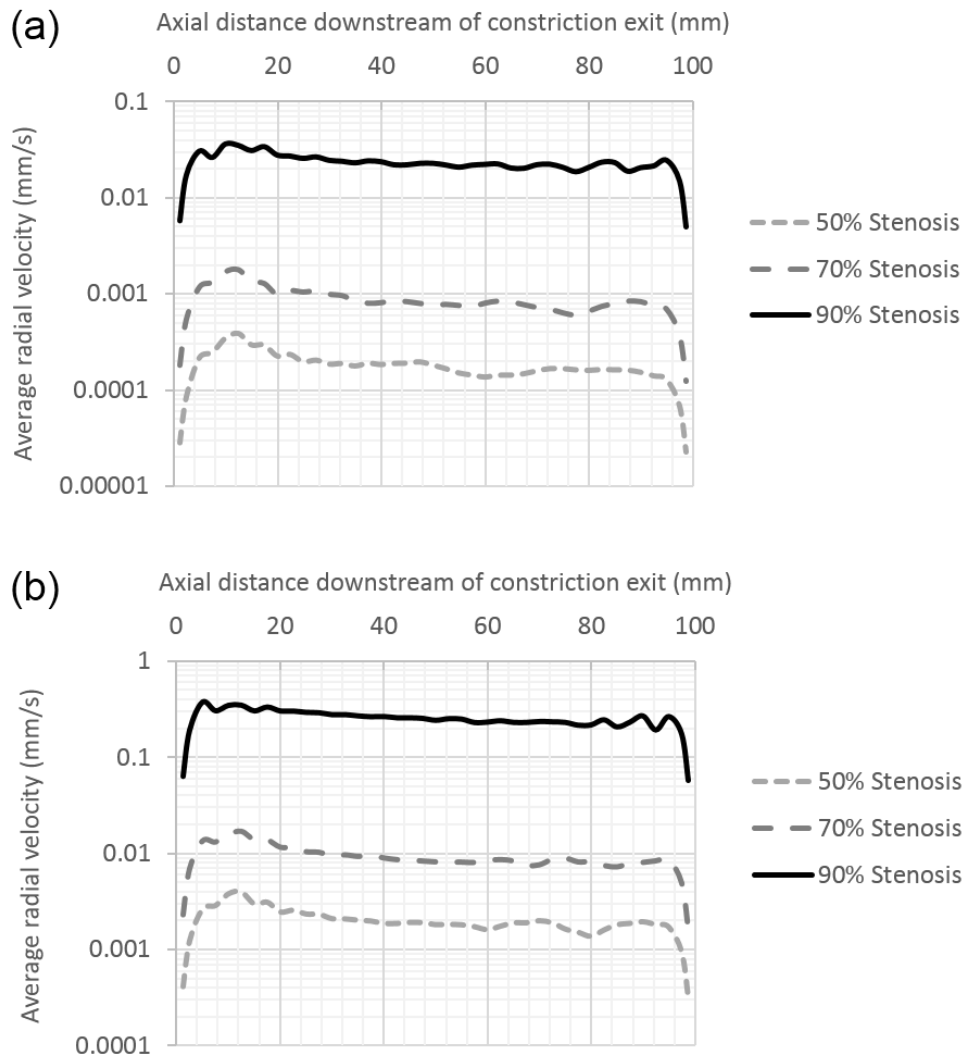


Figure 4.15 Average radial velocity response (within 0-600 Hz) on the outer surface of the artery as function of axial distance downstream of the constriction exit considering 20 x 20 phase map. (a) $Re = 1000$. (b) $Re = 2000$.

For all applied phase maps, the highest average amplitude is about 0.025 mm/s for $Re = 1000$ with 90% stenosis. The highest amplitude increases to 0.2 mm/s for $Re = 2000$ with 90% stenosis. This shows that when the flow rate is doubled, an 8-fold increase is observed for the highest radial velocity amplitude on the outer

surface of the artery. As stated in the literature [19], the acoustic power generated on the inner wall of the artery is proportional to the fourth power of the Reynolds number. Results of the bare artery analysis indicate that this proportionality drops to the third power for the radial velocity responses on the outer surface of the artery. In Figure 4.16, the average responses are compared considering the no phase map, 10 x 10 phase map and 20 x 20 phase map.

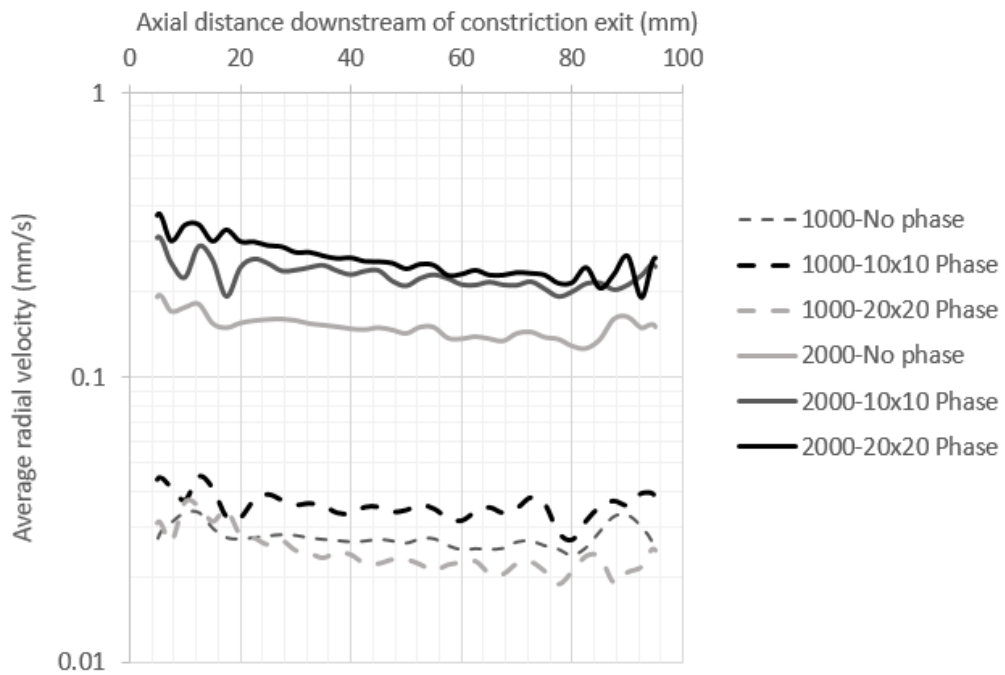


Figure 4.16 Comparison of average radial velocity responses on the outer surface of the artery (within 0-600 Hz) as function of axial distance downstream of the constriction exit considering 90% stenosis for $Re = 1000$ and $Re = 2000$.

The results obtained for the bare artery analysis are reasonable and in good agreement with the findings in the literature, but there is a certain amplitude difference depending on the applied phase map. In this section, a bare artery model is considered as the first step. The results provide important information to

understand the problem. In the next step, the artery is surrounded by soft tissue and the effects observed on the outer surface of the surrounding tissue are investigated.

4.4 Soft tissue surrounded models

In this section, the previously described bare artery model is surrounded by soft tissue. The surrounding soft tissue is modelled as linearly elastic considering three different elastic modulus values of 0.1, 1 and 10 MPa. The Poisson's ratio and the mass density of the soft tissue are used as 0.49 and 1200 kg/m³, respectively. The arterial geometry is the same as the previous bare artery model presented in Figure 4.1. Three different thicknesses are used for the surrounding soft tissue as 6.5, 16.5 and 36.5 mm (i.e., $H = 6.5, 16.5, 36.5$ mm) considering the muscle and subcutaneous tissue thicknesses in arm and neck [63]. Using tissue thicknesses of 6.5, 16.5 and 36.5 mm, the outer diameters of the tissue surrounded models correspond to 20, 40 and 80 mm, respectively.

4.4.1 Responses for the soft tissue surrounded models

Three different meshes are created for each tissue surrounded model to achieve a mesh independent solution. The details of the meshes are given in Table 4.2, Table 4.3 and Table 4.4, considering surrounding soft tissue thicknesses of 6.5, 16.5 and 36.5 mm, respectively.

Table 4.2 Details of the meshes for soft tissue thickness of 6.5 mm

Mesh Density	Medium	Number of nodes in axial direction	Number of nodes in radial direction	Number of nodes in circumferential direction	Total number of nodes	Total number of elements
Mesh 1	Artery	41	2	20	9881	9600
	Blood	41	4	20		
	Tissue	41	9	20		
Mesh 2	Artery	81	2	30	38961	38400
	Blood	81	4	30		
	Tissue	81	13	30		
Mesh 3	Artery	121	3	40	101761	100800
	Blood	121	5	40		
	Tissue	121	16	40		

Table 4.3 Details of the meshes for soft tissue thickness of 16.5 mm

Mesh Density	Medium	Number of nodes in axial direction	Number of nodes in radial direction	Number of nodes in circumferential direction	Total number of nodes	Total number of elements
Mesh 1	Artery	41	2	20	11521	11200
	Blood	41	4	20		
	Tissue	41	11	20		
Mesh 2	Artery	81	2	30	46251	45600
	Blood	81	4	30		
	Tissue	81	16	30		
Mesh 3	Artery	121	2	36	104665	103680
	Blood	121	4	36		
	Tissue	121	21	36		

Table 4.4 Details of the meshes for soft tissue thickness of 36.5 mm

Mesh Density	Medium	Number of nodes in axial direction	Number of nodes in radial direction	Number of nodes in circumferential direction	Total number of nodes	Total number of elements
Mesh 1	Artery	41	2	20	13161	12800
	Blood	41	4	20		
	Tissue	41	13	20		
Mesh 2	Artery	81	2	30	48681	48000
	Blood	81	4	30		
	Tissue	81	17	30		
Mesh 3	Artery	121	2	36	104665	103680
	Blood	121	4	36		
	Tissue	121	21	36		

The radial velocity responses on the outer surface of the surrounding soft tissue are obtained using three different mesh densities, considering a sample case as shown in Figure 4.17. Mesh independence studies are carried out using an elastic modulus of 0.1 MPa, because the highest number of modes is expected to be observed for 0.1 MPa when compared to 1 and 10 MPa. Average response amplitude (within 0-100 mm, 0-300 Hz) is determined for each soft tissue thickness value. Between Mesh 1 and Mesh 2, there are average amplitude differences of 4.32%, 6.91% and 3.45% for 6.5 mm, 16.5 mm and 36.5 mm tissue thickness, respectively. Between Mesh 2 and Mesh 3, there are average amplitude differences of 0.76%, 2.11% and 2.14% for 6.5 mm, 16.5 mm and 36.5 mm tissue thickness, respectively. Mesh 2 with the moderate mesh density is used for the further analysis of the soft tissue surrounded models since average amplitude differences between Mesh 2 and Mesh 3 are less than 3%.

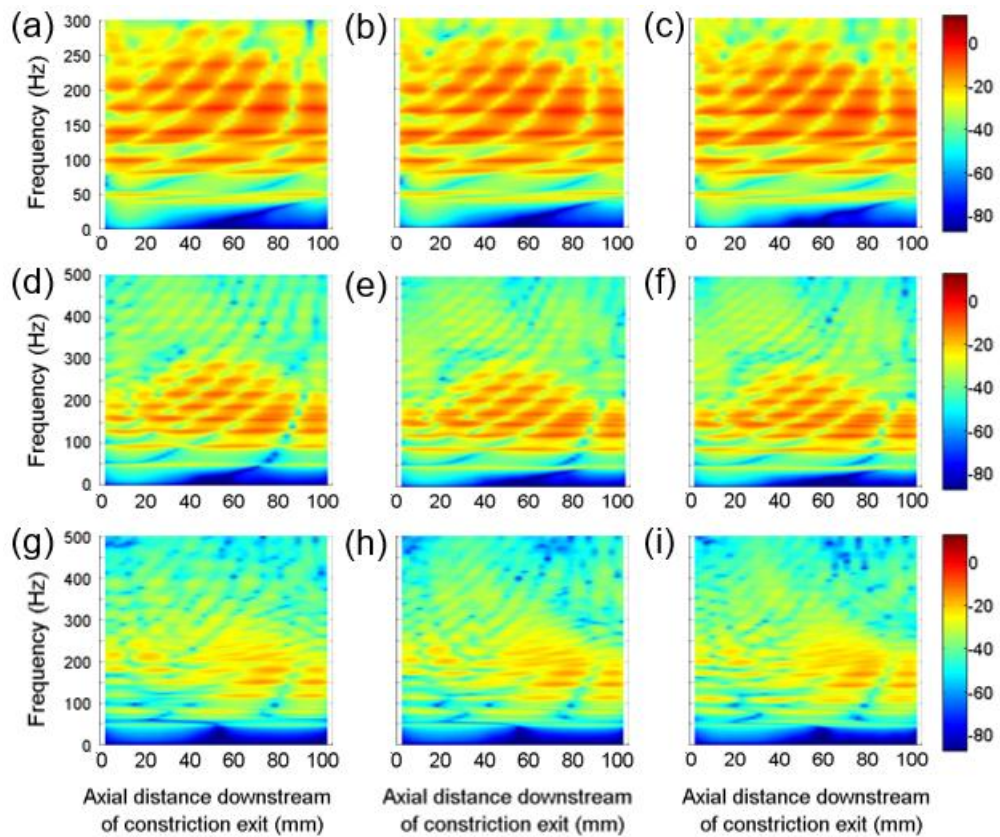


Figure 4.17 Radial velocity response (dB ref: 1 mm/s) on the outer surface of the surrounding soft tissue (0.1 MPa) for $Re = 2000$ with 90% stenosis considering no phase map. (a) 6.5 mm thickness, Mesh 1. (b) 6.5 mm thickness, Mesh 2. (c) 6.5 mm thickness, Mesh 3. (d) 16.5 mm thickness, Mesh 1. (e) 16.5 mm thickness, Mesh 2. (f) 16.5 mm thickness, Mesh 3. (g) 36.5 mm thickness, Mesh 1. (h) 36.5 mm thickness, Mesh 2. (i) 36.5 mm thickness, Mesh 3.

Figure 4.18 shows the radial displacement, velocity and acceleration responses on the outer surface of the surrounding soft tissue for an elastic modulus of 0.1 MPa and a thickness of 36.5 mm, considering no phase map.

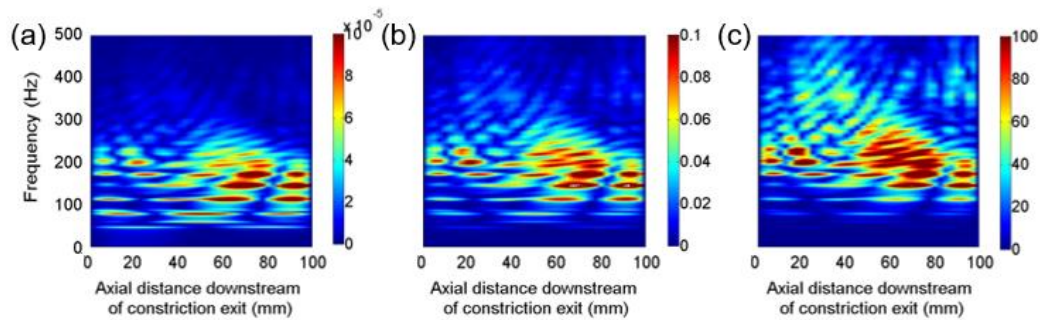


Figure 4.18 Responses on the outer surface of the surrounding soft tissue (0.1 MPa, 36.5 mm thickness) for $Re = 2000$ with 90% stenosis considering no phase map. (a) Radial displacement response (mm). (b) Radial velocity response (mm/s). (c) Radial acceleration response (mm/s^2).

It is seen that the radial displacement, velocity and acceleration responses are similar in terms of general spectral behavior. The main difference is related with the scale of the response amplitudes. The most sensitive variable is the radial acceleration on the outer surface of the tissue and the maximum acceleration appear to be around 100 mm/s^2 . Considering the elastic modulus of 0.1 MPa and the tissue thickness of 36.5 mm, the maximum radial velocity and displacement are approximately $100 \text{ } \mu\text{m/s}$ and $0.1 \text{ } \mu\text{m}$, where velocities greater than $0.02 \text{ } \mu\text{m/s}$ can be sufficiently measured by LDV (IVS-300, Polytech, Auburn, MA).

The radial velocity responses on the tissue surface are presented in Figure 4.19 and Figure 4.20 for various stenosis levels and flow rates, considering no phase map and 10×10 phase map, respectively.

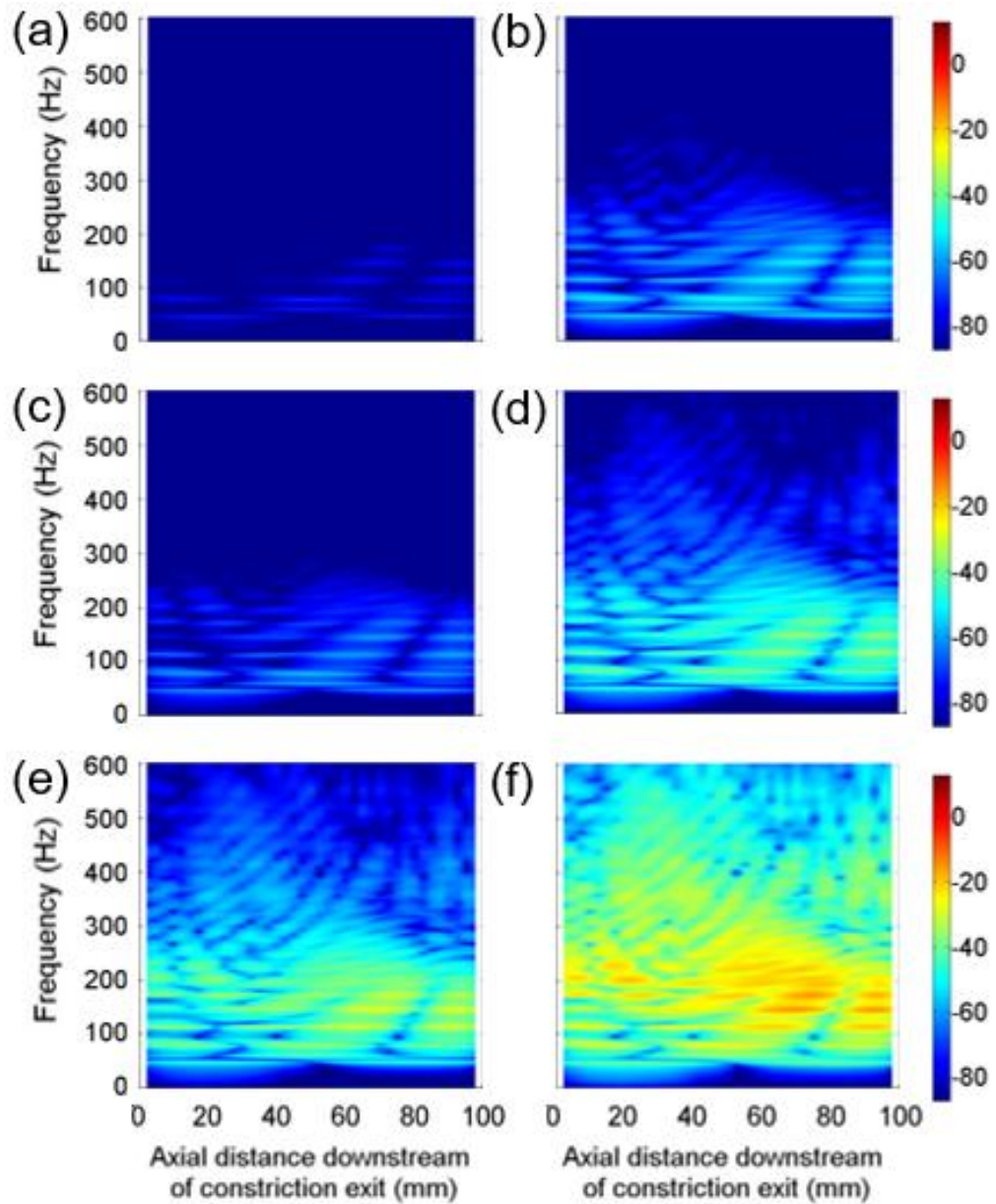


Figure 4.19 Radial velocity response (dB ref: 1 mm/s) on the outer surface of the surrounding soft tissue (0.1 MPa) with 36.5 mm thickness considering no phase map. (a) $Re = 1000$, 50% Stenosis. (b) $Re = 2000$, 50% Stenosis. (c) $Re = 1000$, 70% Stenosis. (d) $Re = 2000$, 70% Stenosis. (e) $Re = 1000$, 90% Stenosis. (f) $Re = 2000$, 90% Stenosis.

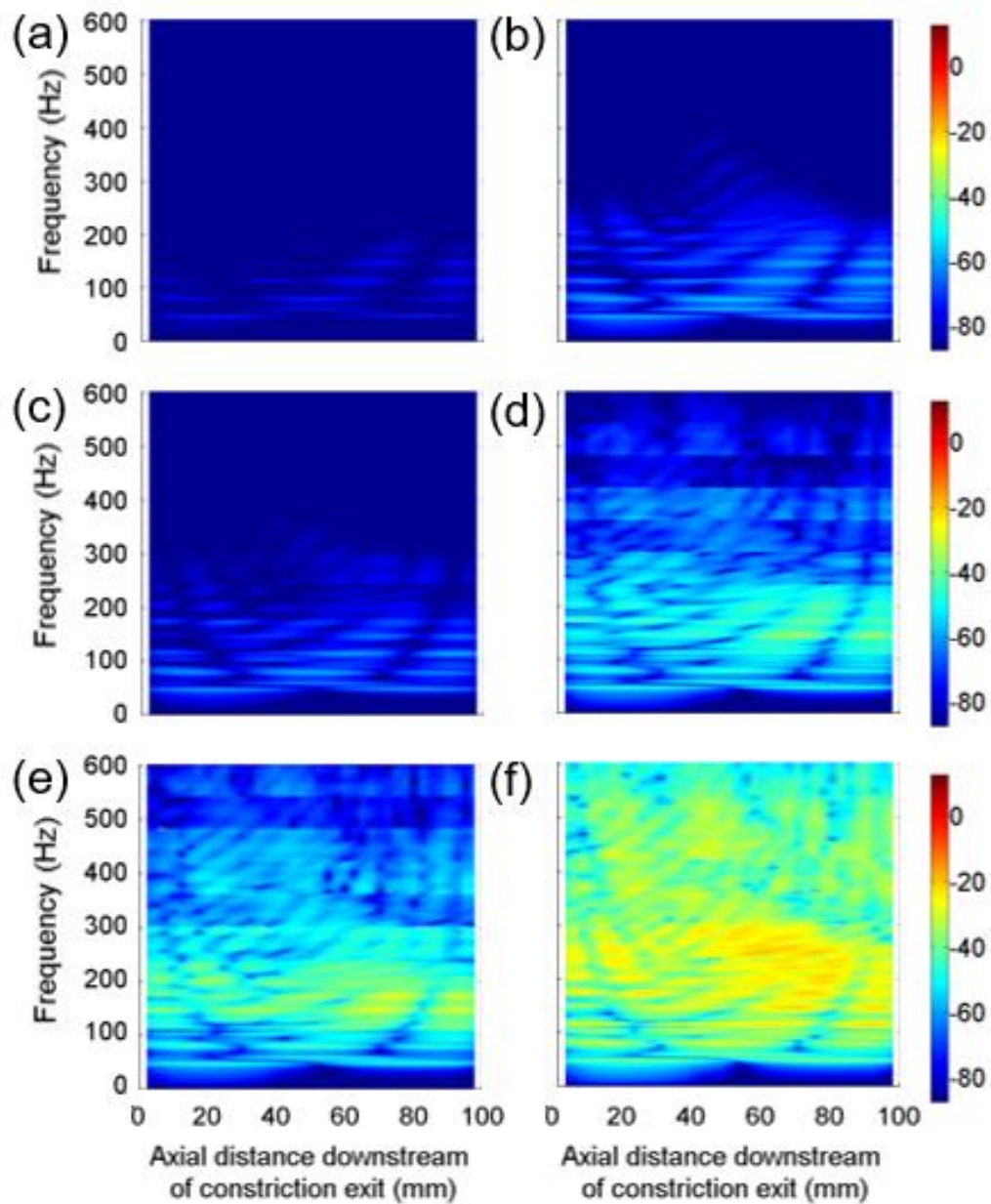


Figure 4.20 Radial velocity response (dB ref: 1 mm/s) on the outer surface of the surrounding soft tissue (0.1 MPa) with 36.5 mm thickness considering 10 x 10 phase map. (a) $Re = 1000$, 50% Stenosis. (b) $Re = 2000$, 50% Stenosis. (c) $Re = 1000$, 70% Stenosis. (d) $Re = 2000$, 70% Stenosis. (e) $Re = 1000$, 90% Stenosis. (f) $Re = 2000$, 90% Stenosis.

As supporting the previous findings, increased flow rate and stenosis severity lead to increased response amplitudes. The modes of the tissue surrounded model are clearly visible in the contour plots of the radial velocity responses. However, the spectral content is more complicated when compared to the bare artery analysis due to the additional mass, damping and stiffness of the soft tissue. The stenosis exit is located at 0 mm, but the maximum response amplitude is observed between 60 to 70 mm for a tissue thickness of 36.5 mm. The amplitude difference due to the applied phase map is lowered for the tissue surrounded model compared to the bare artery model. This indicates that as the tissue thickens, the phase map dependent amplitude difference is suppressed. The radial displacement and acceleration responses of the tissue surrounded models are given in Figure 4.21.

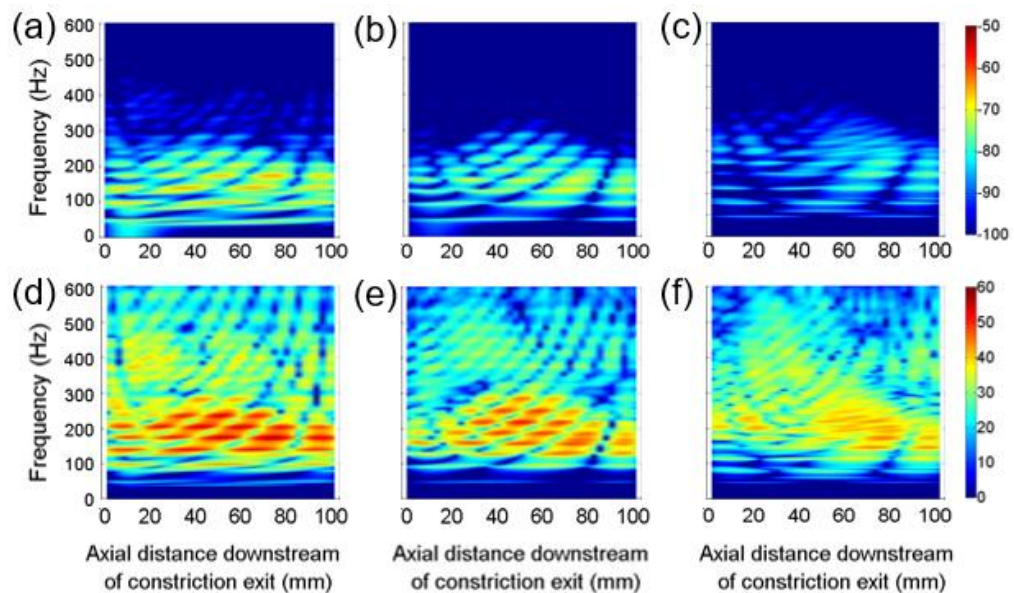


Figure 4.21 Responses on the outer surface of the surrounding soft tissue (0.1 MPa) for $Re = 2000$ with 90% stenosis considering no phase map. (a) Radial displacement (dB ref: 1 mm), 6.5 mm thickness. (b) Radial displacement (dB ref: 1 mm), 16.5 mm thickness. (c) Radial displacement (dB ref: 1 mm), 36.5 mm thickness. (d) Radial acceleration (dB ref: 1 mm/s^2), 6.5 mm thickness. (e) Radial acceleration (dB ref: 1 mm/s^2), 16.5 mm thickness. (f) Radial acceleration (dB ref: 1 mm/s^2), 36.5 mm thickness.

In Figure 4.21, the increase in tissue thickness decreases the response amplitudes, but do not significantly affect the spectrum content. The effect of elastic modulus is investigated in Figure 4.22 and Figure 4.23, considering no phase map and 10 x 10 phase map, respectively.

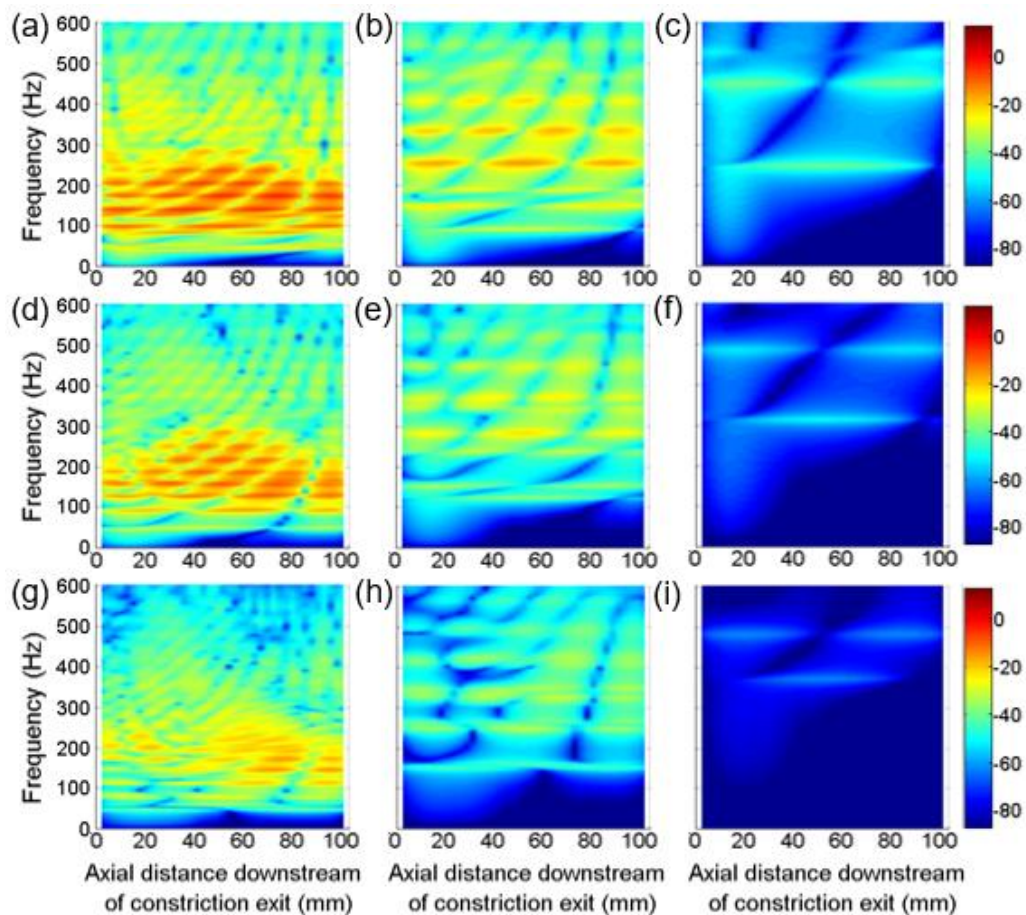


Figure 4.22 Radial velocity response (dB ref: 1 mm/s) on the outer surface of the surrounding tissue for $Re = 2000$ with 90% stenosis considering no phase map.

(a) 6.5 mm thickness, 0.1 MPa. (b) 6.5 mm thickness, 1 MPa. (c) 6.5 mm thickness, 10 MPa. (d) 16.5 mm thickness, 0.1 MPa. (e) 16.5 mm thickness, 1 MPa. (f) 16.5 mm thickness, 10 MPa. (g) 36.5 mm thickness, 0.1 MPa. (h) 36.5 mm thickness, 1 MPa. (i) 36.5 mm thickness, 10 MPa.

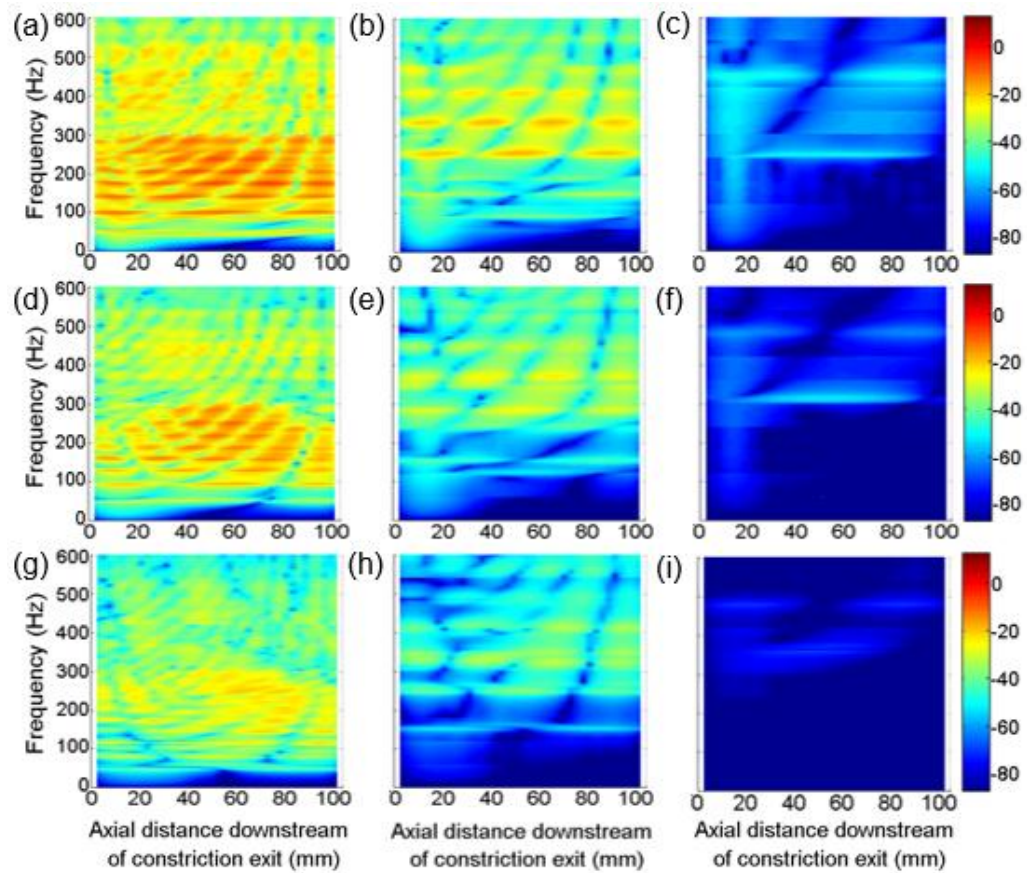


Figure 4.23 Radial velocity response (dB ref: 1 mm/s) on the outer surface of the surrounding tissue for $Re = 2000$ with 90% stenosis considering 10×10 phase map. (a) 6.5 mm thickness, 0.1 MPa. (b) 6.5 mm thickness, 1 MPa. (c) 6.5 mm thickness, 10 MPa. (d) 16.5 mm thickness, 0.1 MPa. (e) 16.5 mm thickness, 1 MPa. (f) 16.5 mm thickness, 10 MPa. (g) 36.5 mm thickness, 0.1 MPa. (h) 36.5 mm thickness, 1 MPa. (i) 36.5 mm thickness, 10 MPa.

In Figure 4.22 and Figure 4.23, it is seen that the effect of tissue thickness is less drastic than the effect of the elastic modulus. The increased elastic modulus significantly reduces the response amplitudes and alters the spectrum content due to the change in structural stiffness matrix (\mathbf{K}). Stiffness matrix (\mathbf{K}) is proportional to the elastic modulus. For this reason, increase in elastic modulus directly increases the natural frequencies in the problem domain. Also, increased stiffness

in the model leads to lowered vibration amplitudes on the outer surface of the surrounding soft tissue. The results of the no phase map and 10 x 10 phase map show the suppressive effect of tissue thickness on the response amplitudes.

As seen in Figure 4.22 and Figure 4.23, the total number of bending modes increases with the reduction of the elastic modulus. The peaks in the response plots show the natural frequencies of the bending modes. For example, when the elastic modulus is 10 MPa, two bending modes are visible within 0-600 Hz. In Figure 4.22(c), the single peak around 250 Hz indicates the first mode and two separate peaks around 450 Hz indicate the second mode of the model. The spectrum content of 0.1 MPa is more complex than 1 and 10 MPa, and the first bending mode is observed at 50 Hz.

4.4.2 Average responses for the soft tissue surrounded models

Similar to the bare artery analysis, the average responses are determined using the results of 41 nodes placed on the top of the surrounding soft tissue. In Figure 4.24, the average responses are given as function of the axial distance downstream of the constriction exit, and the effects of phase mapping and stenosis severity are shown. It is seen that the average responses are in good agreement for the no phase map and 10 x 10 phase map. The radial velocity response on the outer surface of the bare artery is sensitive to the applied phase map, but when the artery is surrounded by a soft tissue, the phase map dependent amplitude difference is significantly reduced. The average response amplitudes on the tissue show an approximately 10-fold increase when the level of stenosis increases from 70% to 90%.

In Figure 4.25, the average displacement and acceleration responses are given considering various tissue thicknesses. When the thickness increases from 6.5 to 16.5 mm, the average response amplitudes decrease by about 35%. If the tissue thickness increases from 16.5 to 36.5, the response amplitudes drop by approximately 50%. The average responses at 0 and 100 mm are zero because of

the boundary conditions applied on both sides of the model. It is assumed that the two sides of the model are motionless joint ends, and therefore zero displacement is used as a boundary condition at 0 and 100 mm. The results are similar to a symmetrical form due to the assumed low damping conditions (2% modal damping) in the analysis. For low damping conditions, the results show a nearly symmetrical behavior for the average responses presented in Figure 4.25, but as the damping increases, the symmetrical response behavior begins to deteriorate as previously observed in Figure 4.8.

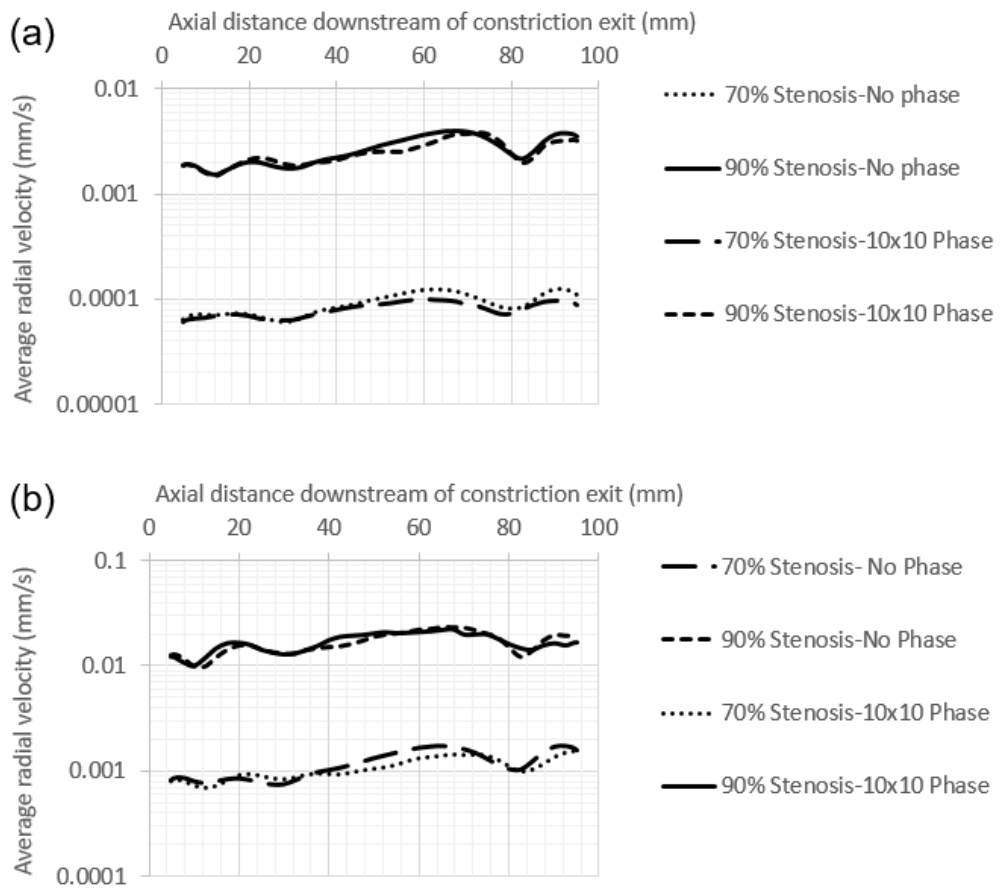


Figure 4.24 Average radial velocity response (within 0-600 Hz) on the outer surface of the surrounding soft tissue (0.1 MPa, 36.5 mm thickness) as a function of axial distance downstream of the constriction exit considering no phase map. (a) $Re = 1000$. (b) $Re = 2000$.

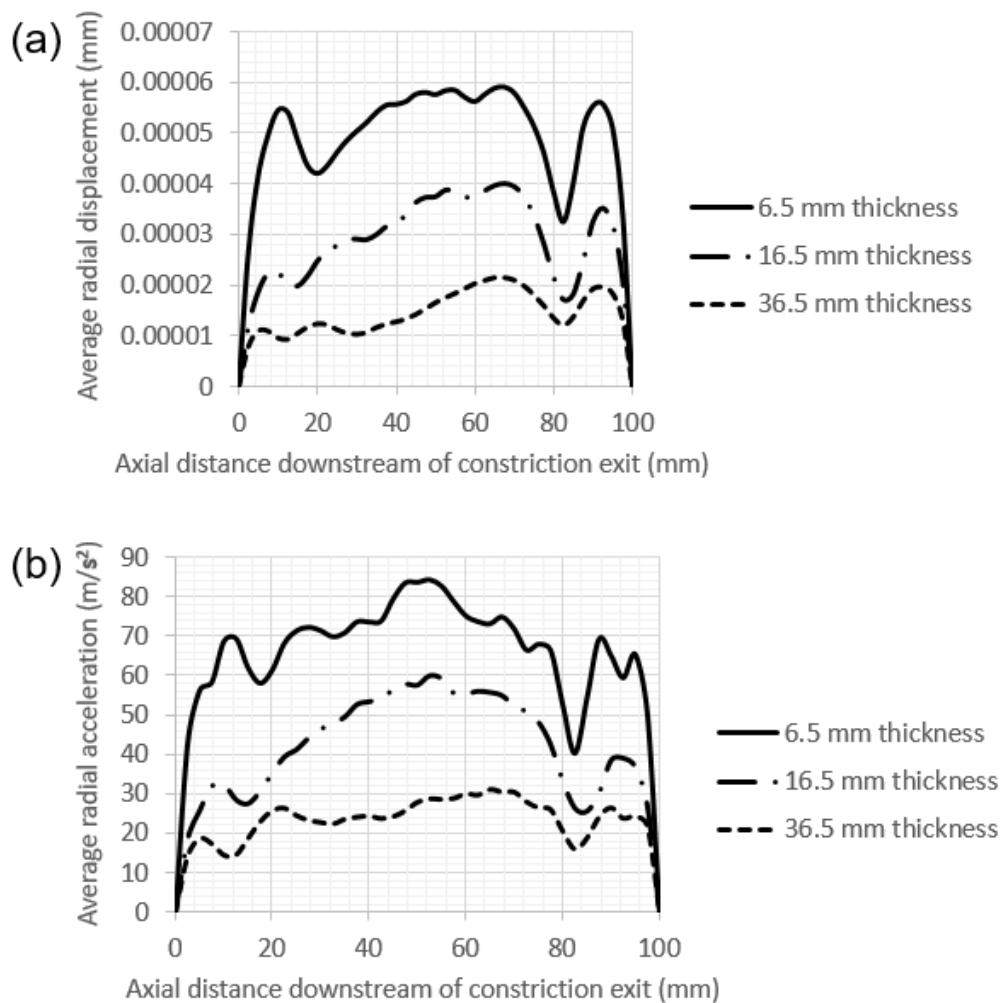


Figure 4.25 Average responses (within 0-600 Hz) on the outer surface of the surrounding soft tissue (0.1 MPa) for $Re = 2000$ with 90% stenosis as function of axial distance downstream of the constriction exit considering no phase map. (a) Average radial displacement response. (b) Average radial acceleration response.

In Figure 4.26, the average radial velocity responses on the surrounding soft tissue are compared to investigate the effects of the elastic modulus and the applied phase map.

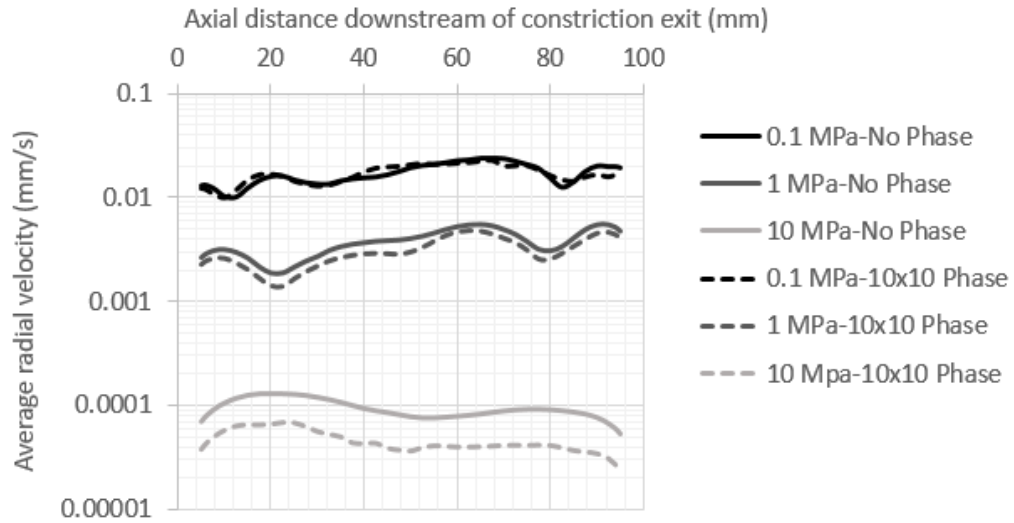


Figure 4.26 Comparison of average radial velocity responses (within 0-600 Hz) on the outer surface of the surrounding soft tissue (36.5 mm thickness) for $Re = 2000$ with 90% stenosis.

The results show that the increasing elastic modulus reduces the radial velocity amplitudes by a significant amount. The amplitude difference based on phase mapping is more pronounced for higher elastic modulus values. The highest response amplitude is observed at 20 mm for 10 MPa. However, the highest excitation is observed at 60 mm from the stenosis exit for 0.1 MPa. As the elastic modulus increases, the highest excitation point moves towards the stenotic zone.

In Figure 4.27, the average responses are presented as a function of frequency considering different phase maps and stenosis severities.

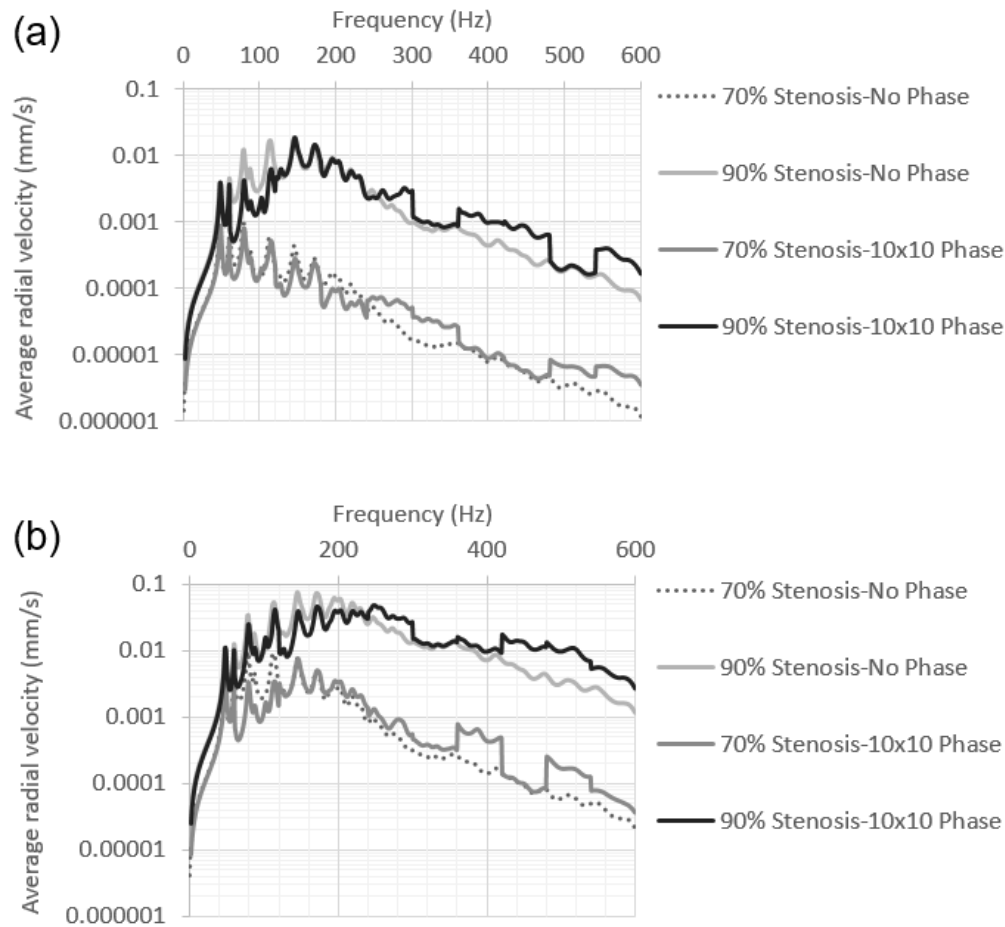


Figure 4.27 Comparison of average radial velocity response (within 0-100 mm) on the outer surface of the surrounding soft tissue (0.1 MPa, 36.5 mm thickness) as function of frequency. (a) $Re = 1000$. (b) $Re = 2000$.

In Figure 4.27, the results of the no phase map and 10 x 10 phase map are again in good agreement, especially within 0-300 Hz. For the frequencies higher than 300 Hz, a segmented response is observed for 10 x 10 phase map due to the piecewise continuous mapping.

In Figure 4.28, the average radial displacement and acceleration responses are given as function of frequency.

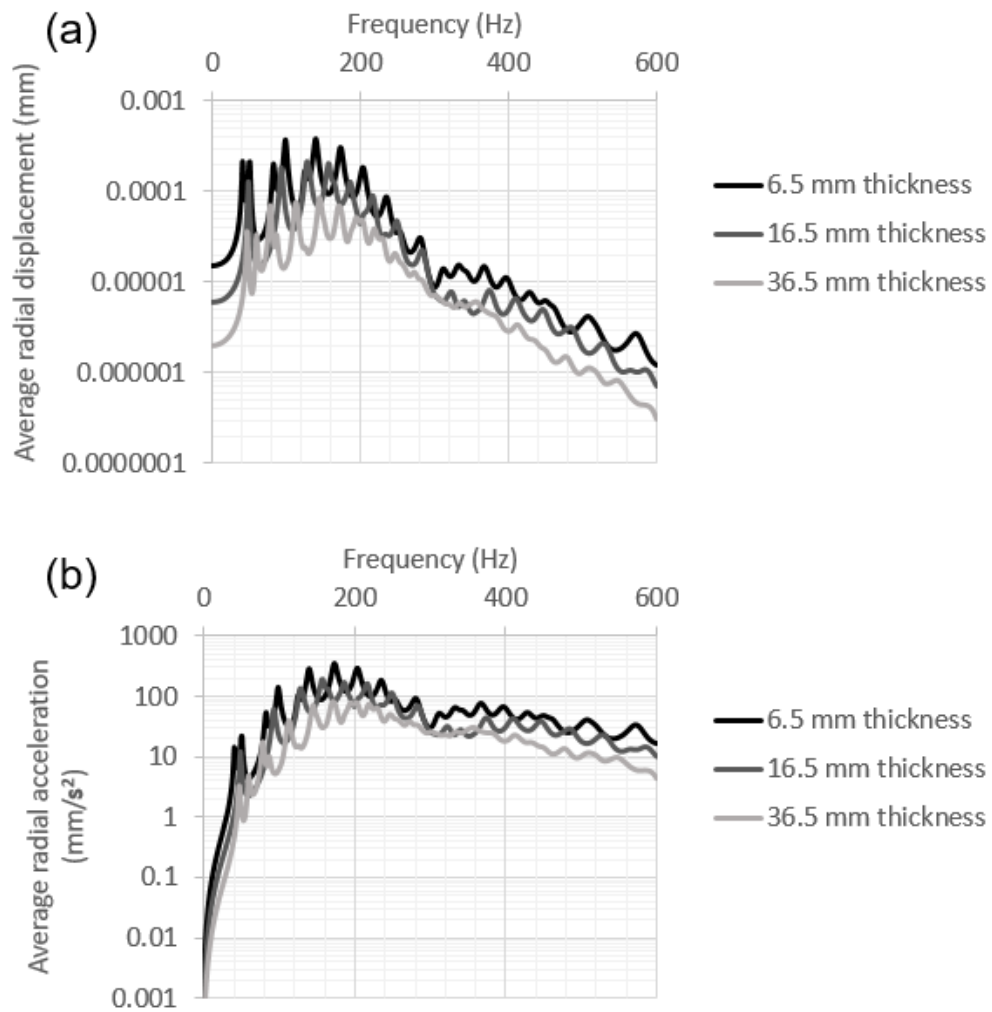


Figure 4.28 Average responses (within 0-100 mm) on the outer surface of the surrounding soft tissue (0.1 MPa) as function of frequency for $Re = 2000$ with 90% stenosis considering no phase map. (a) Average radial displacement response. (b) Average radial acceleration response.

Confirming the previous findings, the increase in the tissue thickness reduces the amplitudes of the radial displacement and acceleration responses on the tissue surface. In Figure 4.29, the average radial velocity responses on the surrounding soft tissue are compared considering different elastic modulus values.

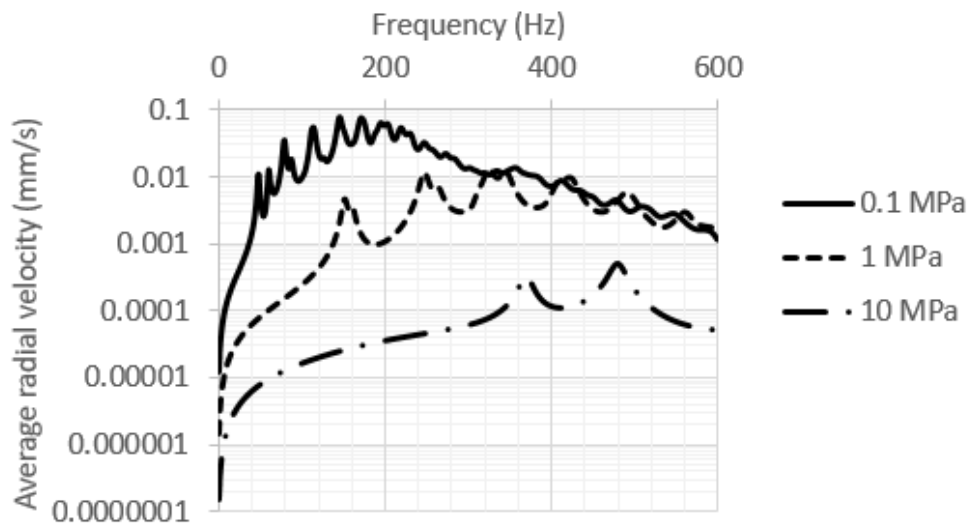


Figure 4.29 Comparison of average radial velocity responses (within 0-100 mm) on the outer surface of the surrounding soft tissue (36.5 mm thickness, no phase map) as function of frequency for $Re = 2000$ with 90% stenosis considering various elastic modulus values.

In Figure 4.29, as the elastic modulus increases, the natural frequencies of the tissue surrounded model shift to the higher frequencies. For 0.1 MPa, more than 10 modes are visible within 0-600 Hz. However, only two modes are apparent within 0-600 Hz when the elastic modulus is increased to 10 MPa. The highest response amplitude is observed at 150 Hz for 0.1 MPa. When the elastic modulus is increased to 1 and 10 MPa, the maximum excitations are observed at about 325 and 480 Hz, respectively. For 0.1, 1 and 10 MPa, the highest average radial velocity amplitudes are about 0.08, 0.01 and 0.0005 mm/s, respectively. It is observed that the elastic modulus and structural material properties have an important role in the spectrum content and response amplitudes on the tissue surface.

CHAPTER 5

REALISTIC COMPUTATIONAL MODELS

In this chapter, realistic material properties and human anatomy based geometric models are introduced for the upper arm, thigh and neck. Muscle, fat, skin, bone, blood and artery are considered in the realistic computational models. Radial velocity and pressure responses on the skin are investigated for diagnostic purposes.

5.1 Mechanical properties of human body tissues

Biological soft tissue is a complex material, which is anisotropic, nonlinear, viscoelastic and nearly incompressible [64]. Soft tissues can be classified as tendons, ligaments, skin, articular cartilages, blood vessels, fat and muscles [65]. Tendons are bone-to-muscle linkages to stabilize the skeleton and to produce movements. Ligaments are bone-to-bone linkages to restrict the relative motion. The largest single organ of the human body is skin as it corresponds to 16% of the weight of an adult. The skin protects the body and internal organs. Articular cartilages provide load distribution to a surface across the joints to minimize the contact stresses and friction.

Soft tissue material properties are influenced by the concentration and arrangement of collagen and elastin [65]. Collagen is a protein which is a major part of the soft tissues. It has a great importance for human physiology and it is the main load carrying constituent. For example, the collagen content of the human achilles tendon is 20 times that of elastin. Elastin is a flexible and linearly elastic constituent

and it can be stretched up to 2.5 times of the initial unloaded length. Relaxation of elastin is very limited but the collagen has larger relaxation when compared to the elastin.

Soft tissues exhibit a nonlinear and time dependent behavior by having a multiphasic and inhomogeneous structure [66]. Mechanical behavior of the soft tissues are identified by certain material phases. These are mainly solid phase with collagen fibers, proteoglycans, other proteins, cells, and interstitial fluid phase composed of water and electrolytes [67]. The resilience of the tissue is depending on binding of water and proteoglycans forming a firm gel. The tensile strength of the tissue is due to the collagen fibers. The arrangement and hierarchy of the fibers have major effect on the mechanical behavior of the tissue [68]. In human body, the arrangement of fibers are optimized according to the specific function of each tissue [69].

Collagen fibers are quantitatively major organic component in the soft tissues. Proteoglycans are the second common organic components which contribute to viscoelastic behavior [67]. Fluid phase also has an important effect on the viscoelasticity. Soft tissues represent analogous structure and properties for different anatomical regions. Thus, the material constitutive laws and modeling approaches can be adapted with little effort for different soft tissues [66].

Soft tissues are anisotropic materials due to the fibers oriented in preferred directions. In micro scale, the soft tissues are non-homogenous because of their composition. They have nonlinear tensile response which is affected by the strain rate. Some of the soft tissues represent viscoelastic characteristics due to the shear interaction of collagen with proteoglycan matrix. A viscous lubrication is provided by proteoglycan matrix between the collagen fibers. Figure 5.1 represents the stress-strain behavior of a typical soft tissue.

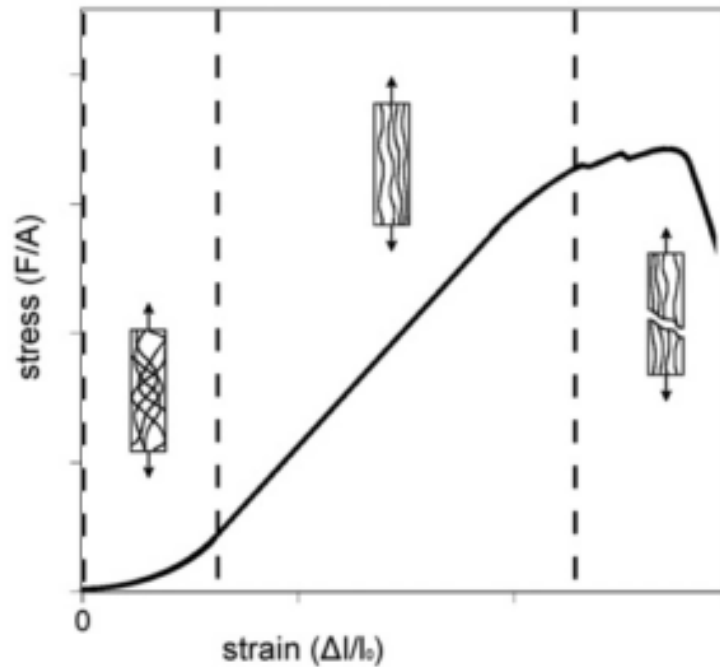


Figure 5.1 Stress-strain response of a typical soft tissue and corresponding collagen fiber alignment (adopted from [66]).

In Figure 5.1, the first region is the toe region in which the collagen fibers are wavy and crimped. As a consequence, the soft tissue behaves almost isotropic in the toe region. The stress-strain curve is nonlinear and the elastic modulus is relatively low in the toe region [65]. The nonlinearity in the toe region is due to the straightening of the collagen fibers [66]. As the loading increases, the crimped structure disappears and the collagen fibers align with a straighter form in the loading direction. Secondly, there is a linearly elastic region, where the collagen fibers are exposed to linear stretch until failure. In this second region, the straightened form of the soft tissue shows anisotropic behavior and resists load strongly.

In the computational analysis, strains observed due to the acoustic pressures are extremely small. For this reason, soft tissues can be assumed as isotropic, since the strains are within the toe region. Skin, fat and skeletal muscle are individually

considered as a single homogeneous medium [70-75] and different layers are considered as tied to its adjacent tissue.

5.1.1 Hyperelasticity

The nonlinear stress-strain (hyperelastic) behavior of the soft tissues can only be described using the large strain theory [66]. In order to use a hyperelastic material, a strain energy density function (W) is defined. The stress can be obtained by taking the derivative of the strain energy density function with respect to the strain. Different methods can be used to define the strain energy function. The simplest model is the Neo-Hookean approach in which an initial linear behavior is described similar to the Hooke's law and the behavior turns into nonlinear at some points [76]. For larger strains, Mooney-Rivlin model is more appropriate in which two invariants are used to define the strain energy density function [77, 78]. Mooney-Rivlin model is usually accurate for strain values less than 100% but the Neo-Hookean model is accurate for strain less than 20% [79]. A more advanced hyperelastic approach is Ogden model [80]. Ogden model is described by using principal stretches. Also there are models which consider anisotropic hyperelasticity [81, 82].

It is stated that Neo-Hookean hyperelastic material model can closely represent mechanical properties of biological soft tissues especially the skin and fat under short term loading [70, 83-88]. Also Mooney-Rivlin model is sufficiently capable of modeling nonlinear behavior and has advantages for the computation time [89].

Sussman and Bathe [90] developed a model of incompressible, isotropic, hyperelastic material based on separable strain energy description in terms of logarithmic strains and piecewise spline interpolations using tension-compression test data [90]. In this model [90], there is no need for the model constants. The model mimics even complicated test data accurately for small and large strains. The strain energy density is represented by piecewise splines. The model is easy to use

and it is a generalization of the Ogden model. In other models such as Mooney-Rivlin and Ogden, the constants are selected to best represent experimental data in the desired range of strain values.

For Mooney-Rivlin [77, 91] hyperelastic model, the strain energy density function is defined as the following:

$$\begin{aligned}
W = & c_{10}(I_1 - 3) + c_{01}(I_2 - 3) + c_{20}(I_1 - 3)^2 + c_{02}(I_2 - 3)^2 \\
& + c_{11}(I_1 - 3)(I_2 - 3) + c_{30}(I_2 - 3)^2 \\
& + c_{03}(I_2 - 3)^3 + c_{21}(I_1 - 3)^2(I_2 - 3) \\
& + c_{12}(I_1 - 3)(I_2 - 3) + D_1(J - 1)^2
\end{aligned} \tag{5.1}$$

where W is the strain energy for unit volume, J is the volume ratio, $c_{10}, c_{01}, c_{20}, c_{02}, c_{11}, c_{30}, c_{03}, c_{21}, c_{12}, D_1$ are the material parameters, I_1, I_2 are the first and the second strain invariants defined as the following:

$$I_1 = \bar{\lambda}_1^2 + \bar{\lambda}_2^2 + \bar{\lambda}_3^2 \tag{5.2}$$

$$I_2 = \bar{\lambda}_1^{-2} + \bar{\lambda}_2^{-2} + \bar{\lambda}_3^{-2} \tag{5.3}$$

where $\lambda_1, \lambda_2, \lambda_3$ are the principal stretches and $\bar{\lambda}_1, \bar{\lambda}_2, \bar{\lambda}_3$ are the deviatoric stretches defined as the following:

$$\bar{\lambda}_1 = J^{-1/3} \lambda_1 \tag{5.4}$$

$$\bar{\lambda}_2 = J^{-1/3} \lambda_2 \tag{5.5}$$

$$\bar{\lambda}_3 = J^{-1/3} \lambda_3 \tag{5.6}$$

For Ogden [80] model, the strain energy density function (W) is defined as the following:

$$W = \sum_{i=1}^N \frac{\mu_i}{\alpha_i} (\lambda_1^{\alpha_i} + \lambda_2^{\alpha_i} + \lambda_3^{\alpha_i} - 3) + \sum_{i=1}^N \frac{1}{D_1} (J - 1)^{2i} \quad (5.7)$$

where N is the number of polynomials, $\lambda_1^{\alpha_i}, \lambda_2^{\alpha_i}, \lambda_3^{\alpha_i}$ are the principle stretches and μ_i, α_i, D_1 are the material parameters.

5.1.2 Viscoelasticity

For an elastic material, the elastic modulus is defined as the slope of the stress-strain curve. For a purely viscous material, stress is proportional to the strain rate and the ratio of stress to strain rate is the viscosity. Materials which do not exactly obey these two classifications are the viscoelastic materials. An instantaneous elastic response is observed for the viscoelastic materials, then it is followed by a continuous and slow response with a decreasing rate. Viscoelastic materials represent properties of both elasticity and viscosity. For a material with elastic property, when the load is removed, the structure returns to its unloaded state. For a material with the property of viscosity, strain increases with time as a load is applied. Similarly, strain decreases with time when the load is removed which is resulting in a time-dependent strain [66].

When a viscoelastic member is loaded at an infinitely slow rate, observed stress-strain behavior is the equilibrium response and follows the path E-E' in Figure 5.2. If the loading is infinitely fast then observed stress-strain behavior is the instantaneous response and follows path I-I'. Both instantaneous and equilibrium responses are elastic responses and the viscoelastic response lies between these two phases [92].

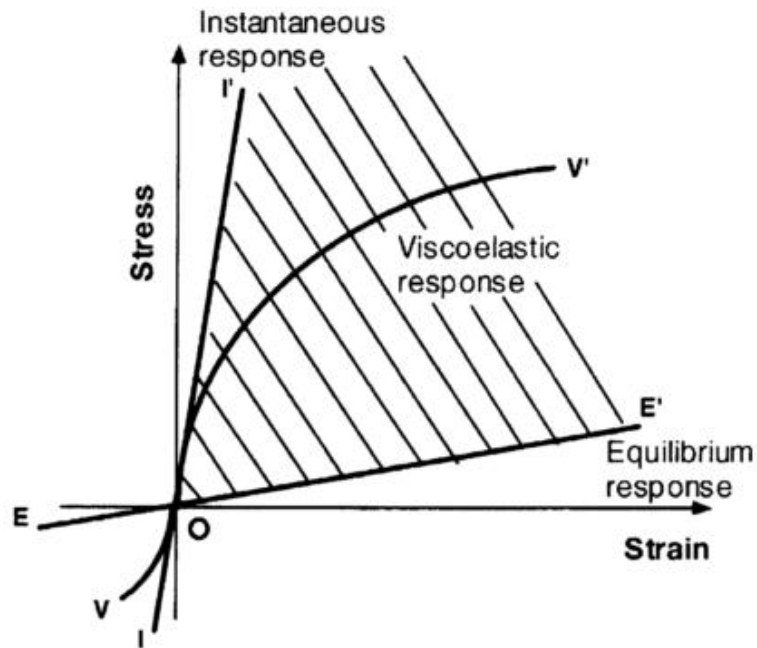


Figure 5.2 Typical response of a viscoelastic solid (adopted from [93]).

A viscoelastic material undergoes a time dependent deformation under loading and a time dependent recovery of deformation with unloading. Creep is the change in strain over time under applied constant stress. Relaxation is the change in stress over time under applied constant strain. For a linearly viscoelastic material, creep and relaxation are dependent only on time and they are independent of stress and strain.

Holzapfel et al. [94] employed generalized Maxwell approach for modelling the viscoelasticity of the arteries. Five Maxwell elements are used for the viscoelastic model as represented in Figure 5.3.

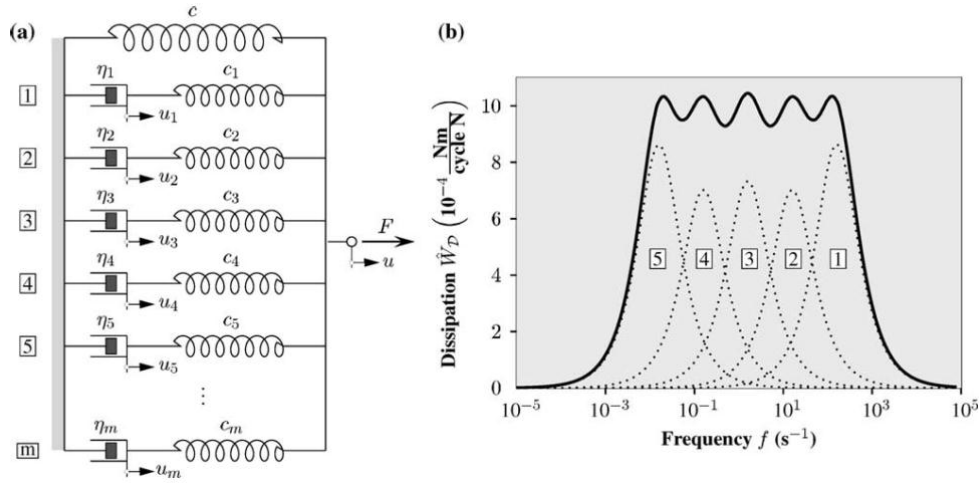


Figure 5.3 (a) Generalized Maxwell model. (b) Normalized dissipation \dot{W}_D versus frequency according to material parameters for artery. Solid line denotes the dissipation of whole model. Each dotted line corresponds to a specific Maxwell element (adopted from [94]).

In Figure 5.3, the normalized dissipation is represented as a function of frequency. For extremely slow and fast loading, viscoelastic effect is nearly obsolete. For the frequency range between 0.01 and 100 Hz, the dissipation is nearly constant and has the maximum value. At 1000 Hz, the dissipation is lower than half of the maximum value. The solution of the generalized Maxwell model is obtained by using Prony series.

In ADINA (Watertown, MA), the viscoelasticity is modelled using generalized Maxwell approach and the relaxation modulus ($E(t)$) is defined using the Prony series expression as the following:

$$E(t) = E^\infty \left[1 + \sum_{\alpha=1}^N \beta^\alpha e^{\left(-\frac{t}{\tau^\alpha}\right)} \right] \quad (5.8)$$

N is the number of Maxwell elements, E^∞ is the long-term elastic modulus, E^α is elastic coefficient and τ^α is the relaxation time. In ADINA (Watertown, MA), the viscoelastic material properties are defined using β^α and τ^α . Relaxation time (τ^α) is directly used without any calculation and β^α is calculated as the following [95]:

$$\beta^\alpha = \frac{E^\alpha}{E^\infty} \quad (5.9)$$

$$E^\infty = 1 - \sum_{\alpha=1}^N E^\alpha \quad (5.10)$$

Viscoelastic parameters of the generalized Maxwell approach are obtained from the related studies in the literature and listed in Table 5.1.

Table 5.1 Viscoelastic material properties

	β_1	β_2	β_3	β_4	β_5	τ_1 (s)	τ_2 (s)	τ_3 (s)	τ_4 (s)	τ_5 (s)
Fat [96]	0.493	0.427				0.3834	4.6731			
Skin [96]	0.288	0.712				0.2136	8.854			
Muscle [95]	2.0216	0.519	0.1125	0.433	0.2424	0.6	6	30	60	300
Artery [94]	0.353	0.286	0.298	0.285	0.348	0.001	0.01	0.1	1	10

5.1.3 Realistic material properties of soft tissues

Realistic mechanical properties of muscles are required for modelling the human body but the data related with muscles are mostly available for animals. In the literature, there are experimental studies which investigate in-vitro mechanical properties of sample animal muscles [97-106]. Chawla et al. [107] and Untaroiu et al. [108] investigated human muscle mechanical properties. In order to obtain hyperelastic behavior of human muscle, the sternocleidomastoideus muscle is

investigated by Aimedieu et al. [109]. In the literature, it is obvious that there is a lack of data related with the material properties of the human tissues.

Muscle is a complex and fibre-oriented structure which is composed of 80% water, 3% fat and 10% collagenous tissues [95]. Muscle is considered as linearly elastic material with an elastic modulus of 100 kPa for the passive state in which the active components due to biochemical energy supply is neglected [83, 110-113]. The elastic modulus of the contracted muscle increases to about 400 kPa [112-114].

In the literature, muscle [110, 115-117], fat [64, 118, 119] and skin [71, 72, 120, 121] are modelled as hyperelastic materials. Mooney-Rivlin [108, 122, 123] and Ogden [101, 124] material models are used to model the passive mechanical properties of muscles with finite element models. Muscle is considered as almost incompressible and the Poisson's ratio is employed as 0.495 [101, 122, 123, 125-127]. It is stated that volume of muscle remains nearly constant after contraction [83]. The muscle is modelled as homogeneous since the mechanical property of the entire structure is investigated and thus the modeling approach is simplified. In Figure 5.4, the stress-strain response of passive muscle tissue is given using Mooney-Rivlin approach.

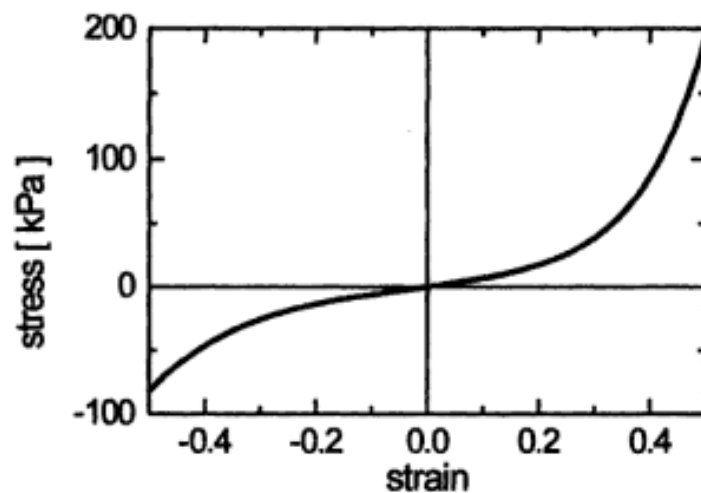


Figure 5.4 Stress-strain response of passive muscle tissue (adopted from [128]).

Skin is the largest single organ of the human body [129] and it is composed of dermis and epidermis. Mechanical properties can be determined using positive or negative external stress using methods of indentation or suction, respectively. Adipose tissue is mainly composed of fat and the mechanical properties are characterized by means of compression tests for human breast [70, 74, 130, 131]. In several studies, skin is modeled as a single-layered hyperelastic material [71, 72]. In the study of Barbarino et al. [132], mass density is used as 1 g/cm^3 for all muscular tissues and fat. Skin density is assigned as 1.1 g/cm^3 in accordance with the results of Duck [133]. Teran et al. [134] stated that the initial elastic moduli of fat is about 20 kPa [135]. Small-deformation slope of skin for the stress-strain relationship is reported as 15 kPa [68]. It is stated that bulk moduli of most soft tissues are close to the bulk modulus of water and the difference is less than 15% [136, 137].

Bone is modelled considering two different parts as cortical (compact) and trabecular (cancellous) regions. The cortical bone surrounds the trabecular bone and the thickness varies for different parts of human body [138]. Cortical and trabecular bones are modeled as homogenous, isotropic and elastic. Spatial variation of density is neglected for the bone and a uniform average density is employed.

Thigh, upper arm and neck are modelled in the realistic computational analysis. The thigh model is composed of blood, femoral artery, bone, muscle, fat and skin. The upper arm model is created considering blood, brachial artery, bone, muscle, fat and skin. The neck model is composed of blood, common carotid artery, vein, bone, trachea, air, fat and skin. The fat and skin are modelled using nonlinear stress-strain relationship of Ogden material model. The muscle and femoral artery are modelled using Mooney-Rivlin model. The material parameters are obtained from the related studies in the literature and summarized in Table 5.2.

Table 5.2 Material parameters employed in the realistic computational analysis

<i>Material</i>	<i>Model</i>	<i>Density</i>	<i>Bulk Modulus</i>				
Blood [24]	Acoustic fluid	1000 kg/m ³	2.2 GPa				
Air	Acoustic fluid	1.225 kg/m ³	100 kPa				
Fat [96]	Ogden	1000 kg/m ³	2.2 GPa	$\mu_1 = 23583 Pa$	$\mu_2 = 40 Pa$	$\mu_3 = -40878 Pa$	$\mu_4 = 19340 Pa$
				$\alpha_1 = -2.0623$	$\alpha_2 = 25$	$\alpha_3 = -3.4784$	$\alpha_4 = -4.4864$
Skin [96]	Ogden	1100 kg/m ³	2.2 GPa	$\mu_1 = 6375.4 Pa$	$\mu_2 = 180 Pa$	$\mu_3 = -3770.7 Pa$	$\mu_4 = 1840 Pa$
				$\alpha_1 = 1.3416$	$\alpha_2 = 25$	$\alpha_3 = -7.8671$	$\alpha_4 = -10.898$
Muscle [128]	Mooney-Rivlin	1000 kg/m ³	2.2 GPa	$c_{10} = 10000 Pa$	$c_{20} = 10000 Pa$	$c_{30} = 6666.7 Pa$	
Trachea [139]	Linear	1000 kg/m ³		Poisson's ratio = 0.499	Elastic modulus = 1.66 MPa		
Femoral artery [140]	Mooney-Rivlin	1000 kg/m ³	2.2 GPa	$c_{10} = 18900 Pa$	$c_{01} = 2750 Pa$	$c_{20} = 590420 Pa$	$c_{11} = 857180 Pa$
Brachial artery [141]	Linear	1086 kg/m ³		Poisson's ratio = 0.490	Elastic modulus = 3.8 MPa		
Common carotid artery [142]	Mooney-Rivlin	1000 kg/m ³	2.2 GPa	$c_{10} = 94600 Pa$			
Cortical bone [108]	Linear	2000 kg/m ³		Poisson's ratio = 0.3	Elastic modulus = 15 GPa		
Trabecular bone [108]	Linear	1100 kg/m ³		Poisson's ratio = 0.3	Elastic modulus = 0.6 GPa		

5.2 Realistic geometries based on the human anatomy

Coronary arteries that provide blood to the heart are smaller in diameter, and stenosis-based sounds are suppressed by valve closure and breathing sounds. The diameters of the brachial artery in the upper arm, the femoral artery in the thigh, and the common carotid artery in the neck are 4 mm [60], 10 mm [61] and 6.4 mm [143], respectively. These arterial diameters are much higher compared to the coronary arteries, therefore it is much easier to distinguish the stenosis-based sounds in the peripheral arteries. The anatomies of the upper arm, thigh and neck are less complicated when compared to the chest and abdomen. It is difficult to model various organs and tissues in the chest and abdominal region considering the mechanical and geometrical properties. In the thigh, upper arm and neck, soft tissues are predominantly skin, fat, muscle and blood vessels. As consequence of the reasons stated, the thigh, upper arm and neck are investigated in the realistic computational models to see the pure effect of stenosis-based sound generation.

Simplistic and Computed Tomography (CT) based models are employed for the realistic computational models. The sizes of the thigh, upper arm and neck depends on age, gender, height and weight of individuals. For the simplistic models, average dimensions are considered using the cross-sectional views of the human cadavers. For the CT based models, patient-specific data is used to generate the model geometry.

For simplistic thigh model, the circumference of the model decreases from 500 to 375 mm. The total length of the thigh is 250 mm and the thickness of fat and skin are 4 mm and 2 mm, respectively [63]. The inner diameter and thickness of the femoral artery are 10 mm [61] and 0.75 mm [144], respectively. Since femur bone is much stiffer compared to the soft tissues, it is assumed as a rigid material. Therefore, the nodes on the surface of the femur bone are fixed with zero displacement. The diameter of the femur bone is 25 mm with an eccentricity of 15 mm between the center of the thigh model and the center of the femur bone. The

distance between the center of femoral artery and the center of the thigh model is 32.5 mm. In Figure 5.5, simplistic and CT based thigh models are represented.

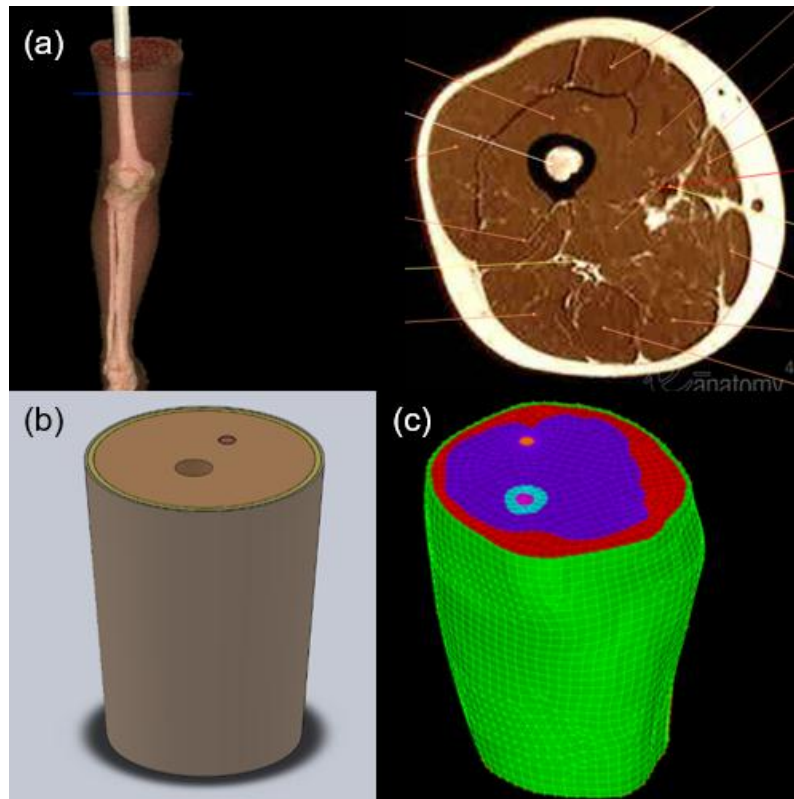


Figure 5.5 (a) Real cross-sectional view of thigh [145]. (b) Simplistic 3D model of thigh. (c) CT-based 3D model of thigh.

For simplistic upper arm model, a uniform circumference about 250 mm is considered. The total length of the upper arm is 140 mm and the thickness of fat and skin are 6 and 2 mm, respectively [63]. The inner diameter and thickness of the brachial artery are 4 mm [60] and 0.4 mm [146], respectively. Humerus bone is modelled considering the trabecular and cortical zones. Trabecular (spongy) and cortical bone diameters are 7 and 20 mm, respectively. There is an eccentricity of 5 mm between the center of the humerus bone and the center of the simplistic upper arm model. The distance between the center of the brachial artery and the center

of the model is 23 mm. In Figure 5.6, simplistic and CT based upper arm models are presented.

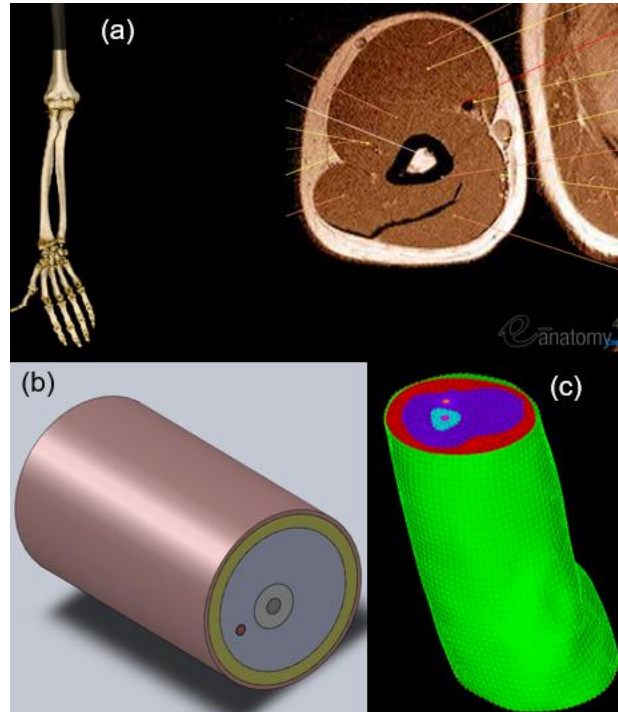


Figure 5.6 (a) Real cross-sectional view of the upper arm [147]. (b) Simplistic 3D model of the upper arm. (c) CT-based 3D model of the upper arm.

A uniform circumference about 315 mm is employed for the simplistic neck model. The total length of the neck is 70 mm. Bones of cervical vertebrae are considered with a diameter of 14 mm. Since these bones are much stiffer than the soft tissues, the boundary nodes of the bones are fixed with zero displacement for the simplistic models. There is an eccentricity of 7 mm between the center of model and the center of cervical vertebrae. The thickness of fat and skin are considered as 4 mm and 2 mm, respectively [63]. The common carotid artery is placed at 20 mm distance from the center of the simplistic neck model. The common carotid artery inner diameter and thickness are 6.4 mm [143] and 0.7 mm [144, 148], respectively. The large vein in the neck is also considered with a diameter of 10 mm. The distance

between the center of the common carotid artery and the center of the neck model is 20 mm. Trachea and the air inside are also considered in the model. The trachea is modelled as a hollow cylindrical structure with an inner diameter of 20 mm and a thickness of 2 mm. In Figure 5.7, simplistic and CT based neck models are presented.

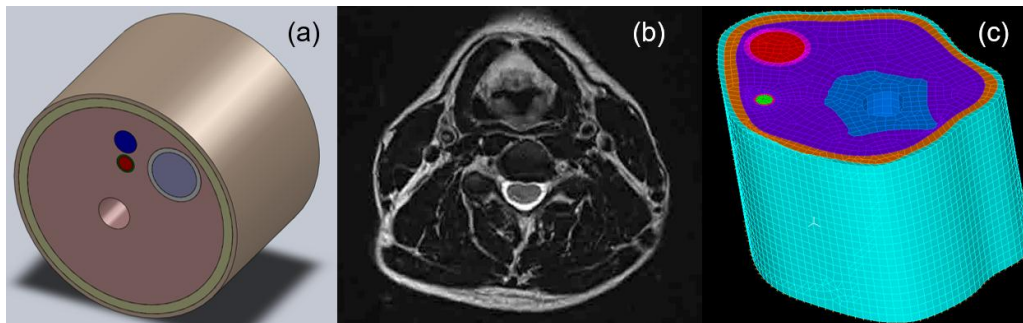


Figure 5.7 (a) Simplistic 3D model of the neck. (b) Real cross-sectional view of the neck [149]. (c) CT-based 3D model of the neck.

Simplistic models and CT based models are investigated separately. Open-access CT data provided by OsiriX DICOM image library (Bernex, Switzerland) is used to obtain three-dimensional models. CT images are processed using Mimics (Materialise, Leuven, Belgium) segmentation software to differentiate the structures by color scales.

The thigh, upper arm and neck models have similar boundary conditions. The joint surfaces on both ends of the models are fixed with zero displacement. The acoustic pressure field is applied radially on the inner arterial wall. For simplistic models, the bone boundary nodes are fixed with zero displacement, since the bones are assumed as rigid materials due to high stiffness.

5.3 Physiological conditions in the peripheral arteries

Blood flow velocity and lumen diameter vary for different peripheral arteries. The peak flow rate for the upper arm brachial artery reaches 650 mm/s [150] for a lumen diameter of 4 mm [60]. The peak flow rate is considered in the analysis since the highest sound generation is observed in the systolic phase as shown in Figure 5.8(b). The average velocity (V_{avg}) for fully developed pipe flow is about half of the peak velocity as shown in Figure 5.8(a). For a peak flow rate of 650 mm/s, the Reynolds number of blood flow reaches 1300 in the upper arm brachial artery. The highest Reynolds number is observed as 3840 in the common carotid artery of the neck. The lowest Reynolds number is 750 in the femoral artery of the thigh. The brachial and common carotid arteries are closer to the heart, and therefore higher Reynolds numbers are observed. As the distance between the heart and the peripheral artery increases, the Reynolds number of blood flow tends to decrease.

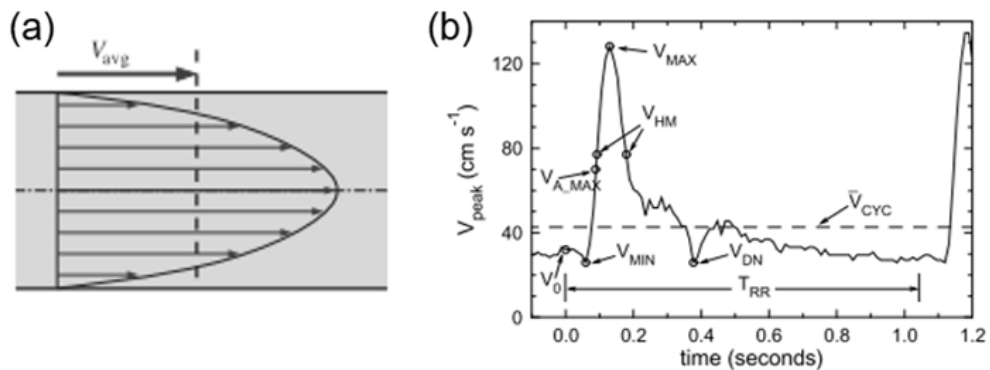


Figure 5.8 (a) Average velocity (V_{avg}) for fully developed pipe flow. (b) Sample blood velocity waveform for a peripheral artery (adopted from [151]).

5.4 Acoustic pressure field in the peripheral arteries

In Chapter 2, acoustic pressure amplitudes are obtained using (2.32). This equation is expressed for a lumen diameter of 6.4 mm using the nonlinear F_{n1} function given

in (2.31). For a different lumen diameter, a modification should be done to define the stenosis-based acoustic pressure field. The upper arm brachial artery has a lumen diameter of 4 mm.

$$D_{brachial} = 4 \text{ mm} \quad (5.11)$$

The modification factor for the brachial artery is defined as the following:

$$C_{mod,brachial} = \frac{6.4}{D_{brachial}} = \frac{6.4}{4} = 1.6 \quad (5.12)$$

Using the modification factor, the nonlinear F_{n1} function given in (2.31) is modified for the brachial artery as the following:

$$F_{n1,brac}[x] = \frac{0.07057C_{mod,brachial}x + 0.3849}{(C_{mod,brachial}x)^2 - 23.22C_{mod,brachial}x + 167.9} \quad (5.13)$$

$$F_{n1,brac}[x] = \frac{0.112912x + 0.3849}{2.56x^2 - 37.152x + 167.9} \quad (5.14)$$

For the brachial artery, the acoustic pressure field is determined using the modified $F_{n1,brac}$ function and the same procedure is applied to find the modified F_{n1} function for the femoral artery in the thigh with a lumen diameter of 10 mm.

In Figure 5.9, Figure 5.10 and Figure 5.11, acoustic pressure fields and corresponding phase maps are represented for femoral, brachial and common carotid arteries, respectively. Acoustic pressure amplitudes are much higher for the common carotid artery in the neck due to high flow rate.

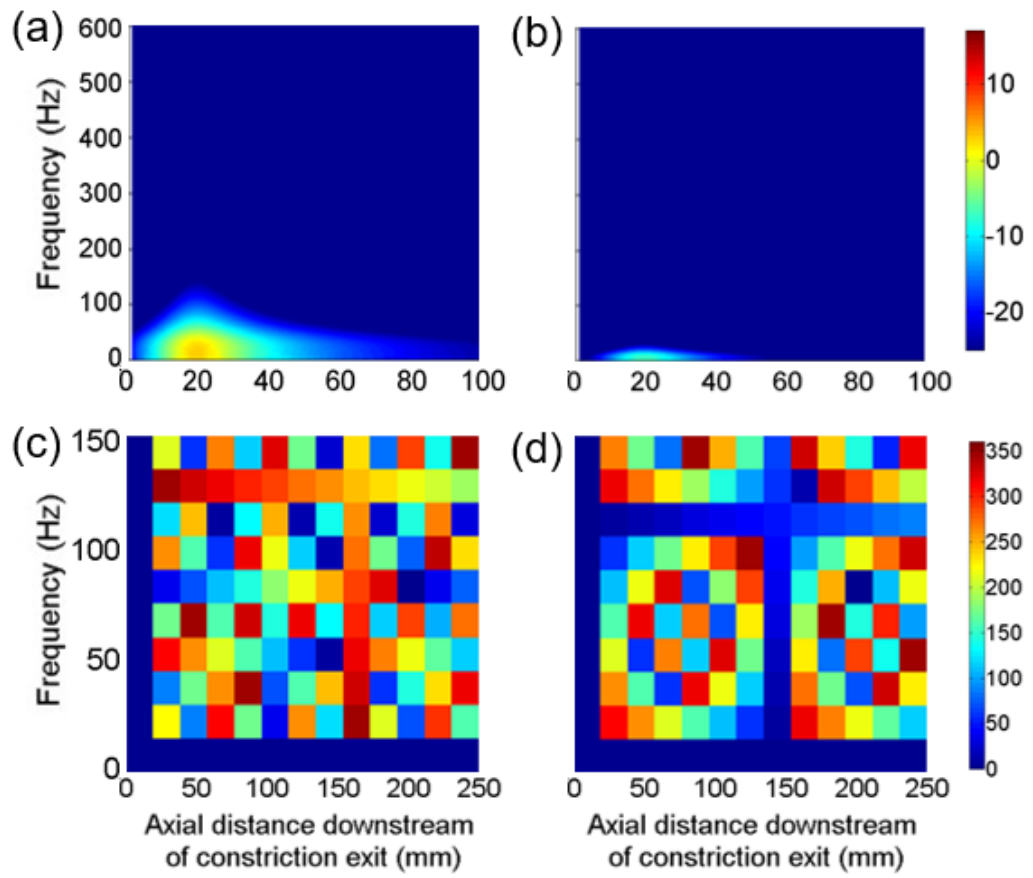


Figure 5.9 Femoral artery in the thigh. (a) Acoustic pressure (dB ref: 1 Pa) for 90% stenosis. (b) Acoustic pressure (dB ref: 1 Pa) for 70% stenosis. (c) Phase map for 90% stenosis. (d) Phase map for 70% stenosis.

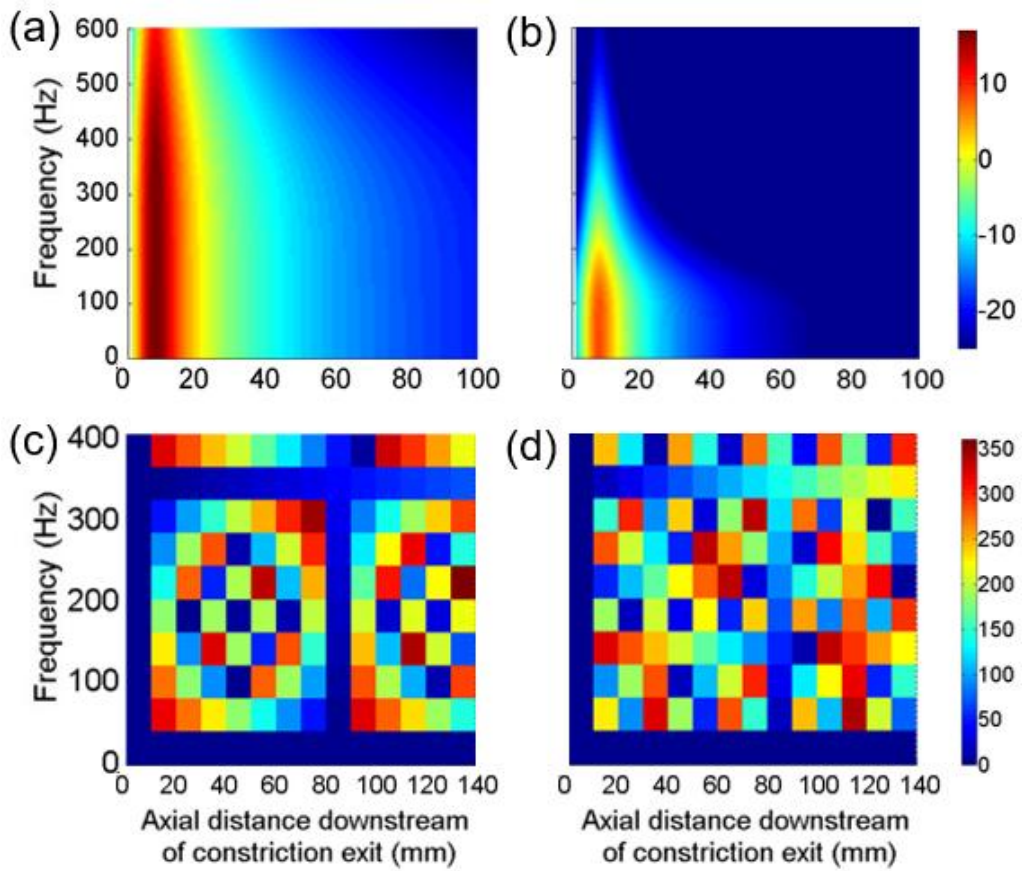


Figure 5.10 Brachial artery in the upper arm. (a) Acoustic pressure (dB ref: 1 Pa) for 90% stenosis. (b) Acoustic pressure (dB ref: 1 Pa) for 70% stenosis. (c) Phase map for 90% stenosis. (d) Phase map for 70% stenosis.

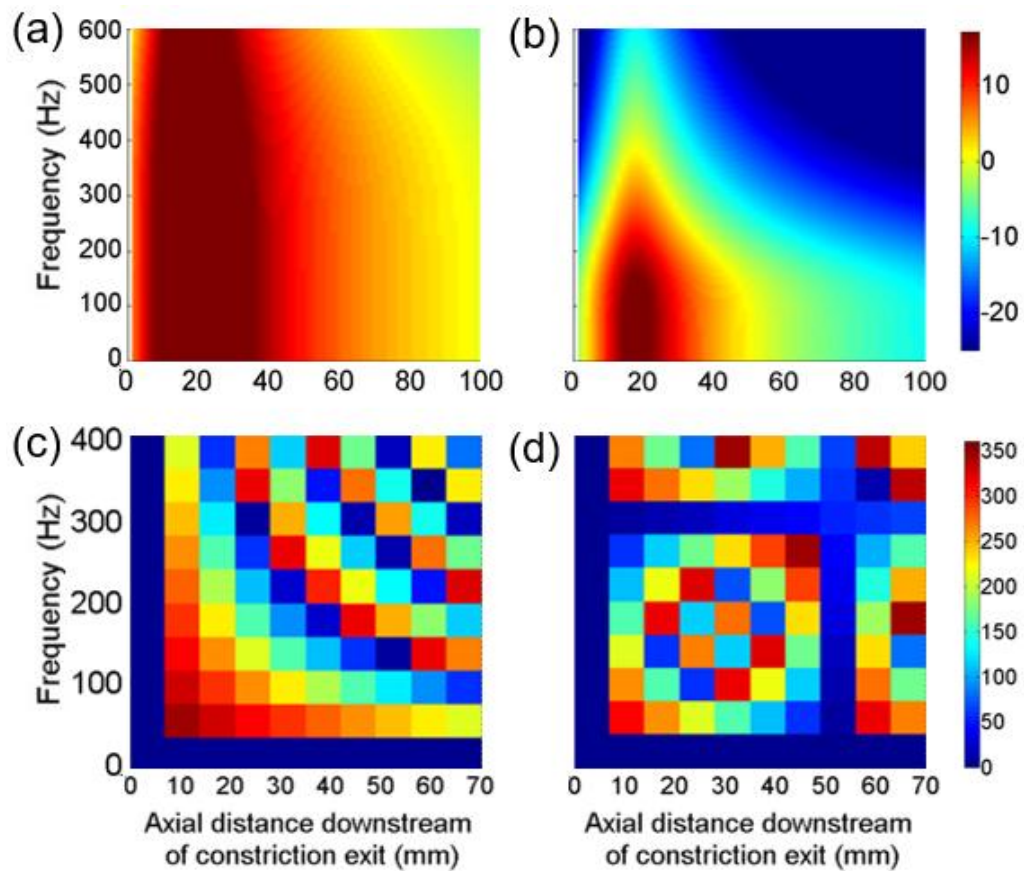


Figure 5.11 Common carotid artery in the neck. (a) Acoustic pressure (dB ref: 1 Pa) for 90% stenosis. (b) Acoustic pressure (dB ref: 1 Pa) for 70% stenosis. (c) Phase map for 90% stenosis. (d) Phase map for 70% stenosis.

5.5 Simplistic thigh models

Radial velocity response on the skin surface is investigated to detect the stenosis location and to observe the effects of severity. The frequency range of interest is 0-150 Hz for the thigh, 0-400 Hz for the upper arm and neck. Since the blood flow velocity is lower for the thigh compared to the upper arm and neck, effects of stenosis are observed only up to 150 Hz. For all models, highest responses are expected at the location which has the closest radial distance to the artery, therefore

the skin nodes on the radially closest line are the main focus of the analyses. Results are indicated in colored dB scale using a reference velocity of 1 mm/s.

A mesh independence study is performed using three different mesh densities. The details and total number of elements of the meshes are provided in Table 5.3. In Figure 5.12, radial velocity responses are given for a sample case with 90% stenosis. Between Mesh 1 and Mesh 2, there is an average amplitude (within 0-250 mm, 0-150 Hz) difference of 25.95%. Between Mesh 2 and Mesh 3, there is an average amplitude difference of 2.85%. Mesh 2 is used for further analysis since the average amplitude difference between Mesh 2 and Mesh 3 is less than 3%.

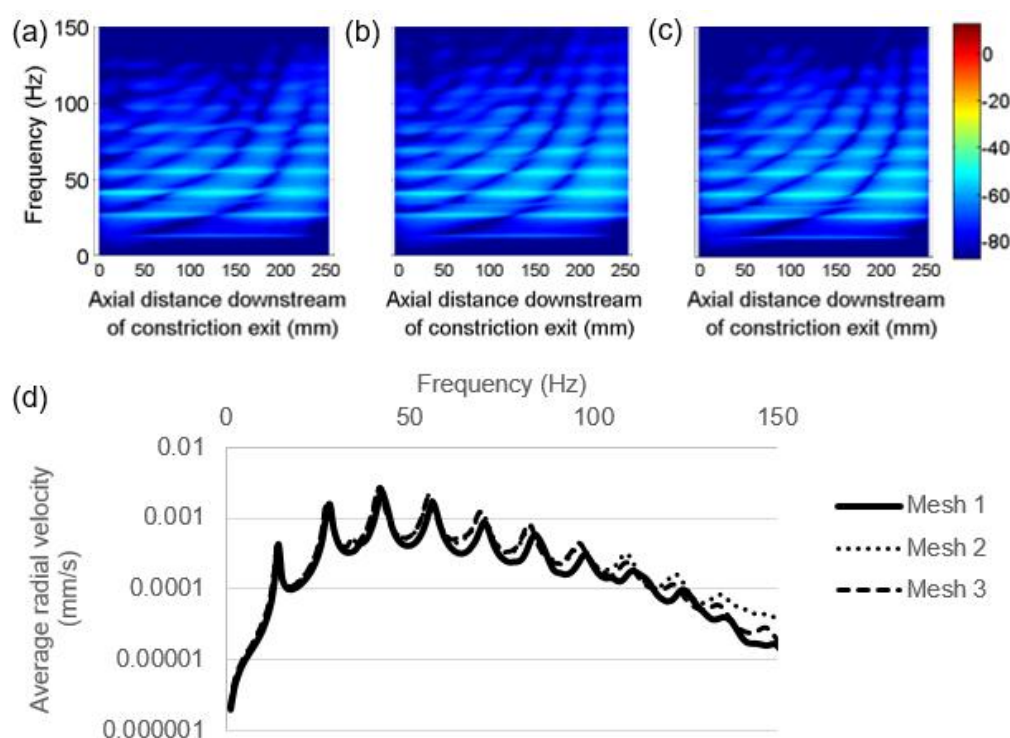


Figure 5.12 Radial velocity response (dB ref: 1 mm/s) as function of axial distance and frequency for simplistic thigh model with 90% stenosis. Stenosis exit is placed at 0 mm. (a) Mesh 1. (b) Mesh 2. (c) Mesh 3. (d) Average of radial velocity responses for simplistic thigh model. Amplitudes within 0-250 mm are averaged at each frequency.

Table 5.3 Mesh details for simplistic thigh model

# of Elements	Mesh 1	Mesh 2	Mesh 3
Skin	4804	27773	11697
Fat	4734	7062	11400
Blood	2693	2693	2693
Femoral Artery	1382	1382	1382
Muscle	40334	56206	108016
Total	53947	95116	135188

As shown by the red line in Figure 5.13(a), the radial velocity responses are investigated for the nodes on the skin that are closest to the femoral artery. In addition to the radial velocity responses, pressure responses on the skin are also investigated. For this purpose, some elements are fixed with zero displacement as shown in Figure 5.14. Pressure responses at those fixed regions indicate the measurements that will be obtained using a stethoscope or contact-type pressure sensor placed on the skin. In Figure 5.13(b), three fixed regions on the skin are named x, y, z, and are shown in circles. The center of y-region has a distance of 125 mm to the both ends of the model. The centers of x and z-regions have a distance of 80 mm from the center of y-region.

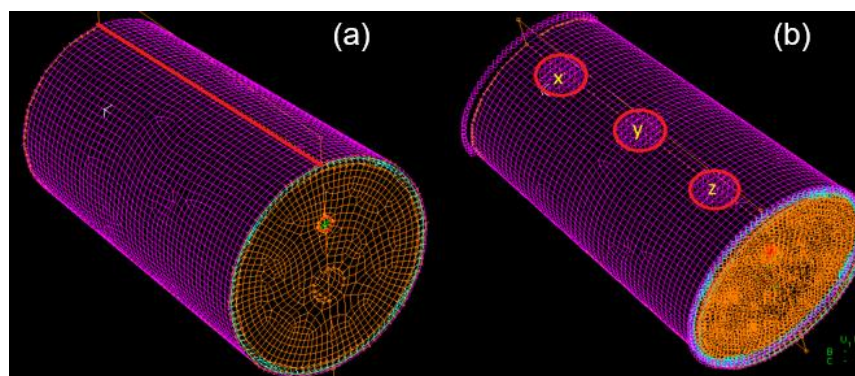


Figure 5.13 (a) Simplistic thigh model – (Top line depicts the nodes on the skin which are closest to the femoral artery in radial direction). (b) Fixed regions used to measure the pressure on the skin.

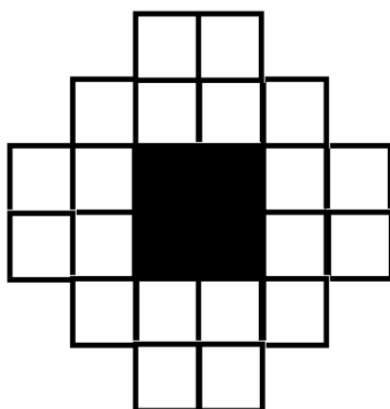


Figure 5.14 Fixed elements to determine the pressure on skin (Black region depicts the center of the fixed region containing four elements used to determine the pressure response).

5.5.1 Pressure response on the simplistic thigh model

In Figure 5.15, three different stenosis locations are considered as 0, 125 and 220 mm. The total length of the thigh model is 250 mm. For low frequencies between 0 and 15 Hz, the pressure responses have higher amplitudes for the regions closer to the stenosis. When the stenosis is placed at 0 mm, region-x has the highest amplitudes within 0-15 Hz, since x is the region closest to 0 mm. Similarly, if the stenosis is placed at 125 mm, the highest amplitudes are observed at region-y within 0-15 Hz, since it is the closest region to the stenosis location. According to these results, low frequency responses give important information about the location of the stenosis.

In Figure 5.16(a), the average pressure responses are determined by taking the mean of the responses in x, y, and z-regions. In the computational analysis, the stenosis is placed at 0 mm unless otherwise stated. The highest pressure amplitudes on the skin are obtained as -40, -15 and -5 dB for 70, 90 and 95% stenosis, respectively. In Figure 5.16(b), the average pressure responses are compared for

phased and no phased conditions. The phased pressure response appears to result in slightly lower amplitudes for the 0-50 Hz frequency range.

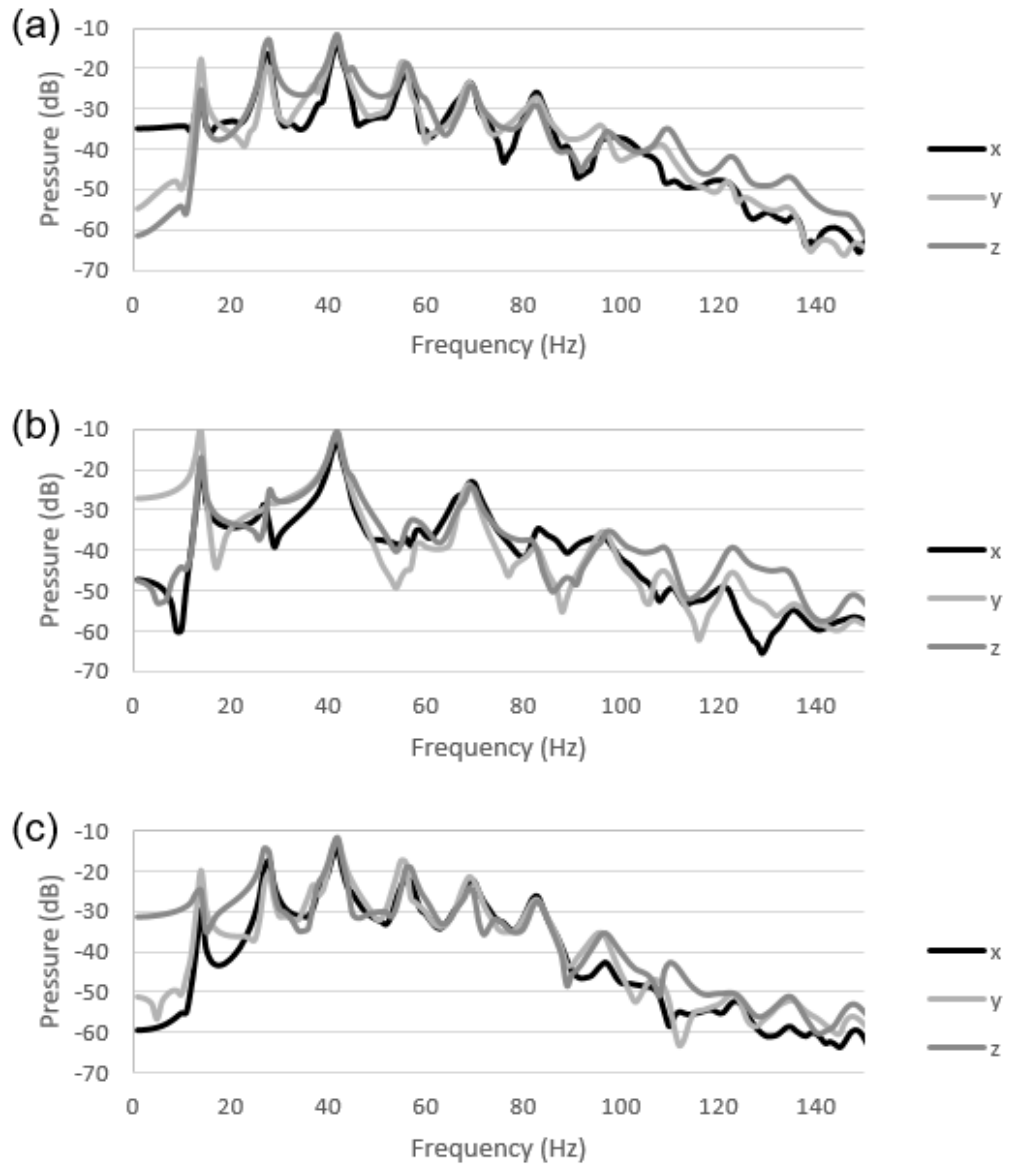


Figure 5.15 Pressure response (dB ref: 1 Pa) on the skin of simplistic thigh model (x, y and z regions are represented in Figure 5.13). (a) Stenosis at 0 mm. (b) Stenosis at 125 mm. (c) Stenosis at 220 mm.

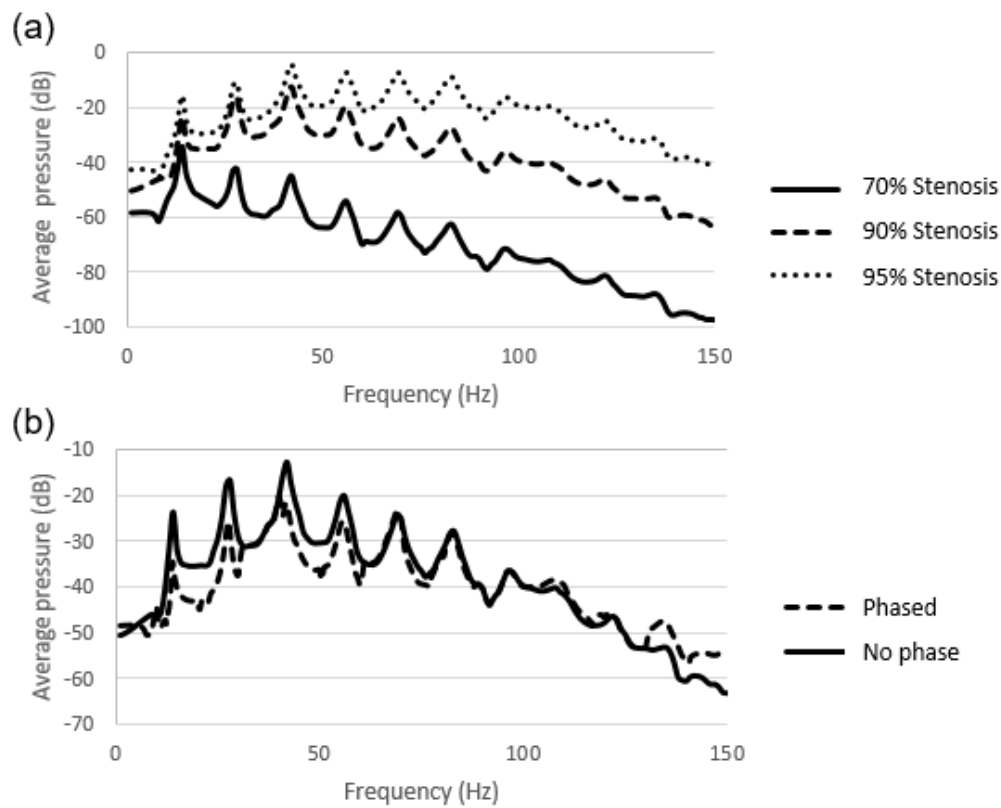


Figure 5.16 (a) Average pressure response (dB ref: 1 Pa) on the skin of simplistic thigh model considering different stenosis levels. (b) Average pressure response of simplistic thigh model for phased and no phased analysis.

5.5.2 Radial velocity response on the simplistic thigh model

In Figure 5.17, radial velocity responses are investigated for phased and no phased conditions considering 90% stenosis severity. It is observed that phased and no phased results give similar conclusions in terms of general trend in the frequency domain. In both analyses, the vibrational modes are apparently seen. In Figure 5.18, effects of different stenosis levels are investigated for the simplistic thigh model.

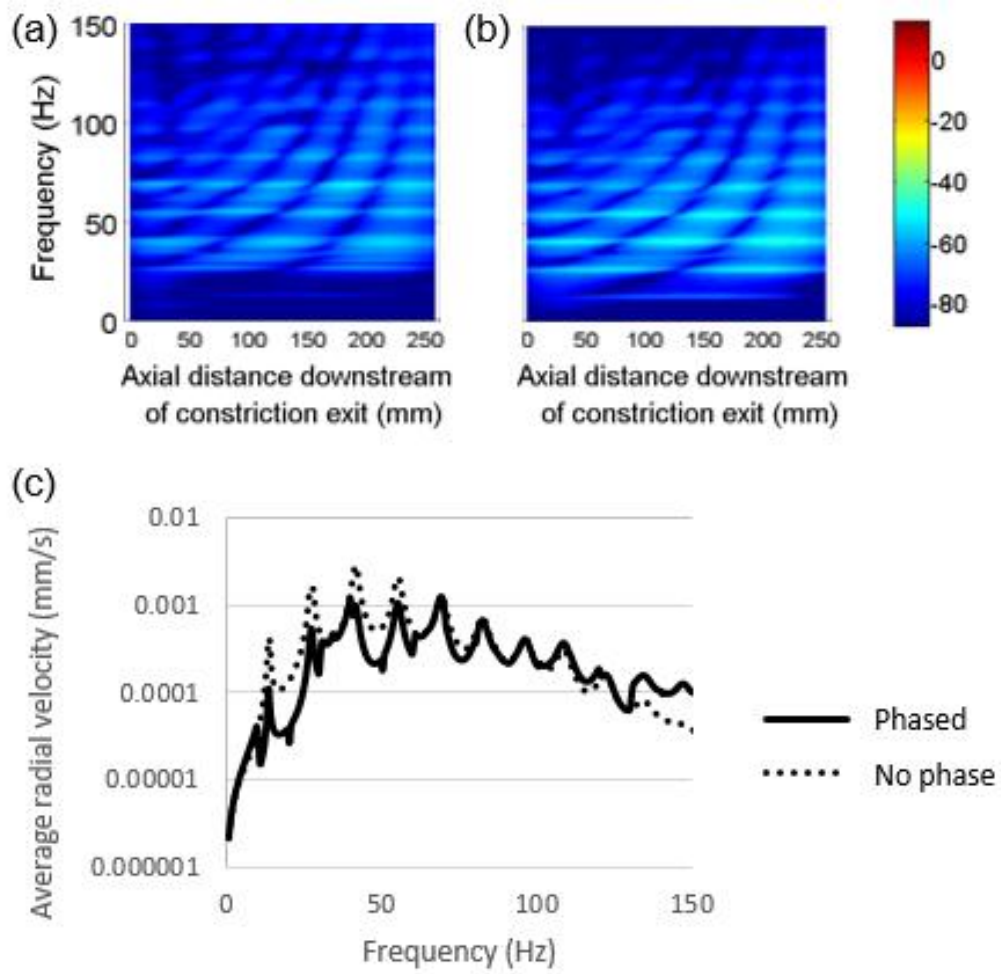


Figure 5.17 Radial velocity response (dB ref: 1 mm/s) as function of axial distance and frequency for simplistic thigh model with 90% stenosis. Stenosis exit is placed at 0 mm. (a) 10 x 10 phase map. (b) No phase map. (c) Average of radial velocity responses considering 10 x 10 phase map and no phase map.

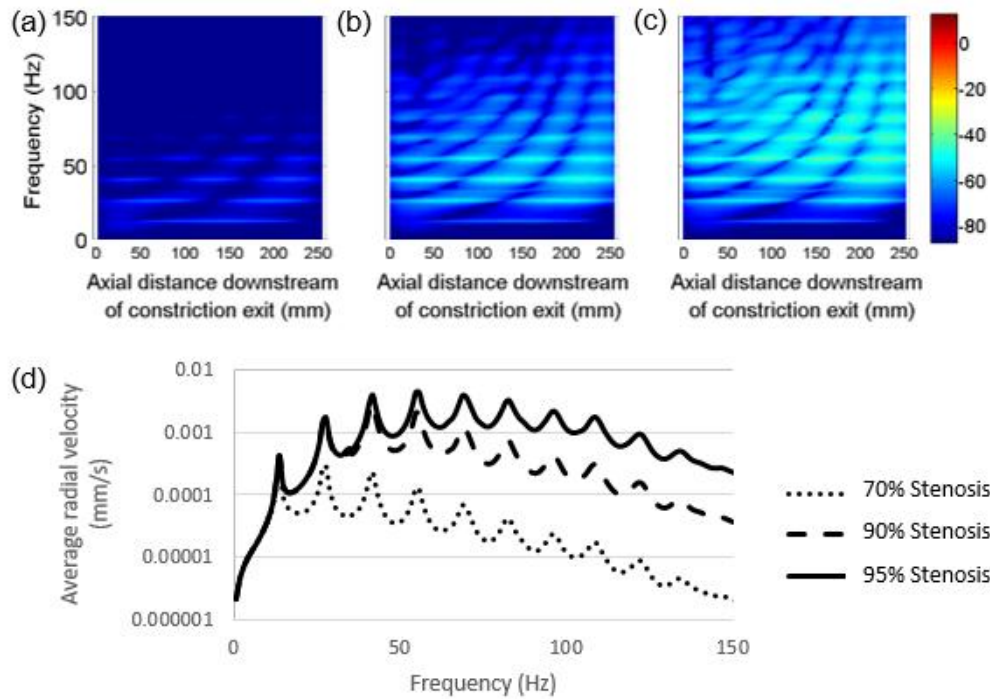


Figure 5.18 Radial velocity response (dB ref: 1 mm/s) as function of axial distance and frequency for simplistic thigh model considering no phase map. Stenosis exit is placed at 0 mm. (a) 70% stenosis. (b) 90% stenosis. (c) 95% stenosis. (d) Average of radial velocity responses considering various stenosis levels.

For 70% stenosis, the radial velocity amplitudes are quite low, but they significantly increase for 90% stenosis. If the stenosis severity is increased from 70% to 90%, the flow velocity u increases by 3 times where u is the flow jet velocity in the constricted region as previously presented in Figure 2.1. Depending on the increase in u , average vibration amplitudes (within 0-150 Hz) on the thigh surface increase by 10.5 times. When the average response amplitudes are investigated for 70% and 90% stenosis, it is found that the vibration amplitudes on the tissue surface are proportional to $u^{2.19}$. In Figure 5.19, the effect of stenosis location is investigated for the simplistic thigh model.

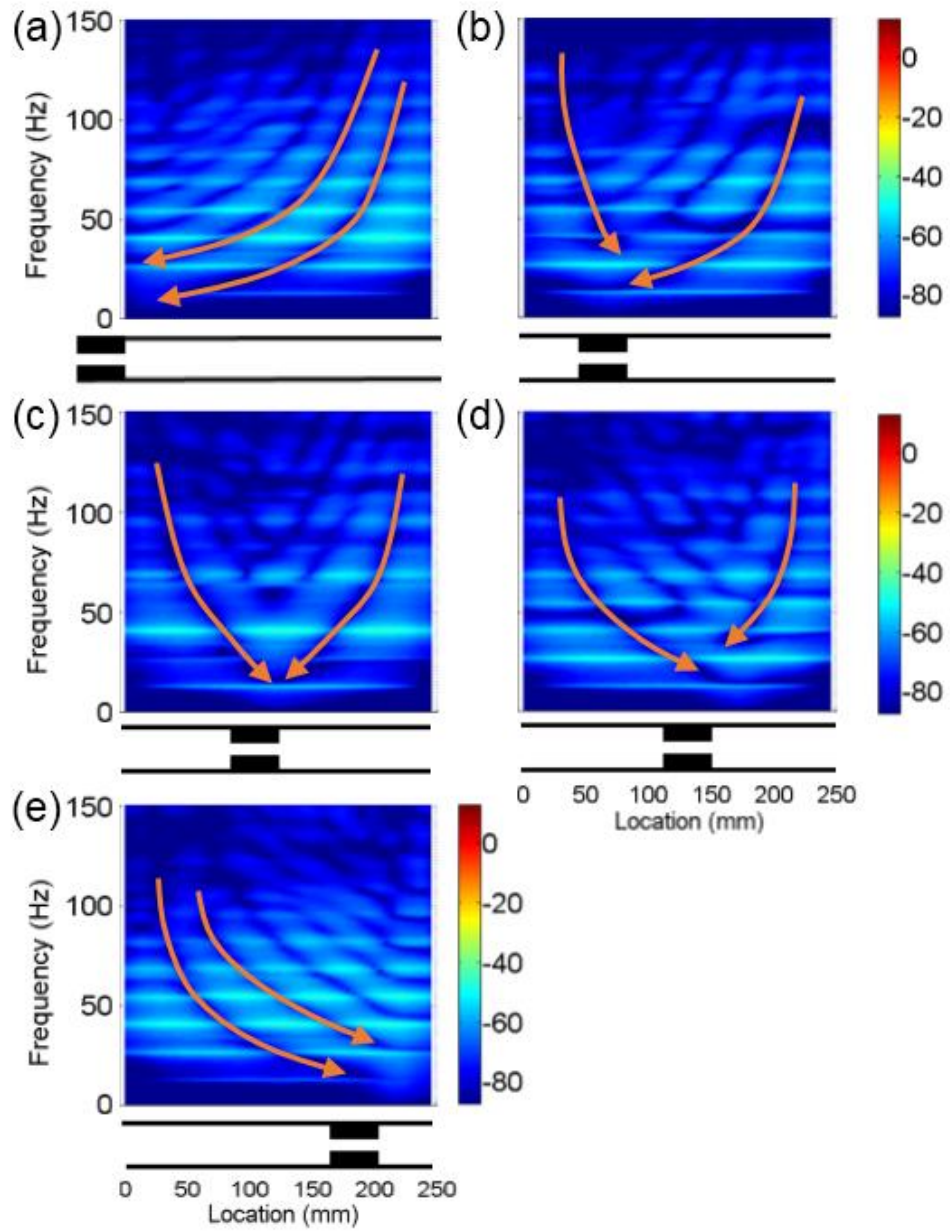


Figure 5.19 Radial velocity response (dB ref: 1 mm/s) as function of axial distance and frequency for simplistic thigh model with 90% stenosis considering different constriction locations. Sample anti-resonance curves are represented on the response contours. (a) Stenosis exit at 0 mm. (b) Stenosis exit at 50 mm. (c) Stenosis exit at 125 mm. (d) Stenosis exit at 150 mm. (e) Stenosis exit at 200 mm.

For all different stenosis locations, first, second and third natural frequencies are seen at 15, 30 and 45 Hz, respectively. Amplitude scales of the response contours do not significantly change, but the spectral contents have certain differences depending on the stenosis location. On the response contours, there are anti-resonance points which have the lowest amplitudes. Locus of these anti-resonance points may be used to create anti-resonance curves that are visualized in Figure 5.19. Anti-resonance curves can be used to provide critical information, since these curves always tend to meet near the stenosis location on the spatial axis of the radial velocity contour plots. In short, anti-resonance curves clearly show the stenosis location in simplistic thigh models.

5.6 Simplistic upper arm models

Mesh independence study is performed using three different meshes. The details and total number of elements of the meshes are provided in Table 5.4. In Figure 5.20, the radial velocity responses are presented for a sample case with 90% stenosis. Between Mesh 1 and Mesh 2, there is an average amplitude (within 0-140 mm, 0-200 Hz) difference of 21.2%. Between Mesh 2 and Mesh 3, there is an average amplitude difference of 2.58%. Mesh 2 is used for further analysis since the average amplitude difference between Mesh 2 and Mesh 3 is less than 3%.

Table 5.4 Mesh details for simplistic upper arm model

# of Elements	Mesh 1	Mesh 2	Mesh 3
Skin	6609	10106	14533
Fat	18386	24992	36488
Blood	537	537	537
Brachial Artery	336	336	336
Muscle	39659	55244	88885
Total	65527	91215	140779

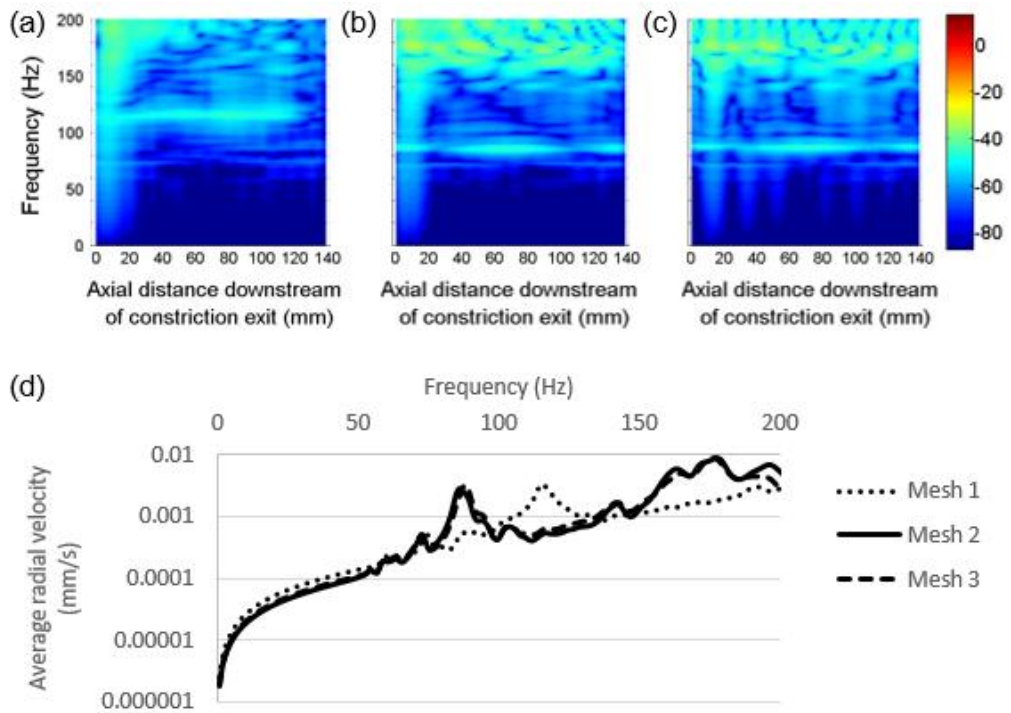


Figure 5.20 Radial velocity response (dB ref: 1 mm/s) as function of axial distance and frequency for simplistic upper arm model with 90% stenosis. Stenosis exit is placed at 0 mm. (a) Mesh 1. (b) Mesh 2. (c) Mesh 3. (d) Average of radial velocity responses for simplistic upper arm model. Response amplitudes within 0-140 mm are averaged at each frequency.

As shown by the red lines in Figure 5.21(a), the radial velocity responses are investigated for top (closest line to the brachial artery), bottom and lateral lines on the skin. Pressure responses are obtained at three fixed regions (x, y, and z) as shown in Figure 5.21(b). The center of y-region has a distance of 70 mm to the both ends of the model. The centers of x and z-regions have a distance of 35 mm from the center of y-region.

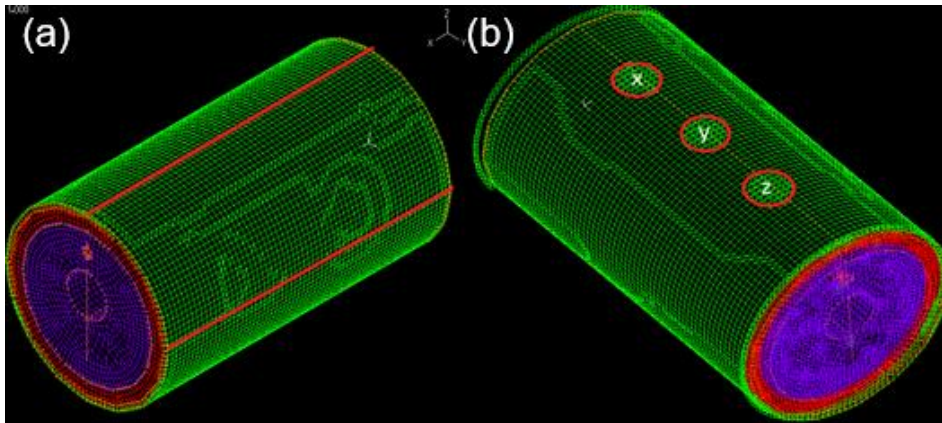


Figure 5.21 (a) Simplistic upper arm model – (Red lines depict the nodes on top and lateral side of the model). (b) Fixed x, y, z-regions used to measure the pressure on skin of the simplistic upper arm model.

5.6.1 Radial velocity response on the simplistic upper arm model

In Figure 5.22, radial velocity responses are presented for simplistic upper arm model to see the effect of stenosis severity in the brachial artery. For all radial velocity response maps presented, the same color scale (-87.5 to 12.5 dB) is employed for ease of comparison. Increased response amplitudes depending on the stenosis severity are observed for the simplistic upper arm model. The spectral content is not as simple as the simplistic thigh model which makes it difficult to distinguish anti-resonance curves. As the geometry of the model is getting complex, detection of anti-resonance curves becomes more difficult. In Figure 5.22(e), it is seen that amplitude increase due to stenosis severity does not have a linear trend. Increase in amplitudes is not critical up to 70%, but severities higher than 70% lead to a major increase. Therefore, 70% of severity can be treated as a critical value for diagnosing a stenosis. Average amplitudes in Figure 5.22(e) indicate that the effect of stenosis severity is more dominant at frequencies higher than 200 Hz. The amplitude difference at high frequencies is an indicator of presence of a stenosis.

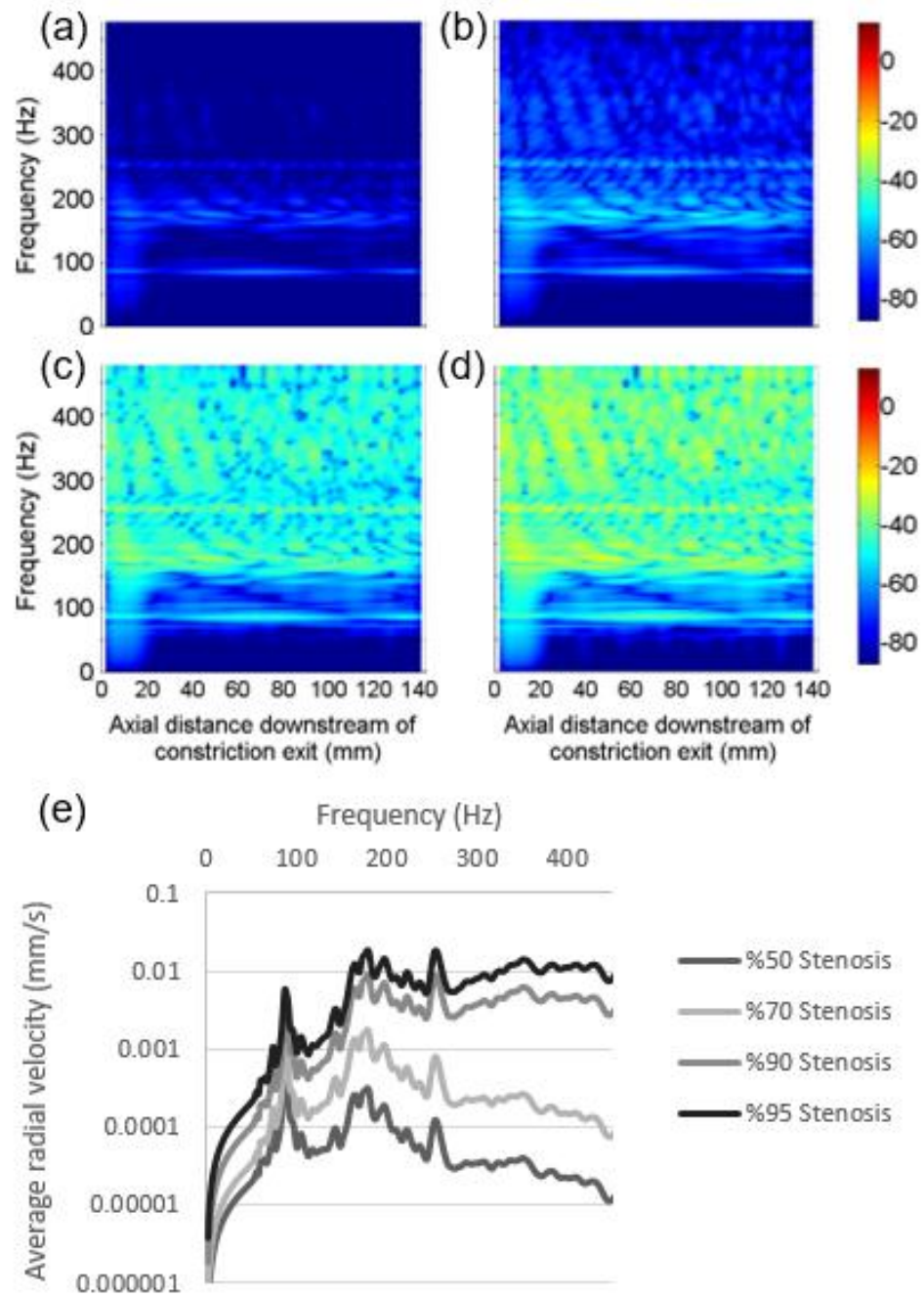


Figure 5.22 Radial velocity response (dB ref: 1 mm/s) as function of axial distance and frequency. Stenosis exit is placed at 0 mm. (a) 50% stenosis. (b) 70% stenosis. (c) 90% stenosis. (d) 95% stenosis. (e) Average of radial velocity responses for simplistic upper arm model. Response amplitudes within 0-140 mm are averaged at each frequency.

In Figure 5.22(e), when the average response amplitudes (within 0-400 Hz) are investigated, it is seen that the vibration amplitudes on the simplistic upper arm surface are proportional to $u^{2.09}$, where u is the flow jet velocity in the constricted region.

In Figure 5.23, radial velocity responses are presented for bottom, lateral side and top lines of the simplistic upper arm model. The highest amplitudes are observed on the top line, since it is the closest line to the brachial artery. Results obtained at bottom and lateral lines are significantly lower when compared to the top line. As the distance from the artery increases, the amplitudes decrease. Also, the presence of bone affects the response on the bottom line, since it partially inhibits wave propagation.

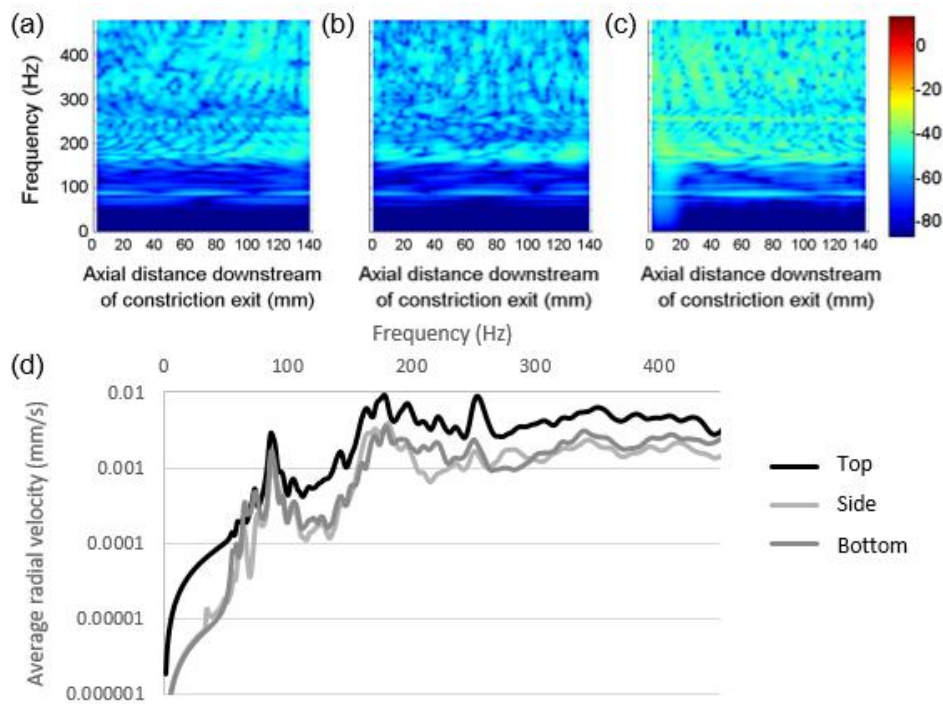


Figure 5.23 Radial velocity response (dB ref: 1 mm/s) as function of axial distance and frequency for simplistic upper arm model with 90% stenosis. Stenosis exit is placed at 0 mm. (a) Bottom line. (b) Lateral line. (c) Top line. (d) Average of radial velocity responses for simplistic upper arm model.

In Figure 5.24, phased and no phased models are compared and it is seen that the phased analysis results in smaller amplitudes especially within 75-225 Hz frequency range.

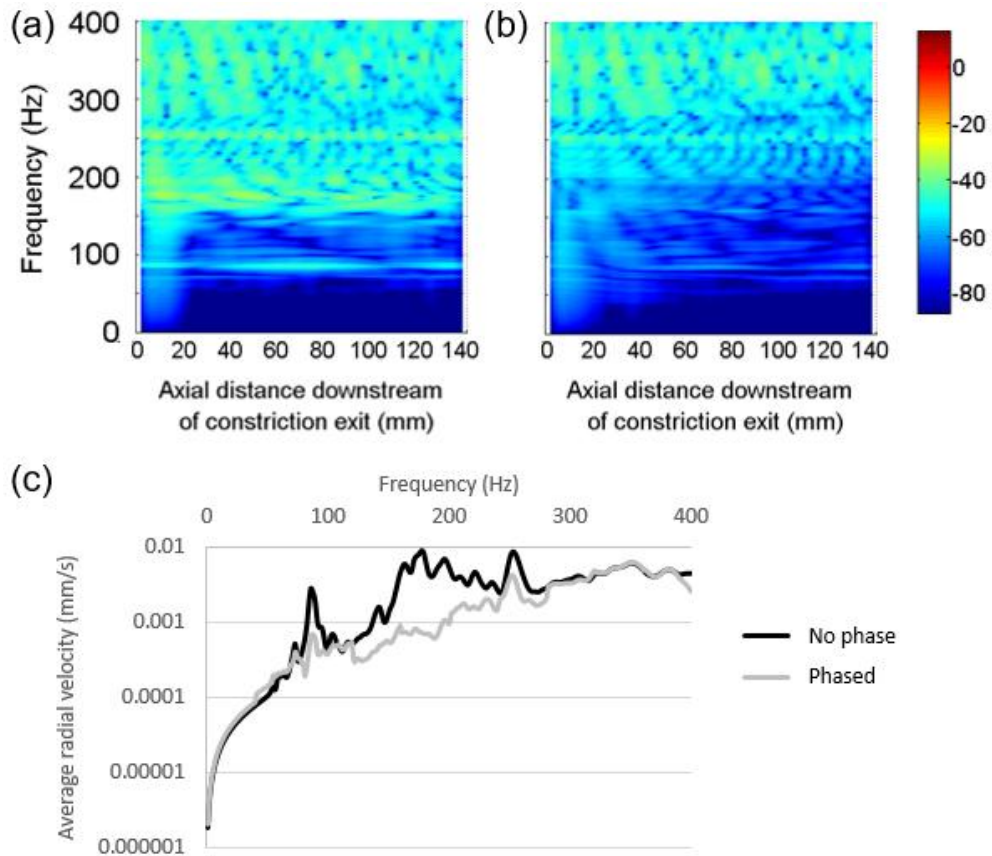


Figure 5.24 Radial velocity response (dB ref: 1 mm/s) as function of axial distance and frequency for simplistic upper arm model with 90% stenosis. Stenosis exit is placed at 0 mm. (a) No phase map. (b) 10 x 10 phase map. (c) Average of radial velocity responses for simplistic upper arm model.

In Figure 5.25, the effect of bone rigidity is investigated. In one of the analyses, the humerus bone is considered to be a rigid body, and border nodes of the bone are fixed with zero displacement instead of modelling the material properties. In the other analysis, the material properties of the bone are modelled realistically. Both

models lead to almost the same spectral behavior. There are slight variations in amplitudes for two different models, but not at the level to affect the main conclusions.

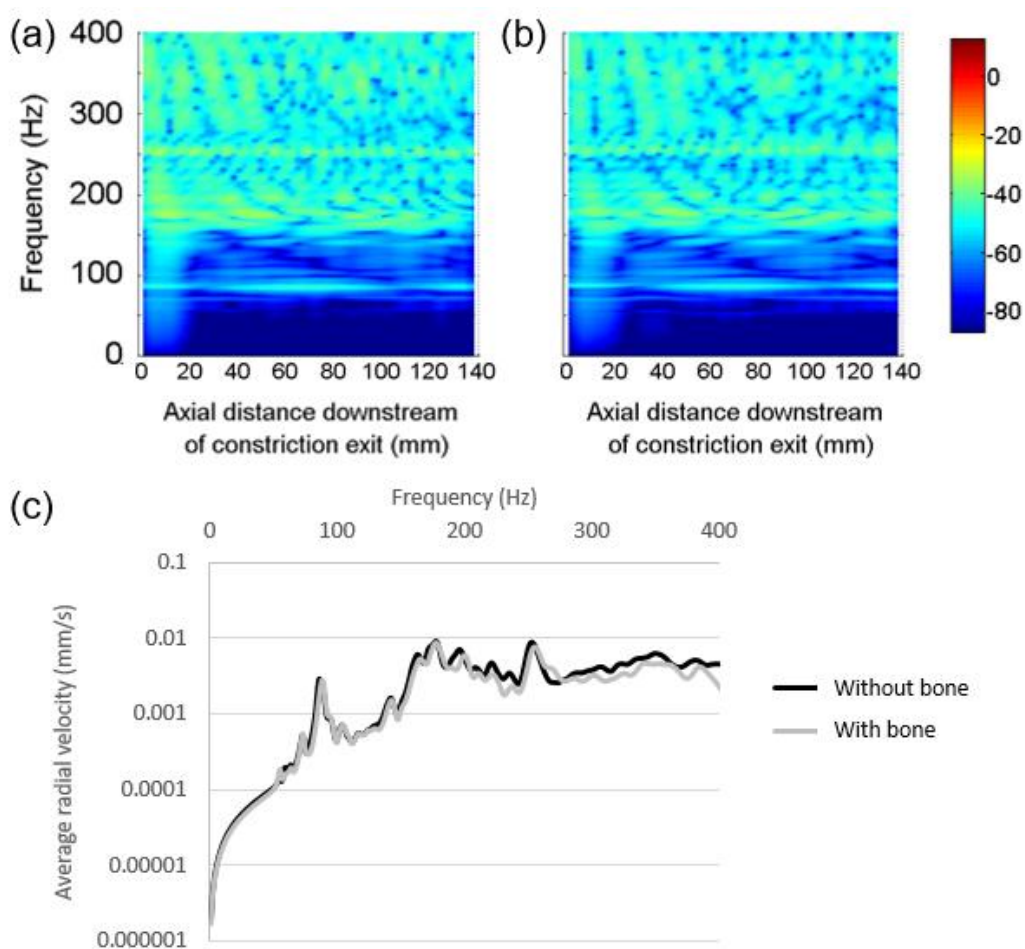


Figure 5.25 Radial velocity response (dB ref: 1 mm/s) as function of axial distance and frequency for simplistic upper arm model with 90% stenosis. (a) Without modelling bone. (b) With modelling bone. (c) Average of radial velocity responses for simplistic upper arm model.

In the computational analysis, realistic material properties are employed considering the nonlinear stress-strain relationship of soft body tissues. In addition,

linear material models of fat and skin are also investigated in the analysis. For linear models of fat and skin, the elastic modulus is used as 25 [135] and 1000 kPa [65], respectively. In Figure 5.26, the results of linear and nonlinear models are provided. It is seen that similar amplitudes are obtained for both nonlinear and linear models, but the spectral content is changed at a certain rate for the frequencies higher than 200 Hz.

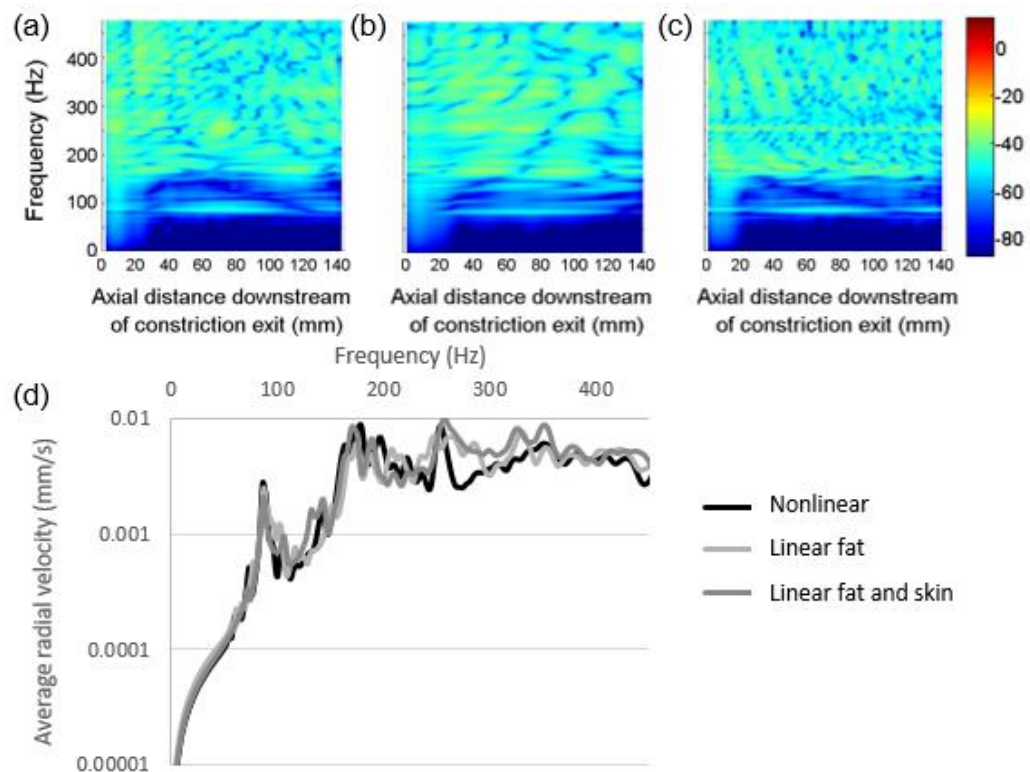


Figure 5.26 Radial velocity response (dB ref: 1 mm/s) as function of axial distance and frequency for simplistic upper arm model with 90% stenosis. Stenosis exit is placed at 0 mm. (a) Linear fat model (25 kPa). (b) Linear fat (25 kPa) and skin (1 MPa) model. (c) Nonlinear model. (d) Average of radial velocity responses for simplistic upper arm model.

In Figure 5.27, the effect of stenosis location is investigated for the simplistic upper arm model. It can be observed that the radial velocity amplitudes are higher at regions closer to the stenosis location. This effect is observed especially in the low frequency range of 0-150 Hz.

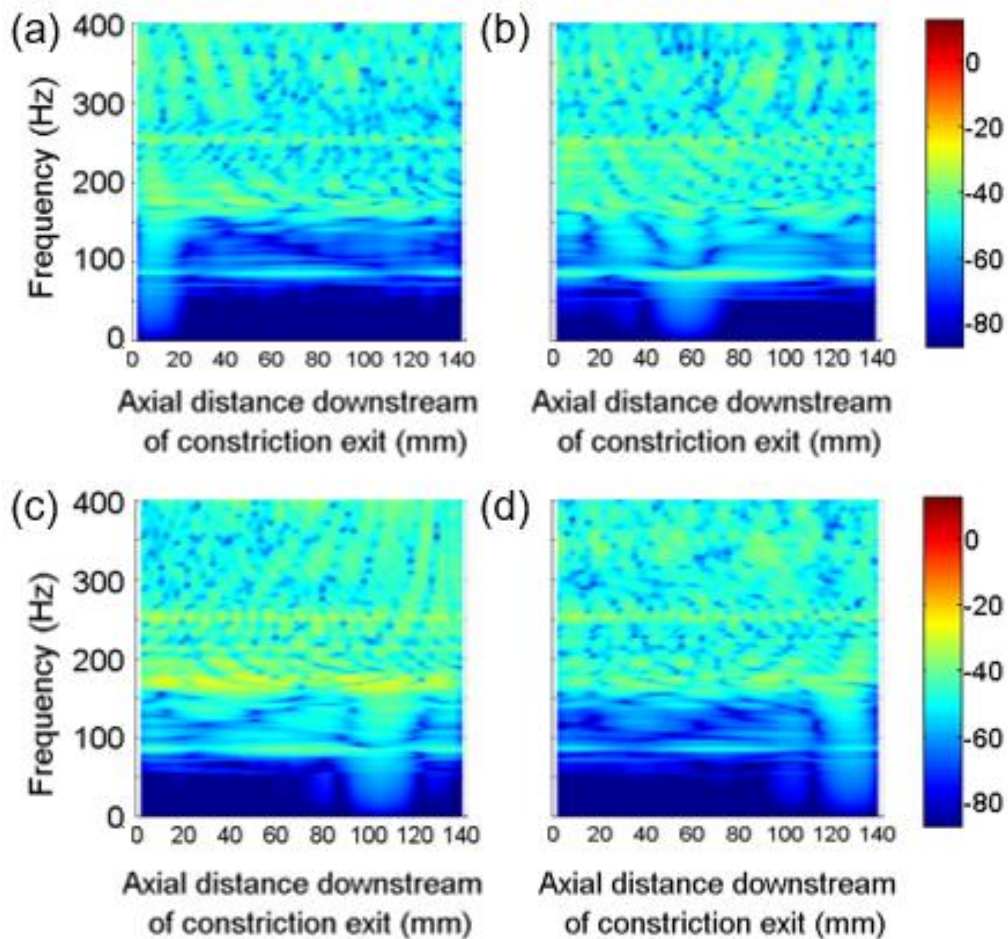


Figure 5.27 Radial velocity response (dB ref: 1 mm/s) as function of axial distance and frequency for simplistic upper arm model with 90% stenosis considering different constriction locations. (a) Stenosis exit at 0 mm. (b) Stenosis exit at 40 mm. (c) Stenosis exit at 80 mm. (d) Stenosis exit at 120 mm.

5.6.2 Pressure response on the simplistic upper arm model

In Figure 5.28, four different stenosis locations are considered as 0, 40, 80 and 120 mm. The total length of the simplistic upper arm model is 140 mm. For low frequencies between 0 and 50 Hz, the pressure responses have higher amplitudes for the regions closer to the stenosis. When the stenosis is placed at 0 mm, region-x has the highest amplitudes within 0-50 Hz, since x is region closest to 0 mm. Similarly, if the stenosis is placed at 120 mm, the highest pressure amplitudes are observed at region-z within 0-50 Hz, since it is the closest region to 120 mm. In Figure 5.29, the average pressure responses are determined by taking the mean of the responses in x, y, and z-regions. The highest pressure amplitudes on the skin are obtained at the top of the model. For frequencies higher than 150 Hz, if the level of stenosis increases from 70 to 90%, the average pressure amplitudes increase by more than 10 dB. Depending on the severity of the stenosis, the amplitude increase is more pronounced in the high frequency range.

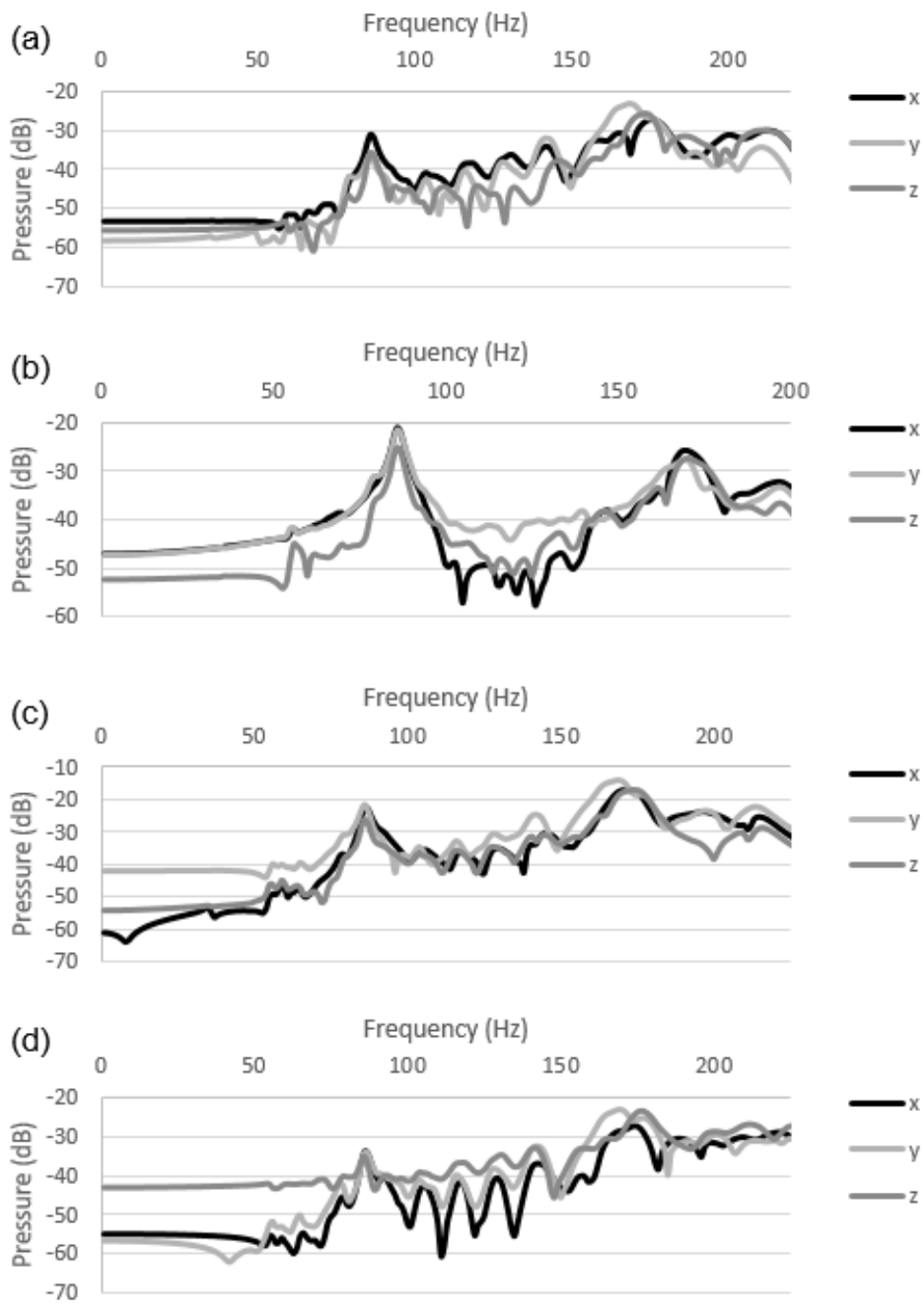


Figure 5.28 Pressure response (dB ref: 1 Pa) on the skin surface of simplistic upper arm model (x, y and z regions are represented in Figure 5.21). (a) Stenosis at 0 mm. (b) Stenosis at 40 mm. (c) Stenosis at 80 mm. (d) Stenosis at 120 mm.

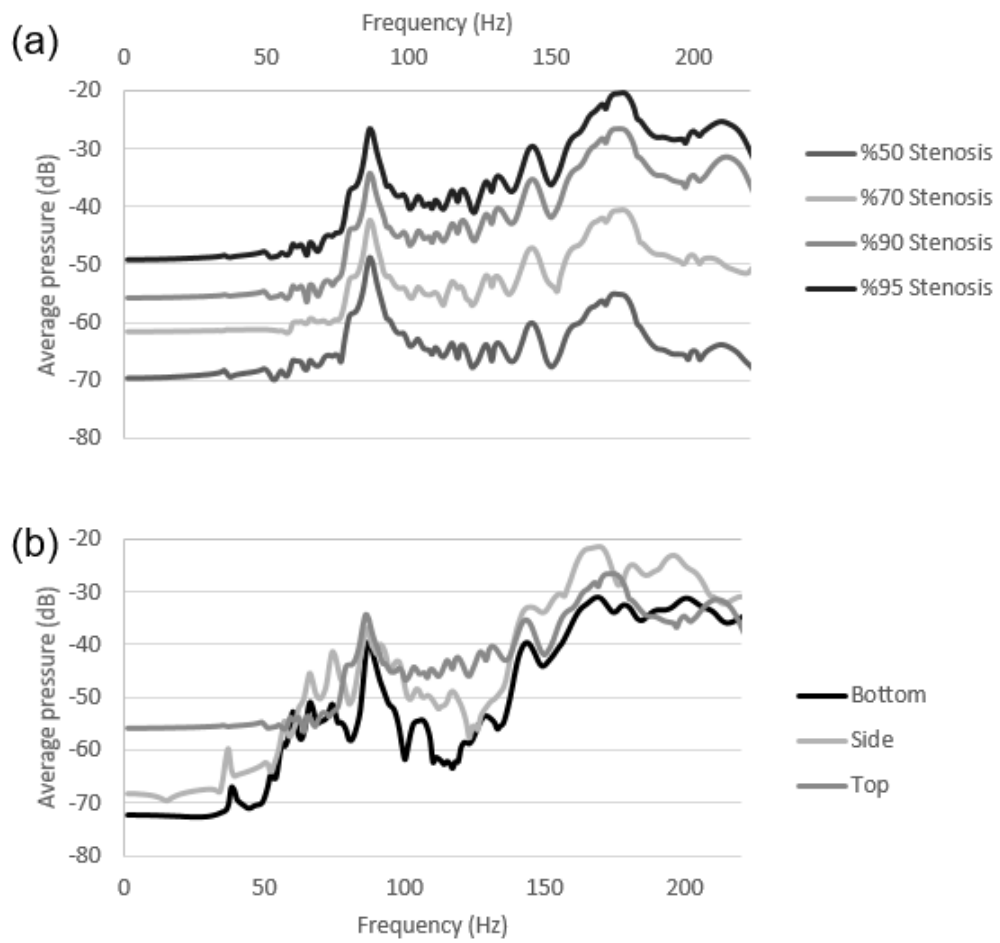


Figure 5.29 (a) Average pressure response (dB ref: 1 Pa) of simplistic upper arm model considering different stenosis levels. (b) Average pressure response of simplistic upper arm model on top, side and bottom lines. The top line is the radially closest line to the brachial artery.

5.7 Simplistic neck models

Mesh independence study is performed using three different mesh densities. The details and total number of elements of the meshes are provided in Table 5.5. In Figure 5.30, the radial velocity responses are presented for a sample case with 90% stenosis. Between Mesh 1 and Mesh 2, there is an average amplitude (within 0-70 mm, 0-350 Hz) difference of 16.2%. Between Mesh 2 and Mesh 3, there is an average amplitude difference of 1.2%. Mesh 2 is used for further analysis since the average amplitude difference between Mesh 2 and Mesh 3 is less than 3%.

Table 5.5 Mesh details for simplistic neck model

# of Elements	Mesh 1	Mesh 2	Mesh 3
Blood	7515	7515	7515
Air	4568	4568	4568
Trachea	1312	1312	1312
Skin	2479	4559	7450
Fat	2782	9515	12763
Common Carotid Artery	2542	2542	2542
Muscle	35511	54564	76159
Total	56709	84575	112309

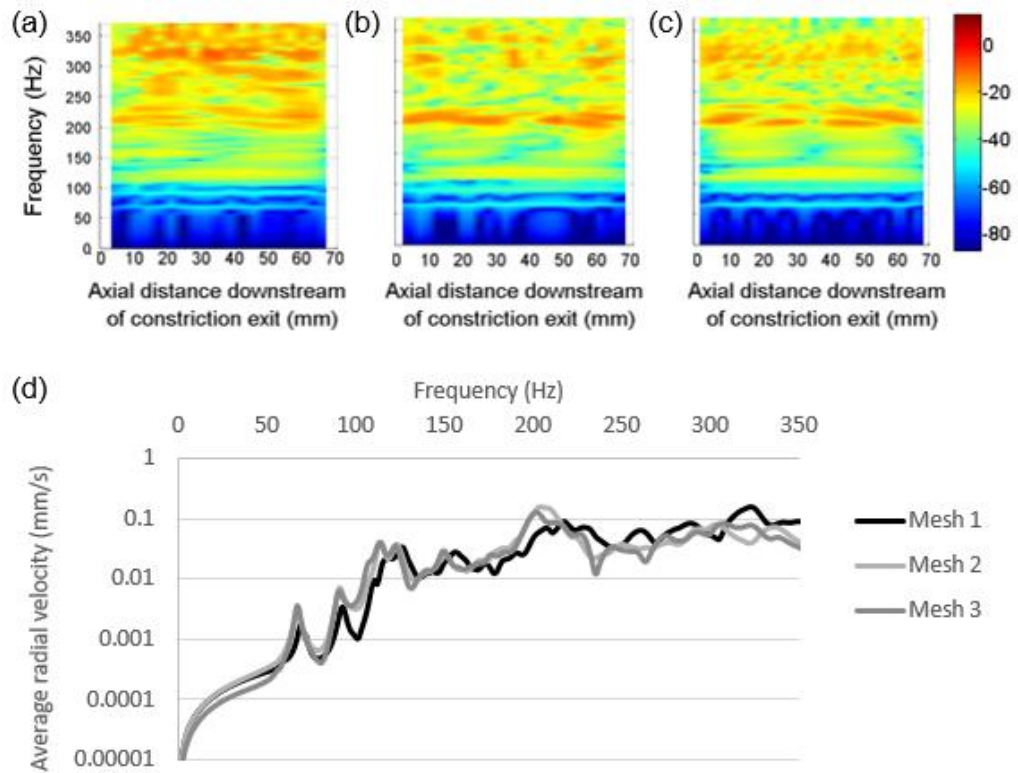


Figure 5.30 Radial velocity response (dB ref: 1 mm/s) as function of axial distance and frequency for simplistic neck model with 90% stenosis. Stenosis exit is placed at 0 mm. (a) Mesh 1. (b) Mesh 2. (c) Mesh 3. (d) Average of radial velocity responses for simplistic neck model. Response amplitudes within 0-70 mm are averaged at each frequency.

As shown by the red lines in Figure 5.31(a), radial velocity responses are investigated on the front line of the neck, the closest line to the common carotid artery, and the back line of the neck. Pressure responses are obtained at two fixed regions (x and y) as shown in Figure 5.31(b).

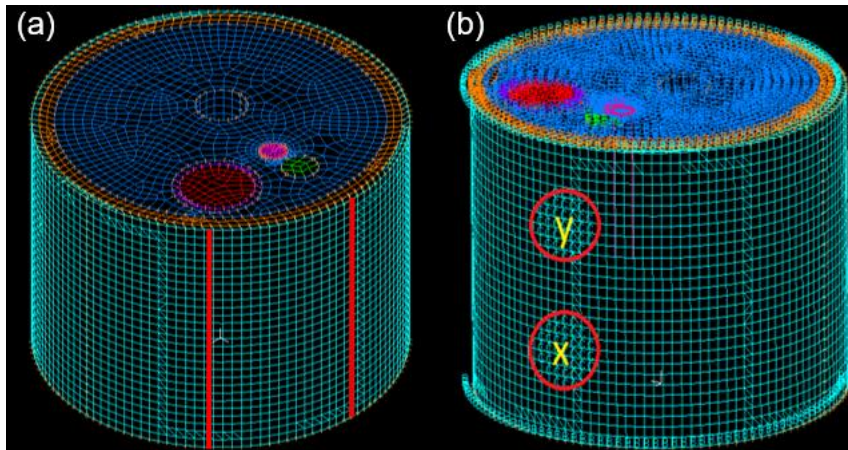


Figure 5.31 (a) Simplistic neck model – (Red lines depict the nodes on the front of trachea and the closest line to the artery in radial direction). (b) Fixed regions used to measure the pressure on skin of the simplistic neck model.

5.7.1 Radial velocity response on the simplistic neck model

In Figure 5.32, radial velocity responses are presented considering different stenosis locations. By confirming the previous findings, the low frequency response within 0-100 Hz indicates the location of stenosis with relatively higher amplitudes.

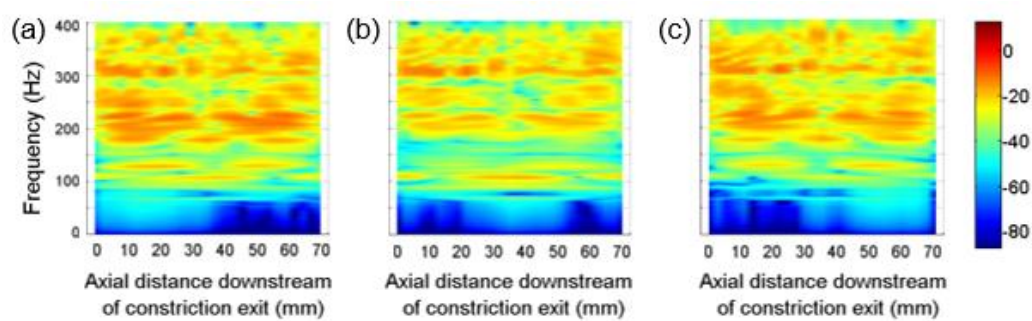


Figure 5.32 Radial velocity response (dB ref: 1 mm/s) as function of axial distance and frequency for simplistic neck model considering 90% stenosis with no phase map. (a) Stenosis at 0 mm. (b) Stenosis at 30 mm. (c) Stenosis at 55 mm.

The effect of stenosis severity is shown in Figure 5.33. The relative increase in response amplitudes due to the stenosis severity is clearly evident at frequencies higher than 200 Hz. In Figure 5.33(e), if the average response amplitudes (within 0-400 Hz) are investigated, it is observed that the vibration amplitudes on the simplistic neck model are proportional to $u^{1.9}$, where u is the flow jet velocity in the constricted region. These proportionality constants are previously found as 2.19 and 2.09 for the simplistic thigh and simplistic upper arm models, respectively.

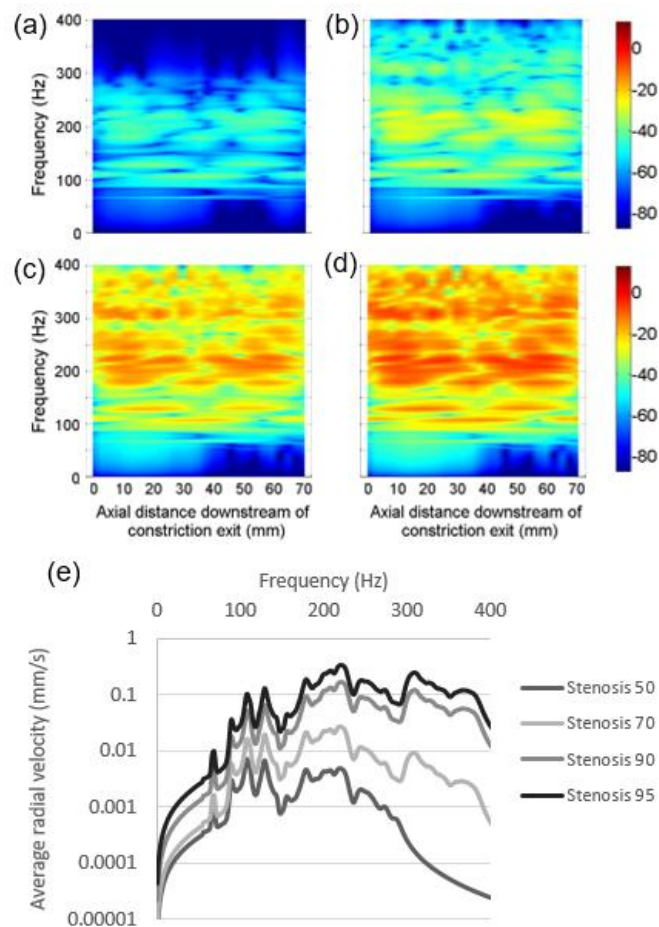


Figure 5.33 Radial velocity response (dB ref: 1 mm/s) as function of axial distance and frequency for simplistic neck model. Stenosis exit is placed at 0 mm. (a) 50% stenosis. (b) 70% stenosis. (c) 90% stenosis. (d) 95% stenosis. (e) Average of radial velocity responses for simplistic neck model. Response amplitudes within 0-70 mm are averaged at each frequency.

In Figure 5.34, the radial velocity responses are compared for phased and no phased analyses for the simplistic neck model. It is seen that the phased case results in lower radial velocity amplitudes within 200-400 Hz, while maintaining a similar spectral content.

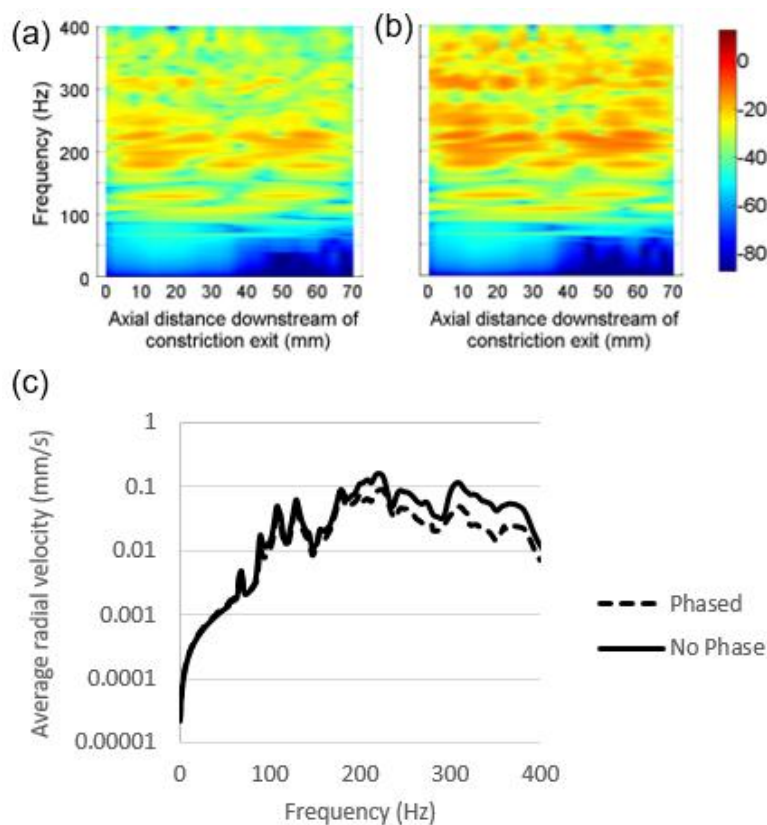


Figure 5.34 Radial velocity response (dB ref: 1 mm/s) as function of axial distance and frequency for simplistic neck model. Stenosis exit is placed at 0 mm. (a) 10 x 10 phase map. (b) No phase map. (c) Average of radial velocity responses for simplistic neck model. Response amplitudes within 0-70 mm are averaged at each frequency.

A large vein is present near the common carotid artery. This large vein is considered in the simplistic neck model due to the mass of blood in it. The effect of the large vein is investigated in Figure 5.35. It is observed that, when the large vein is

included in the analysis, the radial velocity amplitudes slightly decrease. In this section, all neck models contain the large vein unless otherwise stated.

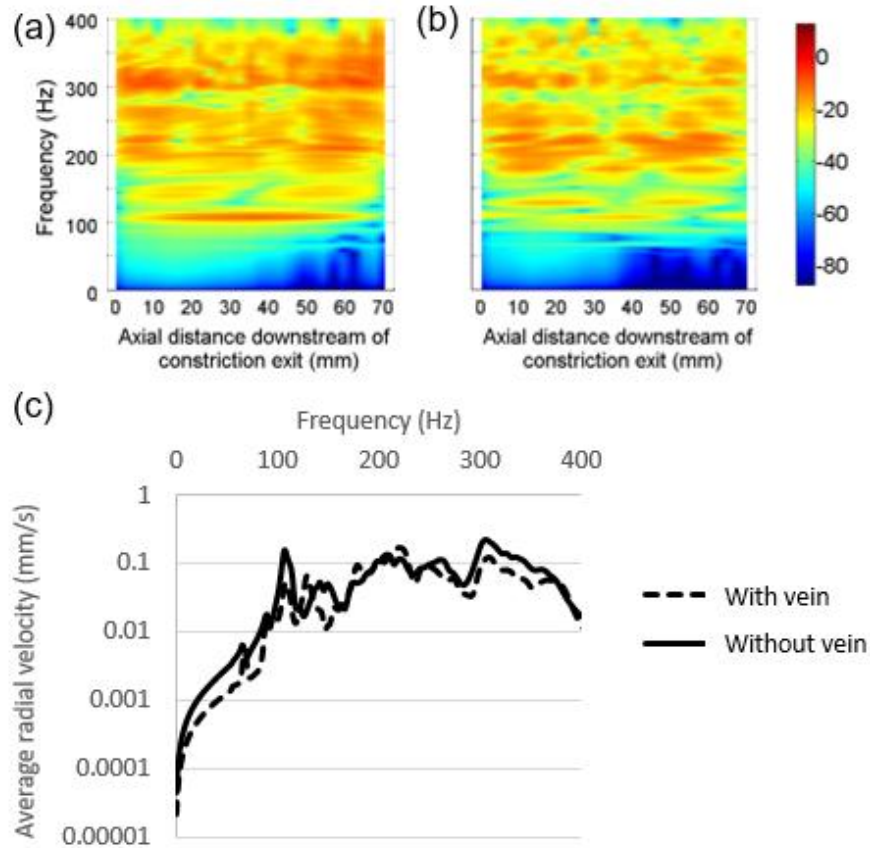


Figure 5.35 Radial velocity response (dB ref: 1 mm/s) as function of axial distance and frequency for simplistic neck model. Stenosis exit is placed at 0 mm. (a) Without modelling the vein. (b) With modelling the vein. (c) Average of radial velocity responses for simplistic neck model. Response amplitudes within 0-70 mm are averaged at each frequency.

In Figure 5.36, the radial velocity responses are compared at different regions of the simplistic neck model. Highest excitation is observed at the closest line to the common carotid artery, and the responses at the front and the back of the neck are

relatively much lower when compared to the closest line. The amplitudes on the closest line are about 5 times higher than the front and the back line of the neck.

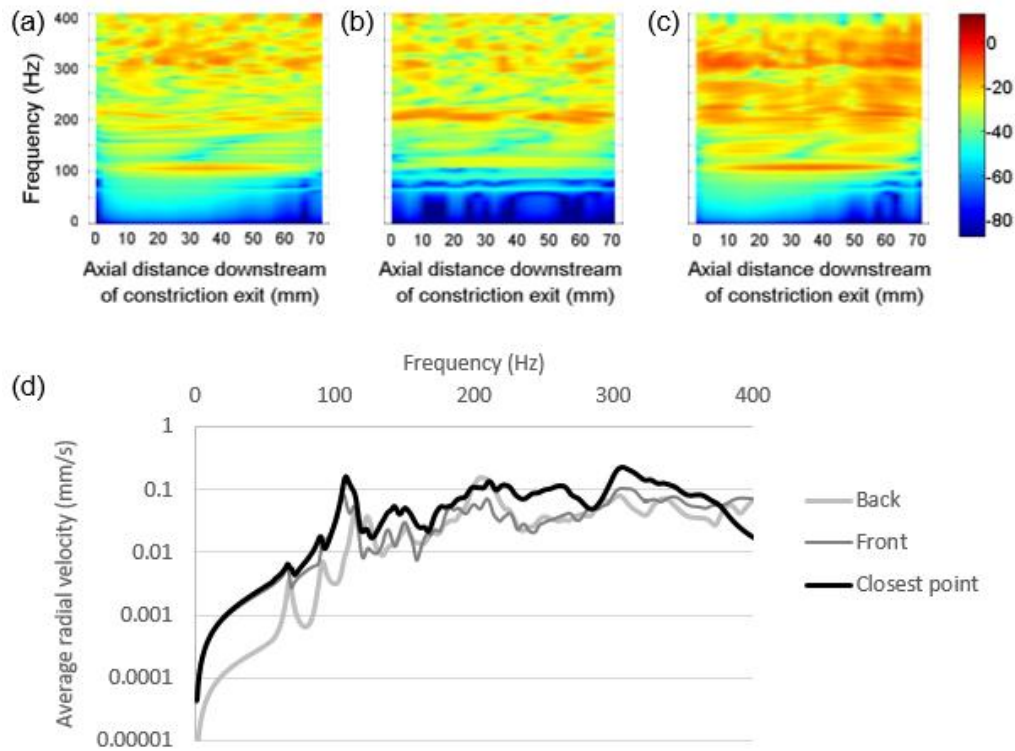


Figure 5.36 Radial velocity response (dB ref: 1 mm/s) as function of axial distance and frequency for simplistic neck model. Stenosis exit is placed at 0 mm. (a) Front line on the neck. (b) Back line on the neck. (c) Closest line to the artery in radial direction. (d) Average of radial velocity responses for simplistic neck model. Response amplitudes within 0-70 mm are averaged at each frequency.

5.7.2 Pressure response on the simplistic neck model

In Figure 5.37, three different stenosis locations are considered as 0, 30 and 55 mm. The total length of the simplistic neck model is 70 mm. If the stenosis is placed at 0 mm, region-x has the highest amplitudes within 0-50 Hz, since this region is closest to 0 mm. Similarly, when the stenosis is placed at 55 mm, the highest pressure amplitudes are observed at region-y within 0-50 Hz, since it is the closest region to 55 mm. This fact is supporting that the low frequency pressure response indicates the location of the stenosis. In Figure 5.38, the average pressure responses are determined by taking the mean of the responses in x and y-regions. The highest pressure amplitudes on the skin are obtained at the closest line to the common carotid artery. For the stenosis severities higher than 90%, average pressure amplitude exceeds 0 dB due to the flow rate in the common carotid artery which is quite high when compared to the upper arm and thigh models.

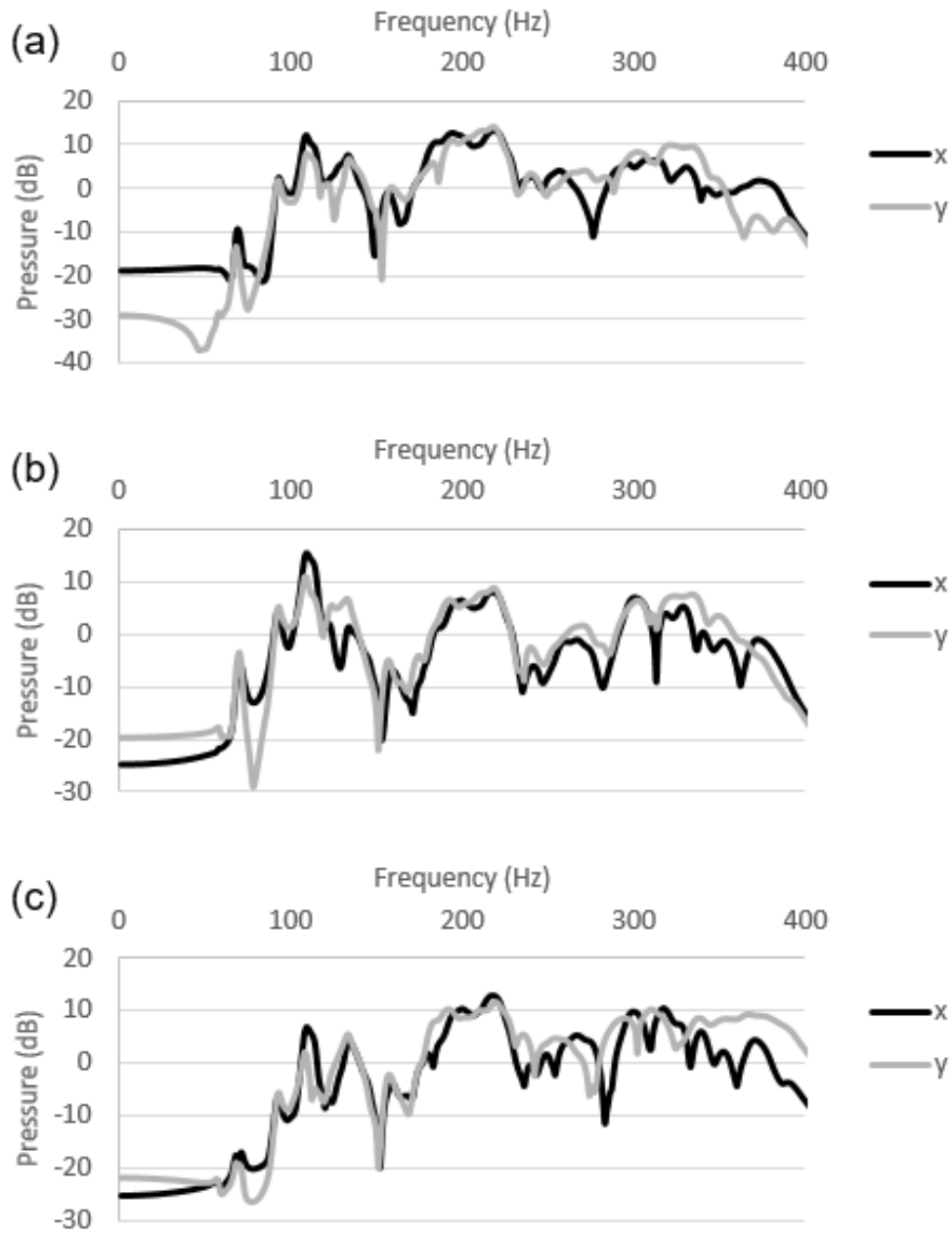


Figure 5.37 Pressure response (dB ref: 1 Pa) on the skin of simplistic neck model (x and y regions are represented in Figure 5.31). (a) Stenosis at 0 mm. (b) Stenosis at 30 mm. (c) Stenosis at 55 mm.

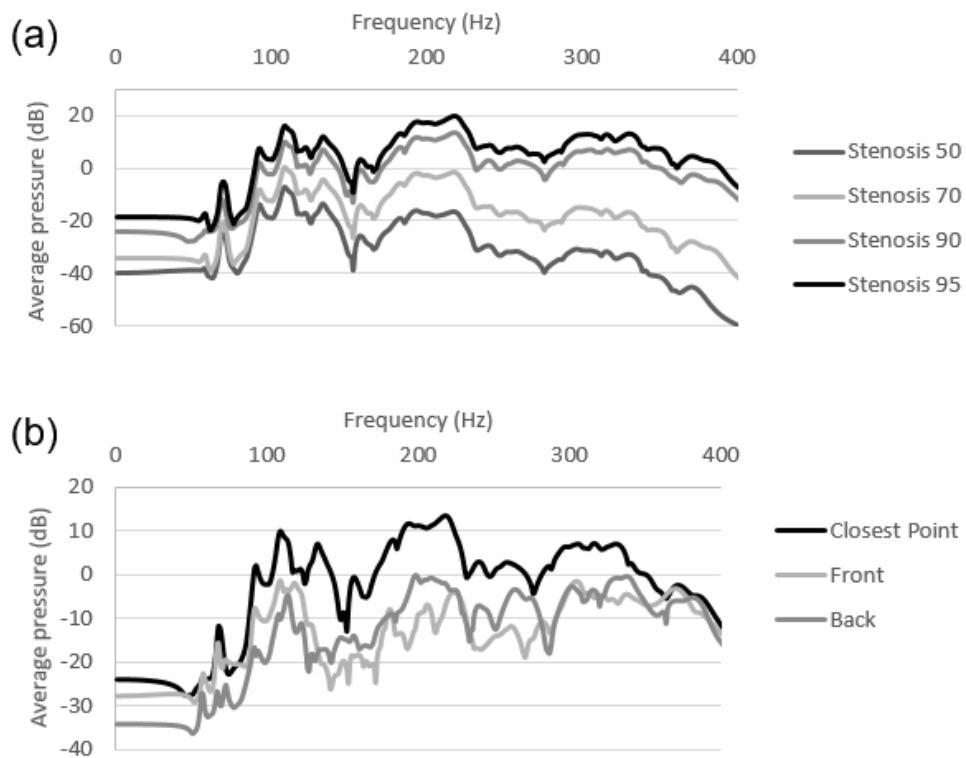


Figure 5.38 (a) Average pressure response (dB ref: 1 Pa) of simplistic neck model considering different stenosis levels. (b) Average pressure responses of simplistic neck model on the front of the neck, the back of the neck and the closest line to the artery in the radial direction.

5.8 CT based models

For CT based models, patient-specific data is utilized. Consequently, there are slight differences in size compared to the simplistic models. The maximum and minimum diameters in the simplistic thigh model are 160 and 120 mm, respectively. However, these values are approximately 172 and 125 mm for the CT based thigh model. The total length of the simplistic thigh model is 250 mm, but the total length of the CT based thigh model is 223 mm. The total length of the CT based upper arm model is 150 mm, while the simplistic upper arm model has a total length of 140 mm. Due to the complexity of the CT data, some simplifications are

done for the CT based neck model. The cervical vertebrae bones in the neck are considered to have a uniform cross-section and also the thicknesses of skin and fat are assumed to be uniform. There is a certain difference in the geometric dimensions of CT based and simplistic models, but this difference is not higher than 10%.

For each model, three different mesh densities are used to achieve mesh independent results. The details of the meshes are provided in Table 5.6, Table 5.7, and Table 5.8 for CT based thigh, upper arm, and neck models, respectively. In Figure 5.39, the radial velocity responses are presented for a sample case with 90% stenosis. Between Mesh 1 and Mesh 2, there are average amplitude differences of 53.66% (within 0-223 mm, 0-140 Hz), 13.71% (within 0-150 mm, 0-300 Hz) and 17.84% (within 0-60 mm, 0-350 Hz) for CT based thigh, CT based upper arm and CT based neck models, respectively. Between Mesh 2 and Mesh 3, there are average amplitude differences of 1.29%, 1.12% and 2.81% for CT based thigh, CT based upper arm and CT based neck models, respectively. Mesh 2 with the moderate mesh density is used for the further analysis of CT based models since the average amplitude differences between Mesh 2 and Mesh 3 are less than 3%.

Table 5.6 Mesh details for CT based thigh model

# of Elements	Mesh 1	Mesh 2	Mesh 3
Skin	6609	10106	14533
Fat	18386	24992	36488
Blood	537	537	537
Femoral Artery	336	336	336
Muscle	39659	55244	88885
Total	65527	91215	140779

Table 5.7 Mesh details for CT based upper arm model

# of Elements	Mesh 1	Mesh 2	Mesh 3
Skin	3103	4116	6134
Fat	3778	8278	16658
Blood	10186	10186	10186
Brachial Artery	2899	2899	2899
Muscle	31626	46122	66504
Trabecular Bone	39	335	789
Cortical Bone	447	1493	2686
Total	52078	73429	105856

Table 5.8 Mesh details for CT based neck model

# of Elements	Mesh 1	Mesh 2	Mesh 3
Blood	7562	7562	7562
Air	497	2717	7051
Trachea	552	923	1948
Skin	1210	3289	6378
Fat	1386	8531	13976
Common Carotid Artery	2272	2272	2272
Muscle	19246	35744	64128
Bone	1357	5257	11158
Total	34052	66295	114567

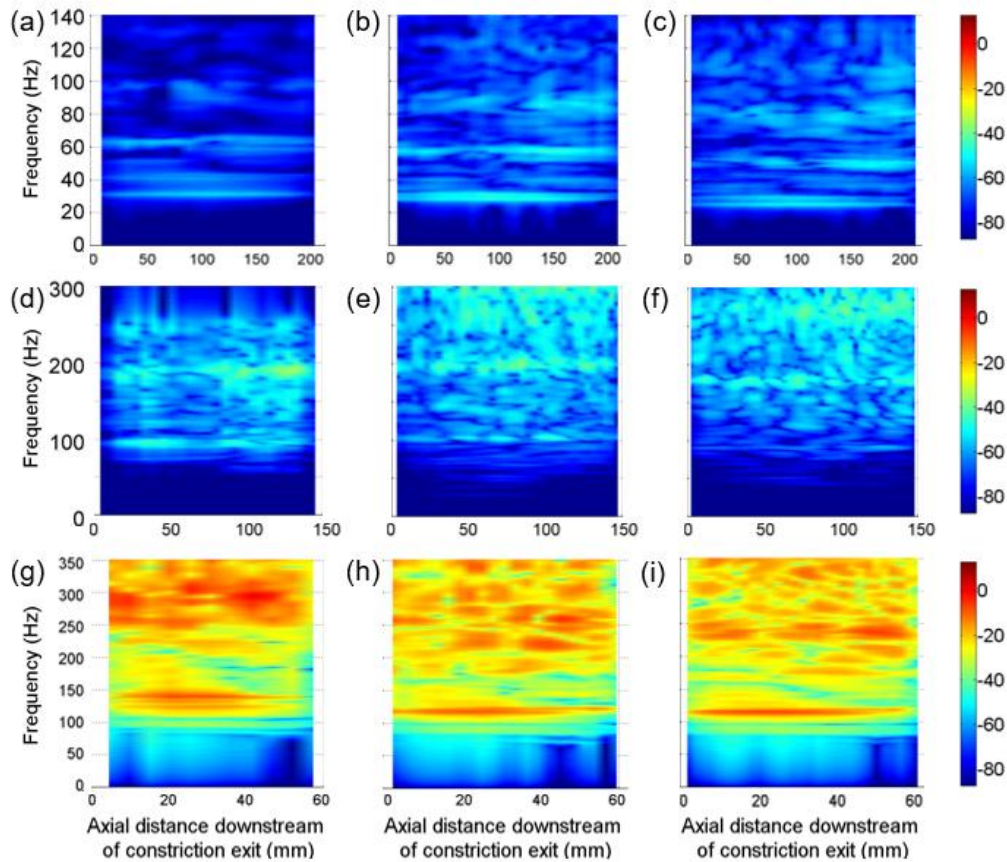


Figure 5.39 Radial velocity response (dB ref: 1 mm/s) as function of axial distance and frequency for CT based models with 90% stenosis considering 2% modal damping. Stenosis exit is placed at 0 mm. (a) Thigh, Mesh 1. (b) Thigh, Mesh 2. (c) Thigh, Mesh 3. (d) Upper arm, Mesh 1. (e) Upper arm, Mesh 2. (f) Upper arm, Mesh 3. (g) Neck, Mesh 1. (h) Neck, Mesh 2. (i) Neck, Mesh 3.

In Figure 5.40, the radial velocity responses are given for CT based thigh, upper arm and neck models to see the effect of stenosis severity. Up to here, 2% modal damping is employed for the simplistic models considering the light damping conditions. For the CT based models, modal damping coefficients of 2, 10 and 20% are employed separately. In the forthcoming section, the effect of damping is investigated in detail.

For CT based thigh, upper arm and neck models, average response amplitudes are investigated within 0-140 Hz, 0-300 Hz and 0-400 Hz, respectively. It is observed that the vibration amplitudes on the CT based thigh, upper arm and neck models are proportional to $u^{2.52}$, $u^{1.92}$ and $u^{2.02}$, respectively, where u is the flow jet velocity in the constricted region. These proportionality constants are previously found as 2.19, 2.09 and 1.9 for the simplistic thigh, upper arm and neck models, respectively. The proportionality constants for u are in good agreement for simplistic and CT based models. The highest proportionality constants are obtained for the thigh models due to thicker fat and muscle layers. Thicker soft tissue layers increase the number of resonant peaks within the interested frequency range.

Geometries of CT based models are quite complex compared to the simplistic models. Therefore, there is a slight difference in the amplitudes of the simplistic and CT based models. Anti-resonance curves are not visible on the response maps of CT based models, therefore an alternative approach is employed to gain information about the stenosis location. For each position downstream of the constriction exit, all the amplitudes within the interested frequency range are summed and a 2D plot is obtained for each radial velocity response contour plot. The sum of amplitudes displayed against the axial position is presented in Figure 5.41 considering the simplistic and CT based upper arm models. It is seen that, these amplitude summations have a maximum value around the stenosis location for both simplistic and CT based upper arm models, and this approach can be utilized to determine the stenosis location in both simplistic and CT based models. Stenosis locations are more clearly distinguished for the simplistic models compared to the CT based models due to less complexity of the geometry.

In Figure 5.41, local peaks in the plots are not the main focus and the highest summation values are the main interest. The local peaks may arise depending on the natural frequencies and mode shapes of the model. The highest peak of the summation is obtained at about 20 mm downstream of the stenosis exit for the simplistic models. For the simplistic cases, the highest peak of the plot is clearly

observed. However, for the CT based models, the highest peak is not as clear as in the simplistic models. For the CT based models, there is another peak close to 0 mm due to the zero-displacement boundary condition applied at the two sides the model considering the joint ends. Therefore, the peaks around 0 mm may not be due to the stenosis for the CT based models and they may depend on the applied boundary conditions. Even if the peak due to the boundary condition is included, the highest peak summation value is again obtained around the stenosis location for the CT based models as presented in Figure 5.41(b), (d), (f) and (h).

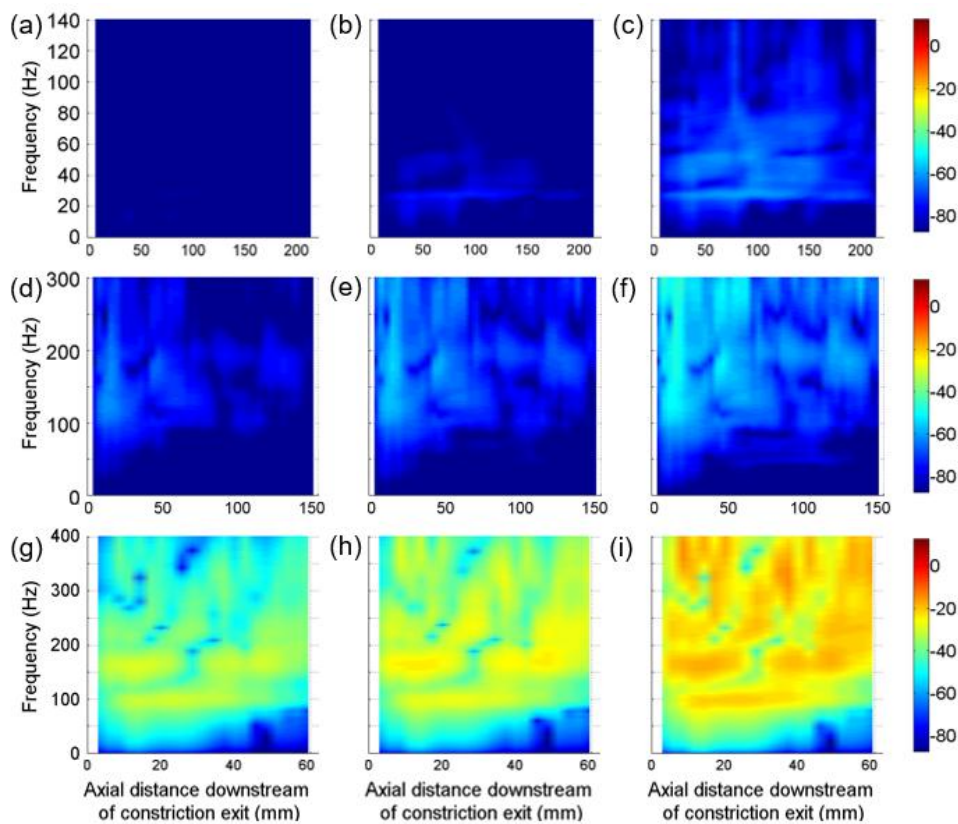


Figure 5.40 Radial velocity response (dB ref: 1 mm/s) as function of axial distance and frequency for CT based models considering 10% modal damping. Stenosis exit is placed at 0 mm. (a) Thigh, 70% stenosis. (b) Thigh, 80% stenosis. (c) Thigh, 90% stenosis. (d) Upper arm, 70% stenosis. (e) Upper arm, 80% stenosis. (f) Upper arm, 90% stenosis. (g) Neck, 70% stenosis. (h) Neck, 80% stenosis. (i) Neck, 90% stenosis.

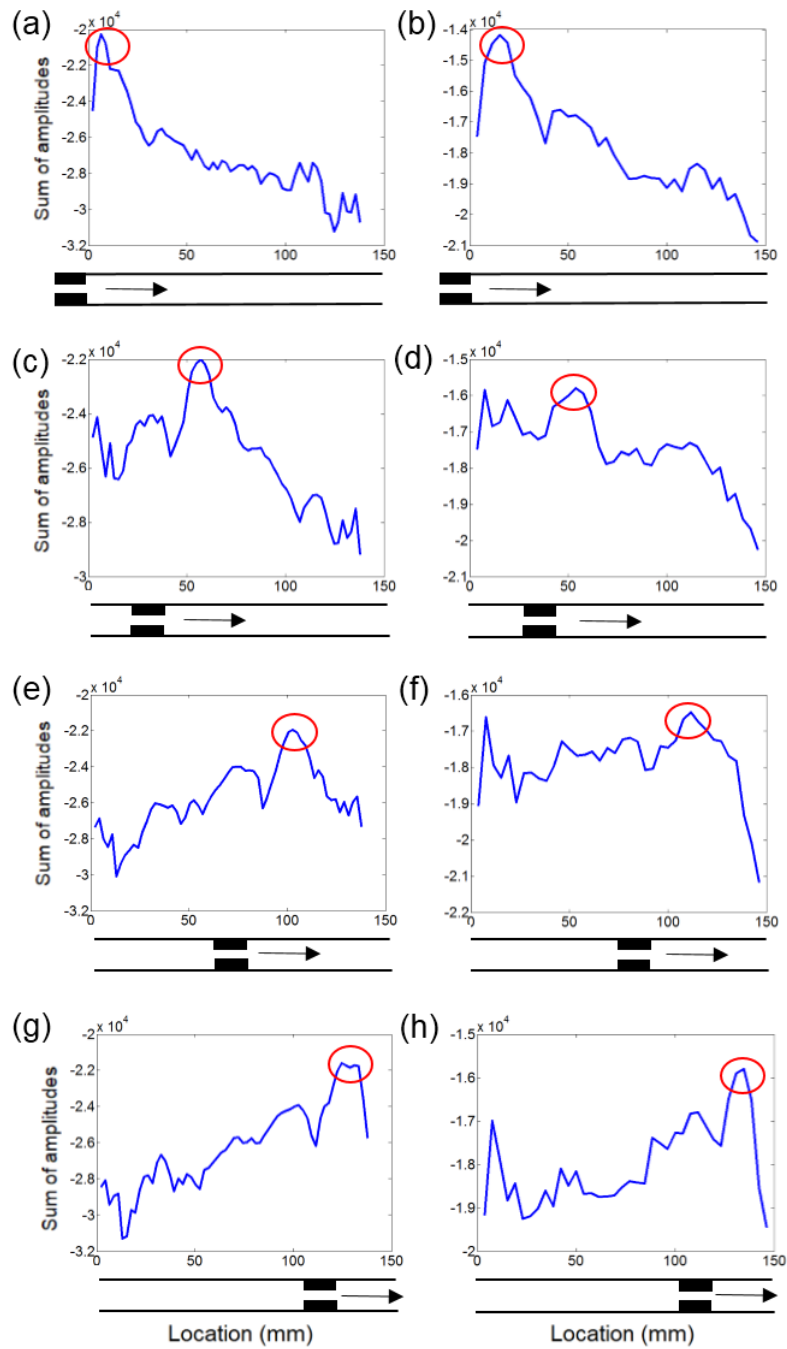


Figure 5.41 Sum of response amplitudes for upper arm models considering 90% stenosis and 10% modal damping. The highest summation amplitudes are shown in circles which are indicating the stenosis location. (a) Simplistic, 0 mm. (b) CT based, 0 mm. (c) Simplistic, 40 mm. (d) CT based, 47 mm. (e) Simplistic, 80 mm. (f) CT based, 93 mm. (g) Simplistic, 120 mm. (h) CT based, 117 mm.

In Figure 5.42, Figure 5.43, and Figure 5.44, the effect of stenosis location is investigated in CT based thigh, upper arm and neck models, respectively. In contrary to the results of the simplistic models, low frequency responses of the CT based models provide limited information about the location of the stenosis. The contour plots of the radial velocity responses are complex and the anti-resonance curves are not visible for the CT based models, since the geometric features are more complex. In CT based thigh models, the response amplitudes are relatively high around the stenosis in the 0-30 Hz frequency range. However, the relative increase is not as clear as the simplistic models. For the CT based thigh model, amplitudes tend to increase at frequencies of 30, 60, and 90 Hz, which represent the natural frequencies. In the CT based upper arm model, the natural frequencies are observed around 100 and 200 Hz. The natural frequencies of the CT based neck model are around 120, 190 and 260 Hz.

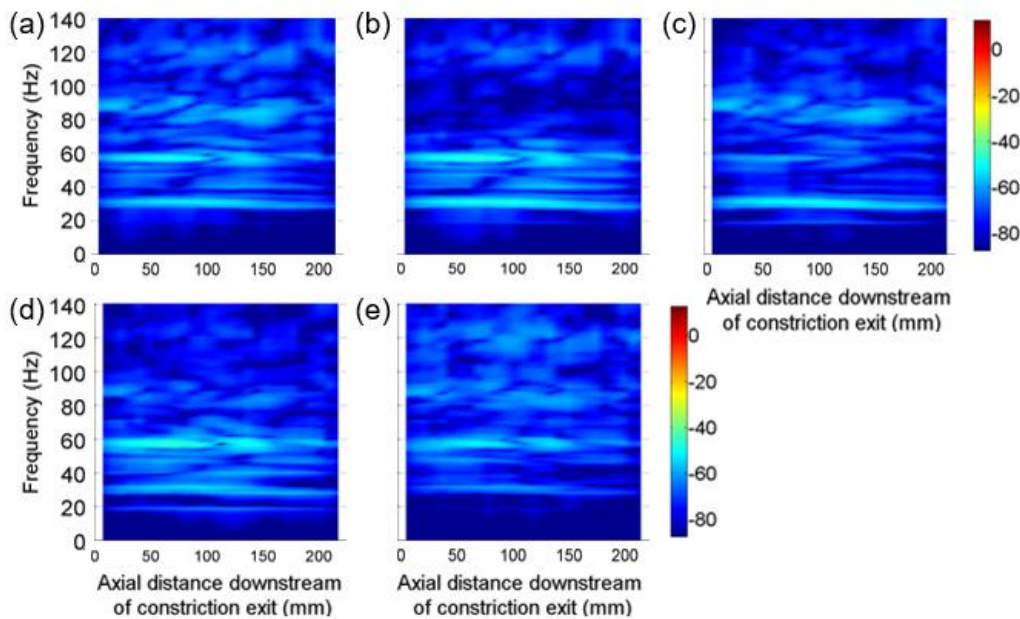


Figure 5.42 Radial velocity response (dB ref: 1 mm/s) as function of axial distance and frequency for CT based thigh model considering 90% stenosis and 2% modal damping. (a) Stenosis at 0 mm. (b) Stenosis at 50 mm. (c) Stenosis at 100 mm. (d) Stenosis at 150 mm. (e) Stenosis at 200 mm.

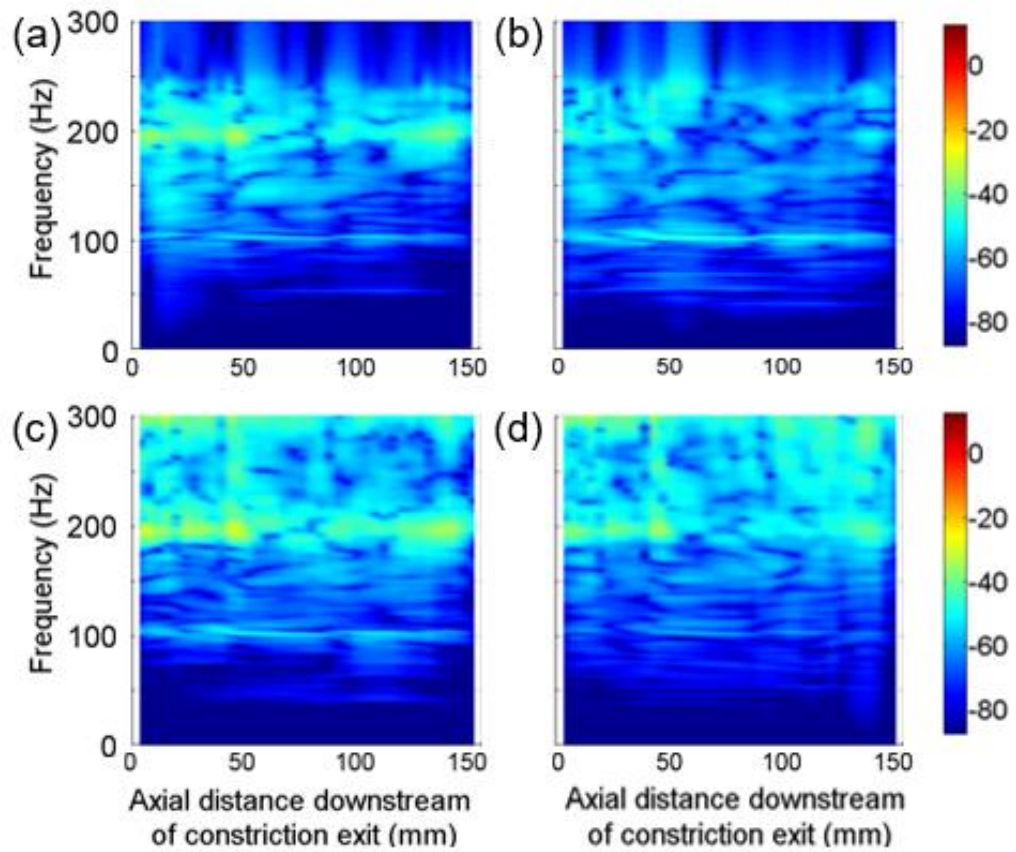


Figure 5.43 Radial velocity response (dB ref: 1 mm/s) as function of axial distance and frequency for CT based upper arm model considering 90% stenosis and 2% modal damping. (a) Stenosis at 0 mm. (b) Stenosis at 47 mm. (c) Stenosis at 93 mm. (d) Stenosis at 117 mm.

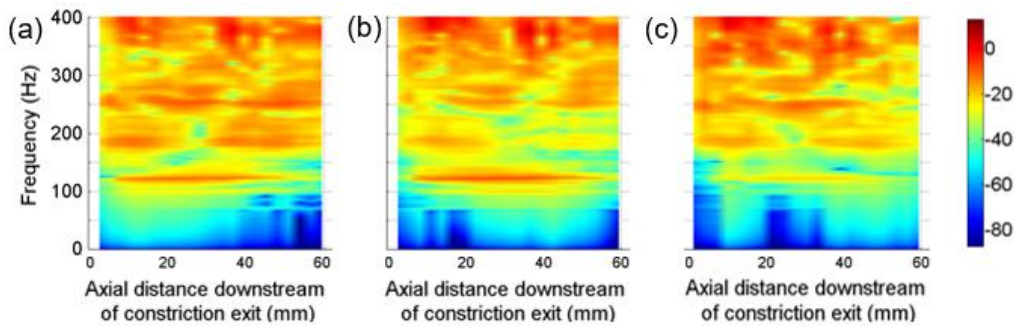


Figure 5.44 Radial velocity response (dB ref: 1 mm/s) as function of axial distance and frequency for CT based neck model considering 90% stenosis and 2% modal damping. (a) Stenosis at 0 mm. (b) Stenosis at 24 mm. (c) Stenosis at 48 mm.

In Figure 5.45, the average pressure responses on the skin are compared for CT based and simplistic models. The results of the thigh models are in good agreement for CT based and simplistic cases. There is a certain difference in the results of the upper arm models. Since upper arm CT data is clinically obtained in the hands up position, a small portion of the shoulder muscles is also included in the CT data of the upper arm. This variation in the geometric features can cause the amplitude difference between the simplistic and CT based upper arm models. At the frequencies other than 100 and 200 Hz, the average pressure amplitudes on the neck models are also in good agreement.

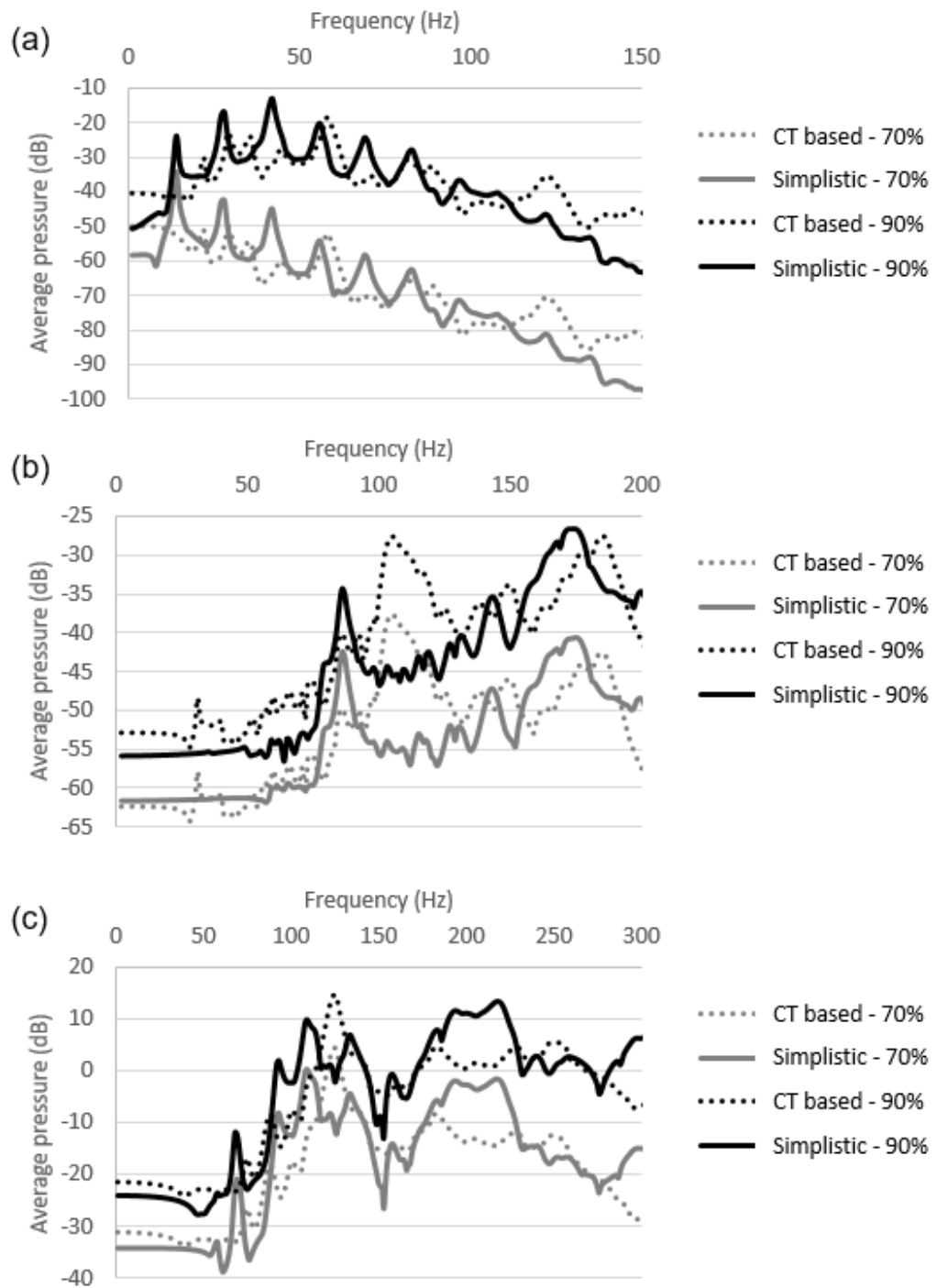


Figure 5.45 Average pressure response (dB ref: 1 Pa) comparison for simplistic and CT based models considering 2% modal damping. Stenosis exit is placed at 0 mm. (a) Thigh model. (b) Upper arm model. (c) Neck model.

5.9 Effect of modal damping coefficient

In Figure 5.46, Figure 5.47, Figure 5.48, Figure 5.49 and Figure 5.50, the effect of modal damping is investigated on the radial velocity contour plots of simplistic thigh, simplistic upper arm, CT based thigh, CT based upper arm, and CT based neck models, considering various stenosis locations. It is observed that by increasing the modal damping coefficient in the model, all radial velocity contour plots seemed more dispersed and the amplitudes of the responses slightly decreased, but the location of stenosis is more clearly observed. Increased modal damping makes it easier to detect the location of the stenosis since the stenosed regions have relatively higher radial velocity amplitudes.

The amplitude decrease due to the modal damping is more pronounced for the positions distant from the stenosis. The vibrational modes are not clearly visible for high damping conditions. However, detection of the stenosis is more practical by using the sum of the amplitudes within the interested frequency range. If the damping in the model is low, anti-resonance curves should be employed to detect the stenosis location. As the damping increases, it is logical to use the alternative approach which employs the sum of the amplitudes in the response contours.

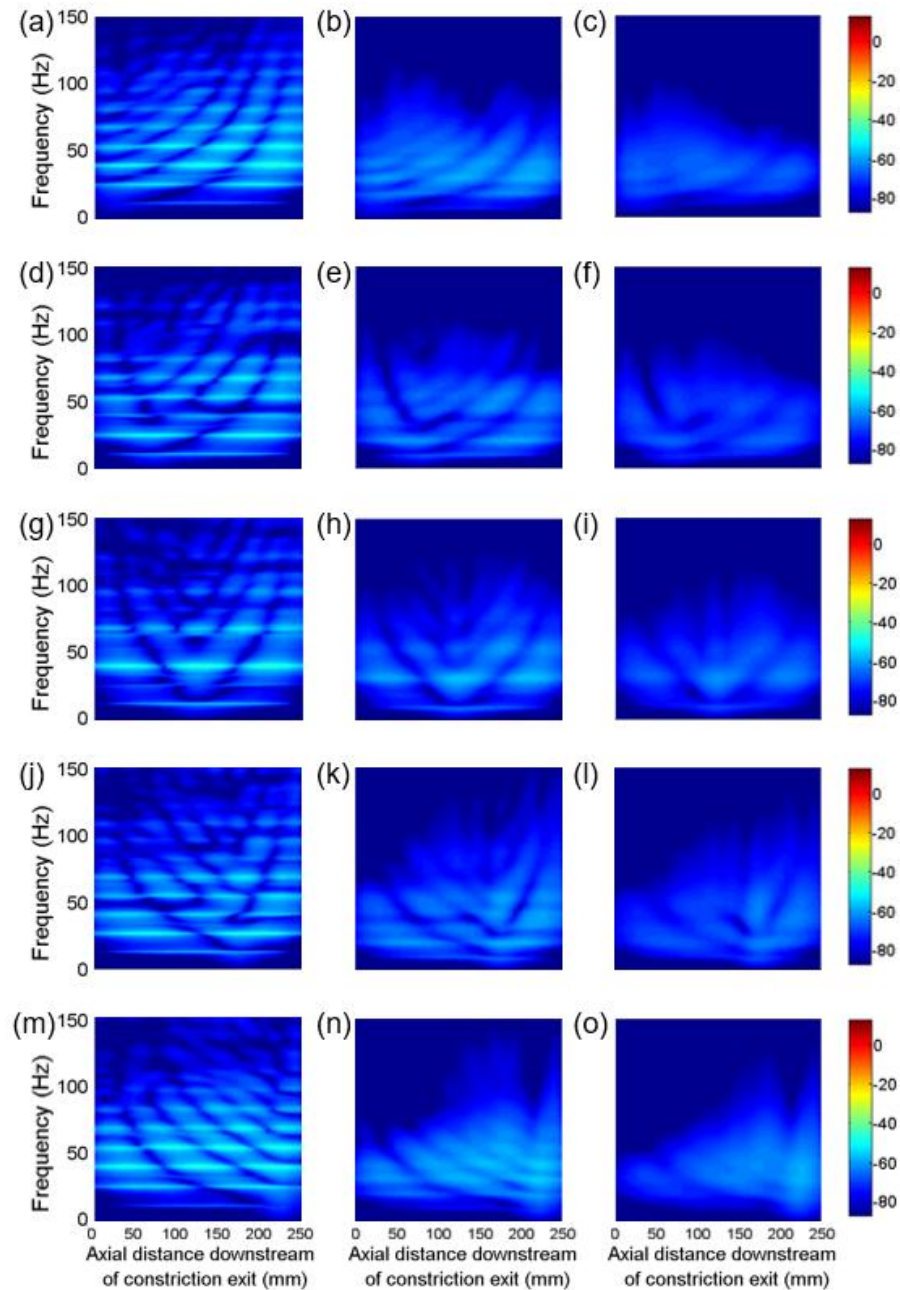


Figure 5.46 Radial velocity response (dB ref: 1 mm/s) as function of axial distance and frequency for simplistic thigh model with 90% stenosis severity, considering different constriction locations and modal damping coefficients. (a) 0 mm, 2%. (b) 0 mm, 10%. (c) 0 mm, 20%. (d) 50 mm, 2%. (e) 50 mm, 10%. (f) 50 mm, 20%. (g) 125 mm, 2%. (h) 125 mm, 10%. (i) 125 mm, 20%. (j) 150 mm, 2%. (k) 150 mm, 10%. (l) 150 mm, 20%. (m) 200 mm, 2%. (n) 200 mm, 10%. (o) 200 mm, 20%.

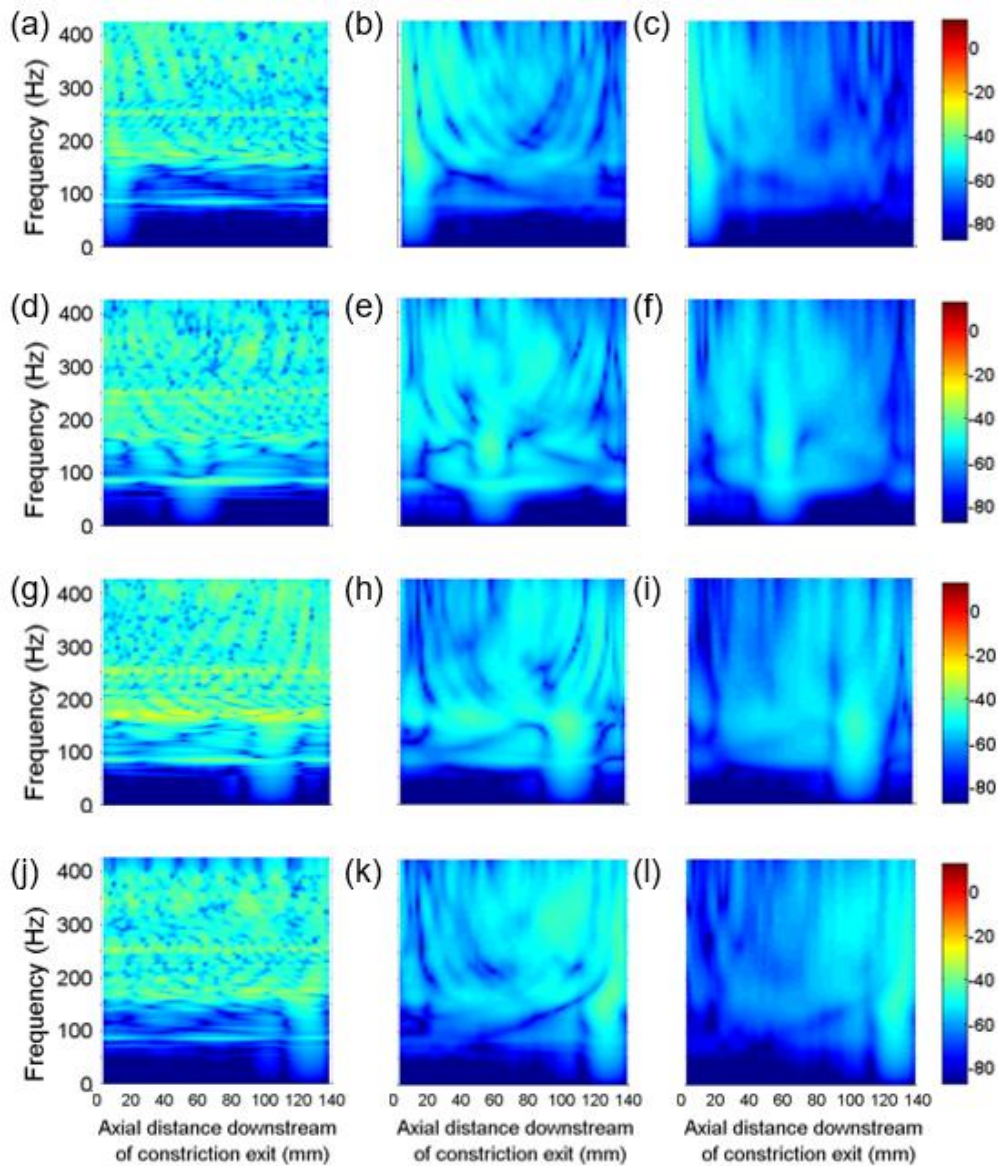


Figure 5.47 Radial velocity response (dB ref: 1 mm/s) as function of axial distance and frequency for simplistic upper arm model with 90% stenosis severity, considering different constriction locations and modal damping coefficients. (a) 0 mm, 2%. (b) 0 mm, 10%. (c) 0 mm, 20%. (d) 40 mm, 2%. (e) 40 mm, 10%. (f) 40 mm, 20%. (g) 80 mm, 2%. (h) 80 mm, 10%. (i) 80 mm, 20%. (j) 120 mm, 2%. (k) 120 mm, 10%. (l) 120 mm, 20%.

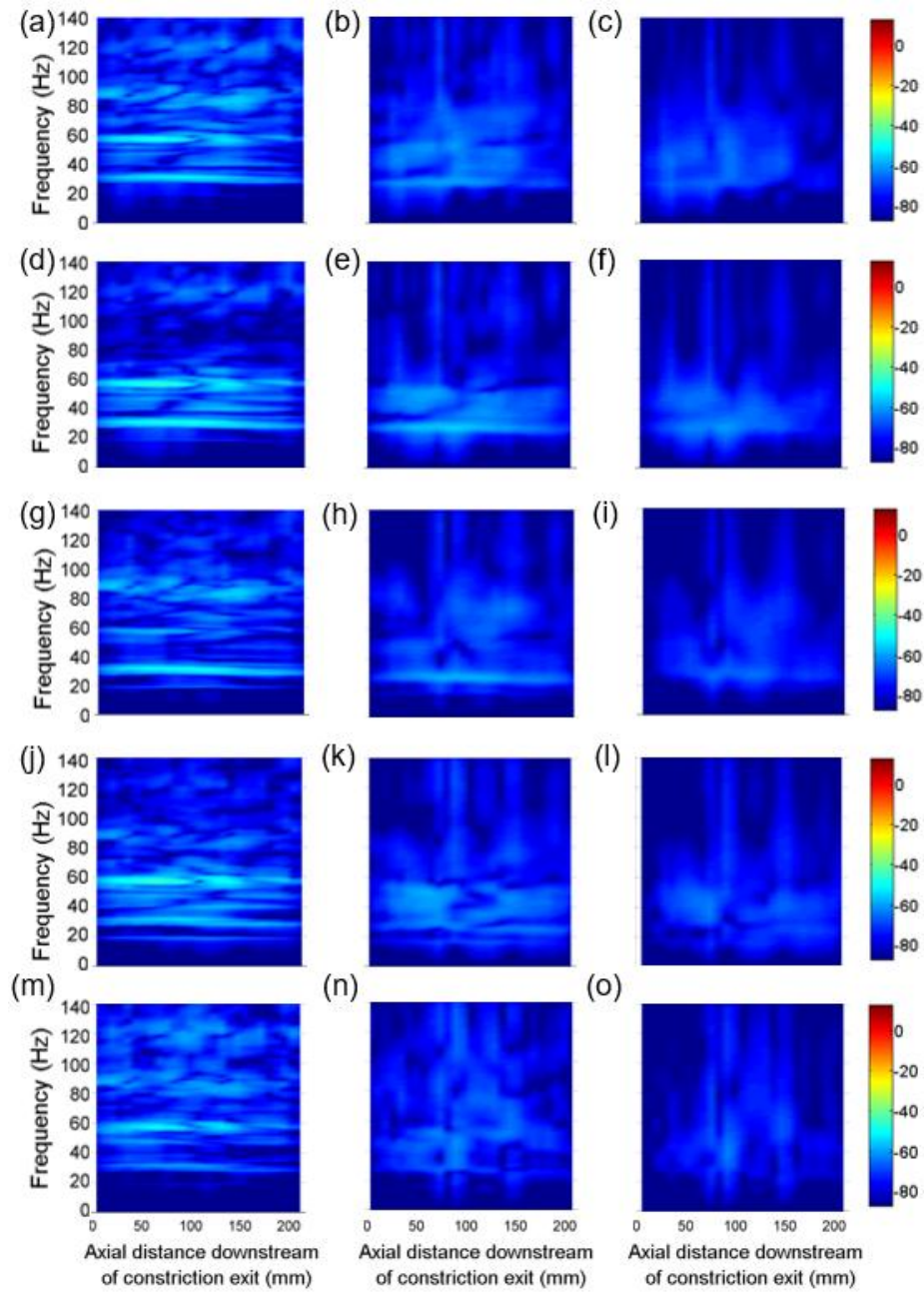


Figure 5.48 Radial velocity response (dB ref: 1 mm/s) as function of axial distance and frequency for CT based thigh model with 90% stenosis severity, considering different constriction locations and modal damping coefficients. (a) 0 mm, 2%. (b) 0 mm, 10%. (c) 0 mm, 20%. (d) 50 mm, 2%. (e) 50 mm, 10%. (f) 50 mm, 20%. (g) 100 mm, 2%. (h) 100 mm, 10%. (i) 100 mm, 20%. (j) 150 mm, 2%. (k) 150 mm, 10%. (l) 150 mm, 20%. (m) 200 mm, 2%. (n) 200 mm, 10%. (o) 200 mm, 20%.

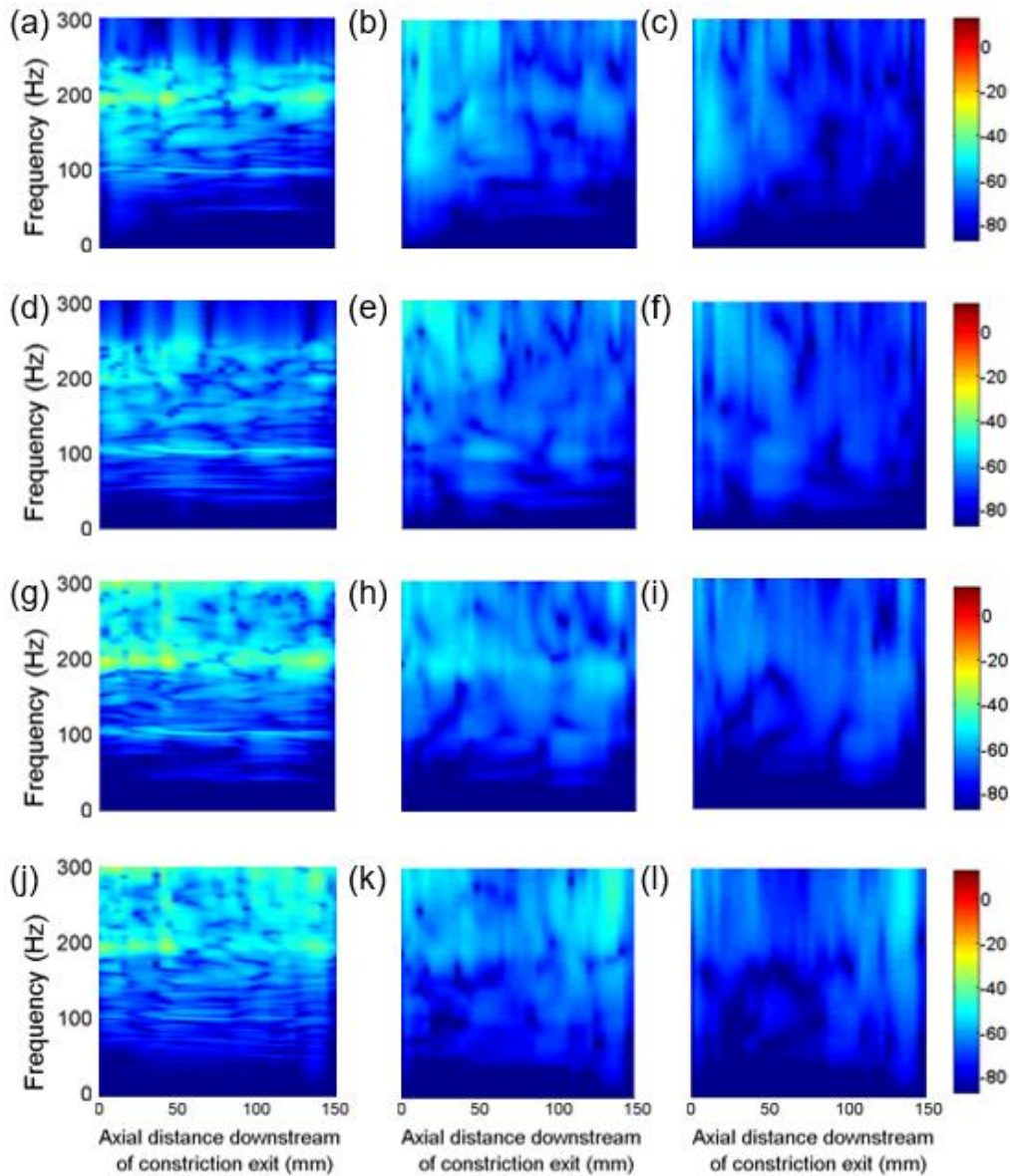


Figure 5.49 Radial velocity response (dB ref: 1 mm/s) as function of axial distance and frequency for CT based upper arm model with 90% stenosis severity, considering different constriction locations and modal damping coefficients. (a) 0 mm, 2%. (b) 0 mm, 10%. (c) 0 mm, 20%. (d) 47 mm, 2%. (e) 47 mm, 10%. (f) 47 mm, 20%. (g) 93 mm, 2%. (h) 93 mm, 10%. (i) 93 mm, 20%. (j) 117 mm, 2%. (k) 117 mm, 10%. (l) 117 mm, 20%.

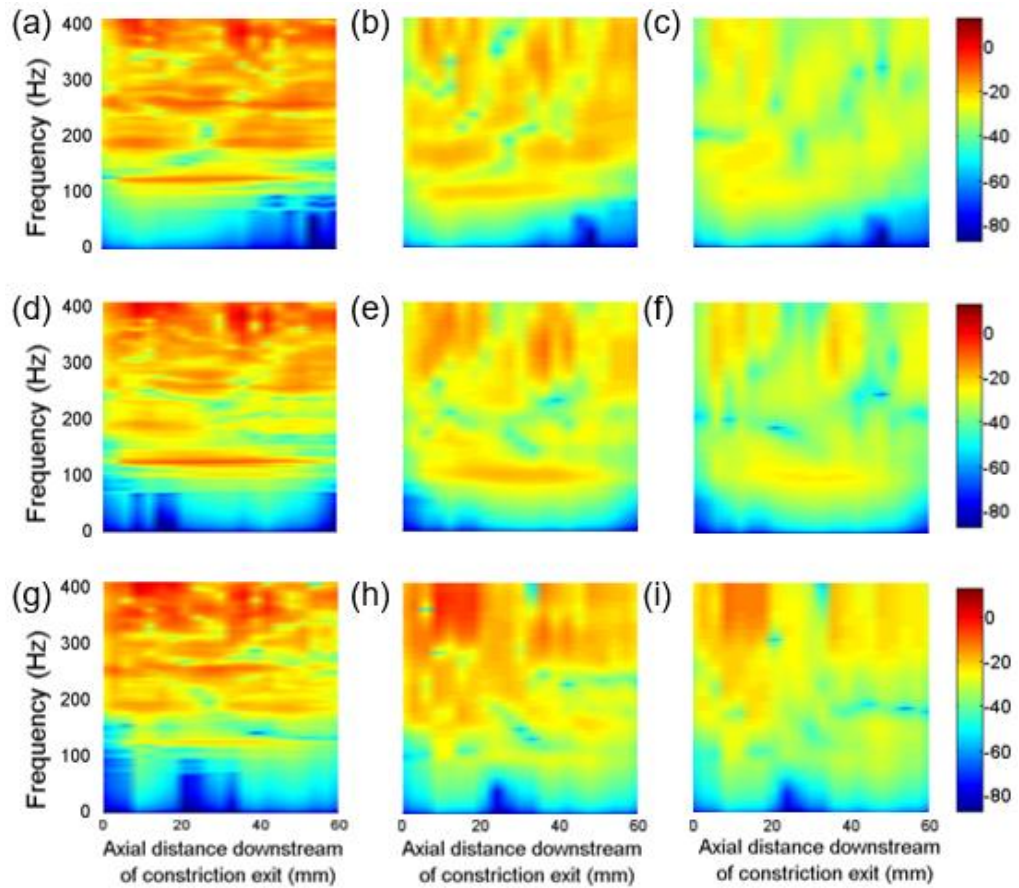


Figure 5.50 Radial velocity response (dB ref: 1 mm/s) as function of axial distance and frequency for CT based neck model with 90% stenosis severity, considering different constriction locations and modal damping coefficients. (a) 0 mm, 2%. (b) 0 mm, 10%. (c) 0 mm, 20%. (d) 24 mm, 2%. (e) 24 mm, 10%. (f) 24 mm, 20%. (g) 48 mm, 2%. (h) 48 mm, 10%. (i) 48 mm, 20%.

5.10 Partial derivative analysis for radial velocity responses

In the investigation of the simplistic models, it is observed that the anti-resonance curves are visible in the radial velocity contour plots and they are directing the stenosis location. Then, CT data are used for the models of the thigh, upper arm and neck. When CT based models are investigated, it is seen that the anti-resonance curves are not visible as in the simplistic models. Using an alternative approach, the sum of radial velocity amplitudes are used to find the stenosis location in the CT based models.

In this section, partial derivatives of the radial velocity responses with respect to distance $\left(\frac{\partial}{\partial x}\right)$ and frequency $\left(\frac{\partial}{\partial f}\right)$ are investigated. The partial derivatives of the responses are determined for all points on the radial velocity contour plots. In Figure 5.51, Figure 5.52 and Figure 5.53, the partial derivative analyses are performed for CT based thigh, upper arm and neck models, respectively. It is concluded that the partial derivatives of the radial velocity responses are not providing critical information to determine the stenosis location. For this reason, the best method for determining the stenosis location in the CT based models is to directly sum the radial velocity responses within the interested frequency range without taking any partial derivatives.

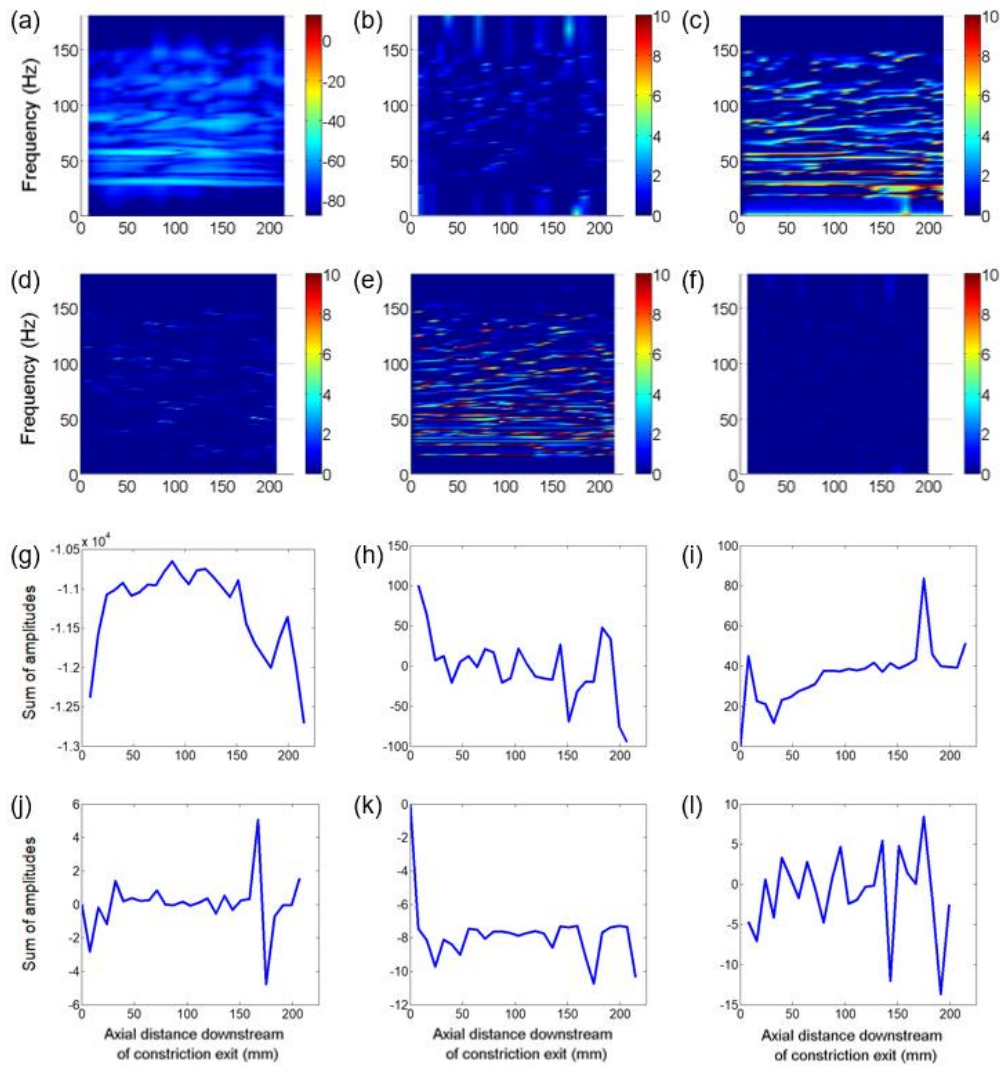


Figure 5.51 Partial derivative analysis for CT based thigh model considering 90% stenosis and 2% damping. Stenosis exit is located at 0 mm. (a) Radial velocity response. (b) First derivative with respect to distance $\left(\frac{\partial}{\partial x}\right)$. (c) First derivative with respect to frequency $\left(\frac{\partial}{\partial f}\right)$. (d) Derivative with respect to distance and frequency $\left(\frac{\partial}{\partial x \partial f}\right)$. (e) Second derivative with respect to frequency $\left(\frac{\partial^2}{\partial f \partial f}\right)$. (f) Second derivative with respect to distance $\left(\frac{\partial^2}{\partial x \partial x}\right)$. (g) Sum of amplitudes in (a). (h) Sum of amplitudes in (b). (i) Sum of amplitudes in (c). (j) Sum of amplitudes in (d). (k) Sum of amplitudes in (e). (l) Sum of amplitudes in (f).

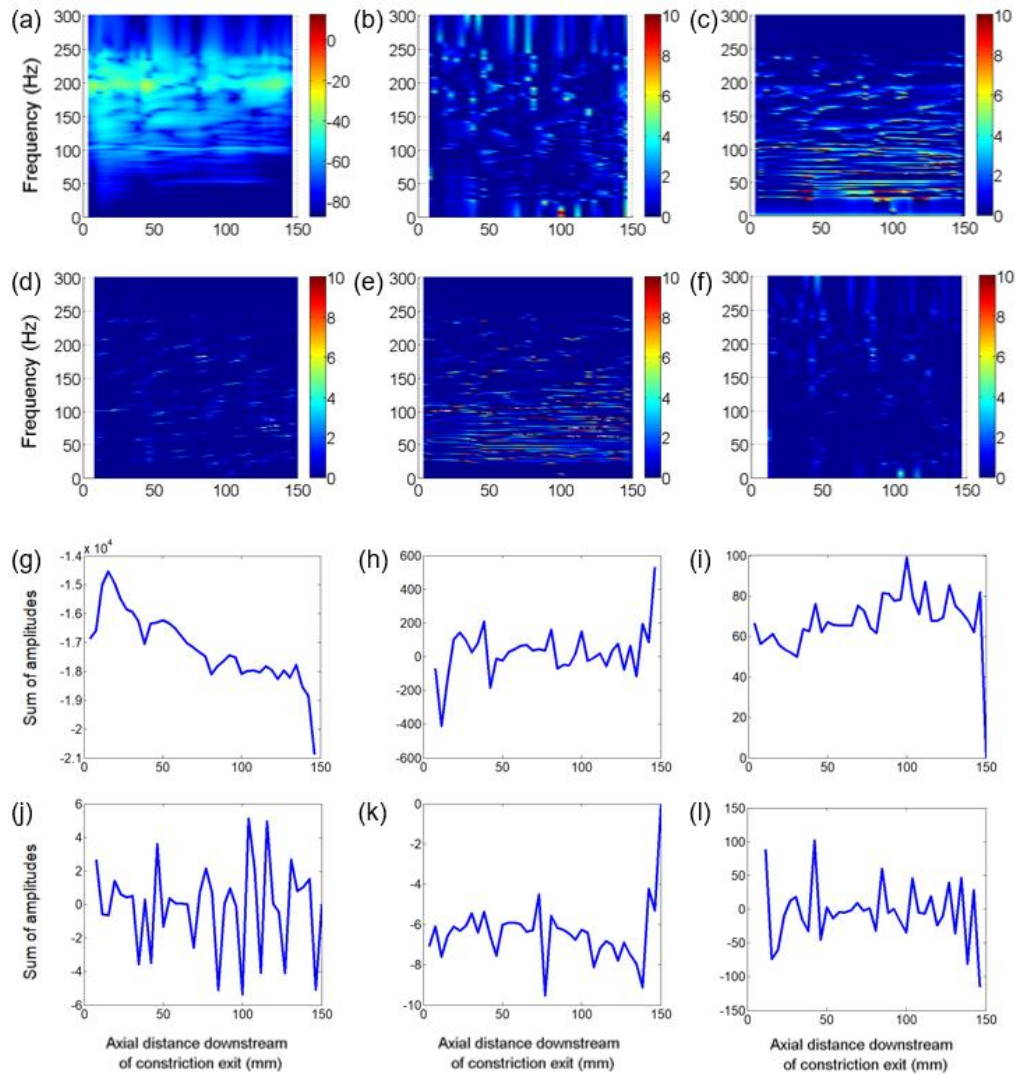


Figure 5.52 Partial derivative analysis for CT based upper arm model considering 90% stenosis and 2% damping. Stenosis exit is located at 0 mm. (a) Radial velocity response. (b) First derivate with respect to distance $\left(\frac{\partial}{\partial x}\right)$. (c) First derivate with respect to frequency $\left(\frac{\partial}{\partial f}\right)$. (d) Derivative with respect to distance and frequency $\left(\frac{\partial^2}{\partial x \partial f}\right)$. (e) Second derivative with respect to frequency $\left(\frac{\partial^2}{\partial f \partial f}\right)$. (f) Second derivative with respect to distance $\left(\frac{\partial^2}{\partial x \partial x}\right)$. (g) Sum of amplitudes in (a). (h) Sum of amplitudes in (b). (i) Sum of amplitudes in (c). (j) Sum of amplitudes in (d). (k) Sum of amplitudes in (e). (l) Sum of amplitudes in (f).

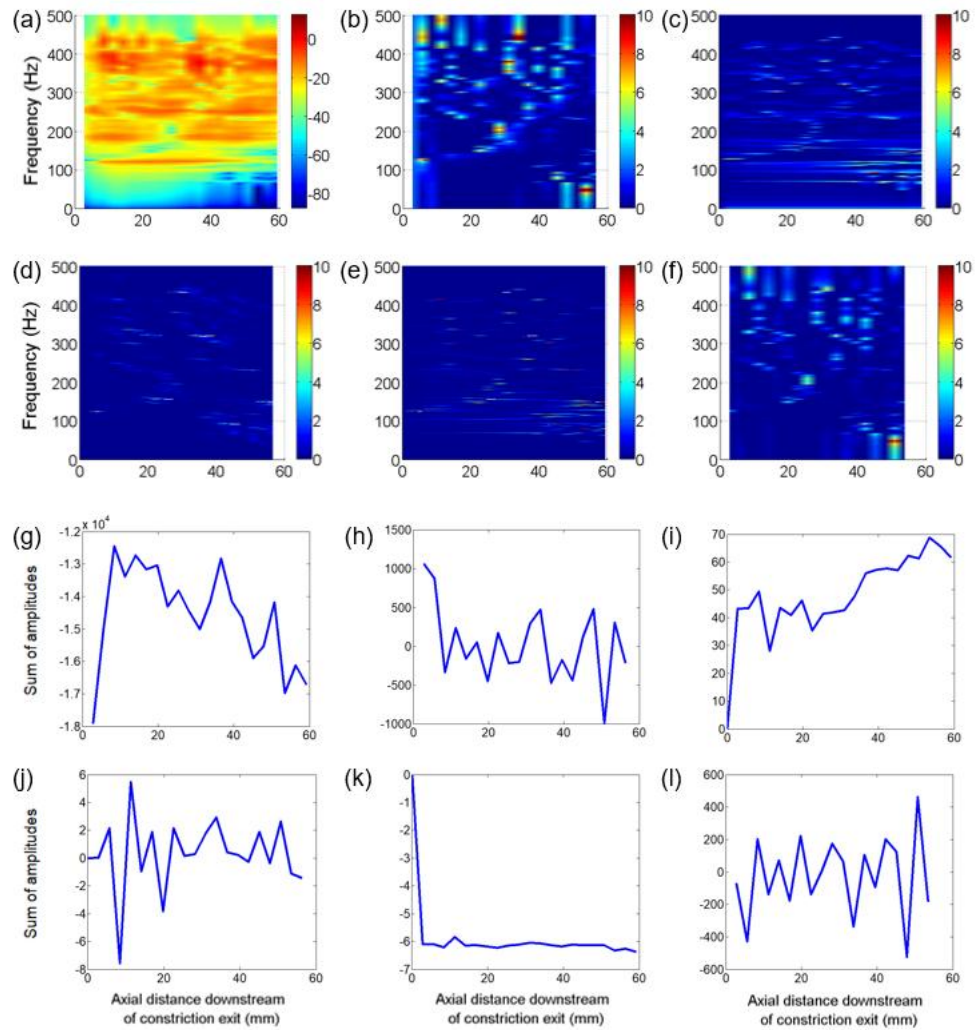


Figure 5.53 Partial derivative analysis for CT based neck model considering 90% stenosis and 2% damping. Stenosis exit is located at 0 mm. (a) Radial velocity response. (b) First derivative with respect to distance $\left(\frac{\partial}{\partial x}\right)$. (c) First derivative with respect to frequency $\left(\frac{\partial}{\partial f}\right)$. (d) Derivative with respect to distance and frequency $\left(\frac{\partial^2}{\partial x \partial f}\right)$. (e) Second derivative with respect to frequency $\left(\frac{\partial^2}{\partial f \partial f}\right)$. (f) Second derivative with respect to distance $\left(\frac{\partial^2}{\partial x \partial x}\right)$. (g) Sum of amplitudes in (a). (h) Sum of amplitudes in (b). (i) Sum of amplitudes in (c). (j) Sum of amplitudes in (d). (k) Sum of amplitudes in (e). (l) Sum of amplitudes in (f).

CHAPTER 6

EXPERIMENTAL STUDIES

6.1 Experimental set-up

Water-filled latex penrose drainage tube with a lumen diameter of 6.4 mm and thickness of 0.3 mm is used for modelling the artery simulated previously in the computational analysis. Compliant latex rubber tube is surrounded by a tissue phantom produced by bovine gelatin (Bloom 250) to mimic human flesh. Phantom models are produced using 3D printed molds with various thicknesses. One volumetric unit of gelatin powder is mixed with nine volumetric units of hot water at 70° Celsius. This liquid mixture is kept at room temperature for two hours. Latex tube is placed at the centerline of the hollow-cylindrical mold before pouring the liquid mixture to have an axisymmetric form. Stenosis element is placed at the intended location inside the latex tube. The stenosis elements and the hollow-cylindrical mold are shown in Figure 6.1. Stenosis element has much higher stiffness compared to the tissue phantom and the latex drainage tube. The mixture is poured into the mold and kept at 4° Celsius for 36 hours. After this process, the phantom material is solidified and taken out of the mold. For each experimental case, this procedure is repeated to have a fresh phantom model. All measurements and experiments are performed within two hours following the removal of phantom model from the mold.

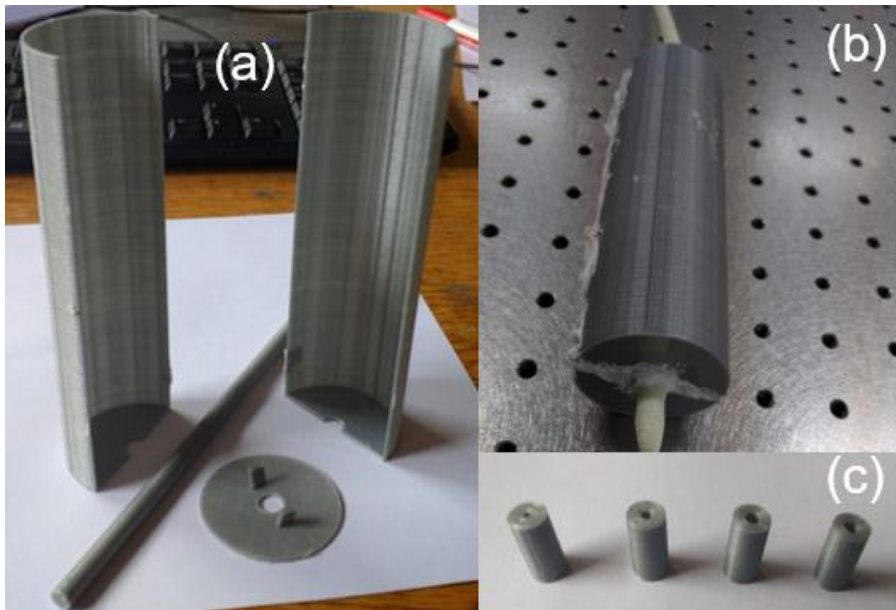


Figure 6.1 (a) Parts of the cylindrical mold. (b) Liquid-mixture poured in the hollow-cylindrical mold. (c) Stenosis elements (Left to right, 95, 90, 80 and 70% stenosis).

In the experimental setup, there are two reservoirs placed at different heights to provide gravity-fed flow as depicted in Figure 6.2. A valve is placed at the downstream of the stenosed latex tube. Intended flow rates and mean pressures inside the tube are achieved by adjusting the height of the upper reservoir and adjusting the valve, independently. In Table 6.1, the required height differences between the two reservoirs are listed to obtain the necessary flow rate and internal dynamic pressure.

Since the latex tube is buried in the phantom model, there is no slip at the interface surface between the tissue phantom and the latex tube. Experimental model is placed on a passively isolated optical table (M-RPR-36-8, Newport, Irvine, CA) to avoid ground vibration and the two ends of the phantom model are free to vibrate with no constraints. Experiments are performed for various cases considering different stenosis severities, stenosis locations, tissue phantom thicknesses, mean

pressures, and Reynolds numbers. Reynolds numbers of 1000 and 1750 are considered to be consistent with the biological relevance [150].

Radial velocity responses on the tissue phantom surface are measured by using a single-point non-contacting Laser Doppler Vibrometer (LDV) (IVS-300, Polytech, Auburn, MA) with a sensitivity of 125 mm/s/V (Low-pass filtered at 5 kHz). Total length of the experimental model is 100 mm and there are 41 measurement points with 2.5 mm spacing in between. Highly reflective grey paint is applied along the measurement points to improve the quality of the LDV signal as seen in Figure 6.3. A digital dynamic signal analyzer (HP 35665A, Hewlett Packard, Washington, USA) is used to capture and record the experimental data. The signals are processed using the dynamic signal analyzer to convert the time domain data into frequency domain by performing Fast Fourier Transform (FFT) with Hanning window. Time data is measured with a sampling rate of 4096 Hz with a corresponding -120 dB/decade anti-aliasing filter set at 1600 Hz. For each measurement point, 64 independent time records are taken to determine the RMS averaged power spectra at the measurement location. All results are post-processed using MATLAB.

Table 6.1 Height difference between the upper and lower reservoirs for all experimental cases

Stenosis severity (%)	Mean dynamic pressure (mmHg gauge)	Reynolds number	Height difference between the upper and lower reservoirs (cm)
90	27	1000	58
90	35	1000	68
90	45	1000	88
0	35	1750	51
55	35	1750	51.5
70	35	1750	52
80	35	1750	60
90	35	1750	103

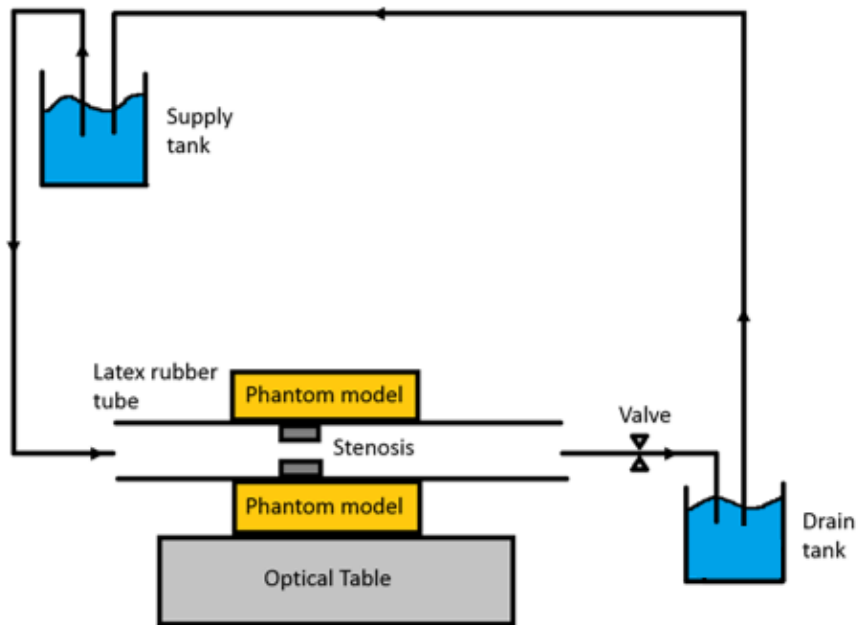


Figure 6.2 Schematic representation of experimental setup.

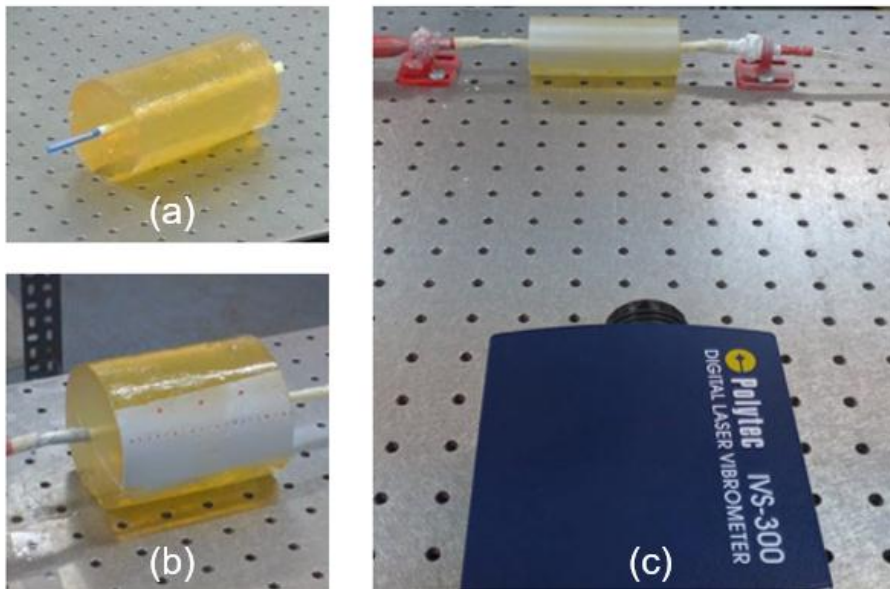


Figure 6.3 (a) Tissue phantom with thickness of 16.5 mm. (b) Retroreflective painted surface to improve LDV signal quality. (c) Experimental setup placed on the optical table to measure radial velocity responses on the phantom surface.

Single-point LDV studies are conducted considering axisymmetric cylindrical tissue phantom models. In addition to the axisymmetric phantom models, a rectangular prismatic tissue phantom is also prepared to investigate the response on flat surface. A constricted latex drainage tube is buried in the rectangular prismatic phantom model similar to the previous applications. The stenosis element is placed to a particular location and the lateral surface of the rectangular prismatic phantom is scanned using a scanning LDV (PSV-400-B, Polytech, Auburn, MA) to study the effects of stenosis location.

6.2 Mechanical characterization of the tissue phantom

Human soft tissue is mimicked using bovine gelatin based tissue phantom. A visco-hyperelastic model is developed by performing tension, compression, and relaxation tests [152] to define the material characteristics of the tissue phantom. The test setup is shown in Figure 6.4(c) and (d). Five independent measurements are recorded for each type of test and averaged test results are used for material property identification. Obtained results are presented in Figure 6.4(a) and (b) to show the stress-strain relation and the relaxation behavior of the tissue phantom, respectively.

Tension and compression behaviors of the phantom material are slightly different. For the case of tension, the slope of stress-strain curve is nearly constant up to 5% strain level. If the compression case is investigated, a variation is observed in the slope of stress-strain curve depending on the strain level. Test results are employed using Sussman-Bathe material model [153] available in ADINA-Structures module where the experimental stress-strain data is directly used as an input to mechanically characterize the tissue phantom.

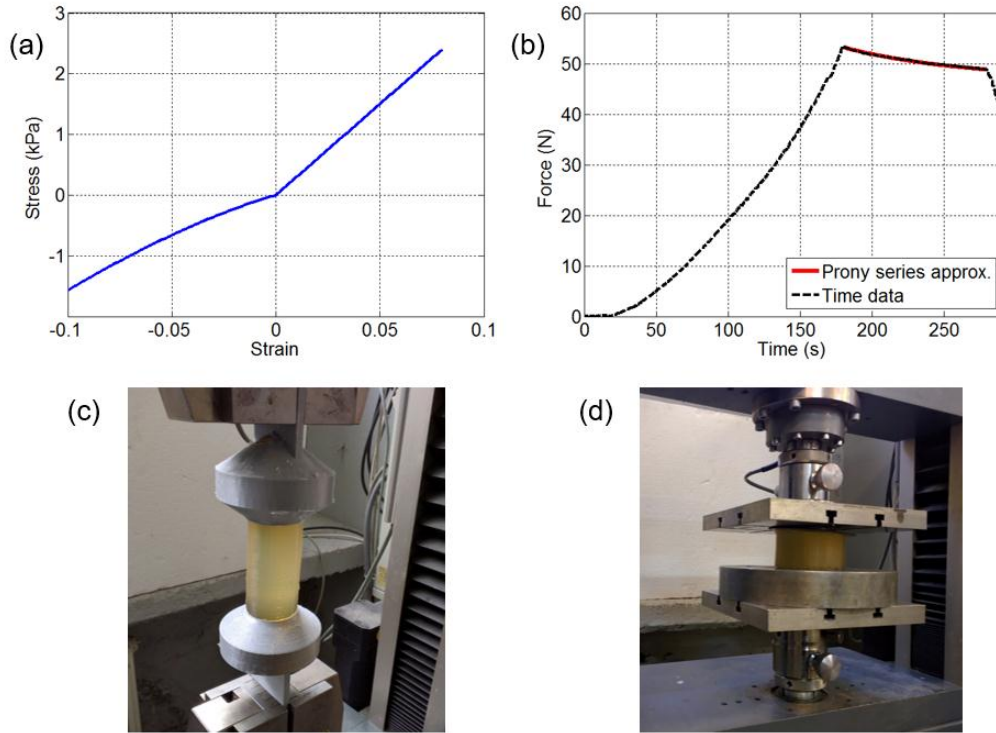


Figure 6.4 (a) Stress-strain data for tissue phantom. (b) Relaxation behavior of tissue phantom. Force relaxation is observed within the range of 180 and 280 s. Relaxation function given in (6.1) is obtained by means of Prony series expansion using the data within 180 and 280 s to determine the viscoelastic material parameters. (c) Test setup for tension tests. (d) Test setup for compression tests.

Effect of viscoelasticity is also considered in the computational studies by employing generalized Maxwell approach available in ADINA [44]. The force relaxation behavior shown in Figure 6.4(b) is obtained by holding the phantom specimen at a fixed strain level during 100 seconds (from 180 to 280 s). The function of force relaxation is accurately defined by using the following Prony series fit,

$$F = 6.2e^{(-0.0123t)} + 46.99 \quad (6.1)$$

where F denotes force and t denotes time. Relaxation modulus ($E(t)$) can be defined in the form of Prony series expression by using the generalized Maxwell approach by [95]. Only one Maxwell element sufficiently modelled the relaxation behavior of the tissue phantom. By using previously defined (5.8), (5.9), (5.10) and using (6.1), viscoelastic parameters are calculated as $\beta^1 = 0.13104$ and $\tau^1 = 81.3008$ s where these two parameters are used for modelling the viscoelasticity of tissue phantom in the computational studies.

6.3 Single-point LDV analysis

In this section, results of computational models and experimental findings are elaborated to clarify the effects of stenosis severity, stenosis location, and surrounding tissue phantom thickness on the radial vibration of tissue surface. Experimental studies are examined in two categories using single-point and scanning LDV observations.

6.3.1 Bare tube analysis

Accuracy of the current experimental findings is verified by implementing the same experimental conditions in Ref. [22]. Stenosis-driven radial vibration on a bare latex tube is determined by laser Doppler vibrometry and compared to the results in Ref. [22] as presented in Figure 6.5.

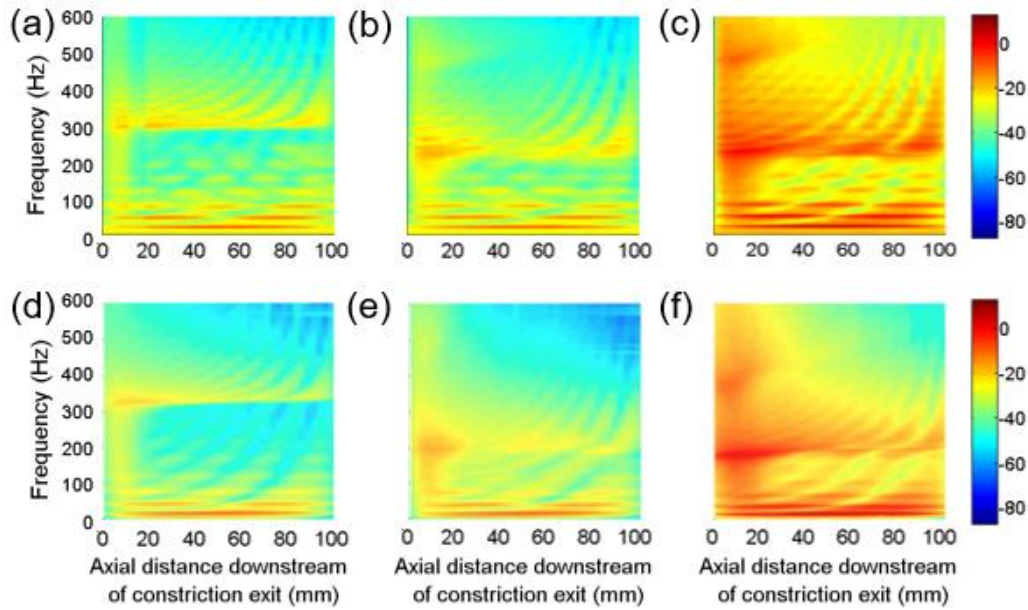


Figure 6.5 Radial velocity response (dB ref: 1 mm/s) on the outer surface of fluid-filled bare latex tube considering 87% stenosis. Stenosis exit is located at 0 mm. (a) $Re = 1000$, ~ 45 mmHg gauge pressure. (b) $Re = 1000$, ~ 15 mmHg gauge pressure. (c) $Re = 2000$, ~ 15 mmHg gauge pressure. (d) Adopted from Ref. [22]. $Re = 1000$, ~ 45 mmHg gauge pressure. (e) Adopted from Ref. [22]. $Re = 1000$, ~ 15 mmHg gauge pressure. (f) Adopted from Ref. [22]. $Re = 2000$, ~ 15 mmHg gauge pressure.

Experimental results agree well with the findings in Ref. [22] in terms of vibration amplitudes and spectral behavior. A highly excited region with relatively increased amplitudes is observed within the range of 0 and 100 Hz where the first three bending modes of the tube are clearly visible. Second highly excited region is observed slightly above 300 Hz in Figure 6.5(a) and (d) for mean (head) pressure adjusted to ~ 45 mmHg gauge. If the mean pressure in the tube is adjusted to ~ 15 mmHg gauge, this highly excited region is scaled down to 250 Hz as seen in Figure 6.5(b) and (e). This situation clarifies the findings, as the increased pre-stress level depending on higher mean pressure leads to a shift towards higher frequencies.

In Figure 6.5(c) and (f), Reynolds number is increased from 1000 to 2000 and as a consequence, the vibration amplitudes are generally increased due to higher acoustic pressure amplitudes generated on the inner wall of the tube. In Figure 6.5(c), three highly excited regions are observable within 0 and 100 Hz, within 200 and 300 Hz, and around 500 Hz. However, these regions are encountered at slightly lower frequencies in Figure 6.5(f). The reason is thought to be the axial pre-stress differences in the experimental conditions.

Axial pre-stress can shift the resonance frequencies as represented in Figure 6.6. In Figure 6.6(a) and (b), all experimental conditions are kept the same except the tube extension. Larger tube extension values increased axial pre-stress and resulted an upwards shift in resonance frequencies. In Figure 6.6(b), highly excited regions are observed around 300 and 600 Hz for 15% tube elongation. However, the corresponding resonance frequencies are seen around 260 and 550 Hz for 0% elongation in Figure 6.6(a).

Clearly visible spectral contents in Figure 6.6(b) and (c) are attributed to the increased axial pre-stress. As the extension and pre-stress scales up, effect of bending mode shapes becomes more prominent at high frequencies. The change in Reynolds number is not an influencing factor on the resonance frequencies.

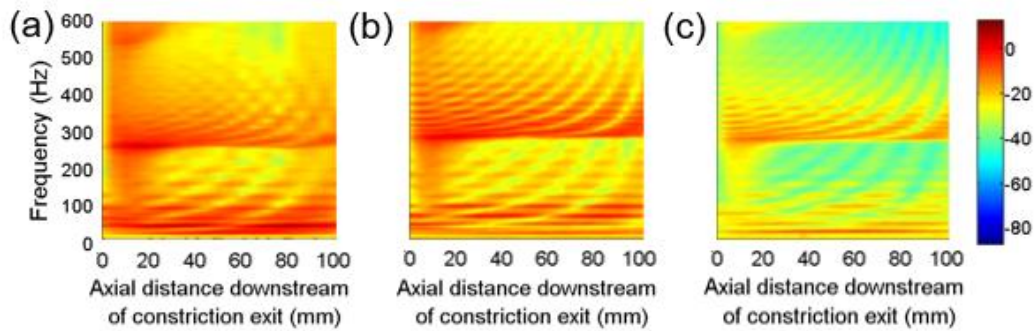


Figure 6.6 Radial velocity response (dB ref: 1 mm/s) on the outer surface of fluid-filled bare latex tube considering 90% stenosis. Mean pressure is adjusted to ~ 35 mmHg gauge. Stenosis exit is located at 0 mm. (a) $Re = 1750$, 0% tube extension. (b) $Re = 1750$, 15% tube extension. (c) $Re = 1000$, 15% tube extension.

6.3.2 Tissue surrounded models

Up to here, experimental results are presented for bare tube wall vibration without considering any surrounding phantom material. Here, the constricted tube is surrounded by a phantom model to mimic human flesh. Radial vibration on the phantom surface is investigated both experimentally and computationally. Using the same procedures followed in Chapter 4 and Chapter 5, the experimental cases are modelled in ADINA.

Three different mesh densities are employed to achieve mesh independent results. Mesh 1, Mesh 2 and Mesh 3 have 3240, 11200 and 45600 elements, respectively. Average response amplitude (within 0-100 mm, 0-600 Hz) has a difference of 5.61% between Mesh 1 and Mesh 2. This difference is obtained as 0.91% between Mesh 2 and Mesh 3. Results are accepted as mesh-independent if the difference in average amplitudes is less than 3%. Results of Mesh 2 are satisfactorily accurate in terms of spectral content and response amplitudes. Mesh 2 with the moderate mesh density is used for the further analysis since the average amplitude difference between Mesh 2 and Mesh 3 is less than 3%.

In experimental studies, modal damping coefficients are uncertain. Consequently, a trial and error method is followed to determine experimental modal damping characteristics. For this purpose, an experimental case is computationally modelled considering various modal damping coefficients as represented in Figure 6.7.

In Figure 6.7(c), (d) and (e), high and low-excited regions are clearly separated by border lines as indicated on the responses. The border line angle with the horizontal axis scales up with increasing modal damping coefficient. In Figure 6.7(a), experimental vibration amplitudes within 0 and 100 Hz are relatively higher and resonant peaks are sharper which is indicating a low damping region. However, as the frequency increases, vibration amplitudes tend to decrease much faster and resonant peaks become broader. Therefore, it is considered that experimental damping coefficients vary depending on the frequency. In Figure 6.7(c), (d) and (e), a constant modal damping coefficient is employed for all frequencies. In Figure 6.7(b), frequency-varying damping behavior given in Table 6.2 is utilized to better reflect the experimental conditions. Experimental vibration amplitudes and spectral content in Figure 6.7(a) best fit with frequency-varying damping case shown in Figure 6.7(b). Therefore, all further computational results are obtained using frequency-varying damping coefficients given in Table 6.2.

Table 6.2 Frequency-varying modal damping coefficients employed in the computational models

Frequency range	Modal damping coefficient
0-25 Hz	1%
25-100 Hz	3%
100-150 Hz	7%
150-600 Hz	12%

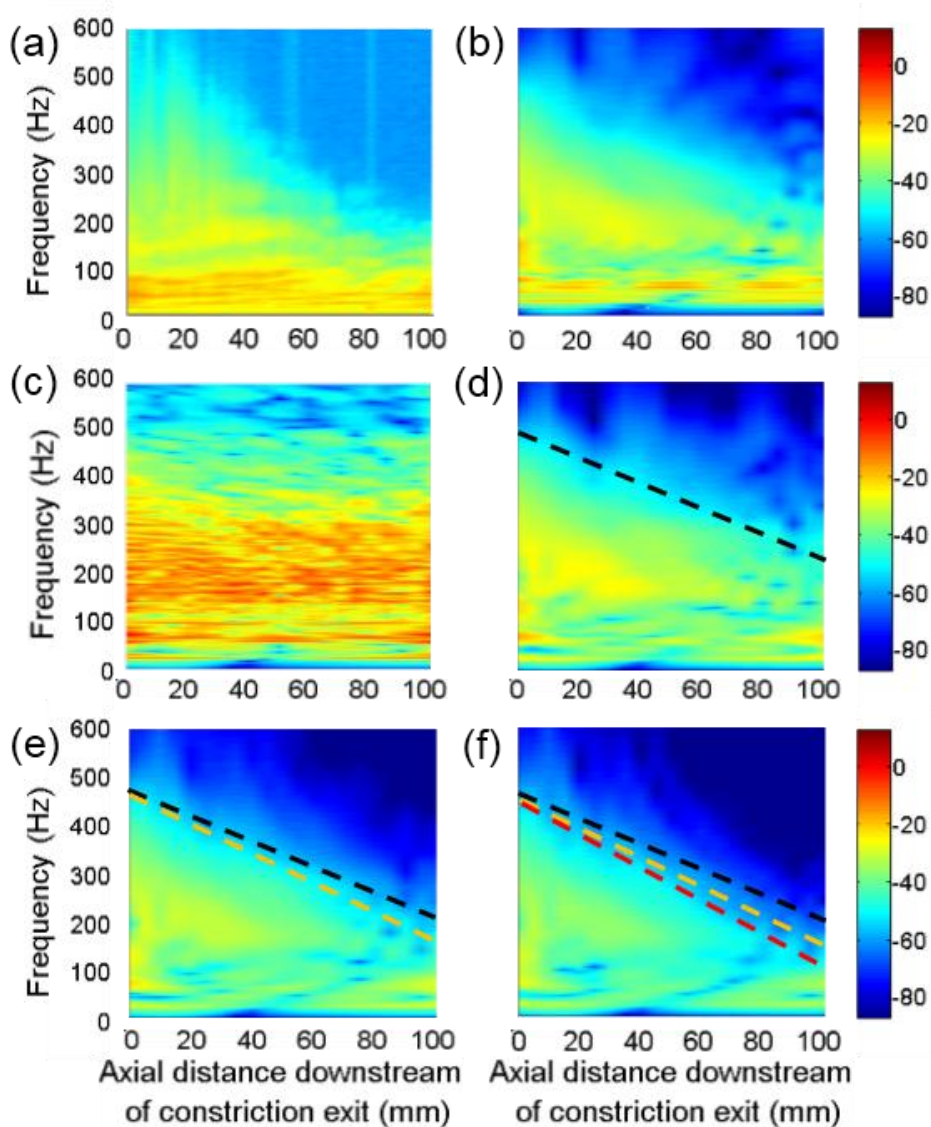


Figure 6.7 Radial velocity response (dB ref: 1 mm/s) on the outer surface of 16.5 mm thickness tissue phantom considering 90% stenosis with $Re = 1750$. Stenosis exit is located at 0 mm. Mean pressure is adjusted to ~ 35 mmHg gauge. (a) Experimental result. (b) Computational result using frequency-varying modal damping coefficients given in Table 6.2. (c) Computational result using 1% modal damping. (d) Computational result using 10% modal damping. Black dash line indicates border line. (e) Computational result using 15% modal damping. Orange dash line indicates border line. (f) Computational result using 20% modal damping. Red dash line indicates border line.

Effect of stenosis severity is investigated in Figure 6.8. Experimental findings agree well with the computational results in terms of spectral content and the relative increase in vibration amplitudes depending on the stenosis severity. There is no background noise in the computational analysis and the lowest response amplitude is obtained at about -80 dB. On the other hand, the lowest experimental response amplitude is measured about -60 dB as a consequence of experimental noise in LDV studies. This fact is the main difference between the experimental and computational results. Up to 70% stenosis, the relative increase in response amplitudes is not at a considerable amount. However, if the stenosis severity exceeds 70%, vibration amplitudes begin to increase significantly. Therefore, 70% stenosis severity is regarded as an important threshold level to effectively detect an occlusion inside a tube. In Figure 6.9, average responses are given for the experimental results by averaging the amplitudes within 0 and 600 Hz. When the stenosis severity is increased from 70 to 80%, approximately 2 dB increase is observed in the average response amplitudes especially around the stenosis location. If the stenosis severity is increased from 80 to 90%, this increase is more than 6 dB. The general increase in the vibration amplitudes can be accepted as an indication of a stenosis.

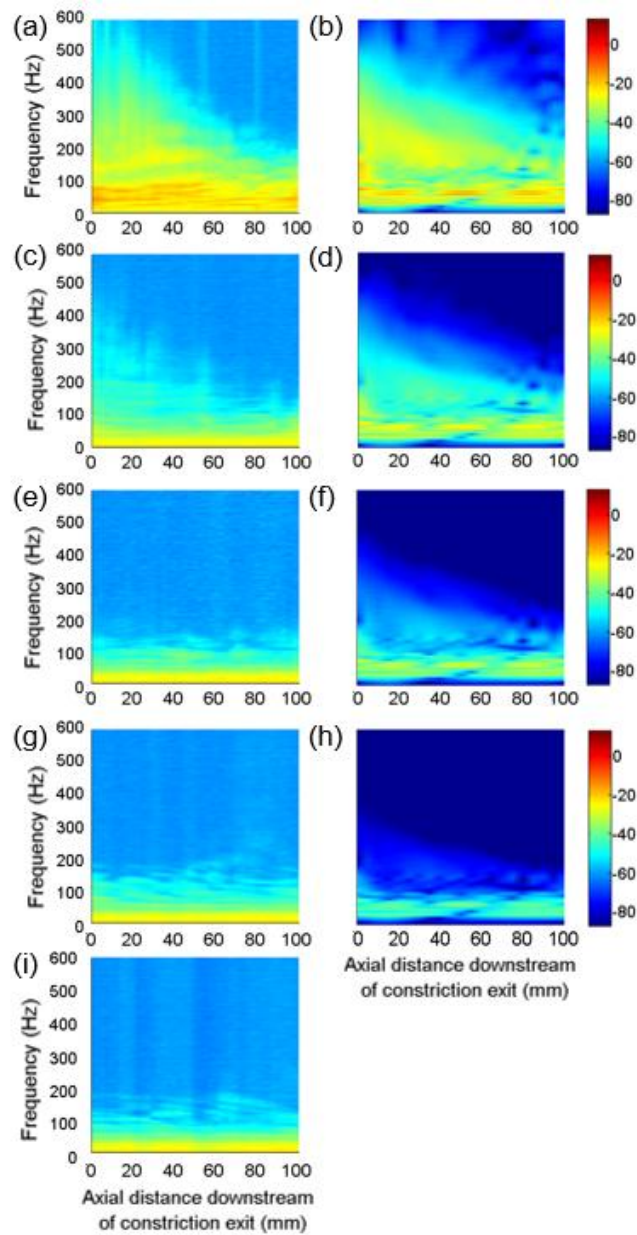


Figure 6.8 Radial velocity response (dB ref: 1 mm/s) on the outer surface of 16.5 mm thickness tissue phantom with $Re = 1750$. Stenosis exit is located at 0 mm. Mean pressure is adjusted to ~ 35 mmHg gauge with 0% tube extension. (a) Experiment, 90% stenosis. (b) Computational result, 90% stenosis. (c) Experiment, 80% stenosis. (d) Computational result, 80% stenosis. (e) Experiment, 70% stenosis. (f) Computational result, 70% stenosis. (g) Experiment, 55% stenosis. (h) Computational result, 55% stenosis. (i) Experiment, 0% stenosis.

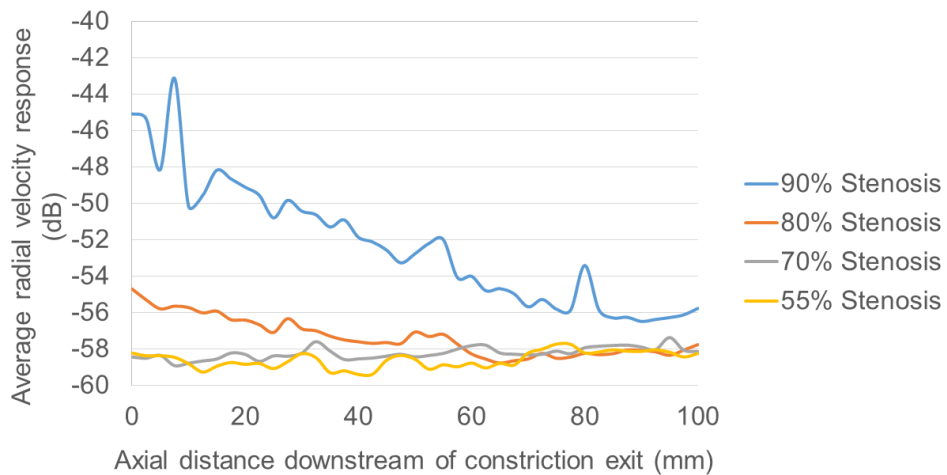


Figure 6.9 Average of the experimental radial velocity responses given in Figure 6.8(a), (c), (e) and (g).

In Figure 6.9, the maximum excitation is observed around the stenosis location. If the stenosis element is moved to a different location, the peak activity point is shifted towards the occlusion as seen in Figure 6.10. Averages of vibration responses in Figure 6.10(a), (b) and (c) are presented in Figure 6.10(d) using the amplitudes within 0 and 600 Hz. The relative increase in amplitudes downstream of the stenosis exit is an important indication to detect the occluded location. For a stenosis placed at 0 mm, the peak activity point is observed at approximately 10 mm downstream of the occlusion. If the stenosis is located at 25 mm, the spatial location of the peak activity is seen at 55 mm. The peak activity point varies within 10 and 30 mm (1.5 and 4.5D) downstream of the constriction exit depending on the stenosis location and tissue phantom thickness.

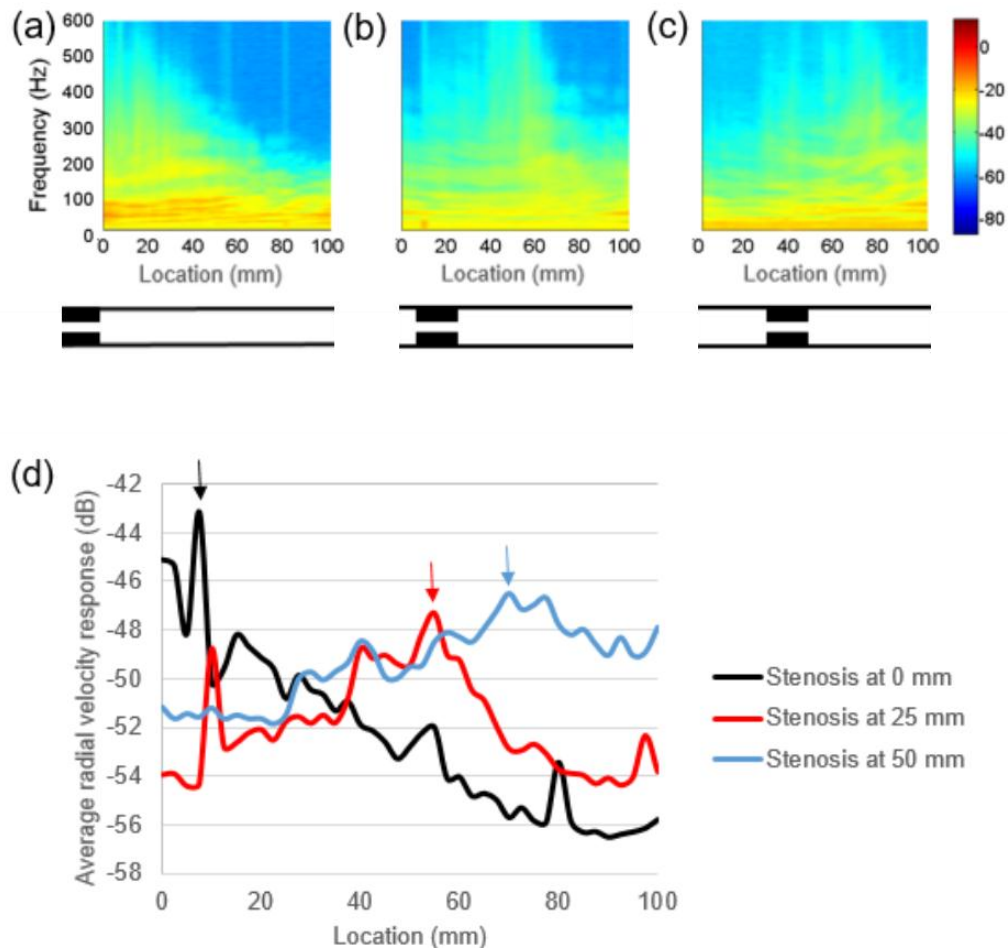


Figure 6.10 Experimental radial velocity response (dB ref: 1 mm/s) on the outer surface of 16.5 mm thickness tissue phantom considering 90% stenosis with $Re = 1750$. Mean pressure is adjusted to ~ 35 mmHg gauge with 0% tube extension. (a) Stenosis exit located at 0 mm. (b) Stenosis exit located at 25 mm. (c) Stenosis exit located at 50 mm. (d) Average responses within 0 and 600 Hz for experimental results presented in (a), (b), and (c). Peak activity points are indicated by arrows.

Effect of tissue phantom thickness is investigated in Figure 6.11. Experimental and computational results show well agreement again in terms of amplitudes and the general spectral trend. Increasing thickness resulted a general decrease in response amplitudes. When the thickness is increased from 6.5 to 16.5 mm, approximately 2 dB decrease is observed in the amplitudes as shown in Figure 6.11(g). If the thickness is increased from 16.5 to 36.5 mm, the amplitude decrease is more than 6 dB around the stenosis location. In Figure 6.11, all stenosis elements are placed at 0 mm, but peak activity points are observed at different locations. The distances between the stenosis exit and the peak activity points are 7.5, 12.5, and 32.5 mm for tissue phantom thicknesses of 6.5, 16.5, and 36.5 mm, respectively. As the thickness of the tissue phantom decreases, the peak activity point is getting closer to the stenosis location. For 36.5 mm tissue phantom thickness, the peak activity point moved away from the stenosis location. Detection of the stenosis location becomes more challenging as the tissue thickness increases since the surrounding tissue attenuates the effects generated on the artery wall.

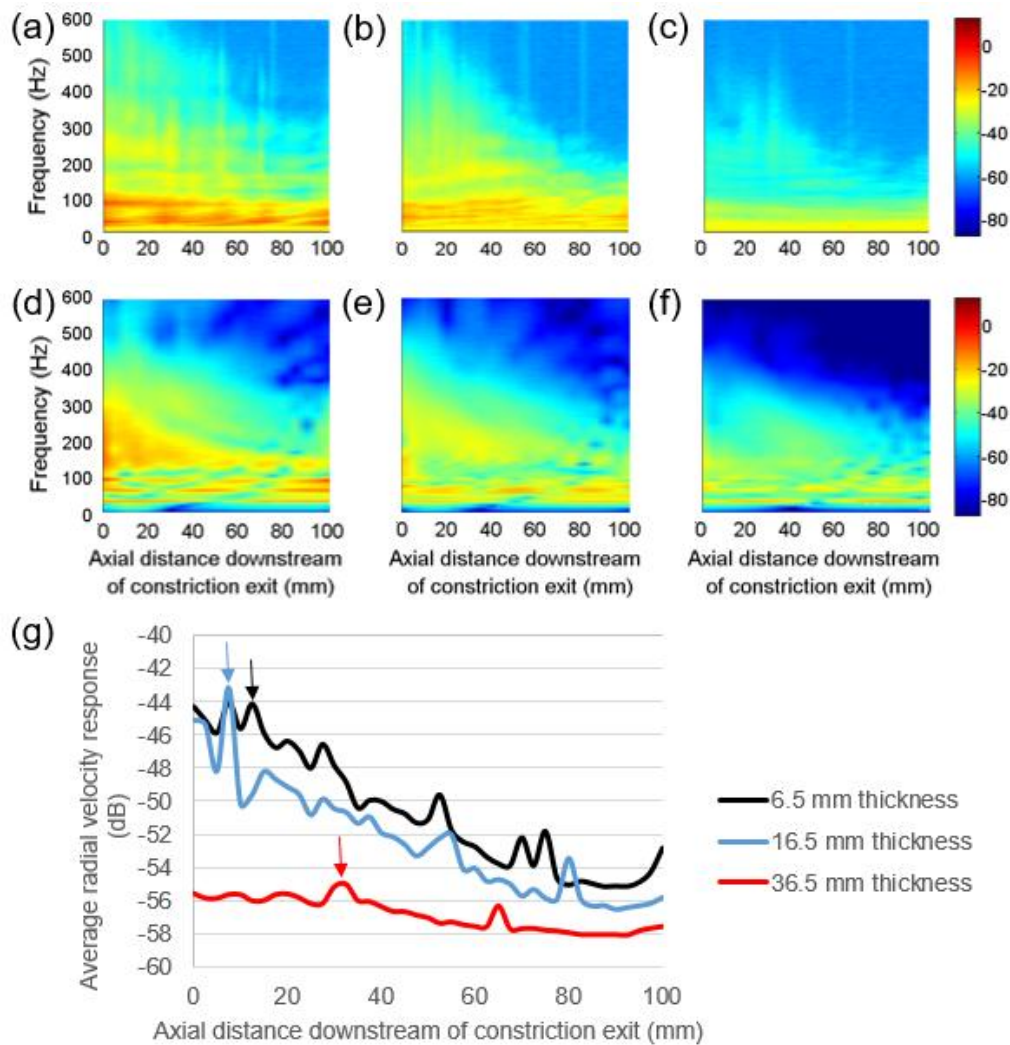


Figure 6.11 Radial velocity response (dB ref: 1 mm/s) on the outer surface of tissue phantom considering 90% stenosis with $Re = 1750$. Mean pressure is adjusted to ~ 35 mmHg gauge with 0% tube extension. Stenosis exit is located at 0 mm. (a) Experiment, 6.5 mm phantom thickness. (b) Experiment, 16.5 mm phantom thickness. (c) Experiment, 36.5 mm phantom thickness. (d) Computational result, 6.5 mm phantom thickness. (e) Computational result, 16.5 mm phantom thickness. (f) Computational result, 36.5 mm phantom thickness. (g) Average responses within 0 and 600 Hz for experimental results presented in (a), (b) and (c). Peak activity points are indicated by arrows.

The influence of mean pressure is investigated in Figure 6.12. There is no significant change in responses which indicates that the tissue phantom subdues the effect of mean pressure. For previously conducted bare tube studies in Figure 6.5, a change in mean pressure affected the tube radius and imparted circumferential pre-stress, resulting in shifted resonance frequencies and slightly changed spectral content. Addition of surrounding phantom material limits the effect of the mean pressure. Effect of Reynolds number is presented in Figure 6.13 which shows the relative increase in response amplitudes depending on increasing flow rate. Both experimental findings and computational results for tissue phantom thickness of 16.5 mm with 90% stenosis indicate that if the flow rate is increased by 75%, the response amplitudes tend to increase more than 6 dB especially around the stenosis location. When the average response amplitudes (within 0-600 Hz) are investigated, it is found that the vibration amplitudes on the phantom tissue surface are proportional to $Re^{1.41}$. This is an important fact, because Borisjuk [19] stated that acoustic pressure generation on inner arterial wall is proportional to Re^4 . Previously presented results in Figure 4.16 showed that vibration amplitudes on the outer surface of the artery are approximately proportional to Re^3 . Here, it is shown that this proportionality drops to the power of 1.41 when the artery is surrounded by a 16.5 mm tissue thickness.

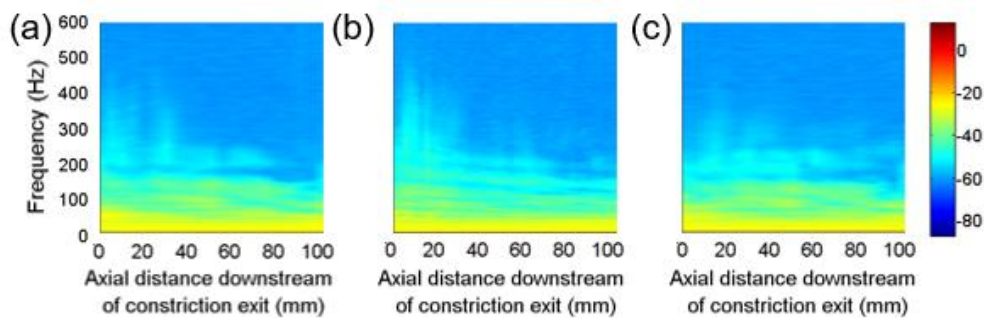


Figure 6.12 Experimental radial velocity response (dB ref: 1 mm/s) on the outer surface of 16.5 mm thickness tissue phantom considering 90% stenosis with $Re = 1000$ and 0% tube extension. (a) Mean pressure of 27 mmHg gauge. (b) Mean pressure of 35 mmHg gauge. (c) Mean pressure of 48 mmHg gauge.

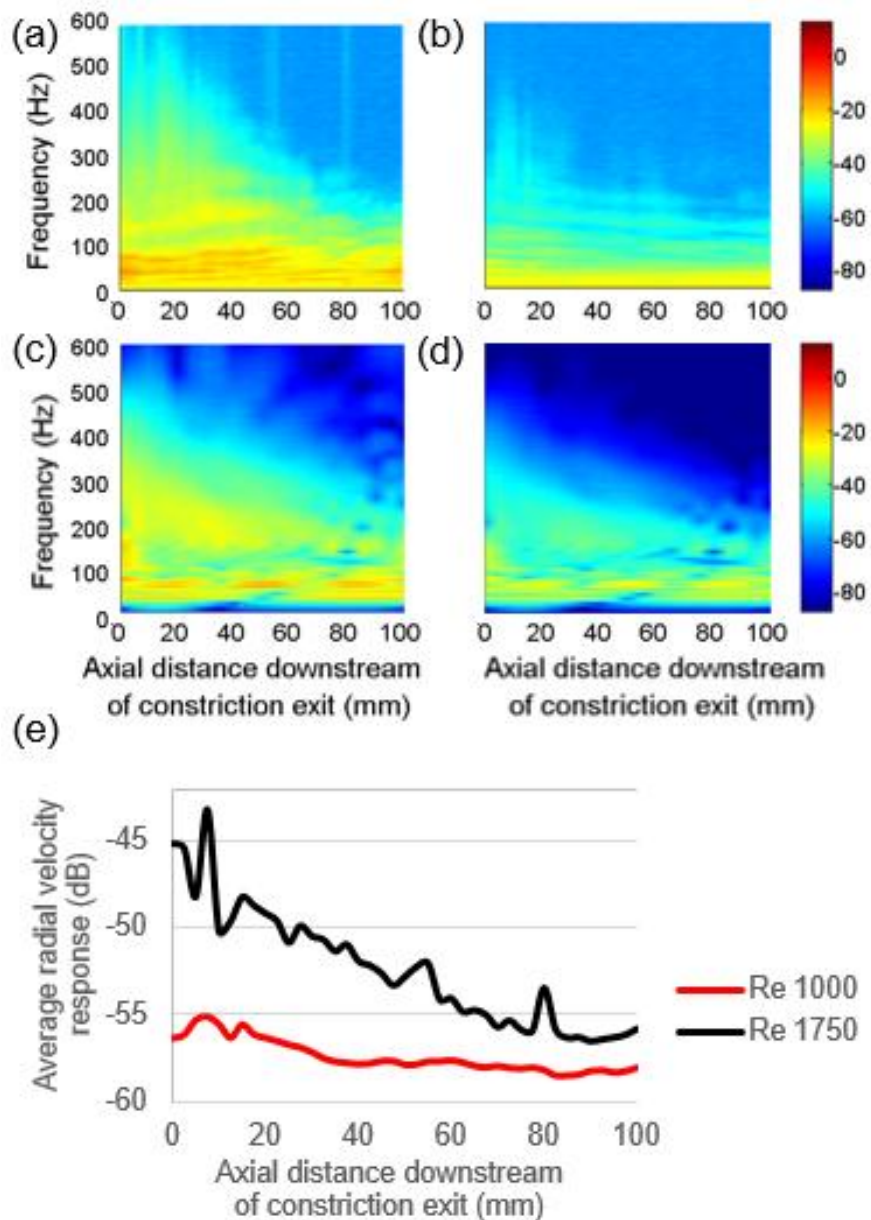


Figure 6.13 Radial velocity response (dB ref: 1 mm/s) on the outer surface of 16.5 mm thickness tissue phantom considering 90% stenosis. Mean pressure is adjusted to ~ 35 mmHg gauge with 0% tube extension. Stenosis exit is located at 0 mm. (a) Experiment, $Re = 1750$. (b) Experiment, $Re = 1000$. (c) Computational result, $Re = 1750$. (d) Computational result, $Re = 1000$. (e) Average responses within 0 and 600 Hz for experimental results presented in (a) and (b).

6.4 Scanning LDV analysis

In the previous experimental studies, investigating a line on the tissue phantom is sufficient to determine the general characteristics of the model due to axisymmetric geometry. Here, a rectangular prismatic tissue phantom model is introduced to investigate a flat surface as shown in Figure 6.14. Stenosis element is placed to a particular location inside the tube. For scanning LDV measurements, data processing procedure is the same with the single-point LDV studies.

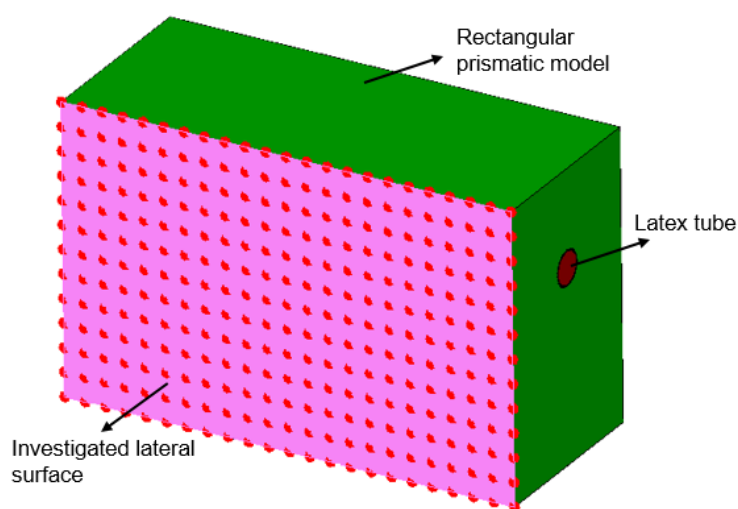


Figure 6.14 Rectangular prismatic tissue phantom model. The length, width and height of the rectangular prism are 95, 40 and 60 mm, respectively. 299 points on the lateral surface (23 x 13 grid) are used for scanning LDV measurements. Latex rubber drainage tube is placed at a height of 40 mm from the ground.

Vibration responses of 299 points on the lateral surface are recorded. Average velocity response amplitude is determined for each measurement point using the amplitudes within 0 and 600 Hz. Average amplitudes on the investigated surface are presented in Figure 6.15 where the stenosis exit is located at a distance of 55 mm from the right side of the prismatic tissue phantom. Unlike the previously presented cases, flow is from right to left in the cases shown below.

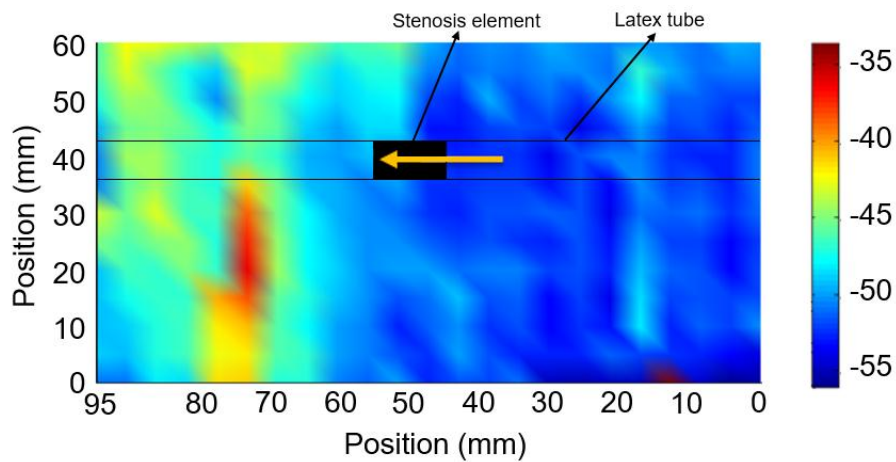


Figure 6.15 Average velocity amplitudes within 0 and 600 Hz (dB ref: 1 mm/s) on the scanned lateral surface of the rectangular prismatic tissue phantom considering 90% stenosis with $Re = 1000$. Mean pressure is adjusted to ~ 20 mmHg gauge with 0% tube extension. Flow is from right to left. Stenosis exit is placed at a height of 40 mm and located at a distance of 55 mm from the right side.

The highest activity is seen around 20 mm downstream of the constriction exit as previously observed in the axisymmetric models presented in Figure 6.10. The general increase in amplitudes immediately starts after passing over the stenosis element and the peak activity is observed about $3.1D$ downstream of the constriction exit. Although the stenosis element is placed at 40 mm height, the point of peak activity is seen at a height of 25 mm. The reason can be explained by the wave propagation phenomena. Since the prismatic tissue phantom is placed on the ground, generated waves are mostly reflected back from the ground. As a consequence, ground-reflected waves lead to relatively higher amplitudes at the region close to the bottom line, due to higher reflection compared to the free surface at the top line.

In Figure 6.16, velocity amplitudes on the scanned surface are displayed at specific frequencies. As previously observed in Figure 6.7, the damping of the system is

low within 0 and 100 Hz. Therefore, the structural modes of the tissue phantom are clearly visible and the effect of stenosis is not dominant at 12 and 30 Hz. But within 100 and 700 Hz, the effect of stenosis is more prominent where relatively higher amplitudes are observed in the downstream of the stenosis exit. For the frequencies higher than 700 Hz, the effect of stenosis is diminished and similar amplitudes are measured at all points on the scanned surface. Results in Figure 6.16 indicate that the optimum frequency range for diagnosing a stenosis is within 200 and 500 Hz, particularly around 300 Hz. A few measurement errors are present on the bottom edge of the scanned surface due to poorly reflected laser beam. Results of these problematic points are disregarded and shown inside blue circled regions in Figure 6.16.

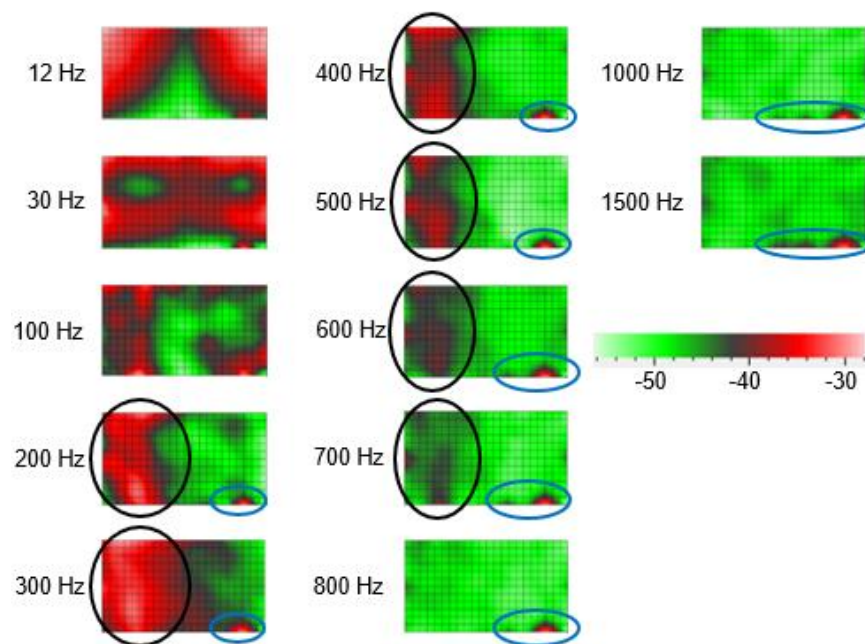


Figure 6.16 Velocity amplitudes at various frequencies (dB ref: 1 mm/s) on the scanned lateral surface of the rectangular prismatic tissue phantom considering 90% stenosis with $Re = 1000$. Flow is from right to left. Mean pressure is adjusted to ~ 20 mmHg gauge with 0% tube extension. Relatively increased amplitudes due to the stenosis are shown in black circled regions. Reflected signal quality is not adequate in blue circled regions.

6.5 Measurements using contact microphone and electronic stethoscope

In this section, results obtained using contact microphone (CM-01B, Measurement Specialties, VA) and electronic stethoscope (Litmann 3200, 3M, MN) are presented. The measurements are performed for a case with Reynolds number 1750, 35 mmHg gauge pressure, 90% stenosis severity and 16.5 mm tissue phantom thickness. The total length of the cylindrical phantom model is 100 mm. Measurements are performed at positions A, B and C, respectively, at distances of 25, 50 and 75 mm from the exit of the stenosis. The stenosis exit is placed at 0 mm. Figure 6.17 and Figure 6.18 show the response amplitudes measured by the contact microphone and the electronic stethoscope, respectively.

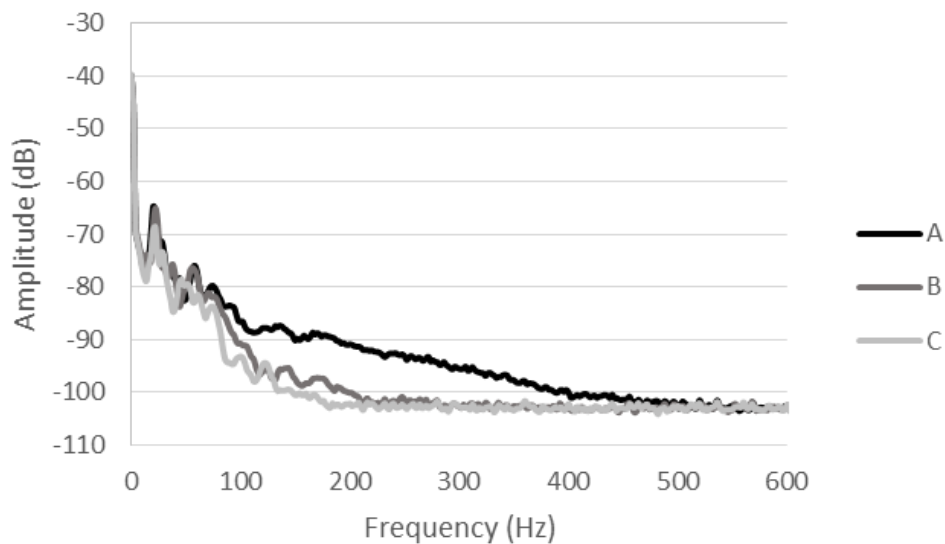


Figure 6.17 Responses at A, B, and C measured by contact microphone for Reynolds number 1750, 16.5 mm phantom material thickness, 35 mmHg gauge pressure and 90% stenosis.

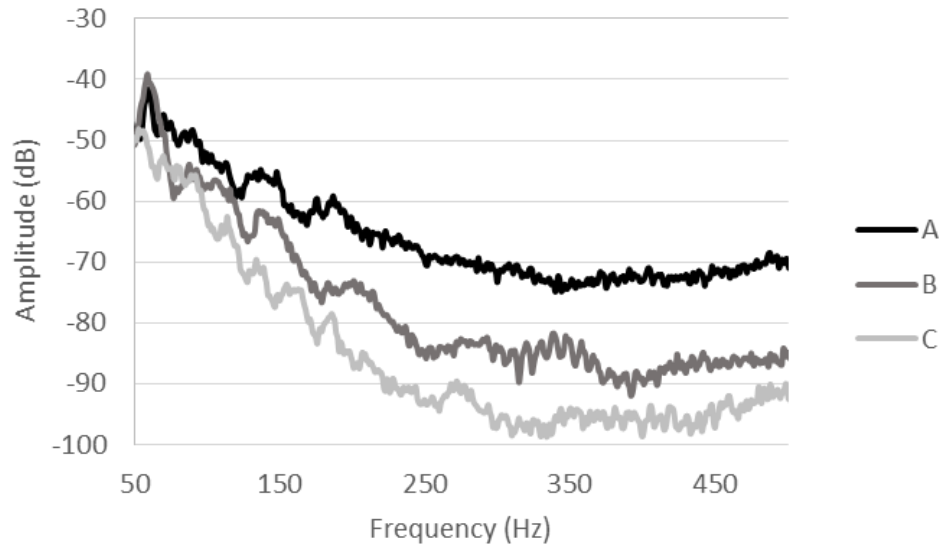


Figure 6.18 Responses at A, B, and C measured by electronic stethoscope for Reynolds number 1750, 16.5 mm phantom material thickness, 35 mmHg gauge pressure and 90% stenosis. Stenosis exit is placed at 0 mm.

Results of the contact microphone are processed using the same procedure followed for the single-point LDV analysis. The data obtained by the electronic stethoscope is the sound measured in the time domain. The measurement data of the electronic stethoscope is converted to the frequency domain by performing fast Fourier transform (FFT) with Hanning windowing. The background noise is present for the measurements of the electronic stethoscope. RMS averaging is performed utilizing 20 independent data sets. By this way, the effect of the background noise is eliminated and the trend of the responses are more clearly observed for the measurements of the electronic stethoscope. The sampling frequency of the electronic stethoscope is 4000 Hz. Each data set is composed of 4000 data to be consistent with the sampling frequency.

Results in Figure 6.17 and Figure 6.18 show that response amplitudes at position-A are the highest since it is the closest position to the highest sound generation due

to the stenosis. The highest sound generation is observed about 20 mm downstream of the stenosis exit. Secondly, the highly excited measurement position is B. The farthest measurement position to the stenosis is point C, therefore the amplitudes at point C are the lowest. From the responses, it can be clearly seen that the obstruction is around the measurement position-A.

In Figure 6.19, the stenosis exit is placed at 25 mm. For this case, the highest sound is generated at 45 mm. Position-B is located at 50 mm and therefore, it is the closest position to the highest sound generation. In the results, it is seen that the response amplitudes on position-B are the highest.

In Figure 6.20, the stenosis exit is placed at 50 mm, which means that the highest sound generation is at 70 mm. Position-C located at 75 mm is the closest position to the highest sound generation. Therefore, the response amplitudes at position-C are the highest within 50-350 Hz frequency range.

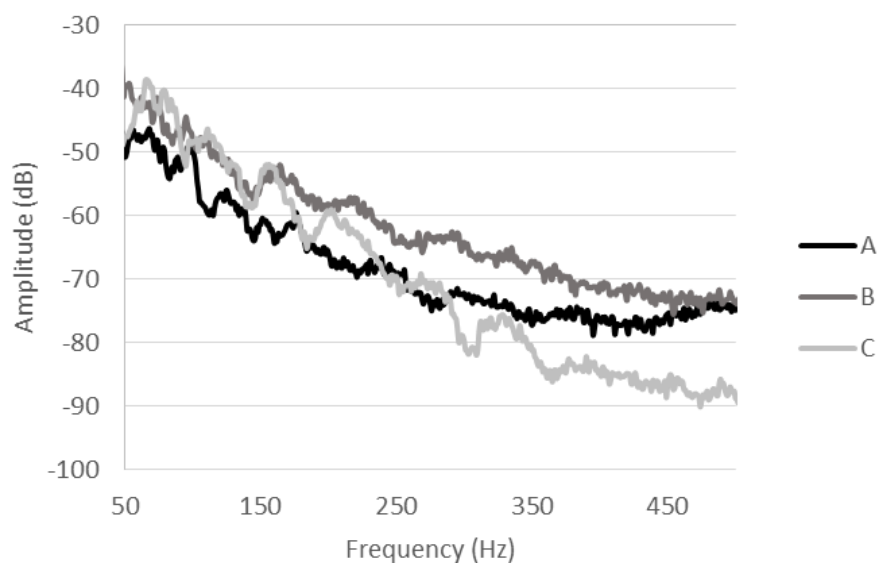


Figure 6.19 Responses at A, B, and C measured by electronic stethoscope for Reynolds number 1750, 16.5 mm phantom material thickness, 35 mmHg gauge pressure and 90% stenosis. Stenosis exit is placed at 25 mm.

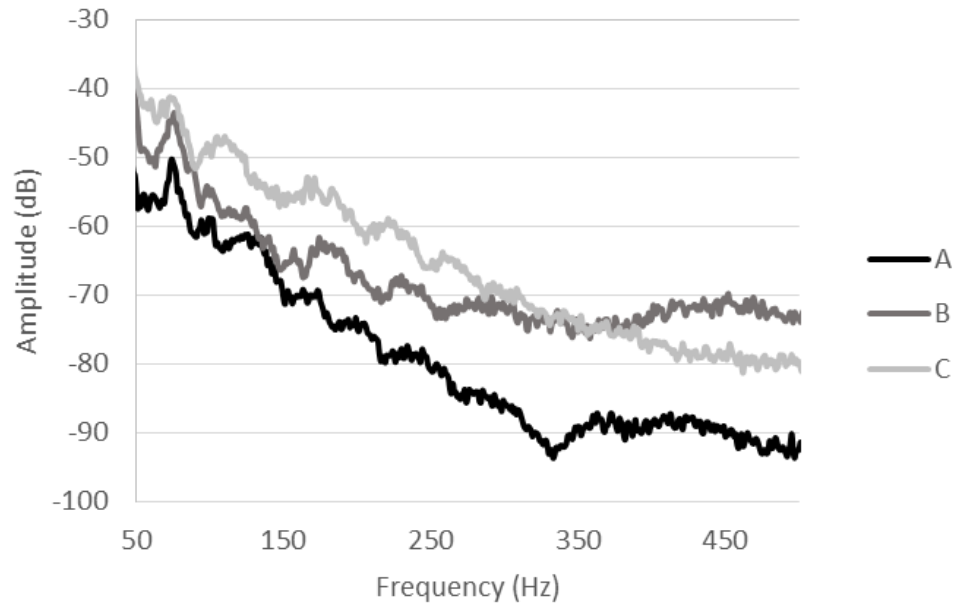


Figure 6.20 Responses at A, B, and C measured by electronic stethoscope for Reynolds number 1750, 16.5 mm phantom material thickness, 35 mmHg gauge pressure and 90% stenosis. Stenosis exit is placed at 50 mm.

For further analyses, the average of A, B and C is determined to compare the results considering different stenosis severities, Reynolds numbers and phantom material thicknesses. In Figure 6.21, the effect of stenosis severity is investigated using the measurements of the contact microphone and the electronic stethoscope.

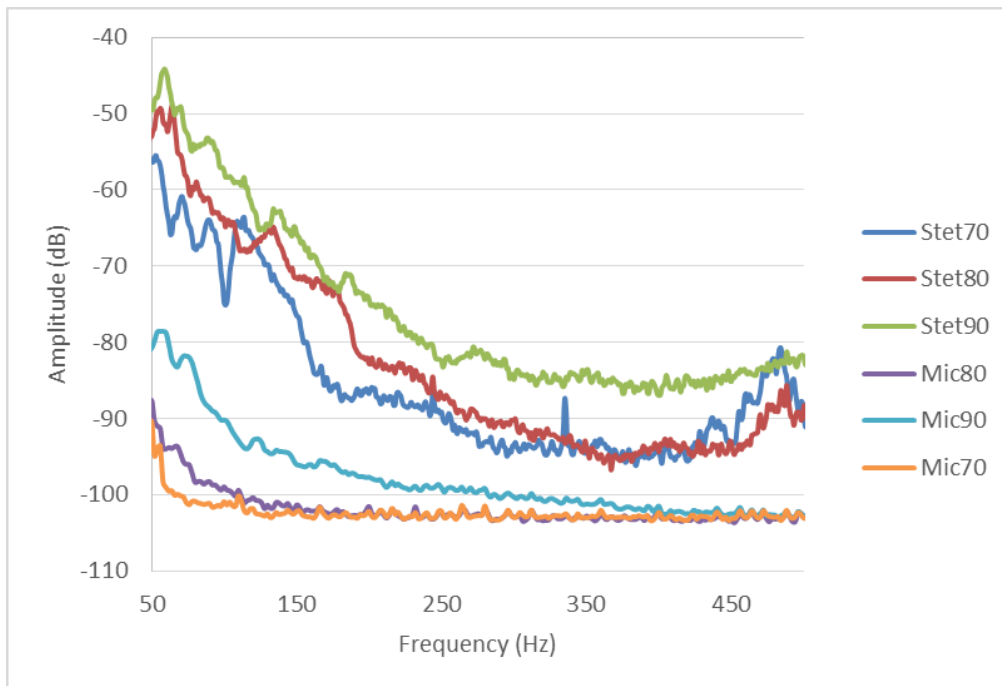


Figure 6.21 Comparison of responses for stenosis severities of 70, 80 and 90%. Reynolds number, phantom thickness and gauge pressure are 1750, 16.5 mm and 35 mmHg, respectively (Stet: Electronic stethoscope, Mic: Contact microphone).

As expected, the response amplitudes increase with the increasing stenosis severity. There is a difference about 5 dB between the results of 80 and 90% stenosis. The relative amplitude difference depending on the stenosis severity is observable up to 450 Hz for the measurements of the electronic stethoscope. The contact microphone provided information within 50-300 Hz frequency range. In Figure 6.22, the effect of phantom thickness is investigated.

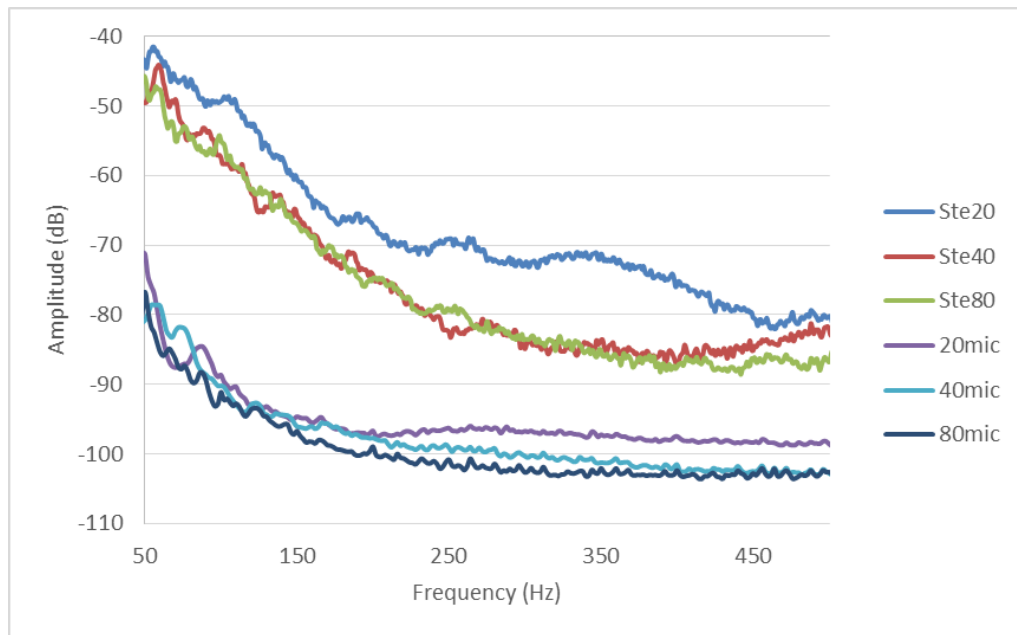


Figure 6.22 Comparison of responses for 6.5, 16.5 and 36.5 mm (20, 40 and 80 mm outer diameters) thicknesses, respectively. Reynolds number, stenosis severity and gauge pressure are 1750, 90% and 35 mmHg, respectively (Ste: Electronic stethoscope, mic: Contact microphone).

As the thickness of the phantom model decreases, the response amplitudes increase especially for 6.5 mm tissue phantom thickness corresponding to 20 mm outer diameter. The amplitude difference between the tissue thicknesses of 6.5 and 16.5 mm reaches to 10 dB. In Figure 6.23, the effect of Reynolds number is investigated using the contact microphone and the electronic stethoscope.

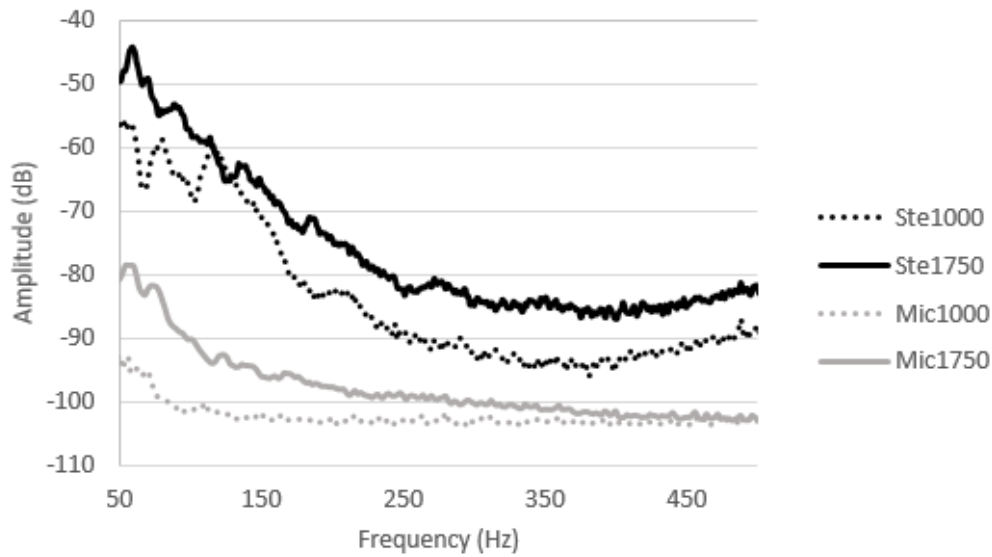


Figure 6.23 Comparison of responses for Reynolds numbers 1000 and 1750. Tissue phantom thickness, stenosis severity and gauge pressure are 16.5 mm, 90% and 35 mmHg, respectively (Ste: Electronic stethoscope, Mic: Contact microphone).

As the Reynolds number increases from 1000 to 1750, a relative amplitude increase about 5 to 10 dB is observed both in the measurements of the electronic stethoscope and the contact microphone. In Figure 6.24, the results of single-point LDV, contact microphone and electronic stethoscope are compared for a sample case. Results in Figure 6.24 indicate that the single-point LDV captures all the peaks up to 500 Hz. The electronic stethoscope clearly provides information up to 400 Hz. However, the contact microphone provides information up to only 250 Hz.

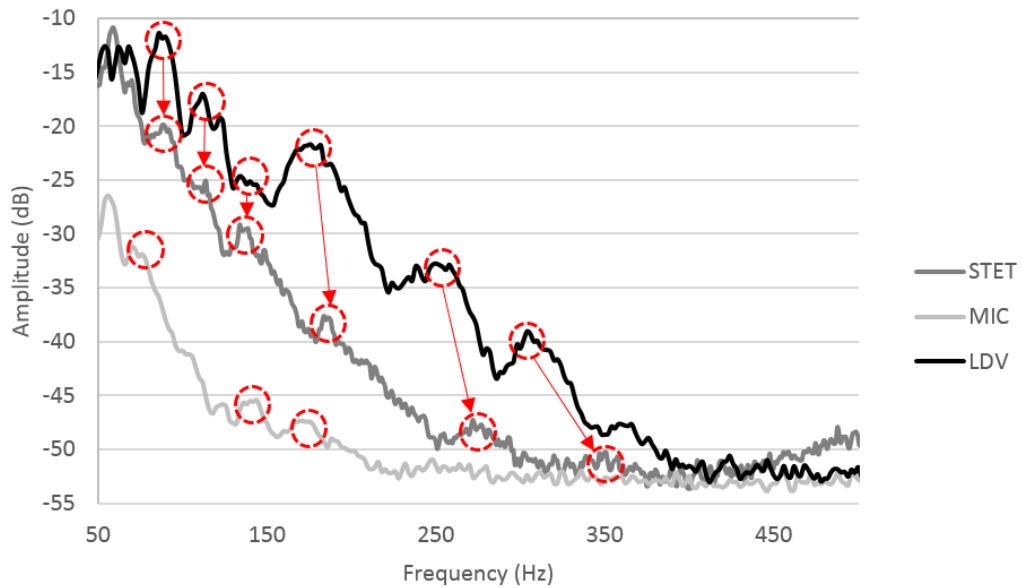


Figure 6.24 Comparison of responses using single-point LDV, contact microphone and electronic stethoscope for Reynolds number 1750, 16.5 mm tissue phantom thickness, 90% stenosis and 35 mmHg gauge pressure (STET: Electronic stethoscope, MIC: Contact microphone, LDV: Single point LDV). The peaks in the responses are shown inside the dashed circles.

LDV is a non-contacting sensor, but contact microphone and electronic stethoscope need to touch to the outer surface of the phantom model which results in a slight tissue deformation. This deformation changes the boundary conditions and leads to a small shift in the natural frequencies as shown by the arrows in Figure 6.24. The arrows showing the shifts in natural frequencies are not parallel to each other. The reason is considered as the uncontrolled deformation of the tissue phantom depending on the weight of the electronic stethoscope head. The diameter of the contacting stethoscope head is around 4 cm which is comparable to the dimensions of the tissue phantom model and this condition changes the boundary conditions of the problem domain.

CHAPTER 7

CONCLUSIONS AND FUTURE WORK

7.1 Idealized computational models

Effect of stenosis inside an artery is investigated computationally using harmonic analysis. First, radial wall velocity response of an artery is obtained without considering any surrounding soft tissue. Bending modes of the artery model is in agreement with previous findings in literature in terms of resonance frequencies and response amplitudes. For 90% stenosis with $Re = 1000$, the highest arterial vibration is about 0.025 mm/s. If the flow rate is doubled for the same case, the highest arterial vibration increases 8-fold and reach about 0.2 mm/s. This condition shows that vibration on the outer surface of the artery is approximately proportional to Re^3 .

Then, effects of surrounding soft tissue are investigated by obtaining radial velocity response on the outer surface of the tissue models. Artery model is surrounded by soft tissue models employing various thicknesses and elastic modulus values. Increasing thickness of soft tissue results in lower surface response amplitudes. Considering 0.1 and 1 MPa elastic modulus, if thickness is doubled, radial velocity amplitudes decrease about 50%; if the elastic modulus is about 10 MPa, then the radial velocity amplitudes decrease about 75% in case of doubling the thickness. When the thickness of soft tissue surrounding the artery is increased from 6.5 to 16.5 mm, the vibration amplitudes are reduced by about 35%. If the tissue thickness increases from 16.5 to 36.5 mm, the vibration amplitudes on the tissue surface drop by approximately 50%. Effect of elastic modulus is found to be more dominant when compared to the effect of tissue thickness. Increasing elastic modulus

decreases the response amplitudes and moves bending modes to the higher frequencies. Effect of phase behavior of internal dynamic pressure loading is also investigated. Without considering surrounding soft tissues, artery radial wall velocity response is affected by the phase difference, as the spectral behavior showed a difference for frequencies upper than 200 Hz. When surrounding soft tissue is taken into account in the structural model, it is observed that soft tissue played down the effect of phase difference and compensated for the change of response amplitudes in a significant amount. Based on the findings of this work, it is possible to gain an insight about constricted flow with varying amounts of area reduction and flow rate buried in different depths and stiffness of tissue including different phase behavior of pressure excitation. In all cases, severe stenosis levels with area reduction higher than 70% resulted in a serious increase in response amplitudes, which are detectable on the skin surface using state of the art sensor technologies.

In the literature, constricted flow problem is mostly studied using fluid-structure interaction analysis. Fluctuating pressures due to stenosis are obtained by solving the flow and this dynamic pressure is applied to the structural model. This coupled analysis requires high computational cost mostly because of the solution of the flow domain. In this study, fluid flow is not solved but empirical relations provided in literature are used to model and apply dynamic pressure field due to stenosis. Harmonically fluctuating pressure field is applied as forcing on the inner surface of an artery model, seriously decreasing the computational cost.

7.2 Realistic computational models

Stenotic upper arm, thigh and neck models are investigated. For the physiological peak flow rates, Reynolds number reaches 750, 1300 and 3840 in the femoral artery of the thigh, in the brachial artery of the upper arm and in the common carotid artery of the neck, respectively. Artery is surrounded by muscle, fat and skin layers by the use of realistic geometrical parameters and material properties. Radial velocity

responses are computationally obtained on the outer skin surface. It is seen that increasing stenosis severity results in nonlinearly increased response amplitudes. 70% of stenosis severity is deemed as a critical threshold for diagnostic purposes since severities higher than 70% result in serious increase in response amplitudes. If the severity of stenosis is increased from 70% to 90%, the vibration amplitudes on the outer surface of tissue increase about 10 times. Amplitude increase depending on stenosis severity is more pronounced at high frequencies, therefore the amplitude difference at frequencies higher than 200 Hz can be an indicator for the presence of a stenosis. The vibration amplitudes on the CT based thigh, upper arm and neck models are proportional to $u^{2.52}$, $u^{1.92}$ and $u^{2.02}$, respectively, where u is the flow jet velocity in the constricted region. The vibration amplitudes on the simplistic thigh, upper arm and neck models are proportional to $u^{2.19}$, $u^{2.09}$ and $u^{1.9}$. The highest proportionality constants are obtained for the thigh models due to thicker fat and muscle layers.

Anti-resonance curves are clearly observed for the simplistic thigh models and they meet near the stenosis location. If anti-resonance curves can be observed in a response map, they can be used to determine the stenosis location. As the geometry gets more complex in CT based models, anti-resonance curves may not be clearly visible. Therefore, a different approach may be used based on the sum of velocity response amplitudes for all frequencies at each spatial location within the interested frequency range. The sum of amplitudes has a maximum value around the stenosis location. In both simplistic and CT based models, the sum of response amplitudes effectively indicate the stenosis location. The first two natural frequencies are determined as 30 and 60 Hz for the thigh, 100 and 200 Hz for the upper arm, 120 and 190 Hz for the neck.

7.3 Experimental findings

The feasibility of noninvasive diagnosis of arterial stenosis is investigated both computationally and experimentally. Experiments are conducted by performing single point and scanning laser Doppler vibrometry. Results of stenosed bare tube experiments showed well agreement with the results in the literature. In bare tube analysis, increasing mean flow pressure led to circumferential pre-stress on the tube and increased the resonance frequencies. Then, the tube is surrounded by an axisymmetric bovine gelatin based tissue phantom. Radial velocity responses on the tissue phantom are obtained considering various stenosis severities, stenosis locations, tissue phantom thicknesses, mean flow pressures, and Reynolds numbers. The peak activity is observed within 1.5D and 4.5D downstream of the constriction exit where D is the unstricted inner diameter of the tube. The peak activity point moved away from the stenosis location as the tissue phantom thickness increased. For the tissue phantom thicknesses of 6.5, 16.5 and 36.5 mm, the highest excitation is observed about 7.5, 12.5 and 32.5 mm downstream of the stenosis exit, respectively. When phantom thickness is increased from 6.5 mm to 16.5 mm, the vibration amplitudes decrease by about 2 dB. If the thickness is increased from 16.5 mm to 36.5 mm, the amplitude reduction is about 6 dB. Stenosis severity significantly affects the vibration amplitudes. If the severity is increased from 70% to 80%, the amplitudes are increased about 4 dB. When the stenosis severity increases from 80% to 90%, the amplitude increase is approximately 10 dB. For a tissue phantom thickness of 16.5 mm, the vibration amplitudes on the phantom tissue surface are proportional to $Re^{1.41}$.

Material characteristics of the tissue phantom are determined by performing tension, compression, and relaxation tests. These test results are employed in the computational models using commercial finite element analysis software ADINA. Computational models agreed well with the experimental findings in terms of spectral content and amplitudes. The conclusions drawn using the experimental findings are also observed in the computational results. At low-excited regions, the

difference in computational and experimental amplitudes is related with the experimental noise at the background.

Also, a rectangular prismatic tissue phantom is employed to investigate the effect of a flat surface using scanning LDV device. Velocity amplitudes at specific frequencies showed that the structural modes of the tissue phantom are dominant between 0 and 100 Hz suppressing the effects generated by the stenosis. The relative amplitude increase at the downstream of the stenosis exit is quite visible between 100 and 700 Hz. According to the experimental results, the optimum range of frequency for detecting a stenosis is found to be between 200 and 500 Hz.

7.4 State of art sensor technologies for non-invasive diagnosis

In the experimental studies, the vibration responses on the outer surface of the tissue phantom models are investigated considering various parameters. Three different sensors are used as LDV, electronic stethoscope and contact microphone. In the experimental studies, the smallest radial velocity amplitude is obtained around the low-excited regions as $1 \mu\text{m/s}$ and the highest amplitude is measured as $300 \mu\text{m/s}$. Laser Doppler Vibrometer (IVS-300, Polytech, Auburn, MA) has a sensitivity of $0.02 \mu\text{m/s}$. Therefore, LDV can capture even the smallest effects generated due to the flow-induced vibration and can be effectively used for diagnosing purposes. Although, it can measure the effects precisely, high cost of the device is a disadvantage for LDV.

The contact microphone (CM-01B, Measurement Specialties, VA) provides limited information up to 300 Hz. The optimum upper limit of frequency is 500 Hz for investigating the effects of stenosis. Therefore, the contact microphone is not capable of capturing the effects due to the stenosis within 300-500 Hz. The limited measuring capacity at high frequencies creates a handicap for the contact microphone. The electronic stethoscope (Litmann 3200, 3M, MN) records the sounds emitted from the stenosis. It is considered as the most suitable sensor in

terms of cost-accuracy balance. The stenosis-based effects measured by LDV can be captured up to 500 Hz using the electronic stethoscope which can be effectively used for non-invasive diagnosis in a cheap and accurate manner.

7.5 Future improvements

The focus of the current study is the peripheral arteries having large-diameter lumens with high vibroacoustic generation. As for the future improvements, coronary arteries can be investigated by using the same approach in addition to more advanced temporal and spectral filtering techniques. Advanced signal processing techniques can be performed as cepstrum analysis by taking the inverse Fourier transform of the interested signal and also superharmonic responses can be investigated. In addition, wavelet analysis can be performed to provide localized temporal and spectral information.

Non-Newtonian fluid behavior and the pulsatile nature of blood flow can be considered for further improvement. The effect of different stenosis shapes can be investigated considering tapered, one sided and CT based complex and more realistic constriction profiles. The stenosis inside peripheral arteries may affect the hemodynamics of the cardiovascular circulation system. Therefore, a more detailed full-body circulation model such as lumped-parameter model can be used to better estimate the physiological conditions in the arteries in case of a stenosis.

Damping models can be improved considering the frequency dependency of the damping values. Rayleigh damping models can be employed to model the damping behavior proportional to the mass and stiffness of the tissue. Experimental studies can be performed to better understand the modal damping characteristics of the human soft tissues. In addition, the results, findings and methods proposed in the current investigation can be utilized in future studies with the aim of diagnosing cardiovascular diseases by employing machine learning algorithms.

REFERENCES

- [1] A. Maton, *Human Biology and Health*, Prentice Hall, 1997.

- [2] W. Rosamond, K. Flegal, G. Friday, K. Furie, A. Go, K. Greenlund, N. Haase, M. Ho, V. Howard, B. Kissela, S. Kittner, D. Lloyd-Jones, M. McDermott, J. Meigs, C. Moy, G. Nichol, C. J. O'Donnell, V. Roger, J. Rumsfeld, P. Sorlie, J. Steinberger, T. Thom, S. Wasserthiel-Smoller and Y. Hong, "Heart disease and stroke statistics - 2007 update: a report from the American Heart Association Statistics Committee and Stroke Statistics Subcommittee," *Circulation*, vol. 115, no. 5, pp. e69-e171, 2007.

- [3] V. L. Feigin, "Stroke epidemiology in the developing world," *Lancet*, vol. 365, no. 9478, pp. 2160-2161, 2005.

- [4] N. W. Shamma, "Epidemiology, classification, and modifiable risk factors of peripheral arterial disease," *Vascular Health and Risk Management*, vol. 3, no. 2, pp. 229-234, 2007.

- [5] S. Glagov, E. Weisenberg, C. K. Zarins, R. Stankunavicius, G. J. Kolettis, "Compensatory enlargement of human atherosclerotic coronary arteries," *New England Journal of Medicine*, vol. 316, no. 22, pp. 1371-1375, 1987.

- [6] S. E. Nissen, S. J. Nicholls, I. Sipahi, P. Libby, J. S. Raichlen, C. M. Ballantyne, J. Davignon, R. Erbel, J. C. Fruchart, J. Tardif, P. Schoenhagen, T. Crowe, V. Cain, K. Wolski, M. Goormastic and E. M. Tuzcu, "Effect of very high-intensity statin therapy on regression of coronary atherosclerosis: The asteroid trial," *Journal of the American Medical Association*, vol. 295, no. 13, pp. 1556-1565, 2006.
- [7] A. O. Borisyuk, "Experimental study of wall pressure fluctuations in a pipe behind a stenosis," *International Journal of Fluid Mechanics Research*, vol. 30, no. 3, pp. 264-278, 2003.
- [8] "Cardiac Surgery Academy web site," [Online]. Available: <http://cardiacsurgeryacademy.org/Coronary-Angiogram.html>. [Accessed 27 December 2012].
- [9] D. F. Young, "Fluid mechanics of arterial stenoses," *Journal of Biomechanical Engineering*, vol. 101, no. 3, pp. 157-175, 1979.
- [10] J. S. Stroud, S. A. Berger and D. Saloner, "Numerical analysis of flow through a severely stenotic carotid artery bifurcation," *Journal of Biomechanical Engineering*, vol. 124, no. 1, pp. 9-20, 2002.
- [11] P. Doriot, P. Dorsaz, L. Dorsaz and W. Rutishauser, "Overestimation of stenosis severity by single plane geometric measurements," *Computers in Cardiology*, pp. 109-112, 1996.

- [12] D. L. Bruns, "A general theory of the causes of murmurs in the cardiovascular system," *The American Journal of Medicine*, vol. 27, no. 3, pp. 360-374, 1959.
- [13] R. S. Lees and C. F. Dewey, "Phonoangiography: a new noninvasive diagnostic method for studying arterial disease," *Proceedings of the National Academy of Sciences of the United States of America*, vol. 67, no. 2, pp. 935-942, 1970.
- [14] H. P. Bakewell, G. F. Carey, J. J. Libuha, H. H. Schloemer and W. A. V. Winkle, "Wall Pressure Correlations in Turbulent Pipe Flow," U.S. Navy Underwater Sound Laboratory Report 559-1-052-00-00, 1962.
- [15] J. Fredberg, "Pseudo-Sound Generation at Atherosclerotic Constrictions in Arteries," Massachusetts Institute of Technology, Fluid Mechanics Laboratory, no. 72-9, 1972.
- [16] J. J. Fredberg, "Origin and character of vascular murmurs: model studies," *Journal of the Acoustical Society of America*, vol. 61, no. 4, pp. 1077-1085, 1977.
- [17] G. W. Duncan, J. O. Gruber, C. F. Dewey, G. S. Myers and R. S. Lees, "Evaluation of carotid stenosis by phonoangiography," *New England Journal of Medicine*, vol. 293, no. 22, pp. 1124-1128, 1975.

- [18] A. O. Borisyuk, "Model study of noise field in the human chest due to turbulent flow in a larger blood vessel," *Journal of Fluids and Structures*, vol. 17, no. 8, pp. 1095-1110, 2003.
- [19] A. O. Borisyuk, "Modeling of noise generation by a vascular stenosis," *International Journal of Fluid Mechanics Research*, vol. 29, no. 1, pp. 65-86, 2002.
- [20] W. Jin-Zhao, T. Bing, W. Welkowitz, J. L. Semmlow and J. B. Kostis, "Modeling sound generation in stenosed coronary arteries," *IEEE Transactions on Biomedical Engineering*, vol. 37, no. 11, pp. 1087-1094, 1990.
- [21] R. A. Cassanova and D. P. Giddens, "Disorder distal to modeled stenoses in steady and pulsatile flow," *Journal of Biomechanics*, vol. 11, no. 10-12, pp. 441-453, 1978.
- [22] Y. Yazicioglu, T. J. Royston, T. Spohnholtz, B. Martin, F. Loth and H. S. Bassiouny, "Acoustic radiation from a fluid-filled, subsurface vascular tube with internal turbulent flow due to a constriction," *Journal of the Acoustical Society of America*, vol. 118, no. 2, pp. 1193-1209, 2005.
- [23] R. J. Tobin and I. D. Chang, "Wall pressure spectra scaling downstream of stenoses in steady tube flow," *Journal of Biomechanics*, vol. 9, no. 10, pp. 633-640, 1976.

- [24] H. E. Salman, C. Sert and Y. Yazicioglu, "Computational analysis of high frequency fluid-structure interactions in constricted flow," *Computers & Structures*, vol. 122, pp. 145-154, 2013.
- [25] J. H. Seo and R. Mittal, "A coupled flow-acoustic computational study of bruits from a modeled stenosed artery," *Medical and Biological Engineering and Computing*, vol. 50, no. 10, pp. 1025-1035, 2012.
- [26] S. E. Lee, S. Lee, P. F. Fischer, H. S. Bassiouny and F. Loth, "Direct numerical simulation of transitional flow in a stenosed carotid bifurcation," *Journal of Biomechanics*, vol. 41, no. 11, pp. 2551-2561, 2008.
- [27] K. Khanafer and R. Berguer, "Fluid-structure interaction analysis of turbulent pulsatile flow within a layered aortic wall as related to aortic dissection," *Journal of Biomechanics*, vol. 42, no. 16, pp. 2642-2648, 2009.
- [28] D. Tang, C. Yang, Y. Huang and D. N. Ku, "Wall stress and strain analysis using a three-dimensional thick-wall model with fluid-structure interactions for blood flow in carotid arteries with stenoses," *Computers and Structures*, vol. 72, no. 1, pp. 341-356, 1999.
- [29] A. Valencia and M. Villanueva, "Unsteady flow and mass transfer in models of stenotic arteries considering fluid-structure interaction," *International Communications in Heat and Mass Transfer*, vol. 33, no. 8, pp. 966-975, 2006.

- [30] D. Tang, J. Yang, C. Yang and D. N. Ku, "A nonlinear axisymmetric model with fluid-wall interactions for steady viscous flow in stenotic elastic tubes," *Journal of Biomechanical Engineering*, vol. 121, no. 5, pp. 494-501, 1999.
- [31] T. Shurtz, *Analysis of Induced Vibrations in Fully-Developed Turbulent Pipe Flow using a Coupled LES and FEA Approach*, M.Sc. Thesis in Brigham Young University, 2009.
- [32] J. Semmlow, W. Welkowitz, J. Kostis and J. W. Mackenzie, "Coronary artery disease: correlates between diastolic auditory characteristics and coronary artery stenoses," *IEEE Transactions on Biomedical Engineering*, vol. 30, no. 2, pp. 136-139, 1983.
- [33] M. Akay, J. L. Semmlow, W. Welkowitz, M. D. Bauer and J. B. Kostis, "Detection of coronary occlusions using autoregressive modeling of diastolic heart sounds," *IEEE Transactions on Biomedical Engineering*, vol. 37, no. 4, pp. 366-373, 1990.
- [34] N. L. Owsley, A. J. Hull, "Beamformed nearfield imaging of a simulated coronary artery containing a stenosis," *IEEE Transactions on Medical Imaging*, vol. 17, no. 6, pp. 900-909, 1998.
- [35] N. Owsley, A. Hull, M. Ahmed and J. Kassal, "A proof-of-concept experiment for the detection of occluded coronary arteries using array sensor technology," in *IEEE Engineering in Medicine and Biology 17th Annual Conference*, Montreal, PQ, Canada, 1995.

- [36] W. H. Pitts and C. F. Dewey, "Spectral and temporal characteristics of post-stenotic turbulent wall pressure fluctuations," *Journal of Biomechanical Engineering*, vol. 101, no. 2, pp. 89-95, 1979.
- [37] H. T. Banks, S. Hu, Z. R. Kenz, C. Kruse, S. Shaw, J. Whiteman, M. P. Brewin, S. E. Greenwald and M. J. Birch, "Model validation for a noninvasive arterial stenosis detection problem," *Mathematical Biosciences and Engineering: MBE*, vol. 11, no. 3, p. 427, 2014.
- [38] F. Azimpour, E. Caldwell, P. Tawfik, S. Duval and R. F. Wilson, "Audible coronary artery stenosis," *The American Journal of Medicine*, vol. 129, no. 5, pp. 515-521, 2016.
- [39] J. Semmlow and K. Rahalkar, "Acoustic detection of coronary artery disease," *Annual Review of Biomedical Engineering*, vol. 9, pp. 449-469, 2007.
- [40] K. Tomczak and R. Kaszynski, "A nonlinear analysis of vibration properties of intracranial saccular aneurysms," in *Advances in Systems Science*, Springer, 2014, pp. 513-521.
- [41] A. Lowe, W. Harrison, E. El-Aklouk, P. Ruygrok and A. Al-Jumaily, "Non-invasive model-based estimation of aortic pulse pressure using suprasystolic brachial pressure waveforms," *Journal of Biomechanics*, vol. 42, no. 13, pp. 2111-2115, 2009.

- [42] A. Campo, P. Segers, H. Heuten, I. Goovaerts, G. Ennekens, C. Vrints, R. Baets and J. Dirckx, "Non-invasive technique for assessment of vascular wall stiffness using laser Doppler vibrometry," *Measurement Science and Technology*, vol. 25, no. 6, p. 065701, 2014.
- [43] A. Campo and J. Dirckx, "Dual-beam laser Doppler vibrometer for measurement of pulse wave velocity in elastic vessels," in *Proceedings SPIE*, 2011.
- [44] "Volume I: ADINA Solids & Structures," in *ADINA Theory and Modeling Guide*, Massachusetts, ADINA R&D Inc., 2012.
- [45] K. J. Bathe and E. L. Wilson, "Solution methods for eigenvalue problems in structural mechanics," *International Journal for Numerical Methods in Engineering*, vol. 6, no. 2, pp. 213-226, 1973.
- [46] R. W. Clough and J. Penzien, *Dynamics of structures*, Computers & Structures Inc., 2003.
- [47] W. C. Hurty and M. F. Rubinstein, "Dynamics of structures," *Prentice-Hall Series in Engineering of the Physical Sciences, Englewood Cliffs: Prentice-Hall*, 1964.
- [48] T. Sussman and J. Sundqvist, "Fluid-structure interaction analysis with a subsonic potential-based fluid formulation," *Computers & Structures*, vol. 81, no. 8, pp. 949-962, 2003.

- [49] L. G. Olson and K. J. Bathe, "Analysis of fluid-structure interactions. A direct symmetric coupled formulation based on the fluid velocity potential," *Computers & Structures*, vol. 21, no. 1-2, pp. 21-32, 1985.
- [50] L. G. Olson and K.-J. Bathe, "A study of displacement-based fluid finite elements for calculating frequencies of fluid and fluid-structure systems," *Nuclear Engineering and Design*, vol. 76, no. 2, pp. 137-151, 1983.
- [51] A. Borisyuk, "Experimental study of noise produced by steady flow through a simulated vascular stenosis," *Journal of Sound and Vibration*, vol. 256, no. 3, pp. 475-498, 2002.
- [52] A. Borisyuk, "Experimental study of wall pressure fluctuations in rigid and elastic pipes behind an axisymmetric narrowing," *Journal of Fluids and Structures*, vol. 26, no. 4, pp. 658-674, 2010.
- [53] W. L. Keith and B. M. Abraham, "Effects of convection and decay of turbulence on the wall pressure wavenumber-frequency spectrum," *Journal of Fluids Engineering, Transactions of the ASME*, vol. 119, no. 1, pp. 50-55, 1997.
- [54] Y. M. Akay, M. Akay, W. Welkowitz, J. L. Semmlow and J. B. Kostis, "Noninvasive acoustical detection of coronary artery disease: a comparative study of signal processing methods," *IEEE Transactions on Biomedical Engineering*, vol. 40, no. 6, pp. 571-578, 1993.

- [55] J. Ness and W. S. Aronow, "Prevalence of coexistence of coronary artery disease, ischemic stroke, and peripheral arterial disease in older persons, mean age 80 years, in an academic hospital-based geriatrics practice," *Journal of the American Geriatrics Society*, vol. 47, no. 10, pp. 1255-1256, 1999.
- [56] C. Clark, "The fluid mechanics of aortic stenosis—I. Theory and steady flow experiments," *Journal of Biomechanics*, vol. 9, no. 8, pp. 521-528, 1976.
- [57] C. Clark, "Turbulent wall pressure measurements in a model of aortic stenosis," *Journal of Biomechanics*, vol. 10, no. 8, pp. 461-472, 1977.
- [58] R. L. Kirkeeide, D. F. Young and N. R. Cholvin, "Wall vibrations induced by flow through simulated stenoses in models and arteries," *Journal of Biomechanics*, vol. 10, no. 7, pp. 431-437, 1977.
- [59] J. Z. Wang, B. Tie, W. Welkowitz, J. Semmlow and J. Kostis, "Modeling sound generation in stenosed coronary arteries," *IEEE Transactions on Biomedical Engineering*, vol. 37, no. 11, pp. 1087-1094, 1990.
- [60] H. A. Chami, M. J. Keyes, J. A. Vita, G. F. Mitchell, M. G. Larson, S. Fan, R. S. Vasani, G. T. O'Connor, E. J. Benjamin and D. J. Gottlieb, "Brachial artery diameter, blood flow and flow-mediated dilation in sleep-disordered breathing," *Vascular Medicine*, vol. 14, no. 4, pp. 351-360, 2009.

- [61] T. Sandgren, B. Sonesson, R. Ahlgren and T. Lanne, "The diameter of the common femoral artery in healthy human: influence of sex, age, and body size," *Journal of Vascular Surgery*, vol. 29, no. 3, pp. 503-510, 1999.
- [62] H. E. Salman and Y. Yazicioglu, "Flow-induced vibration analysis of constricted artery models with surrounding soft tissue," *The Journal of the Acoustical Society of America*, vol. 142, no. 4, pp. 1913-1925, 2017.
- [63] S. M. Jain, K. Pandey, A. Lahoti and P. K. Rao, "Evaluation of skin and subcutaneous tissue thickness at insulin injection sites in Indian, insulin naive, type-2 diabetic adult population," *Indian Journal of Endocrinology and Metabolism*, vol. 17, no. 5, p. 864, 2013.
- [64] J. Z. Wu, D. E. Welcome and R. G. Dong, "Three-dimensional finite element simulations of the mechanical response of the fingertip to static and dynamic compressions," *Computer Methods in Biomechanics and Biomedical Engineering*, vol. 9, no. 1, pp. 55-63, 2006.
- [65] G. A. Holzapfel, *The handbook of materials behavior models*, Academic Press, 2001.
- [66] M. Freutel, H. Schmidt, L. Dürselen, A. Ignatius and F. Galbusera, "Finite element modeling of soft tissues: Material models, tissue interaction and challenges," *Clinical Biomechanics*, vol. 29, no. 4, pp. 363-372, 2014.
- [67] V. C. Mow and R. Huiskes, *Basic orthopaedic biomechanics & mechanobiology*, Lippincott Williams & Wilkins, 2005.

- [68] Y. C. Fung, *Biomechanics: mechanical properties of living tissues*, Springer Science & Business Media, 2013.
- [69] D. J. Schneck and J. D. Bronzino, *Biomechanics: principles and applications*, CRC press, 2002.
- [70] J. H. Chung, V. Rajagopal, P. M. F. Nielsen and M. P. Nash, "A biomechanical model of mammographic compressions," *Biomechanics and Modeling in Mechanobiology*, vol. 7, no. 1, pp. 43-52, 2008.
- [71] A. Delalleau, G. Josse, J. Lagarde, H. Zahouani and J. Bergheau, "A nonlinear elastic behavior to identify the mechanical parameters of human skin in vivo," *Skin Research and Technology*, vol. 14, no. 2, pp. 152-164, 2008.
- [72] F. M. Hendriks, D. Brokken, J. T. W. M. van Eemeren, C. W. J. Oomens, F. P. T. Baaijens and J. B. A. M. Horsten, "A numerical-experimental method to characterize the non-linear mechanical behavior of human skin," *Skin Research and Technology*, vol. 9, no. 3, pp. 274-283, 2003.
- [73] F. M. Hendriks, D. Brokken, C. W. J. Oomens and F. P. T. Baaijens, "Influence of hydration and experimental length scale on the mechanical response of human skin in vivo, using optical coherence tomography," *Skin Research and Technology*, vol. 10, no. 4, pp. 231-241, 2004.

- [74] A. Samani, J. Bishop, M. J. Yaffe and D. B. Plewes, "Biomechanical 3-D finite element modeling of the human breast using MRI data," *IEEE Transactions on Medical Imaging*, vol. 20, no. 4, pp. 271-279, 2001.
- [75] V. Rajagopal, A. Lee, J. H. Chung, R. Warren, R. P. Highnam, P. M. Nielsen and M. P. Nash, "Towards tracking breast cancer across medical images using subject-specific biomechanical models," *MICCAI International Conference on Medical Image Computing and Computer-Assisted Intervention*, vol. 10, pp. 651-658, 2007.
- [76] R. W. Ogden, *Non-linear elastic deformations*, Courier Dover Publications, 1997.
- [77] M. Mooney, "A theory of large elastic deformation," *Journal of Applied Physics*, vol. 11, no. 9, pp. 582-592, 1940.
- [78] R. Rivlin, "Large elastic deformations of isotropic materials. IV. Further developments of the general theory," *Philosophical Transactions of the Royal Society of London. Series A, Mathematical and Physical Sciences*, vol. 241, no. 835, pp. 379-397, 1948.
- [79] A. N. Gent, *Engineering with rubber: how to design rubber components*, Carl Hanser Verlag GmbH Co KG, 2012.
- [80] R. W. Ogden, "Large deformation isotropic elasticity - on the correlation of theory and experiment for incompressible rubberlike solids," *Rubber Chemistry and Technology*, vol. 46, no. 2, pp. 398-416, 1973.

- [81] G. A. Holzapfel, T. C. Gasser and R. W. Ogden, "A new constitutive framework for arterial wall mechanics and a comparative study of material models," *Journal of Elasticity*, vol. 61, no. 1-3, pp. 1-48, 2000.
- [82] J. A. Weiss and J. C. Gardiner, "Computational modeling of ligament mechanics," *Critical Reviews in Biomedical Engineering*, vol. 29, no. 3, pp. 303-371, 2001.
- [83] J. T. Iivarinen, R. K. Korhonen, P. Julkunen and J. S. Jurvelin, "Experimental and computational analysis of soft tissue stiffness in forearm using a manual indentation device," *Medical Engineering and Physics*, vol. 33, no. 10, pp. 1245-1253, 2011.
- [84] S. Portnoy, Z. Yizhar, N. Shabshin, Y. Itzchak, A. Kristal, Y. Dotan-Marom, I. Siev-Ner and A. Gefen, "Internal mechanical conditions in the soft tissues of a residual limb of a trans-tibial amputee," *Journal of Biomechanics*, vol. 41, no. 9, pp. 1897-1909, 2008.
- [85] A. P. del Palomar, B. Calvo, J. Herrero, J. López and M. Doblaré, "A finite element model to accurately predict real deformations of the breast," *Medical Engineering and Physics*, vol. 30, no. 9, pp. 1089-1097, 2008.
- [86] A. M. Sims, T. Stait-Gardner, L. Fong, J. W. Morley, W. S. Price, M. Hoffman, A. Simmons and K. Schindhelm, "Elastic and viscoelastic properties of porcine subdermal fat using MRI and inverse FEA," *Biomechanics and Modeling in Mechanobiology*, vol. 9, no. 6, pp. 703-711, 2010.

- [87] H. V. Tran, F. Charleux, M. Rachik, A. Ehrlacher and M. C. Ho Ba Tho, "In vivo characterization of the mechanical properties of human skin derived from MRI and indentation techniques," *Computer Methods in Biomechanics and Biomedical Engineering*, vol. 10, no. 6, pp. 401-407, 2007.
- [88] M. Geerligs, L. van Breemen, G. Peters, P. Ackermans, F. Baaijens and C. Oomens, "In vitro indentation to determine the mechanical properties of epidermis," *Journal of Biomechanics*, vol. 44, no. 6, pp. 1176-1181, 2011.
- [89] E. Samur, M. Sedef, C. Basdogan, L. Avtan and O. Duzgun, "A robotic indenter for minimally invasive measurement and characterization of soft tissue response," *Medical Image Analysis*, vol. 11, no. 4, pp. 361-373, 2007.
- [90] T. Sussman and K. J. Bathe, "A model of incompressible isotropic hyperelastic material behavior using spline interpolations of tension-compression test data," *Communications in Numerical Methods in Engineering*, vol. 25, no. 1, pp. 53-63, 2009.
- [91] R. S. Rivlin and D. Saunders, "Large elastic deformations of isotropic materials. VII. Experiments on the deformation of rubber," *Philosophical Transactions of the Royal Society of London A: Mathematical, Physical and Engineering Sciences*, vol. 243, no. 865, pp. 251-288, 1951.
- [92] N. Huber and C. Tsakmakis, "Finite deformation viscoelasticity laws," *Mechanics of Materials*, vol. 32, no. 1, pp. 1-18, 2000.

- [93] A. Amin, M. Alam and Y. Okui, "An improved hyperelasticity relation in modeling viscoelasticity response of natural and high damping rubbers in compression: experiments, parameter identification and numerical verification," *Mechanics of Materials*, vol. 34, no. 2, pp. 75-95, 2002.
- [94] G. A. Holzapfel, T. C. Gasser and M. Stadler, "A structural model for the viscoelastic behavior of arterial walls: continuum formulation and finite element analysis," *European Journal of Mechanics, A/Solids*, vol. 21, no. 3, pp. 441-463, 2002.
- [95] M. Van Loocke, C. G. Lyons and C. K. Simms, "Viscoelastic properties of passive skeletal muscle in compression: stress-relaxation behaviour and constitutive modelling," *Journal of Biomechanics*, vol. 41, no. 7, pp. 1555-1566, 2008.
- [96] J. Wu, R. Dong and D. Welcome, "Analysis of the point mechanical impedance of fingerpad in vibration," *Medical Engineering & Physics*, vol. 28, no. 8, pp. 816-826, 2006.
- [97] J. Anderson, Z. Li and F. Goubel, "Models of skeletal muscle to explain the increase in passive stiffness in desmin knockout muscle," *Journal of Biomechanics*, vol. 35, no. 10, pp. 1315-1324, 2002.
- [98] J. Anderson, Z. Li and F. Goubel, "Passive stiffness is increased in soleus muscle of desmin knockout mouse," *Muscle and Nerve*, vol. 24, no. 8, pp. 1090-1092, 2001.

- [99] S. Bensamoun, L. Stevens, M. J. Fleury, G. Bellon, F. Goubel and M. C. Ho Ba Tho, "Macroscopic-microscopic characterization of the passive mechanical properties in rat soleus muscle," *Journal of Biomechanics*, vol. 39, no. 3, pp. 568-578, 2006.
- [100] T. M. Best, "Characterization of the passive responses of live skeletal muscle using the quasi-linear theory of viscoelasticity," *Journal of Biomechanics*, vol. 27, no. 4, pp. 413-419, 1994.
- [101] E. M. H. Bosboom, M. K. C. Hesselink, C. W. J. Oomens, C. V. C. Bouten, M. R. Drost and F. P. T. Baaijens, "Passive transverse mechanical properties of skeletal muscle under in vivo compression," *Journal of Biomechanics*, vol. 34, no. 10, pp. 1365-1368, 2001.
- [102] G. J. C. Ettema and P. A. Huijing, "Frequency response of rat gastrocnemius medialis in small amplitude vibrations," *Journal of Biomechanics*, vol. 27, no. 8, pp. 1015-1022, 1994.
- [103] F. Gottsauner-Wolf, J. J. Grabowski, E. Chao and K. N. An, "Effects of freeze/thaw conditioning on the tensile properties and failure mode of bone-muscle-bone units: a biomechanical and histological study in dogs," *Journal of Orthopaedic Research*, vol. 13, no. 1, pp. 90-95, 1995.
- [104] L. Gras, D. Mitton, N. Crevier-Denoix and S. Laporte, "The non-linear response of a muscle in transverse compression: assessment of geometry influence using a finite element model," *Computer Methods in Biomechanics and Biomedical Engineering*, vol. 15, no. 1, pp. 13-21, 2012.

- [105] D. Hawkins and M. Bey, "Muscle and tendon force-length properties and their interactions in vitro," *Journal of Biomechanics*, vol. 30, no. 1, pp. 63-70, 1997.
- [106] R. Lin, G. Chang and L. Chang, "Biomechanical properties of muscle-tendon unit under high-speed passive stretch," *Clinical Biomechanics*, vol. 14, no. 6, pp. 412-417, 1999.
- [107] A. Chawla, S. Mukherjee and B. Karthikeyan, "Characterization of human passive muscles for impact loads using genetic algorithm and inverse finite element methods," *Biomechanics and Modeling in Mechanobiology*, vol. 8, no. 1, pp. 67-76, 2009.
- [108] C. Untaroiu, K. Darvish, J. Crandall, B. Deng and J.-T. Wang, "Characterization of the lower limb soft tissues in pedestrian finite element models," in *19th International Technical Conference on the Enhanced Safety of Vehicles*, 2005.
- [109] L. Gras, D. Mitton, P. Viot and S. Laporte, "Hyper-elastic properties of the human sternocleidomastoideus muscle in tension," *Journal of the Mechanical Behavior of Biomedical Materials*, vol. 15, pp. 131-140, 2012.
- [110] E. Linder-Ganz and A. Gefen, "Mechanical compression-induced pressure sores in rat hindlimb: muscle stiffness, histology, and computational models," *Journal of Applied Physiology*, vol. 96, no. 6, pp. 2034-2049, 2004.

- [111] S. W. Ohl, E. Klaseboer and B. C. Khoo, "The dynamics of a non-equilibrium bubble near bio-materials," *Physics in Medicine and Biology*, vol. 54, no. 20, pp. 6313-6336, 2009.
- [112] S. F. Levinson, M. Shinagawa and T. Sato, "Sonoelastic determination of human skeletal muscle elasticity," *Journal of Biomechanics*, vol. 28, no. 10, pp. 1145-1154, 1995.
- [113] A. S. Zil'bergleit, I. N. Zlatina, V. S. Sinyakov and M. I. Khaikova, "A method of measuring the modulus of elasticity of human muscle tissue," *Bulletin of Experimental Biology and Medicine*, vol. 96, no. 6, pp. 1781-1785, 1983.
- [114] J. L. Gennisson, C. Cornu, S. Catheline, M. Fink and P. Portero, "Human muscle hardness assessment during incremental isometric contraction using transient elastography," *Journal of Biomechanics*, vol. 38, no. 7, pp. 1543-1550, 2005.
- [115] A. Gefen and S. S. Margulies, "Are in vivo and in situ brain tissues mechanically similar?," *Journal of Biomechanics*, vol. 37, no. 9, pp. 1339-1352, 2004.
- [116] S. L. Cox, K. Mithraratne and N. P. Smith, "An anatomically based finite element model of the lower limbs in the seated posture," *Conference Proceedings : Annual International Conference of the IEEE Engineering in Medicine and Biology Society*, pp. 6327-6330, 2007.

- [117] Z. Jia, Z. Du and W. Monan, "A novel finite element method based biomechanical model for HIT-robot assisted orthopedic surgery system," *Conference Proceedings: Annual International Conference of the IEEE Engineering in Medicine and Biology Society*, pp. 1735-1738, 2006.
- [118] J. Z. Wu, R. G. Dong, W. P. Smutz and A. W. Schopper, "Modeling of time-dependent force response of fingertip to dynamic loading," *Journal of Biomechanics*, vol. 36, no. 3, pp. 383-392, 2003.
- [119] J. Z. Wu, R. G. Dong and A. W. Schopper, "Analysis of effects of friction on the deformation behavior of soft tissues in unconfined compression tests," *Journal of Biomechanics*, vol. 37, no. 1, pp. 147-155, 2004.
- [120] C. Flynn and B. A. O. McCormack, "Finite element modelling of forearm skin wrinkling," *Skin Research and Technology*, vol. 14, no. 3, pp. 261-269, 2008.
- [121] F. M. Hendriks, D. Brokken, C. W. J. Oomens, D. L. Bader and F. P. T. Baaijens, "The relative contributions of different skin layers to the mechanical behavior of human skin in vivo using suction experiments," *Medical Engineering and Physics*, vol. 28, no. 3, pp. 259-266, 2006.
- [122] T. Johansson, P. Meier and R. Blickhan, "A finite-element model for the mechanical analysis of skeletal muscles," *Journal of Theoretical Biology*, vol. 206, no. 1, pp. 131-149, 2000.

- [123] J. A. Weiss, B. N. Maker and S. Govindjee, "Finite element implementation of incompressible, transversely isotropic hyperelasticity," *Computer Methods in Applied Mechanics and Engineering*, vol. 135, no. 1-2, pp. 107-128, 1996.
- [124] S. Hedenstierna, P. Halldin and G. P. Siegmund, "Neck muscle load distribution in lateral, frontal, and rear-end impacts: A three-dimensional finite element analysis," *Spine*, vol. 34, no. 24, pp. 2626-2633, 2009.
- [125] M. Behr, P. Arnoux, T. Serre, L. Thollon and C. Brunet, "Tonic finite element model of the lower limb," *Journal of Biomechanical Engineering*, vol. 128, no. 2, pp. 223-228, 2006.
- [126] S. S. Blemker, P. M. Pinsky and S. L. Delp, "A 3D model of muscle reveals the causes of nonuniform strains in the biceps brachii," *Journal of Biomechanics*, vol. 38, no. 4, pp. 657-665, 2005.
- [127] S. S. Blemker and S. L. Delp, "Rectus femoris and vastus intermedius fiber excursions predicted by three-dimensional muscle models," *Journal of Biomechanics*, vol. 39, no. 8, pp. 1383-1391, 2006.
- [128] P. Meier and R. Blickhan, "FEM-simulation of skeletal muscle: the influence of inertia during activation and deactivation," *Skeletal Muscle Mechanics: from Mechanisms to Function*, p. 207, 2000.

- [129] F. Xu, T. J. Lu and K. A. Seffen, "Biothermomechanics of skin tissues," *Journal of the Mechanics and Physics of Solids*, vol. 56, no. 5, pp. 1852-1884, 2008.
- [130] A. Samani and D. Plewes, "A method to measure the hyperelastic parameters of ex vivo breast tissue samples," *Physics in Medicine and Biology*, vol. 49, no. 18, pp. 4395-4405, 2004.
- [131] R. Wang, Y. Liu, X. Luo, Y. Li and S. Ji, "A finite-element mechanical contact model based on Mindlin-Reissner shell theory for a three-dimensional human body and garment," *Journal of Computational and Applied Mathematics*, vol. 236, no. 5, pp. 867-877, 2011.
- [132] G. Barbarino, M. Jabareen, J. Trzewik, A. Nkengne, G. Stamatias and E. Mazza, "Development and validation of a three-dimensional finite element model of the face," *Journal of Biomechanical Engineering*, vol. 131, no. 4, p. 041006, 2009.
- [133] F. A. Duck, *Physical properties of tissues: a comprehensive reference book*, Academic Press, 1990.
- [134] J. Teran, E. Sifakis, S. S. Blemker, V. Ng-Thow-Hing, C. Lau and R. Fedkiw, "Creating and simulating skeletal muscle from the visible human data set," *IEEE Transactions on Visualization and Computer Graphics*, vol. 11, no. 3, pp. 317-328, 2005.

- [135] T. A. Krouskop, T. M. Wheeler, F. Kallel, B. S. Garra and T. Hall, "Elastic moduli of breast and prostate tissues under compression," *Ultrasonic Imaging*, vol. 20, no. 4, pp. 260-274, 1998.
- [136] J. F. Greenleaf, M. Fatemi and M. Insana, "Selected methods for imaging elastic properties of biological tissues," *Annual Review of Biomedical Engineering*, vol. 5, no. 1, pp. 57-78, 2003.
- [137] G. Tragardh and K. Olund, "A method for characterization of ultrafiltration membranes," *Desalination*, vol. 58, no. 3, pp. 187-198, 1986.
- [138] S. C. Cowin, *The mechanical properties of cortical bone tissue*, CRC Press, Boca Raton, FL, 1989.
- [139] M. R. Webster, R. De Vita, J. N. Twigg and J. J. Socha, "Mechanical properties of tracheal tubes in the American cockroach (*Periplaneta americana*)," *Smart Materials and Structures*, vol. 20, no. 9, p. 094017, 2011.
- [140] P. Prendergast, C. Lally, S. Daly, A. Reid, T. Lee, D. Quinn and F. Dolan, "Analysis of prolapse in cardiovascular stents: a constitutive equation for vascular tissue and finite-element modelling," *Journal of Biomechanical Engineering*, vol. 125, no. 5, pp. 692-699, 2003.

- [141] C. A. Leguy, E. M. H. Bosboom, H. Gelderblom, A. P. Hoeks and F. N. van de Vosse, "Estimation of distributed arterial mechanical properties using a wave propagation model in a reverse way," *Medical Engineering & Physics*, vol. 32, no. 9, pp. 957-967, 2010.
- [142] H. Liu, G. Canton, C. Yuan, C. Yang, K. Billiar, Z. Teng, A. H. Hoffman and D. Tang, "Using in vivo Cine and 3D multi-contrast MRI to determine human atherosclerotic carotid artery material properties and circumferential shrinkage rate and their impact on stress/strain predictions," *Journal of Biomechanical Engineering*, vol. 134, no. 1, p. 011008, 2012.
- [143] J. Krejza, M. Arkuszewski, S. E. Kasner, J. Weigele, A. Ustymowicz, R. W. Hurst, B. L. Cucchiara and S. R. Messe, "Carotid artery diameter in men and women and the relation to body and neck size," *Stroke*, vol. 37, no. 4, pp. 1103-1105, 2006.
- [144] T. J. Smilde, F. W. van den Berkmortel, G. H. Boers, H. Wollersheim, T. de Boo, H. van Langen and A. F. Stalenhoef, "Carotid and femoral artery wall thickness and stiffness in patients at risk for cardiovascular disease, with special emphasis on hyperhomocysteinemia," *Arteriosclerosis, Thrombosis, and Vascular Biology*, vol. 18, no. 12, pp. 1958-1963, 1998.
- [145] "Imaios - Thigh cross-section," [Online]. Available: <https://www.imaios.com/br/e-Anatomy/Extremidades/Membro-inferior-IRM>. [Accessed 8 May 2015].

- [146] A. Suessenbacher, J. Dorler, J. Wunder, F. Hohenwarter, H. F. Alber, O. Pachinger and M. Frick, "Comparison of brachial artery wall thickness versus endothelial function to predict late cardiovascular events in patients undergoing elective coronary angiography," *The American Journal of Cardiology*, vol. 111, no. 5, pp. 671-675, 2013.
- [147] "Cross-sectional view of Upper Arm," [Online]. Available: <http://www.imaios.com/en/e-Anatomy/Limbs/Upper-extremity-MRI>. [Accessed 8 May 2015].
- [148] P. C. Simons, A. Algra, M. L. Bots, D. E. Grobbee, Y. van der Graaf, "Common carotid intima-media thickness and arterial stiffness indicators of cardiovascular risk in high-risk patients the smart study (second manifestations of arterial disease)," *Circulation*, vol. 100, no. 9, pp. 951-957, 1999.
- [149] "Cross-sectional view of Neck," [Online]. Available: <https://www.imaios.com/en/e-Anatomy/Head-and-Neck/Face-and-neck-MRI>. [Accessed 8 May 2015].
- [150] K. Gayathri and K. Shailendhra, "Pulsatile blood flow in large arteries: comparative study of Burton's and McDonald's models," *Applied Mathematics and Mechanics*, vol. 35, no. 5, pp. 575-590, 2014.

- [151] D. Holdsworth, C. Norley, R. Frayne, D. Steinman and B. Rutt, "Characterization of common carotid artery blood-flow waveforms in normal human subjects," *Physiological Measurement*, vol. 20, no. 3, p. 219, 1999.
- [152] J. M. Benitez and F. J. Montans, "The mechanical behavior of skin: structures and models for the finite element analysis," *Computers & Structures*, vol. 190, pp. 75-107, 2017.
- [153] T. Sussman and K.J. Bathe, "A finite element formulation for nonlinear incompressible elastic and inelastic analysis," *Computers & Structures*, vol. 26, no. 1-2, pp. 357-409, 1987.

CURRICULUM VITAE

PERSONAL INFORMATION

Surname, Name: SALMAN, Hüseyin Enes

Nationality: Turkish (TC)

Date and Place of Birth: 04.05.1987, ANKARA

Marital Status: Single

Phone: 0506 797 0561

e-mail: salman@metu.edu.tr

EDUCATION

Degree	Institution	Year
M.S.	Mechanical Engineering Department, METU	2012
B.S.	Mechanical Engineering Department, METU	2009
High School	Çankaya Milli Piyango Anatolian High School	2005

PROFESSIONAL EXPERIENCE

Year	Place	Enrollment
2010-2018	METU/ME Department	Teaching & Research Assistant
2009-2010	Tübitak UZAY	Mechanical Engineer

AWARDS

- **Middle East Technical University (METU) Graduate Course Performance Award:**

“This is to certify that Hüseyin Enes Salman has been the most successful student in the Ph.D. Program of the Department of Mechanical Engineering, in the 2012-2013 Academic Year with CGPA of 3.93/4.00.”

PUBLICATIONS

International Conference Publications, Oral Presentations

- H. E. Salman, Y. Yazicioglu, "Investigation of on skin surface response due to acoustic radiation from stenosed blood vessels," *170th Meeting of the Acoustical Society of America, ASA2015*, Jacksonville, FL, USA, November 2-6, 2015.
- H. E. Salman, Y. Yazicioglu, "Skin surface response due to acoustic radiation from stenosed femoral artery," *23rd International Congress on Sound and Vibration, ICSV23*, Athens, Greece, July 10-14, 2016.
- H. E. Salman, Y. Yazicioglu, "Modelling of a neck with stenosed common carotid artery," *3rd International Conference on Biomedical Technology, ICBT2017*, Hannover, Germany, November 6-8, 2017.

National Conference Publications, Oral Presentations

- H. E. Salman, Y. Yazicioglu, "Damar tıkanıklıkları nedeniyle oluşan akustik yayılımın deri yüzeyine etkisinin irdelenmesi," *11. Ulusal Akustik Kongresi ve Sergisi, UAK2015*, Istanbul, Turkey, October 19-20, 2015.

Journal Publications

- H. E. Salman, C. Sert, Y. Yazicioglu, "Computational analysis of high frequency fluid-structure interactions in constricted flow," *Computers & Structures*, vol. 122, pp. 145-154, 2013.
- H. E. Salman, Y. Yazicioglu, "Flow-induced vibration analysis of constricted artery models with surrounding soft tissue," *Journal of the Acoustical Society of America*, vol. 142, no. 4, pp. 1913-1925, 2017.

Submitted Journal Publications (Under review)

- H. E. Salman, Y. Yazicioglu, "Computational analysis for noninvasive detection of stenosis in peripheral arteries," *Medical Engineering & Physics*, 2018.
- H. E. Salman, Y. Yazicioglu, "Experimental and numerical investigation on soft tissue dynamic response due to turbulence-induced arterial vibration," *Biomechanics and Modeling in Mechanobiology*, 2018.